DYNAMICS OF MULTI-PHOTON PROCESSES IN SEMICONDUCTOR HETEROSTRUCTURES

THÈSE N^{O} 2854 (2003)

PRÉSENTÉE À LA FACULTÉ DES SCIENCES DE BASE

Institut de photonique et d'électronique quantiques

SECTION DE PHYSIQUE

ÉCOLE POLYTECHNIQUE FÉDERALE DE LAUSANNE

POUR L'OBTENTION DU GRADE DE DOCTEUR ÈS SCIENCES

PAR

Daniel MARTI

ingénieur physicien diplômé EPF
de nationalité suisse et originaire d'Etziken (SO)

acceptée sur proposition du jury:

Dr M.-A. Dupertuis, directeur de thèse
Prof. J.-Ph. Ansermet, rapporteur
Prof. D. Citrin, rapporteur
Prof. B. Deveaud-Plédran, rapporteur
Prof. P. Thomas, rapporteur

Lausanne, EPFL
2003

Abstract

The present work is devoted to the study of the dynamics of multi-photon processes in semiconductor heterostructures. A time-dependent description is important for understanding in detail the transient response of semiconductors excited by ultrashort optical pulses.

In the first part of this thesis, we set up a phenomenological model based on rate equations, in order to investigate the possibility of measuring degenerate two-photon gain in a semiconductor microcavity. The amplification predicted by the model is fairly low ($\sim 2\%$) and mainly limited by the intra-band relaxation of the carriers, which leads to rapid saturation.

In the second part, we develop a general theory for the dynamics of multi-photon processes in semiconductors. It will give insight into complex effects related to the coherence between the bands, which are not included in usual absorption coefficients or susceptibilities. For this purpose, we derive effective multi-band Bloch equations that include resonant multi-photon processes induced by two linearly polarized electromagnetic pulses of frequency close to the band gap and close to the half of the band gap respectively. The benefit of the proposed approach is two-fold. First, the description of the dynamics is restricted to a reduced number of bands. However, the discarded bands are not neglected, but consistently taken into account in the higher order processes. Second, all quantities appearing in the effective multi-band Bloch equations vary on the same time scale, which makes the numerical integration much more efficient. The time-dependent polarization current, as well as some susceptibilities, are derived on a consistent level of approximation, and are discussed in detail. The propagation of the electromagnetic fields is neglected.

Such a model is appropriate for the description of low-dimensional quantum confined systems (*e.g.* quantum wells or quantum wires) excited by two colinearly propagating pulses. It accounts for various linear and nonlinear optical processes, such as one- and two-photon absorption, second-harmonic generation, difference-frequency mixing, or coherent control of photocurrent. In this thesis, the general theory is applied to the study of three specific physical situations.

First, we investigate the charge and spin current in a symmetric AlGaAs/GaAs quantum well, injected by interference between one- and two-photon inter-band transitions. We identify new coherent terms in the expression of the current, which contribute significantly to the terahertz emission. The effects of the Stark shifts and the inter-valence band two-photon transitions are also calculated and discussed.

Second, we calculate the anisotropic two-photon absorption spectra of an AlGaAs/GaAs V-shaped quantum wire with realistic band structure. The Coulomb interaction is taken into account within the Hartree-Fock approximation. The various excitonic peaks are identified with respect to the involved subbands and to the symmetry properties. We also show that excitons that are dark for one-photon excitation may become bright for two-photon spectroscopy, when the light is polarized perpendicularly to the growth direction, but not along a symmetry axis of the wire.

Finally, the last application focuses on the optical injection of current in the presence of excitonic effects. Concentrating on the same AlGaAs/GaAs V-shaped quantum wire, we show that the Coulomb interaction within the Hartree-Fock approximation induces terahertz oscillations in the injected charge current. The oscillation frequency corresponds to the energy spacing between the two lowest excitonic resonances, slightly below the band gap, excited respectively by the laser pulse with frequency close to the band gap, and the one with frequency close to the half of the band gap.

Version abrégée

La présente thèse est dédiée à l'étude de la dynamique des processus à plusieurs photons dans les hétérostructures à semi-conducteurs. Une description de la dépendance temporelle est importante pour une compréhension détaillée de la réponse transitoire de semi-conducteurs excités par des impulsions optiques ultracourtes.

Dans la première partie de la thèse, nous développons un modèle phénoménologique basé sur un ensemble d'équations de bilan, afin d'étudier le gain à deux photons dégénérés dans une microcavité à semi-conducteurs. L'amplification prédite par le modèle est relativement faible ($\sim 2\%$) et limitée principalement par la relaxation intra-bande des porteurs, qui débouche sur une saturation rapide.

Dans la seconde partie, nous développons une théorie générale pour la dynamique des processus à plusieurs photons dans les semi-conducteurs. Elle permettra d'accéder à des effets complexes, liés à la cohérence entre les bandes, qui ne sont pas inclus dans les habituels coefficients d'absorption ou susceptibilités. Dans ce contexte, nous dérivons un ensemble d'équations de Bloch effectives à plusieurs bandes, incluant des processus résonants à plusieurs photons induits par deux impulsions électromagnétiques linéairement polarisées, de fréquence ω_1 et ω_2, avec $\hbar\omega_1$ et $2\hbar\omega_2$ proches de l'énergie de la bande interdite (ou «gap»). L'approche proposée présente essentiellement deux avantages. Premièrement, la description de la dynamique est restreinte à un nombre limité de bandes. Toutefois, les bandes éliminées ne sont pas négligées, mais inclues de manière consistante dans les processus d'ordre supérieur. Deuxièmement, toutes les quantités apparaissant dans les équations de Bloch effectives varient sur la même échelle de temps, ce qui permet une intégration numérique beaucoup plus efficace. Le courant de polarisation dépendant du temps, ainsi que certaines susceptibilités, sont dérivés de manière consistante avec les approximations précédentes, et sont discutés en détail. La propagation des champs électromagnétiques est négligée.

Un tel modèle est approprié pour décrire des systèmes à basse dimension avec confinement quantique (puit quantique, fil quantique, etc.) excités par deux impulsions avec directions de propagation colinéaires. Il tient compte d'une variété de processus optiques, linéaires et non linéaires, tels que l'absorption à un ou deux photons, la génération de seconde harmonique, le mélange de fréquences, ou encore le contrôle cohérent de photo-courant. Dans cette thèse, la présente théorie générale est employée pour décrire trois situations physiques spécifiques.

Tout d'abord, nous étudions les courants de charge et de spin dans un puit quantique symétrique en AlGaAs/GaAs, injectés à l'aide d'interférences entre transitions à un et à deux photons. Nous identifions de nouveaux termes cohérents dans l'expression pour le courant, qui contribuent de manière significative à l'émission terahertz. L'impact de l'effet Stark dynamique et des transitions à deux photons entre bandes de valences est également évalué et discuté.

Ensuite, nous calculons le spectre d'absorption à deux photons, anisotropique, d'un fil quantique en V (en AlGaAs/GaAs), décrit par une structure de bande réaliste, en tenant compte de l'interaction coulombienne dans l'approximation de Hartree-Fock. Les différents pics excitoniques sont identifiés en fonction des sous-bandes impliquées et des propriétés de symétrie de l'exciton. De plus, nous montrons que les excitons inaccessibles par excitation à un photon peuvent être visibles par spectroscopie à deux photons, si le faisceau est polarisé dans une direction perpendiculaire à l'axe de croissance, mais différente d'un axe de symétrie du fil.

Finalement, la dernière application de la théorie concerne l'injection de photocourant en présence d'effets excitoniques. Prolongeant notre étude sur le fil quantique en V ci-dessus, nous montrons que l'interaction coulombienne, dans l'approximation de Hartree-Fock, provoque des oscillations terahertz dans le courant de charge injecté. La fréquence d'oscillation correspond à l'espacement en énergie entre les deux plus basses résonances excitoniques dans la bande interdite (ou «gap»), excitées respectivement par l'impulsion laser de fréquence ω_1 proche du gap et par celle de fréquence ω_2 proche du milieu gap.

Remerciements

En premier lieu, je tiens à remercier chaleureusement Marc-André Dupertuis, mon directeur de thèse, pour sa disponibilité et son soutien tout au long de ce travail. Je lui suis très reconnaissant d'avoir partagé sa connaissance scientifique et sa passion pour la physique lors des longs entretiens suivant mes nombreuses intrusions dans son bureau.

Je remercie également Benoît Deveaud-Plédran pour toutes les discussions enrichissantes, notamment sur les liens entre le monde idéal, cadre de mon travail théorique, et le monde réel dont il faut finalement s'accommoder.

Un grand merci à tous les membres de l'institut que j'ai eu la chance de côtoyer ces quatre années durant, et dont beaucoup sont devenus et, je l'espère, resteront d'excellents amis. Sans eux, cette période n'aurait jamais eu la même valeur à mes yeux.

Finalement, je tiens à exprimer ma profonde reconnaissance à mes parents, ma soeur et mon frère qui m'ont toujours soutenu (et supporté) au cours de ces années.

Contents

1 Introduction

In recent decades, electronic transitions involving more than one photon have attracted much attention in many fields of optics. Although the theory of multiple quantum transitions was first studied in 1931 by Maria Göppert-Mayer [1], it was necessary to await the appearance of lasers, and thus of the possibility to generate radiation of very high intensity, to open the way to experimental studies at the beginning of the Sixties [2, 3]. Since then, the importance of multi-photon transitions was demonstrated for many applications. The generation of coherent light by stimulated two-photon emission is rapidly proposed [4], but the first continuous two-photon laser was realized only much later in a gaseous medium [5]. Other major applications of the multi-photon transitions appeared in spectroscopy. First, let us mention the Doppler-free two-photon spectroscopy in gases [6], thanks to which the Doppler broadening related to the motion of the atoms can be eliminated. Second, one takes advantage of the fact that the selection rules for electronic transitions involving several photons differ in general from those for transitions implying only a single photon. Consequently, multi-photon spectroscopy becomes an interesting tool to collect complementary information to conventional spectroscopy, in particular on energy levels inaccessible to one-photon absorption. Moreover it provides additional degrees of freedom by varying the polarizations of the various electromagnetic waves with respect to one another and to the crystal axes. The theoretical description of these selection rules and polarization dependence for the different crystallographic point groups was initiated by Inoue and Toyozawa [7] and eventually extended by several authors [8–12].

In semiconductors, two-photon absorption plays a significant role in many applications. Let us mention the ultrafast dynamics of optical amplifiers [13], ultrafast optical switching [14], generation of squeezed electromagnetic states [15] and coherent control of photocurrent [16].

From the theoretical point of view, two different approaches are usually used to evaluate the multi-photon transition probabilities. The least spread, proposed by Keldysh [17], works in the so-called S-matrix formalism and was applied to semiconductors by various authors for simple isotropic effective-mass models [18–20]. The wave functions of the initial and final states required by this method are derived from the exact solutions of the Schrödinger equation for an electron subjected to an electromagnetic plane wave (Volkov states).

The second approach uses perturbation theory to higher orders [1] to calculate the electronic transition probability. In this method, the multi-photon transitions involve a complete set of intermediate states, usually Bloch functions or excitonic states, whose individual contributions are weighted by the optical coupling and the energy spacing. An alternative use of the perturbation theory is the calculation of optical susceptibilities in the formalism of the nonlinear response [21]. The absorption coefficient and the refractive index can then be extracted from the real and imaginary parts of the susceptibilities. In practice, it is in general necessary to restrict the complete set of intermediate states to a finite sub-set supposed to provide the main contribution to the transition probability. In this context, many models including various bands were proposed for two-photon excitation of an electron from a valence band to a conduction band. For three-dimensional crystals, let us mention models with two bands [22–24], three bands [25, 26], four bands [27–29] and seven bands [30, 31]. Furthermore, several authors included also excitonic effects in their theories [22, 23, 30, 32].

With the progress in crystal growth techniques, the research on two-photon transitions extended to semiconductor nanostructures in the eighties. It turned out that the two-photon conduction-to-valence-band absorption in quantum wells depends strongly upon the polarization of the electromagnetic field with respect to the direction of quantum confinement [33, 34]. Furthermore, a precise calculation of the two-photon transition rate in quantum wells with finite barriers may require the contribution due to the continuum states. Pasquarello *et al.* [35] concluded that the continuum contribution is negligible for polarization in the layer plane, whereas it becomes important in the case of polarization along the growth axis. Excitonic effects have also been included within different models [36–38].

Whereas two-photon absorption has been studied extensively in quantum wells, both experimentally and theoretically, it has received much less attention in quantum wires. First measurements of two-photon absorption spectra were reported in rectangular [39] and V-shaped quantum wires [40], while Shimizu *et al.* [41] and Ogawa *et al.* [42] developed a simple effective-mass model with excitons included through an analytically solvable model for an electron-hole pair interacting with a modified Coulomb potential [43]. Khurgin [44] also computed the two-photon absorption for quantum wires with square cross section of different widths, but neglected excitonic effects.

The calculation of accurate transition probabilities requires a good knowledge of the electronic band structure. Most of the results published (and all studies quoted above) were obtained with a $\boldsymbol{k}\cdot\boldsymbol{p}$ theory [45] valid around the band extrema, associated to envelope function methods [46, 47] in the case of heterostructures. Other ab-initio approaches, known as "tight-binding" and pseudo-potential models were sometimes used for bulk crystals [48–51].

The previous overview concentrated on two-photon absorption. This is a peculiar multi-photon process related to the third-order susceptibility $\chi^{(3)}$, which also describes several other nonlinear optical processes, as, for instance, stimulated Raman scattering. On the other hand, many common nonlinear processes, such as sum- and difference-frequency mixing, including second-harmonic generation and parametric amplification, are related to the second-order susceptibility $\chi^{(2)}$. For the latter to be nonzero, the system must not have a center of symmetry. This is easily achieved in semiconductors, by engineering asymmetric heterostructures and/or applying an external electric field. Furthermore, the optical nonlinearities are enhanced when certain frequencies fall in the vicinity of transition frequencies of the medium ("resonance enhancement"). In this context, several theoretical studies focused on the second-order susceptibility in asymmetric (multi-) quantum wells, especially for second-harmonic generation, enhanced by conduction-to-valence band transitions [52–63], or enhanced by inter-subband transitions between conduction subbands [64, 65] or valence subbands [66–70].

All theoretical works quoted above focused on absorption probabilities and/or susceptibilities and are valid for multi-photon transitions *in the stationary regime only.* The approach used to include their effects on the dynamics is generally limited to a phenomenological description based on rate equations [71–73]. The subject of this thesis is to fill this gap by developing a theory for the dynamics of multi-photon transitions, initiated in the past nineties by Selbmann *et al.* [74] who studied the interaction of an electromagnetic wave with a one-dimensional diatomic chain.

In the first part of this thesis, we consider the feasibility of two-photon gain in a semiconductor microcavity. This question is addressed in chapter 2 with a simple model of rate equations describing the interplay between the density of electromagnetic energy in the cavity and the density of electron-hole pairs in two parabolic bands of the embedded quantum wells.

The second part of this thesis is dedicated to a microscopic theory for the *dynamics* of multi-photon processes in semiconductors. A time-dependent description is important for understanding in detail the transient response of semiconductors excited by ultrashort pulses, as is the case for instance by pump and probe measurements. It gives insight into complex effects related to the coherence between the bands, which are not included in usual absorption coefficients or susceptibilities. For this purpose, effective multi-band Bloch equations are derived in chapter 3. The theory includes resonant one- and two-photon processes (and their interplay), induced by two linearly polarized electromagnetic pulses of frequencies close to the band gap and close to the half of the band gap respectively. The benefit of the proposed approach is two-fold. First, the description of the dynamics is restricted to a reduced number of bands. However, the discarded bands are not neglected, but consistently taken into account in the higher order processes. Second, all quantities remaining in the effective multi-band Bloch equations vary on the same time scale, which makes their numerical integration much more efficient.

The model is appropriate for the description of low-dimensional quantum confined systems (*e.g.* quantum wells or quantum wires) excited by two colinearly propagating pulses. It accounts for various linear and nonlinear optical processes, such as one- and two-photon absorption, second-harmonic generation, difference-frequency mixing, or coherent control of photocurrent.

The nonlinear phenomena described by the effective equations of motion may be strongly coupled, especially when the optical frequencies become equal to transition frequencies of the medium. In this context, an interesting issue that can be properly addressed by our model is the interplay between different processes. By way of example, let us mention the competition between two-photon absorption/gain and parametric amplification (a $\chi^{(3)}$ and $\chi^{(2)}$ process respectively), when the optical frequencies approach and eventually cross the band gap.

An accurate description of the optical transition rates requires also a detailed band structure. In chapter 4, we thus summarize the envelope function technique and calculate the energy bands and momentum matrix elements of a typical quantum well, including the valence-band mixing. Some important symmetry properties are also discussed.

The effective multi-band Bloch equations are finally applied to three situations, discussed in chapter 5, 6 and 7 respectively. First we study the optical injection of pure charge and spin current in a quantum well by interference between one- and two-photon transitions induced by two phase-related femtosecond laser pulses of frequency ω and 2ω. Second, the two-photon absorption spectrum of a V-shaped quantum wire is computed, taking into account the Coulomb interaction within the Hartree-Fock approximation. And third, with the same model including excitonic effects, we show that the interferences between excitonic coherences result in an oscillating charge current, when the quantum wire is excited slightly below the band gap by two laser pulses of frequency ω and 2ω. Finally, the conclusions are drawn in chapter 8.

The content of this thesis can be divided in two parts of unequal length. The first part contains only chapter 2, which addresses the feasibility of two-photon gain in a semiconductor microcavity. The second part gathers chapter 3–7, which focus on the microscopic theory and its applications. Although both parts concern the dynamics of multi-photon processes in semiconductor heterostructures, they may in principle be read independently. The reader interested only in the microscopic theory can skip chapter 2 and start with chapter 3.

2 Feasibility study for degenerate two-photon gain in a semiconductor microcavity

2.1 Introduction

Whilst two-photon absorption in semiconductors received much attention, degenerate two-photon gain has virtually not been looked at in semiconductors. A few years ago, Ironside estimated two-photon gain [75] and concluded about the feasibility of amplification devices. There are peculiarities linked with two-photon gain that makes it attractive. While the one-photon gain does not depend on the amplified beam intensity, the two-photon transition gain increases linearly with intensity. As a result, the amplification is boosted at high optical powers, and a two-photon laser displays a threshold typical of a first order phase transition [5, 76]. The two-photon laser has been a recurring theme in quantum optics since its proposition in 1964 [4]. It has also been a quite elusive experimental goal, mainly because of the smallness of typical two-photon stimulated emission rates and the high saturation intensities. The first population inversion and gain was achieved 14 years after the first proposition [77], the first pulsed two-photon laser operation in 1981 [78], the two-photon micromaser in 1987 [79], and finally CW operation was reached in 1992 [5]. From the theoretical point of view, the field has remained quite vivid [80–91], with semi-classical or quantum models, addressing many interesting aspects of two-photon laser operation, like threshold behavior, dynamic instabilities, quantum features, the good and bad cavity limit, few and many atom situations, non-degenerate operation, driven operation, chaotic dynamics, etc... Today the field is spurred by applications involving the purely quantum aspects of light, like quantum cryptography and precision measurements, as well as quantum teleportation [92, 93]. In semiconductors, two-photon gain could also be advantageous by releasing constraints linked with the semiconductor band-gap of common practical materials, *e.g.* provide lasing at 1.55μm in GaAs.

In this chapter, we restrict to the investigation of "pure" degenerate two-photon gain in semiconductors. By the adjective "pure", we mean that only pure population effects are the source of the two-photon gain. The characteristic of a pure two-photon amplifier or laser is to provide *phase independent* gain. In principle, such a population can be achieved by electrical or optical pumping, the main requirement on the pumping mechanism being that it does not inject coherence. Ironside [75], who investigated the feasibility of two-photon gain in semiconductors, did neglect a number of important effects like saturation. In this chapter, we take a closer look at this issue and analyze realistically the magnitude of pure two-photon gain in the case of several quantum wells (QWs) embedded in a resonant microcavity. The role of the microcavity is to provide integrated mirrors at the mid-gap wavelength and enhance the photon lifetime.

Let us discuss a suitable pumping mechanism. In semiconductors, the required high injection rates eliminate in practice electrical pumping, and suggest the use of intense pulsed coherent optical beams. The optical pumping efficiency is in principle maximum at resonance. However, at resonance, (phase-dependent) parametric processes would occur simultaneously and significantly contribute to the two-photon gain/absorption. We are thus left with *off-resonant optical pumping*, which requires an efficient internal relaxation mechanism.

In the following, the dynamics of the degenerate two-photon transition at the semiconductor band-edge is studied with the help of a set of coupled phenomenological rate equations. The system is modeled by considering electron-hole pair densities, interacting with two electromagnetic fields described by homogeneous photon densities. The pairs created by the pumping field relax to lower energy states, where they interact with the two-photon resonant field. The relaxation is specified by a characteristic time and the two-photon transition cross-section is estimated from two-photon absorption measurements [94]. The photon lifetimes are set by the Bragg mirror reflectivities, and the effect of the feeding pulses is described by source terms. Using these equations, we estimate, with realistic physical parameters, the integrated gain that can be expected in a pump-probe measurement. We also derive an analytical formula for the differential transmission, resulting from various approximations on the rate equations.

The chapter is organized as follows. In section 2.2 the rate equation model is derived. The numerical results are discussed in section 2.3. Section 2.4 presents an analytical approximation showing clearly the dependence of the gain on the various physical parameters. Finally, conclusions are drawn in section 2.5.

2.2 Model

In the following, we assume the injection of two different quasi-monochromatic electromagnetic fields: the pump pulse of frequency ω_1 (wavelength λ_1) and the seed pulse of frequency ω_2 (wavelength λ_2). Their frequencies fulfill the condition $\omega_1 > 2\omega_2$ and their pulse shapes (intensities) are Fourier transform-limited, and are

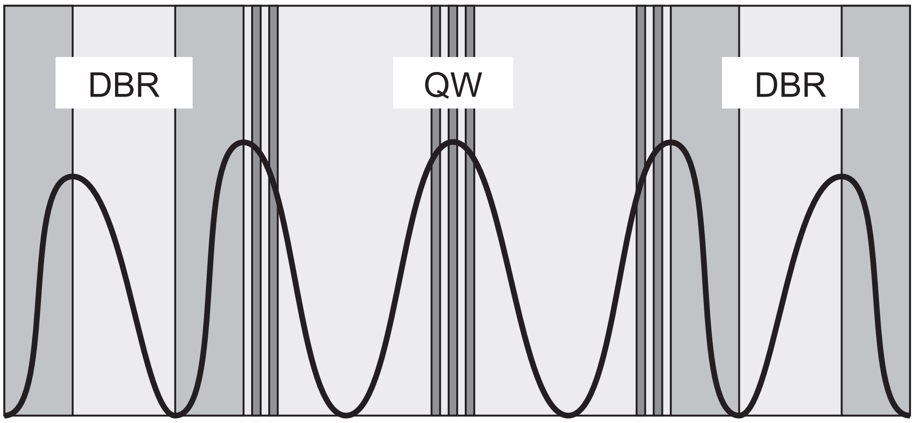

Figure 2.1: Several quantum wells (QW) at maxima of the field intensity in a λ-cavity ($\sim 0.5\ \mu$m) delimited by two distributed Bragg reflectors (DBR). The length of the whole structure is about 15 μm.

given by

$$I_i(t) = \bar{I}_i \cosh^{-2}(t/T_i)\,, \quad i = 1, 2 \tag{2.1}$$

where the pulse durations at half maximum correspond to $1.76\,T_i$.

2.2.1 Heterostructure

We assume the optimized microcavity structure shown in Figure 2.1. An AlGaAs λ_2-cavity is delimited by two AlGaAs/AlAs $\lambda_2/4$ Bragg reflectors with an aluminum concentration of 31.5%. Several identical GaAs quantum wells are placed at antinodes of the electric field in the cavity. The number of wells is included in the model through the *total* width l of the active region and the density of states in the QWs. The right and left reflectivities R_r and R_l, the spectral width of the cavity mode, and the effective length L of the cavity are obtained by solving the Helmholtz equation by a numerical method equivalent to standard transfer matrix calculations.

For our calculations, GaAs QWs have been used. However, in order to avoid absorption in the substrate, they could be replaced by deeper InGaAs QWs.

2.2.2 Rate equations

The electromagnetic waves are included in the model in terms of the photon densities S_1 and S_2 for the ω_1- and degenerate ω_2-photons respectively. The cavity does not significantly affect the ω_1-pulse, as the frequency ω_1 can easily be set to a lateral node of the harmonic of the λ_2-cavity reflectivity. The pump photon density is therefore proportional to the time dependent field intensity in the well:

$$S_1 = \frac{n_\mathrm{w}}{c} \frac{I_1}{\hbar\omega_1} \,. \tag{2.2}$$

The seed photons are introduced in the cavity by a source term

$$R_2 = \frac{I_2}{\hbar\omega_2 L} \tag{2.3}$$

with a finite lifetime

$$\frac{1}{\tau_2} = -\frac{1}{2L} \ln(R_l R_r)(c/n_\mathrm{c}) \tag{2.4}$$

due to the mirror losses. c is the speed of light and n_c (n_w) the refractive index in the cavity (well) for the corresponding frequency. The time evolution of the homogeneous S_2 density is therefore given by

$$\dot{S}_2 = -S_2/\tau_2 + R_2 \,. \tag{2.5}$$

Here, I_1 and I_2 have to be understood as the intensities of the light *entering the cavity* and must therefore be divided by adequate in-coupling coefficients to retrieve the intensities outside the microstructure.

The band structure of the quantum wells is modeled by two parabolic bands and the corresponding carriers described by three electron-hole pair densities N_1, N_2 and N_3 (Figure 2.2). The N_1 states are excited by absorption of single ω_1-photons. Due to intra-band scattering, the created e-h pairs relax with a characteristic time τ_r to the N_2 states, where they couple to the ω_2-pulse by stimulated two-photon transitions. Because of the energy conservation, the densities N_1 and N_2 of e-h pairs interacting with photons are limited by the spectral widths of the ω_1-pulse and the cavity mode respectively. N_3 regroups all optically inactive pairs with energy between $2\hbar\omega_2$ and $\hbar\omega_1$, and are used as intermediate states for the relaxation from N_1 to N_2. Direct transfer from N_1 to N_2 is neglected. The states with energy below $2\hbar\omega_2$ do not contribute to the dynamics, and are considered to be always occupied. The whole process is described by the following set of rate equations.

$$\dot{N}_1 = -A(N_1 - \bar{N}_1)S_1 - \theta(N_1)\,(N_3^\mathrm{max} - N_3)/\tau_r \tag{2.6}$$

$$\dot{N}_2 = -\frac{1}{2}B(N_2 - \bar{N}_2){S_2}^2 + \theta(N_3)\,(N_2^\mathrm{max} - N_2)/\tau_r \tag{2.7}$$

$$\dot{N}_3 = +\theta(N_1)\,(N_3^\mathrm{max} - N_3)/\tau_r - \theta(N_3)\,(N_2^\mathrm{max} - N_2)/\tau_r \tag{2.8}$$

$$\dot{S}_2 = +B(N_2 - \bar{N}_2){S_2}^2 - S_2/\tau_2 + R_2 \,, \tag{2.9}$$

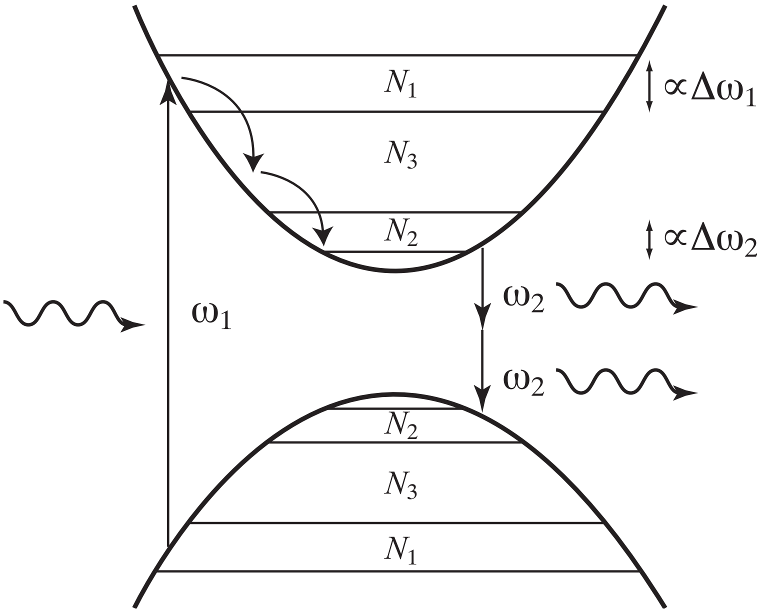

Figure 2.2: Parabolic subbands e$_1$-h$_1$ of the quantum wells divided in three regions with electron-hole densities N_1, N_2 and N_3. The densities N_1 and N_2 are coupled to the electromagnetic fields of frequency ω_1 and ω_2 by one- and two-photon transitions respectively. The energy ranges of the optically active carriers are related to the spectral widths $\Delta\omega_i$ of the two fields, and the maximal densities $N_1^{\max}$ and $N_2^{\max}$ are thus given by (2.10). One must keep in mind that the number of states in the two bands are identical despite the different curvatures (not shown here).

where $\theta(N)$ is the Heaviside function taking the value 1 or 0 for positive or negative N respectively. The density of states of a two-dimensional parabolic band is given by $m/(\pi\hbar^2)$. The total densities of optically active states $N_1^{\max}$ and $N_2^{\max}$ are limited by the spectral width $\Delta\omega_1$ and $\Delta\omega_2$ of the corresponding field, and thus obtained by

$$N_i^{\max} = \frac{jm_r}{\pi\hbar}\,\Delta\omega_i\,, \tag{2.10}$$

where j is the number of QWs and m_r is the reduced mass of the e-h pairs. $N_3^{\max}$ corresponds to the sum of intermediate states between $2\hbar\omega_2$ and $\hbar\omega_1$. $\bar{N}_1$ (respectively, $\bar{N}_2$) is the transparency density and A (B) is related to the differential gain of the one-photon (two-photon) transition. These quantities are defined more precisely in what follows. All densities S and N correspond to a *surface* unit.

The physical model for the relaxation process in the rate equations (2.6) to (2.8) deserves some comments. The maximal two-photon amplification should be achieved in high excitation regime, and the priority in our model is thus given to the situation of strongly occupied bands, which means N_1 and N_3 close to their maximal values. The central assumption related to this configuration is that the density of unoccupied states $(N_2^{\max} - N_2)$ decreases with a characteristic *in*-scattering time τ_r, *that does not depend on the large population density at higher energy.* On the contrary, a carrier transfer modeled by an *out*-scattering rate, *i.e.* $\dot{N}_1 = -N_1/\tau_r$ and $\dot{N}_3 = -N_3/\tau_r$, would imply $\dot{N}_2 = N_3/\tau_r$ in order to fulfill carrier conservation. The transfer rate from the large reservoir N_3 to the optically active density N_2 would then strongly depend on the value of N_3. The Heaviside functions just stop the relaxation process if there are no more carriers available, and ensure so that the densities remain positive. This blocking mechanism is very simple, but describes the main effects and contributes only during the initial phase where the inversion is building up. The Pauli blocking, on the other hand, is described by the fact that the relaxation slows down when the density of unoccupied final states $N_i^{\max} - N_i$ decreases, and eventually stops when all states are occupied $(N_i = N_i^{\max})$.

As a final remark, we do not assume thermal equilibrium, although it is clear that the model does not take into account the details of the carrier distributions *within* the three groups. The densities N_i are not related by a Fermi distribution but evolve independently out of mutual equilibrium, due to the fields and to the transfer between the three populations. However, if the relaxation is faster than the optical transitions, one recovers thermal equilibrium in the sense that the density N_3 (respectively, N_1) remains zero as long as the states of lower energy are not all occupied, *i.e.*, as long as the density N_2 (respectively, N_3) is not maximal.

The linear material gain g_1 is defined by $dI_1/dz = g_1\, I_1$ where I_1 is the light intensity and z the position. The carrier density dependence of the gain is approximated by the linear relation $g_1(N_1) = a(N_1 - \bar{N}_1)$ where the differential gain a and the transparency density $\bar{N}_1$ are related to the usual absorption coefficient α and the maximal density $N_1^{\max}$ through the two conditions $g_1(0) = -\alpha$ and $g_1(N_1^{\max}) = +\alpha$. The positive absorption coefficient α is defined/measured for an unexcited system. The first condition thus expresses the fact that the gain is the negative of the absorption, whereas the second equation assumes that the gain at full population inversion is equal to the absorption at zero population.

The two-photon gain can be described by $dI_2/dz = g_2\, {I_2}^2$ (note the square here, and the units implied). In a similar way as for the one-photon case, it is reasonable to assume $g_2(N_2) = b(N_2 - \bar{N}_2)$ and the relations $g_2(N_2^{\max}) = +\beta$ and $g_2(0) = -\beta$ where β is the usual two-photon absorption coefficient. For our case, β depends on the two-photon absorption cross-section, which can be obtained from measurements, and $N_2^{\max}$ is the full inversion density and will be estimated from the corresponding one-photon case (at λ_2).

We want to stress here that $\bar{N}_1$ and $\bar{N}_2$ are not the transparency densities at thermal equilibrium usually used in lasers [95], because they relate only to the optically active population within $\hbar\Delta\omega_1$ and $\hbar\Delta\omega_2$ (Figure 2.2). This explains the low values in Table 2.1.

For the gain in the QWs, we finally get

$$g_1(N_1) = (2\alpha/N_1^{\max})(N_1 - N_1^{\max}/2) \tag{2.11}$$
$$g_2(N_2) = (2\beta/N_2^{\max})(N_2 - N_2^{\max}/2)\,. \tag{2.12}$$

In order to take into account the standing wave pattern and the length of the active region (QWs) in the microcavity, a confinement factor Γ_2 has to be included in the two-photon term, and is calculated below. It describes the fact that S_2 represents the averaged photon density in the whole cavity and not only in the wells. As a result, the quantities A, B and $\bar{N}_i$ in the rate equations can be written as

$$A = (2\alpha/N_1^{\max})(c/n_{\mathrm{w}}) \tag{2.13}$$
$$B = (2\beta/N_2^{\max})(c/n_{\mathrm{w}})^2(\Gamma_2)^2\hbar\omega_2/l \tag{2.14}$$

and

$$\bar{N}_1 = N_1^{\max}/2 \tag{2.15}$$
$$\bar{N}_2 = N_2^{\max}/2\,. \tag{2.16}$$

n_{w} is the refractive index in the well for the corresponding frequency. Our description by means of averaged photon densities implies that any change by mirror losses or absorption/emission in the QWs is instantaneously spread over the entire cavity.

The confinement factor Γ for the one-photon transition is defined by the equation

$$R = \Gamma g_t U \tag{2.17}$$

connecting the electromagnetic energy variation per time unit R to the total electromagnetic energy U in the cavity. g_t is the gain coefficient per time unit. If the influence of the QWs is neglected, the energy density u is constant over the cavity, and

$$U = L\,u = L\,(u^{(e)} + u^{(m)}) \tag{2.18}$$

where $u^{(e)}$ and $u^{(m)}$ are related to the electric and magnetic fields respectively. According to the continuity equation, the source term for the energy density is given by $r = 2g_t u^{(e)}$. As the QWs are narrow with respect to the wavelength, R can be approximated by $R \simeq l\,r = 2g_t l\,u_{\mathrm{w}}^{(e)}$, and the confinement factor expressed as

$$\Gamma = 2(l/L)(u_{\mathrm{w}}^{(e)}/u_{\mathrm{c}})\,. \tag{2.19}$$

The subscripts label the energy in the cavity (c) and in the well (w). Whereas the total energy density u is constant over the cavity, its electric and magnetic contributions display a standing wave pattern. At a maximum of the electric field, the magnetic energy vanishes and $u_{\mathrm{w}}^{(e)} = u_{\mathrm{w}}$. As the electric field is continuous at interfaces, the confinement factor for the linear regime finally becomes

$$\Gamma = 2(l/L)(n_{\mathrm{w}}/n_{\mathrm{c}})^2\,. \tag{2.20}$$

It can be shown (Appendix A) that in the limit where the influence of the active region is neglectable, the confinement factor Γ_2 for *two-photon* transitions is related to Γ by

$$\Gamma_2 = \frac{\Gamma}{\sqrt{\Gamma^2 + (1-\Gamma)^2}}\,. \tag{2.21}$$

For small Γ as is the case in our structure, Γ_2 is therefore close to Γ.

We define the total relative amplification as the ratio $\Delta S_2/S_2^{\mathrm{tot}}$ between the additional ω_2-photons ΔS_2 resulting from the stimulated two-photon emission, and the total photon density S_2^{tot} introduced in the cavity. The former is calculated by the difference between the time-integrated mirror losses with and without the pump laser, and the latter is given by the time-integrated photon density carried by the pulse:

$$S_2^{\mathrm{tot}} = \frac{2\bar{I}_2 T_2}{\hbar\omega_2}\,. \tag{2.22}$$

$\Delta S_2/S_2^{\mathrm{tot}}$ is therefore equivalent to the differential transmission.

2.3 Numerical results

In the following, we choose realistic parameters and solve numerically the two-photon gain dynamics for an optimized λ_2-cavity containing 11 QWs of 70 Å width. As the two-photon absorption increases with the transition energy, the latter should be chosen well above the band gap. Therefore we take $\hbar\omega_2 = 0.80$ eV for the two-photon frequency, and $\hbar\omega_1 = 1.65$ eV for the one-photon frequency. We use high mirror reflectivities of 99.76% and 99.80%, which corresponds to 59 layers on a GaAs substrate for the right facet and 52 layers with an air-AlGaAs interface for the left (input-) facet respectively. This leads to an effective cavity length $L = 2.3\ \mu$m and a confinement factor $\Gamma_2 \simeq 0.077$. Taken into account the reduced effective mass $m_r = 0.0556\, m_0$ of the e-h pairs, the spectral width $\hbar\Delta\omega_2 \simeq 0.056$ meV of the microcavity corresponds to a density of optically active states per well $N_2^{\mathrm{tot}}/j = 1.3 \cdot 10^9\ \mathrm{cm}^{-2}$. Such a narrow linewidth is in accordance with present growth possibilities, as a

One-photon transition energy	$\hbar\omega_1$	1.65 eV
Two-photon transition energy	$2\hbar\omega_2$	1.60 eV
Left mirror reflectivity	R_l	99.80%
Right mirror reflectivity	R_r	99.76%
Effective length of the cavity	L	2.3 μm
Number of quantum wells	j	11
Width of the quantum wells	l	11 × 70 Å
Confinement factor	Γ_2	0.077
Carrier relaxation time	τ_r	100 fs
λ_2-photon lifetime in the cavity	τ_2	11.5 ps
One-photon absorption coefficient	α	2000 cm^{-1}
Two-photon absorption coefficient	β	20 cm/GW
Refractive index in the well (ω_1/ω_2)	n_w	3.72/3.38
Refractive index in the cavity (ω_1/ω_2)	n_c	3.48/3.27
Reduced effective mass	m_r	$0.0556\,m_0$
Density of states available for the one-photon transitions	N_1^max	$11 \times 3.0 \cdot 10^{10}$ cm^{-2}
Density of states available for the two-photon transitions	N_2^max	$11 \times 1.3 \cdot 10^{9}$ cm^{-2}
Density of intermediate states for the relaxation	N_3^max	$11 \times 1.2 \cdot 10^{12}$ cm^{-2}

Table 2.1: Physical parameters used in the rate equations.

Fabry-Pérot resonator with a measured linewidth of 0.84 Å (0.12 meV) at 930 nm (1.33 eV) has already been grown [96].

The details of the pumping scheme are not important as long as the pump is strong enough. Thus, a pump pulse with a peak intensity $\bar{I}_1 = 1$ GW/cm^2 and a duration of 1 ps at half maximum is well suited for our purpose, and its spectral width $\hbar\Delta\omega_1 = 1.3$ meV corresponds to a density of available e-h states $N_1^\text{max}/j \simeq 3.0 \cdot 10^{10}$ cm^{-2}. According to the energy spacing between the one- and two-photon transitions, the density of intermediate states for the relaxation is $N_3^\text{max}/j \simeq 1.2 \cdot 10^{12}$ cm^{-2}. The crucial two-photon absorption coefficient $\beta \simeq 20$ cm/GW at 0.8 eV is taken from measurements in a multiple quantum well waveguide [94], and the less important one-photon absorption coefficient α is set to a reasonable value of 2000 cm^{-1}. Finally, the high carrier density injected by the pump suggests to take a short relaxation time τ_r of 100 fs. All these physical parameters are summarized in Table 2.1.

Figure 2.3 shows the differential transmission $\Delta S_2/S_2^\text{tot}$ versus the peak intensity $\bar{I}_2$ of the two-photon field for a pulse duration of 1 ps at half maximum. The curve displays a clear unique maximum of $\sim 2.3\%$ at the optimal peak intensity $I_2^\text{opt} \simeq 7$ MW/cm^2. Numerical calculations taking into account the spectral distribution of the pulse and the structure of the microcavity indicate that $\sim 9\%$ of the pulse energy couples to the cavity mode. The peak intensity *outside* the microstructure

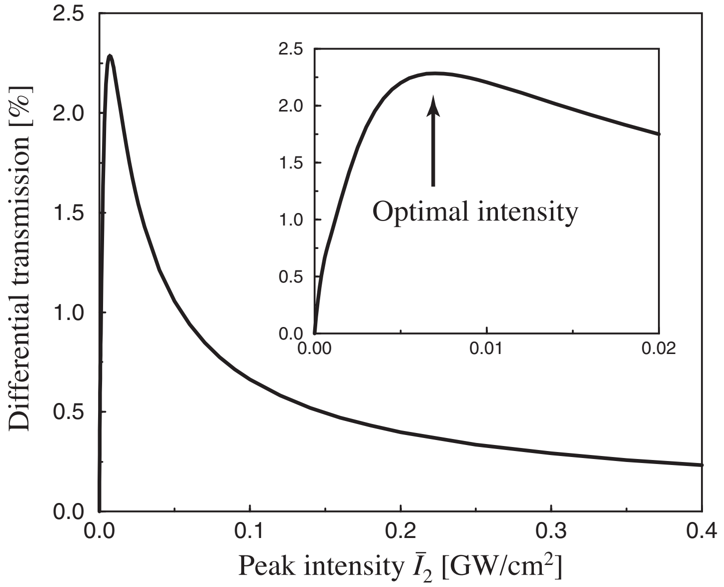

Figure 2.3: Differential transmission as a function of the peak intensity of the two-photon pulse. The inset is a blow-up of the low $\bar{I}_2$ intensity region.

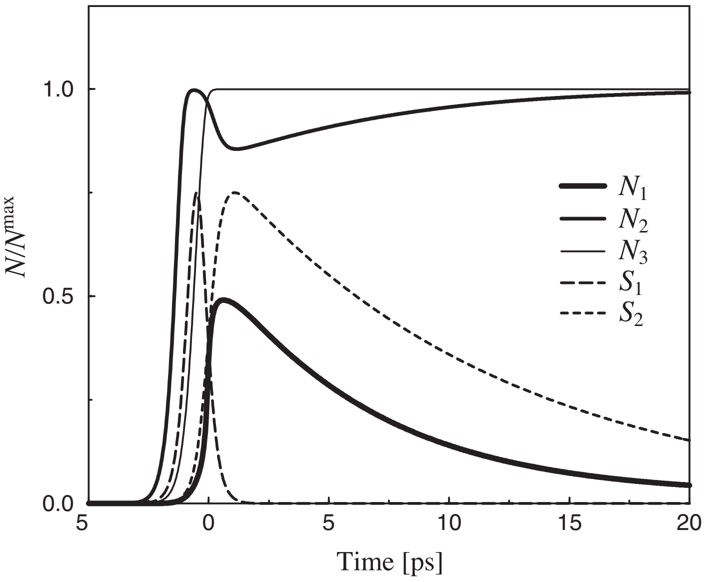

Figure 2.4: Time evolution of the carrier and photon densities for a two-photon peak intensity $\bar{I}_2 = 2.5$ MW/cm^2 below the optimal value. The photon densities S_1 and S_2 have been scaled.

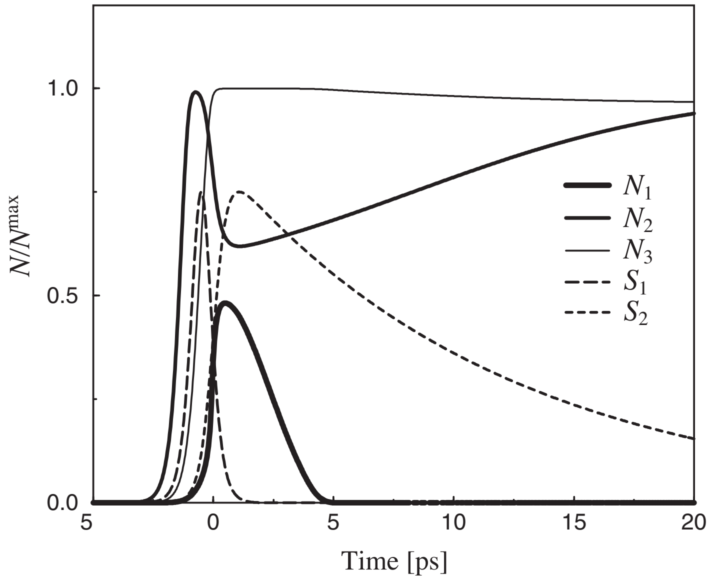

Figure 2.5: Time evolution of the carrier and photon densities for the optimal two-photon peak intensity $\bar{I}_2 = 7$ MW/cm^2. The photon densities S_1 and S_2 have been scaled.

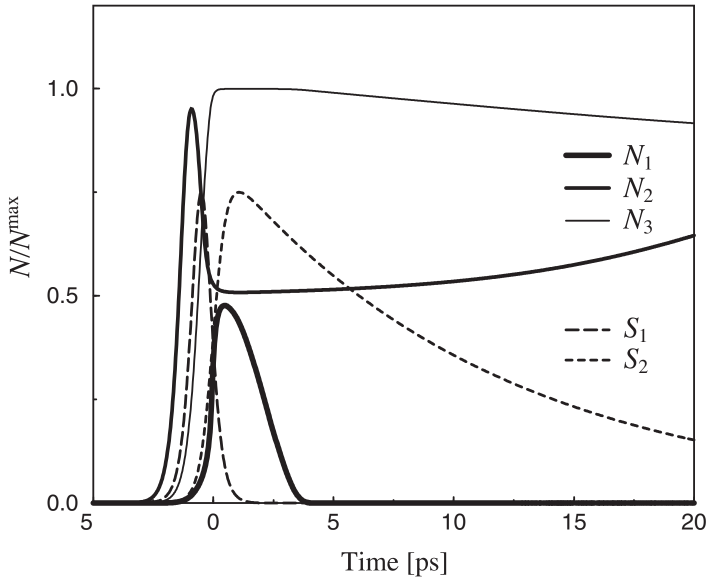

Figure 2.6: Time evolution of the carrier and photon densities for a two-photon peak intensity $\bar{I}_2 = 30$ MW/cm^2 above the optimal value. The photon densities S_1 and S_2 have been scaled.

should therefore be about 80 MW/cm^2. The increase of the relative gain reflects the nonlinear behavior of the two-photon amplification, whereas, for higher optical power, saturation takes place. The time evolution of the carrier and photon densities is shown in Figures 2.4–2.6 for two-photon intensities below, at, and above the optimal value, respectively. As the pump pulse transits through the cavity, the e-h pairs are excited and relax rapidly to the bottom of the bands. The carrier density N_2 increases until it reaches full inversion ($N_2 = N_2^{\max}$). Then, the intermediate N_3 states start to be filled, whereas N_1 can not exceed the transparency density $N_1^{\max}/2$. The ω_2-pulse enters the microstructure with a delay of 0.5 ps, in order to interact with already strongly excited quantum wells. So, when the seed pulse feeds the cavity, the photon density S_2 increases, and eventually starts to deplete the N_2 states. For intensities below I_2^{opt}, N_2 only slightly decreases, whereas for $I_2 \geq I_2^{\text{opt}}$, the quantum wells become transparent at the two-photon frequency ($N_2 = N_2^{\max}/2$). This shows that from I_2^{opt} upwards, the optical intensity is high enough to recombine more pairs than actually available through the relaxation process. This excess energy is therefore not amplified, and reduces the differential transmission.

After the entire ω_2-pulse entered the cavity, the photon density S_2 decreases exponentially with time constant given by the transmission of the mirrors, and eventually reaches once again the optical intensity at which the two-photon transition rate exactly compensates the relaxation. N_2 then increases once more, as there are still carriers at higher energy.

These results indicate that the two-photon pulse burns a narrow spectral hole in the carrier density. The amplification is therefore seriously limited by the finite relaxation rate of the e-h pairs and the narrow spectral width of the optically active region. Furthermore, the related saturation of the gain implies the existence of an optimal input intensity maximizing the differential transmission.

2.4 Analytical approximations

In order to get a better insight into the dependence of the differential transmission on the various physical parameters in the model, it is useful to dispose of a simple analytical formula. The two-photon transition requiring high optical intensities, it is not possible to work with a CW excitation, and the steady state solution of the rate equations is not very appropriate. In the following, we use several approximations to derive an expression for the maximal amplification $\Delta S_2/S_2^{\text{tot}}$. We also demonstrate numerically that this analytical expression is adequate in our parameter range.

The upper limit for the carrier relaxation from N_1 to N_2 is given by $\dot{N}_2 = N_2^{\max}/(2\tau_r)$, and the maximal two-photon emission rate reads $\dot{S}_2 = N_2^{\max}/\tau_r$. The intensity of the two-photon pulse in the cavity is sufficient to recombine all available e-h pairs only during a finite time Δt, which leads to the integrated two-photon gain

$$\frac{\Delta S_2}{S_2^{\mathrm{tot}}} = \frac{N_2^{\mathrm{max}}}{S_2^{\mathrm{tot}}} \frac{\Delta t}{\tau_r} \,. \tag{2.23}$$

If the photon lifetime τ_2 is much longer than the pulse duration, the photon density in the cavity can be approximated by

$$S_2(t) = S_2^{\mathrm{tot}} \exp(-t/\tau_2)\,, \tag{2.24}$$

which means that all photons are injected simultaneously in the cavity. The light-matter interaction during the rise time of the photon density is therefore neglected, and one expects the corresponding differential transmission to be underestimated. By using the condition $S_2(\Delta t) = S_2^{\mathrm{min}}$, where S_2^{min} is the smallest density required to maintain the transparency ($N_2 = \bar{N}_2$), one finds

$$\frac{\Delta S_2}{S_2^{\mathrm{tot}}} \simeq \frac{\tau_2}{\tau_r} \frac{N_2^{\mathrm{max}}}{S_2^{\mathrm{tot}}} \ln \frac{S_2^{\mathrm{tot}}}{S_2^{\mathrm{min}}} \,. \tag{2.25}$$

The upper limit to the two-photon amplification is given by the number of e-h pairs injected by the pump, and eventually feeding the density N_2. The carrier relaxation to the region 2, and therefore the potential gain, increases as N_2 decreases. However, as we neglect spontaneous and non-radiative recombination, N_2 can not become smaller than $N_2^{\mathrm{max}}/2$ under operation. On the other hand, the two-photon emission is maximal for full inversion ($N_2 = N_2^{\mathrm{max}}$), and vanishes at transparency ($N_2 = N_2^{\mathrm{max}}/2$). To estimate the lowest ω_2-photon density needed to achieve the maximal amplification, we therefore set $\dot{N}_2 = 0$ in equation (2.7), and put $N_2 = N_2^{\mathrm{max}}/2$ in the relaxation term and $N_2 = N_2^{\mathrm{max}}$ in the two-photon transition term. As a result, we obtain

$$S_2^{\mathrm{min}} = \frac{1}{\Gamma_2\, c/n_{\mathrm{w}}} \sqrt{\frac{N_2^{\mathrm{max}}\, l}{\hbar\omega_2\, \beta\, \tau_r}} \,. \tag{2.26}$$

The last free parameter in (2.25) is S_2^{tot}, which is proportional to the pulse intensity. As can be easily shown, the relative gain $\Delta S_2/S_2^{\mathrm{tot}}$ is maximal for $S_2^{\mathrm{tot}} = S_2^{\mathrm{min}} \exp(1)$. Together with the condition $S_2^{\mathrm{min}} = S_2^{\mathrm{tot}} \exp(-\Delta t/\tau_2)$, it implies $\Delta t = \tau_2$, and the equation (2.25) finally becomes

$$\frac{\Delta S_2}{S_2^{\mathrm{tot}}} \simeq \frac{c}{n_{\mathrm{w}}} \frac{\Gamma_2\, \tau_2}{2.718} \sqrt{\frac{\hbar\omega_2\, \beta\, N_2^{\mathrm{max}}}{l\, \tau_r}} \,. \tag{2.27}$$

The required ω_2-pulse intensity is also related to the cavity photon density by

$2\bar{I}_2 T_2 = \hbar\omega_2\, S_2^{\text{tot}}$, and can therefore be written as

$$\bar{I}_2 = \frac{2.718}{2\,T_2\,\Gamma_2\,c/n_{\text{w}}}\sqrt{\frac{\hbar\omega_2\,N_2^{\max}\,l}{\beta\,\tau_r}}\,. \tag{2.28}$$

In order to check the validity of the approximations, we compare the value of the previous expressions with the numerical solution of the rate equations, using the same parameters as in section 2.3. With the full model, we obtained $\Delta S_2/S_2^{\text{tot}} = 2.29\%$ and $\bar{I}_2 = 7.0\ \text{MW/cm}^2$, whereas the formulas (2.27) and (2.28) give 2.00% and 10.5 MW/cm^2, which is in good agreement considering the rather crude approximations.

As expected, the relative gain augments with increasing two-photon absorption coefficient β, density of optically active states $N_2^{\max}$, or relaxation rate $1/\tau_r$. A ten times faster relaxation (τ_r=10 fs) would increase the gain by a factor three to reach 6%–7%. However, it is probably more useful to know how it depends on the geometrical quantities like the number of QWs, the effective cavity length and the mirror reflectivity, as they can be easily engineered. For this purpose, let us consider a cavity resonant at wave vector k_0 with two identical reflectivities $R_l = R_r \equiv r^2$. At the cavity center, where the interferences are constructive, the electric field for an incoming plane wave of wave vector $k = k_0 + \delta k$ is given by

$$E(k) \propto \frac{1 + r\,e^{-i\delta kL}}{1 - r^2\,e^{-i2\delta kL}}\,. \tag{2.29}$$

Thus, the spectral width $2\delta k$ of the corresponding intensity $I(k) \propto |E(k)|^2$ at half maximum is given by

$$\cos(\delta kL) = 1 - \frac{(1-r)^2}{2\,r}\,. \tag{2.30}$$

As the optically active density of states is related to the spectral width by $N_2^{\max} \propto j\Delta\omega_2 = j2\delta k\,c/n_{\text{c}}$, it can be replaced by

$$N_2^{\max} \propto \frac{l}{L}\,\arccos\left[1 - \frac{(1-r)^2}{2\,r}\right], \tag{2.31}$$

where we forget about the prefactor, which does not depend on the geometry. We also made use of the fact that the active length l is proportional to the number of wells j. Furthermore, by expressing the photon lifetime and the confinement factor as $\tau_2 \propto L/\ln(1/r)$ and $\Gamma_2 \propto l/L$, we finally obtain

$$\frac{\Delta S_2}{S_2^{\text{tot}}} \propto \frac{l}{\ln(1/r)}\sqrt{\frac{1}{L}\,\arccos\left[1 - \frac{(1-r)^2}{2\,r}\right]}\,. \tag{2.32}$$

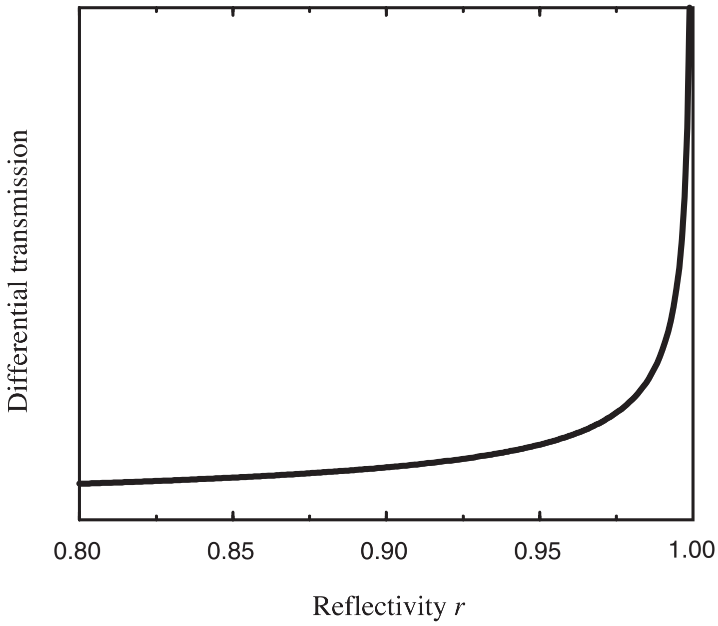

Figure 2.7: Maximal differential transmission calculated by the analytical expression (2.32).

First, as the active length l is given by the total width of all QWs, the amplification increases linearly with the number of wells. This is, however, limited by the fact that the position of the active material has to be close to the field maxima in the cavity. Furthermore, the factor $l/\sqrt{L}$ implies that lengthening the cavity and adding the same number of QWs at each new maximum of the interference pattern also lead to better performance. Second, higher mirror reflectivities improve the gain, as depicted in Figure 2.7, showing that the narrowing of the cavity mode is more than compensated by the increase of the photon lifetime.

Non-radiative recombination has been neglected in our model, but it should not significantly alter our results. These losses indeed remove excited carriers, but it occurs on a much longer timescale than the cavity lifetime.

2.5 Conclusion

We have developed a model of rate equations for the pure degenerate two-photon gain in an optically pumped microcavity containing several quantum wells. We limited ourselves to off-resonant pumping in order to eliminate the phase-dependent two-photon parametric gain. Using this rate equation model, we estimated, with realistic parameters, the integrated differential transmission that can be expected in a pump-probe measurement. The two-photon amplification turns out to be mainly limited by the relaxation time of the electron-hole pairs and the narrow spectral width of the cavity mode, both restricting the number of carriers available for the optical transitions. As expected, the gain increases with the light intensity, but rapidly reaches a maximal value of a few percent and then decreases, because the fast two-photon stimulated recombination is no longer compensated by the relaxation of the electron-hole pairs injected at higher energy by the pump. Typically, a λ-cavity containing 11 QWs would give a maximal integrated amplification of $\sim 2.3\%$ for a peak intensity of ~ 80 MW/cm^2. This result suggests that two-photon gain *may indeed be observable*, but the low value will severely limit its possible usefulness. Non-radiative recombination and other cavity losses have been neglected but should not significantly alter our estimates.

An analytical formula for the differential transmission, resulting from various approximations on the rate equations, has been derived and shown to be adequate. Its structure highlights the influence of the multiple physical parameters entering the model. The increase of the mirror reflectivities can, in principle, especially be used to improve the amplification, despite the narrowing of the optical cavity mode.

3 General theory: effective multi-band Bloch equations, current and susceptibility

3.1 Introduction

The main scope of this thesis is to develop a dynamical theory for multi-photon transitions. It will also provide theoretical foundations for the phenomenological model used in chapter 2, and extend the field of research to processes where different electromagnetic fields excite the same states.

In particular, a theory accounting for the dynamics of the system is required for investigating the transient response of a medium excited by ultrashort pulses. This is, for instance, important for a detailed description of pump and probe measurements. Furthermore, various nonlinear processes may occur simultaneously and interfere, especially when the optical frequencies of the electromagnetic fields are close to transition frequencies of the medium. In this context, a time-dependent description also gives insight into complex effects related to the coherence (or microscopic polarization) between the bands.

In the last decades, extensive work was done on the calculation of two-photon transition probabilities or third-order susceptibilities [22–31, 33–38, 41, 42, 44, 48–51]. However, the time-dependent modeling of two-photon processes in semiconductors is generally limited to a phenomenological description based on rate equations [71–73]. On a microscopic level, the study of the dynamics of multi-photon transitions was initiated only in the past nineties by Selbmann *et al.* [74] who considered a one-dimensional diatomic chain. More recently, Král and Sipe [97] included two-photon transitions within a Green's functions formalism for the study of optically injected current, but they limited their model to two isotropic and parabolic bands.

In the following, we develop a dynamical theory for multi-photon transitions by deriving a reduced set of effective multi-band semiconductor Bloch equations. No restricting assumptions will be made on the details of the energy and momentum dispersion. The model can thus be applied to any heterostructure defined by its band structure.

The benefit of the proposed approach is two-fold. First, the description of the dynamics is restricted to a reduced number of bands. Yet, the discarded bands are not neglected, but consistently taken into account in the higher order processes. Second, all quantities remaining in the effective multi-band Bloch equations vary on the same time scale, which makes their numerical integration much more efficient.

This theory does not account for the wavevectors of the electromagnetic fields. Thus, all pulses are assumed to propagate along the same direction. Morever, it implies that propagation effects must be negligible. However, the theory can be extended to propagating fields, when completed by Maxwell's equations.

The proposed model is well appropriate for the description of low-dimensional systems, like quantum wells or quantum wires, excited along a direction of confinement. It takes into account various linear and nonlinear optical processes, such as one- and two-photon absorption, second-harmonic generation, difference-frequency mixing, or coherent control of photocurrent.

First, we discuss the choice of the gauge for the electromagnetic interaction in the dipole approximation. The equations of motion are then established in the density matrix formalism and expressed in the rotating frame. A perturbative approach is used to eliminate the far off-resonant bands and reduce the density matrix to a finite set of states. The withdrawn states are included in the equations as a perturbation up to first order in the inverse of the detuning between the corresponding inter-band frequency and the optical frequency [21]. The transitions to the eliminated bands have thus to be far off-resonant, *i.e.* with a large detuning, for the perturbative expansion to be valid. One is left with an effective Schrödinger equation for a reduced density matrix where the withdrawn bands appear as intermediate states in an *effective* interaction which is *quadratic* in the field (and linear in the inverse of the detuning). In a second step, we collect the part of the interaction giving rise to quasi-resonant transitions and neglect the (small) off-resonant contributions (generalized rotating wave approximation). The resulting equations are specialized to the case of quasi-resonant one- and two-photon transitions from valence to conduction bands.

Once the main equations are established, we detail how the time-dependent polarization current is calculated from the reduced density matrix and extract the one- and two-photon absorption coefficients. We then outline how the Coulomb interaction can be included within the Hartree-Fock approximation. Finally, the decoherence and thermalization of the carrier distributions are added through phenomenological relaxation times.

3.2 Interaction with an electromagnetic field: choice of gauge

The one-particle Hamiltonian for a crystal interacting with an electromagnetic (EM) field can be expressed as $H = H_0 + H_I$, where H_0 is the Hamiltonian in the absence of the field. The form of the EM interaction Hamiltonian H_I depends on the gauge. In the dipole approximation, H_I is given by $-e\boldsymbol{E}\boldsymbol{r}$ or $e\boldsymbol{A}\boldsymbol{p} + e^2\boldsymbol{A}^2/2m_0$ in the length gauge or velocity gauge respectively. The equivalence between these two electromagnetic interaction forms has been widely discussed in the last decades. It is a matter of fact that they are related to each other by a gauge transformation and therefore describe the same physical situation. In practice however, they may lead to different results, in particular for transition rates, due to approximations usually needed to perform explicit calculations. The exact Hamiltonian is indeed often replaced by a simpler effective Hamiltonian, and the gauge invariance can be affected. In the following, we review some aspects of the gauge invariance, and discuss our choice of the velocity gauge.

3.2.1 The current gauge

Starace [98] showed that for Hamiltonians containing non-local potentials, the dipolar interaction terms $\boldsymbol{E}\boldsymbol{r}$ and $\boldsymbol{A}\boldsymbol{p}$ are no more related by the usual gauge transformation. Thus, he modified the interaction by applying the principle of minimal electromagnetic coupling, in order to preserve gauge invariance. This new interaction form couples the electrons to the field by their current $\boldsymbol{v} \propto [\boldsymbol{r}, H_0]$ and is sometimes referred to as interaction in the current gauge. This procedure was generalized to multi-photon processes by Girlanda *et al.* [99], extended to arbitrary fields (beyond the long wavelength approximation) by Ismail-Beigi *et al.* [100], and used on several occasions [34, 35, 50, 99, 101, 102]. The justification of this modified electromagnetic coupling is based on two central properties. First, in the case of Hamiltonians containing only local potentials, the modified interaction reduces to the usual $\boldsymbol{A}\boldsymbol{p}$ interaction in the velocity gauge. Second, it is equivalent to the $\boldsymbol{E}\boldsymbol{r}$ interaction in the length gauge through the usual gauge transformation.

In practice, non-local potentials may arise when the complete set of eigenstates of an initial Hamiltonian containing only local potentials is restricted to a given subset which is then used as an approximate basis for the problem. In this case, it is not surprising that the gauge invariance is affected, as the latter is related to unitary transformations in the *complete* Hilbert space. The subspace spanned by the restricted set of eigenfunctions is not necessarily gauge invariant. The procedure of Starace is an elegant way to restore gauge invariance in such a case.

3.2.2 Extended Bloch states and $\boldsymbol{E}\boldsymbol{r}$ interaction in crystals

One should also note that the dipole interaction $\boldsymbol{E}\boldsymbol{r}$ is not well defined in solid state material because the electron state is not spatially localized as is in atoms. Arnold and Hutchings [103] thus argue that the momentum interaction $\boldsymbol{A}\boldsymbol{p}$ is the natural one to use for electrons in crystals even though the material in form of nanostructures may exhibit bound states. On the other hand, Aversa and Sipe [104] applied standard length gauge perturbation theory to calculate nonlinear susceptibilities in crystals by using the treatment of the position operator previously described by Blount [105], to overcome the problem related to the extended Bloch states. They also showed that this length gauge formulation leads to an additional term in the Bloch equations, coupling states with different wavevectors.

In the case of heterostructures, one has to calculate either momentum or position matrix elements in the framework of an envelope function method. In Burt's theory [47], this is easily achieved for the momentum operator $\boldsymbol{p}$. As the latter exhibits the full translational symmetry, its action on the envelope functions and periodic basis functions can be separated in a convenient and exact way. By contrast, the position operator $\boldsymbol{r}$ is not periodic at all and leads to strongly non-local expressions in the equation for envelope functions. Thus, from the technical point of view, it is much more convenient to work in the velocity gauge.

3.2.3 Choice of a basis

We stress that it is possible to expand the wave functions in any *arbitrary*, but complete, set of basis functions. Yet, sometimes one may need to interpret the expansion coefficients as occupation probabilities, which requires the basis functions to be eigenstates of a gauge invariant observable[1]. Also note that a same quantum mechanical wave function may correspond to different physical states in different gauges. Thus, one should always be aware of the gauge that is currently used.

The expansion in terms of eigenfunctions $|n\rangle$ of the unperturbed Hamiltonian H_0 may be interpreted in two ways: i) the complete set of functions $|n\rangle$ is a mathematical basis of the Hilbert space, without referring to a physical observable, or ii) the basis functions correspond to eigenstates of a gauge invariant observable: the energy.

The second approach requires a more careful analysis. Indeed, the expansion coefficient must be gauge invariant to yield unambiguous occupation probabilities. The basis functions should thus be defined as eigenstates of a gauge invariant observable. Unfortunately, this condition is not fulfilled by the Hamiltonian (it is the time-dependent Schrödinger equation, that is gauge independent, not the Hamiltonian). Yang [106] suggested to use what he called the particle's gauge-invariant energy operator to define the basis states for the expansion. In the length gauge, this energy observable reduces to the unperturbed Hamiltonian H_0 and the physical interpretation of the basis states $|n\rangle$ as energy eigenstates remains unambiguous even in presence of an electric field. This led Kobe [107] to argue that if eigenstates of the unperturbed Hamiltonian H_0 are to be used for the basis states, the dipole

---

[1] An observable is always gauge invariant

interaction in the length form is the proper perturbation. Although this is a specific choice of gauge, it is the only one for which the basis functions do not depend on the electromagnetic field.

3.2.4 Present choice of gauge: the velocity gauge

In this thesis, we want to develop a theory for multi-photon transitions in *crystalline* heterostructures. As discussed above, the dipole interaction in the length gauge ($\boldsymbol{Er}$) is inadequate for periodic systems, because the position matrix elements between extended Bloch states are ill-defined. Similar difficulties arise in the current gauge, when evaluating the matrix elements of $\boldsymbol{v} \propto [\boldsymbol{r}, H_0]$ appearing in the corresponding interaction. By contrast, the momentum matrix elements can be calculated in a proper way with Burt's envelope function method, which makes the interaction in the velocity gauge ($\boldsymbol{Ap}$) a much better candidate. Therefore, we prefer to work in the velocity gauge, despite the fact that the Hamiltonian may not remain gauge invariant after the system is restricted to a limited number of energy bands. This choice implies that, *in the presence of an EM field*, the basis functions $|n\rangle$ are no more eigenstates neither of the Gauge invariant energy operator introduced by Yang, nor of the total Hamiltonian including the EM interaction. So we adopt here the interpretation where the complete set of eigenfunctions of H_0 is simply used as a mathematical basis for the expansion. Nevertheless, note that before and after the interaction with electromagnetic pulses, the physical interpretation as energy eigenstates is always well justified because the eigenfunctions of the Hamiltonian have an identical form in the different gauges.

Finally, we emphasize that we want to consider *macroscopic* quantities that do not refer to a *restricted* set of states but involve the whole system, like the macroscopic polarization. Thus, the choice of the gauge and of the expansion basis, as well as its physical interpretation, should not affect the end-result. The restriction to a limited number of bands *is* an approximation that may indeed break gauge invariance. However the level of accuracy is in the end set by the judicious choice of the basis and by the degree of validity of the approximations, and not by an a posteriori restoration of gauge invariance (*e.g.* the current gauge procedure), though the latter is always a desirable property.

3.3 Bloch equations

As a basis of the Hilbert space, we use the eigenstates of the effective one-particle crystal Hamiltonian H_0, defined by

$$H_0|n, \boldsymbol{k}\rangle = E_{n,\boldsymbol{k}}|n, \boldsymbol{k}\rangle \,, \tag{3.1}$$

where n and $\boldsymbol{k}$ label respectively the energy bands and the wavevectors in the unconfined directions. Note that the information on the crystal geometry is contained in the exact form of H_0. The equations in this chapter are therefore valid for any heterostructure.

In the velocity gauge, the Hamiltonian for an electron interacting with a classical electromagnetic field is given by

$$H = H_0 + \frac{e}{m_0}\boldsymbol{A}\cdot\boldsymbol{\pi}\,, \tag{3.2}$$

where $\boldsymbol{A}$ is the classical vector potential, and

$$\boldsymbol{\pi} = \boldsymbol{p} + \frac{\hbar}{4m_0c^2}\boldsymbol{\sigma}\wedge\nabla V(\boldsymbol{r}) \tag{3.3}$$

is the momentum operator including the spin-orbit coupling. Here $V(\boldsymbol{r})$ is the microscopic potential of the crystal and $\boldsymbol{\sigma}$ is the vector $(\sigma_x\ \sigma_y\ \sigma_z)$ with the Pauli matrices as components. The elementary charge e is positive. For optical frequencies, the momentum of the electromagnetic field can be neglected compared to the crystal momentum of the electrons. As a consequence, the spatial variation of the potential vector $\boldsymbol{A}$ can be ignored[2] (dipole approximation) and only electronic states with equal wavevector are coupled by the electromagnetic interaction. This approximation restricts the application domain of the theory to excitation schemes with co-linear beams. Moreover, it neglects the propagation of the electromagnetic fields. Thus, this theory is essentially valid for small active regions like quantum wells and quantum wires, excited by beams propagating along a confinement direction. Note that it can be extended to propagating fields, when completed by Maxwell's equations.

We now assume that a certain density of carriers can be excited. In the many-body formalism, the time-dependent Hamiltonian in the dipole approximation then becomes

$$H = \sum_n \sum_{\boldsymbol{k}} E_{n,\boldsymbol{k}} c^\dagger_{n,\boldsymbol{k}} c_{n,\boldsymbol{k}} - \boldsymbol{A}(t) \sum_{mn} \sum_{\boldsymbol{k}} \boldsymbol{\Pi}_{mn,\boldsymbol{k}} c^\dagger_{m,\boldsymbol{k}} c_{n,\boldsymbol{k}}\,, \tag{3.4}$$

where $c^\dagger_{n,\boldsymbol{k}}$ and $c_{n,\boldsymbol{k}}$ are respectively the creation and annihilation operators for the state $|n,\boldsymbol{k}\rangle$. The matrix $\boldsymbol{\Pi}$ is defined by

$$\boldsymbol{\Pi}_{mn,\boldsymbol{k}} \equiv \frac{-e}{m_0}\langle m,\boldsymbol{k}|\boldsymbol{\pi}|n,\boldsymbol{k}\rangle\,. \tag{3.5}$$

---

[2] The typical wavelength of the optical fields inducing inter-band transitions in GaAs is about several hundred nanometers, which is large compared to the lattice period (< 1 nm).

The Schrödinger equation $-i\hbar\partial_t\rho = [\rho, H]$ for the density matrix

$$\rho_{mn,\boldsymbol{k}} = \langle c^\dagger_{m,\boldsymbol{k}} c_{n,\boldsymbol{k}}\rangle^* \tag{3.6}$$

(note the complex conjugate) is given by

$$\partial_t\rho_{nn',\boldsymbol{k}} = -i\Omega_{nn',\boldsymbol{k}}\,\rho_{nn',\boldsymbol{k}} - \frac{i}{\hbar}\boldsymbol{A}(t)\sum_m \left[\rho_{nm,\boldsymbol{k}}\boldsymbol{\Pi}_{mn',\boldsymbol{k}} - \boldsymbol{\Pi}_{nm,\boldsymbol{k}}\rho_{mn',\boldsymbol{k}}\right], \tag{3.7}$$

where $\Omega_{nn',\boldsymbol{k}} = (E_{n,\boldsymbol{k}} - E_{n',\boldsymbol{k}})/\hbar$ are the inter-band frequencies. As the electromagnetic interaction in the dipole approximation couples only states with equal wavevectors, the Hamiltonian is diagonal in $\boldsymbol{k}$. We are therefore left with an independent set of differential equations for each wavevector. For the sake of conciseness, the indices $\boldsymbol{k}$ will thus be omitted in what follows, except when explicitly required.

We emphasize that the band-diagonal momentum matrix elements, which are usually neglected in the Bloch equations, are taken into account here since they give an important contribution to the inter-band two-photon transitions [74]. The diagonal elements are in fact zero at zone center in a centro-symmetric crystal, but may become large with increasing $\boldsymbol{k}$-vector.

3.4 Unitary transformation to the rotating frame

A first step to obtain differential equations for slowly varying functions is to eliminate the oscillations related to the diagonal part of the Hamiltonian. This is best achieved in the rotating frame defined by the unitary transformation $\tilde{\rho} = U\rho U^\dagger$ where $U = \exp(i\Lambda)$ is diagonal with [74]

$$\Lambda_{mn}(t) = \delta_{mn}\,\hbar^{-1}\left[E_n\,t - \boldsymbol{\Pi}_{nn}\int^t dt'\boldsymbol{A}(t')\right]. \tag{3.8}$$

The Schrödinger equation (3.7) then becomes

$$\partial_t\tilde{\rho}_{nn'} = -\frac{i}{\hbar}\boldsymbol{A}(t)\Big[\sum_{m\neq n'}\tilde{\rho}_{nm}\boldsymbol{\Pi}_{mn'}e^{i\Phi_{mn'}} - \sum_{m\neq n}\boldsymbol{\Pi}_{nm}e^{i\Phi_{nm}}\tilde{\rho}_{mn'}\Big] \tag{3.9}$$

with

$$\tilde{\rho}_{mn}(t) = \rho_{mn}(t)\,e^{i\Phi_{mn}(t)} \tag{3.10}$$

and

$$\Phi_{mn}(t) = \Omega_{mn}\,t - \hbar^{-1}\left(\boldsymbol{\Pi}_{mm} - \boldsymbol{\Pi}_{nn}\right)\int^t dt'\boldsymbol{A}(t'). \tag{3.11}$$

We emphasize that the transformation of the Schrödinger equation (3.7) into (3.9) is exact. The rotating wave approximation has not yet been done.

3.5 Expansion into multi-photon transitions involving diagonal momentum matrix elements

The diagonal part of the initial Hamiltonian containing the band-diagonal momentum matrix elements $\mathbf{\Pi}_{nn}$ is eliminated by the unitary transformation (3.8). In the transformed Schrödinger equation (3.9), these elements appear exclusively in the time dependent phases Φ_{mn}, and can be treated separately from the terms involving the off-diagonal momentum matrix elements. The diagonal contribution can now be easily expanded in a form highlighting the underlying multi-photon transitions [74], as it is shown in this section.

In the following, we consider a superposition of s linearly polarized quasi-monochromatic waves

$$\boldsymbol{A}(t) = \sum_{j=1}^{s} \boldsymbol{A}_j(t)\, \cos(\omega_j\, t + \phi_j)\,, \qquad \boldsymbol{A}_j = \begin{pmatrix} A_j^x & A_j^y & A_j^z \end{pmatrix}^T \in \mathbb{R}^3\,, \tag{3.12}$$

with slowly varying envelopes $\boldsymbol{A}_j(t)$. Note that elliptically polarized light can be described in (3.12) by the superposition of two cross-polarized fields with same frequency. According to the vector potential (3.12), the phases (3.11) become

$$\Phi_{mn}(t) \simeq \Omega_{mn}\, t - (\mathbf{\Pi}_{mm} - \mathbf{\Pi}_{nn}) \sum_{j=1}^{s} \frac{\boldsymbol{A}_j(t)}{\hbar\omega_j} \sin(\omega_j\, t + \phi_j)\,, \tag{3.13}$$

where for the integration, the time dependence of the envelopes $\boldsymbol{A}_j$ was neglected compared to the fast oscillations with optical frequencies ω_j. We also assumed that the electromagnetic fields vanish in distant past: $\boldsymbol{A}(-\infty) = 0$. To handle the sine functions in (3.13), we expand the exponentials $e^{i\Phi}$ appearing in the Schrödinger equation (3.9) into an infinite sum of Bessel functions J_n (Appendix B):

$$e^{iz\sin\theta} = \sum_{n\in\mathbb{Z}} \mathrm{J}_n(z)\, e^{in\theta}\,. \tag{3.14}$$

Thus, the Bloch equations (3.9) can be rewritten as

$$\begin{aligned}\partial_t \tilde{\rho}_{nn'} = &-\frac{i}{\hbar}\sum_{j=1}^{s}\boldsymbol{A}_j(t)\\ &\times\Big[+\sum_{m\neq n'}\tilde{\rho}_{nm}\boldsymbol{\Pi}_{mn'}\sum_{N}\mathcal{G}^j_{mn'}(N)\,e^{i(\Omega_{mn'}-N\circ\omega)t-iN\circ\phi}\\ &\quad-\sum_{m\neq n}\boldsymbol{\Pi}_{nm}\tilde{\rho}_{mn'}\sum_{N}\mathcal{G}^j_{nm}(N)\,e^{i(\Omega_{nm}-N\circ\omega)t-iN\circ\phi}\Big]\,,\end{aligned}\tag{3.15}$$

where we have introduced the shorthand notations

$$N \equiv \begin{pmatrix}N_1 & N_2 & \cdots & N_s\end{pmatrix} \qquad N_i \in \mathbb{Z}\tag{3.16}$$

$$\omega \equiv \begin{pmatrix}\omega_1 & \omega_2 & \cdots & \omega_s\end{pmatrix}\tag{3.17}$$

$$\phi \equiv \begin{pmatrix}\phi_1 & \phi_2 & \cdots & \phi_s\end{pmatrix}\tag{3.18}$$

with the scalar products

$$N\circ\omega \equiv \sum_{j=1}^{s} N_j\,\omega_j\,, \qquad\qquad N\circ\phi \equiv \sum_{j=1}^{s} N_j\,\phi_j\,,\tag{3.19}$$

and the sum

$$\sum_{N} \equiv \sum_{N_1\in\mathbb{Z}}\;\sum_{N_2\in\mathbb{Z}}\cdots\sum_{N_s\in\mathbb{Z}}\,.\tag{3.20}$$

The expression $\mathcal{G}^j_{mn}$ appearing in the Bloch equations is defined by

$$\mathcal{G}^j_{mn}(N) \equiv \frac{N_j}{Z^j_{mn}}\prod_{k=1}^{s}\mathrm{J}_{N_k}(Z^k_{mn})\tag{3.21}$$

with

$$Z^j_{mn} \equiv (\boldsymbol{\Pi}_{mm}-\boldsymbol{\Pi}_{nn})\frac{\boldsymbol{A}_j(t)}{\hbar\omega_j}\,,\tag{3.22}$$

and contains the product of Bessel functions related to the sum over the frequencies ω_j in (3.13). The value of $\mathcal{G}^j_{mn}$ at $Z^j_{mn}=0$ is defined by the limit

$$\lim_{Z^j_{mn}\to 0}\mathcal{G}^j_{mn}(N) = \begin{cases}\frac{1}{2}\prod_{k\neq j}\mathrm{J}_{N_k}(Z^k_{mn}) & N_j = \pm 1\,,\\ 0 & N_j \neq \pm 1\,.\end{cases}\tag{3.23}$$

Finally, the property $\mathrm{J}_{-n}(z) = \mathrm{J}_n(-z)$ of the Bessel functions leads to the useful symmetry $\mathcal{G}^j_{mn}(-N) = \mathcal{G}^j_{nm}(N)$.

3.6 Resonant and off-resonant states

The Schrödinger equation (3.15) gives the time evolution of the density matrix for the complete system consisting in an infinite number of energy bands. Yet, all these states do not participate to the same degree to the dynamics. For a given set of electromagnetic waves (3.12), the dominant contribution comes from the bands with inter-band energy spacings close to a frequency combination $N \circ \omega = \sum_j N_j \omega_j$. Furthermore, the larger the N_j's, the smaller the associated transition probability. Consequently, it is well justified to consider only the terms with small N_j's among the resonant transitions. According to this, we divide the bands into two sets:

- A set $\mathbb{A}$ containing the finite number of bands with inter-band frequencies close to $N \circ \omega$ for N_j restricted to the multi-photon transitions we are interested in. The bands belonging to $\mathbb{A}$ are labeled by a, a', …(or A, A' used later).

- A set $\mathbb{B}$ containing all remaining bands. The dynamics of the electrons described by them is assumed to be negligible. The bands belonging to $\mathbb{B}$ are labeled by b, b', … .

In the following, the bands of group $\mathbb{A}$ will be called (quasi-) resonant bands and the bands of group $\mathbb{B}$ off-resonant bands, with respect to the energy mismatch between the optical frequencies and the inter-band frequencies. According to this distinction, the Schrödinger equation (3.15) splits into three sets of differential equations mixing $\tilde{\rho}_{aa'}$, $\tilde{\rho}_{ab}$ and $\tilde{\rho}_{bb'}$:

$$\begin{aligned}
\partial_t \tilde{\rho}_{aa'} = &-\frac{i}{\hbar} \sum_j \boldsymbol{A}_j(t) \\
\times \Big[&+ \sum_{a'' \neq a'} \tilde{\rho}_{aa''} \boldsymbol{\Pi}_{a''a'} \sum_N \mathcal{G}^j_{a''a'}(N)\, e^{i(\Omega_{a''a'} - N\circ\omega)t - iN\circ\phi} \\
&- \sum_{a'' \neq a} \boldsymbol{\Pi}_{aa''} \tilde{\rho}_{a''a'} \sum_N \mathcal{G}^j_{aa''}(N)\, e^{i(\Omega_{aa''} - N\circ\omega)t - iN\circ\phi} \\
&+ \sum_b \tilde{\rho}_{ab} \boldsymbol{\Pi}_{ba'} \sum_N \mathcal{G}^j_{ba'}(N)\, e^{i(\Omega_{ba'} - N\circ\omega)t - iN\circ\phi} \\
&- \sum_b \boldsymbol{\Pi}_{ab} \tilde{\rho}_{ba'} \sum_N \mathcal{G}^j_{ab}(N)\, e^{i(\Omega_{ab} - N\circ\omega)t - iN\circ\phi} \Big],
\end{aligned} \tag{3.24}$$

$$\begin{aligned}
\partial_t \tilde{\rho}_{ab} = &-\frac{i}{\hbar}\sum_j \boldsymbol{A}_j(t) \\
&\times\Big[+ \sum_{a''} \tilde{\rho}_{aa''}\boldsymbol{\Pi}_{a''b}\sum_N \mathcal{G}^j_{a''b}(N)\, e^{i(\Omega_{a''b}-N\circ\omega)t-iN\circ\phi} \\
&\quad - \sum_{a''\neq a} \boldsymbol{\Pi}_{aa''}\tilde{\rho}_{a''b}\sum_N \mathcal{G}^j_{aa''}(N)\, e^{i(\Omega_{aa''}-N\circ\omega)t-iN\circ\phi} \\
&\quad + \sum_{b'\neq b} \tilde{\rho}_{ab'}\boldsymbol{\Pi}_{b'b}\sum_N \mathcal{G}^j_{b'b}(N)\, e^{i(\Omega_{b'b}-N\circ\omega)t-iN\circ\phi} \\
&\quad - \sum_{b'} \boldsymbol{\Pi}_{ab'}\tilde{\rho}_{b'b}\sum_N \mathcal{G}^j_{ab'}(N)\, e^{i(\Omega_{ab'}-N\circ\omega)t-iN\circ\phi} \Big],
\end{aligned} \tag{3.25}$$

$$\begin{aligned}
\partial_t \tilde{\rho}_{b'b} = &-\frac{i}{\hbar}\sum_j \boldsymbol{A}_j(t) \\
&\times\Big[+ \sum_{a'} \tilde{\rho}_{b'a'}\boldsymbol{\Pi}_{a'b}\sum_N \mathcal{G}^j_{a'b}(N)\, e^{i(\Omega_{a'b}-N\circ\omega)t-iN\circ\phi} \\
&\quad - \sum_{a'} \boldsymbol{\Pi}_{b'a'}\tilde{\rho}_{a'b}\sum_N \mathcal{G}^j_{b'a'}(N)\, e^{i(\Omega_{b'a'}-N\circ\omega)t-iN\circ\phi} \\
&\quad + \sum_{b''\neq b} \tilde{\rho}_{b'b''}\boldsymbol{\Pi}_{b''b}\sum_N \mathcal{G}^j_{b''b}(N)\, e^{i(\Omega_{b''b}-N\circ\omega)t-iN\circ\phi} \\
&\quad - \sum_{b''\neq b'} \boldsymbol{\Pi}_{b'b''}\tilde{\rho}_{b''b}\sum_N \mathcal{G}^j_{b'b''}(N)\, e^{i(\Omega_{b'b''}-N\circ\omega)t-iN\circ\phi} \Big].
\end{aligned} \tag{3.26}$$

As the bands of $\mathbb{A}$ are coupled through quasi-resonant (multi-) photon transitions, at least one of the complex exponentials on the r.h.s. of (3.24) is slowly varying in time. Thus, the *reduced density matrix*[3] elements $\tilde{\rho}_{aa'}$ are expected to display essentially a *slow* dominant time-dependence. By contrast, the remaining matrix elements $\tilde{\rho}_{ab}$ and $\tilde{\rho}_{b'b}$ show rapid oscillations governed by the detunings between $N\circ\omega$ and the inter-band frequencies. Taking advantage of this, we derive a closed set of differential equations for the time-evolution of the reduced density matrix $\tilde{\rho}_{aa'}$, by iteratively replacing $\tilde{\rho}_{ab'}$, $\tilde{\rho}_{ba'}$ and $\tilde{\rho}_{b'b}$ in (3.24) by the r.h.s. of (3.25) and (3.26), integrated from $-\infty$ to t. This procedure results in a series of imbricated integrals of the form[4]

$$i\int_0^\infty dt'\, e^{i(\Omega-\omega)(t-t')}\, F(t-t')\,\tilde{\rho}(t-t')\,, \tag{3.27}$$

---

[3] The density matrix limited to the bands of group $\mathbb{A}$

[4] with the change of variable $\int_{-\infty}^{t} dt' f(t') = \int_0^\infty dt' f(t-t')$

where $\tilde{\rho}(t)$ is the reduced density matrix in the rotating frame and $F(t)$ a function of the field envelopes $\boldsymbol{A}_j(t)$. Both are slowly varying in time. Here the frequency $\Omega-\omega$ is a generic symbol for the detunings of the type $\Omega_{ab} - N \circ \omega$ or $\Omega_{bb'} - N \circ \omega$. The resonant and off-resonant bands are chosen in order to ensure that these detunings are large enough for the approximation

$$i \int_0^\infty dt'\, e^{i(\Omega-\omega)(t-t')}\, F(t-t')\, \tilde{\rho}(t-t') \simeq \frac{e^{i(\Omega-\omega)t}}{\Omega-\omega}\, F(t)\, \tilde{\rho}(t) \tag{3.28}$$

to be valid. The latter will be detailed in section 3.8. It is assumed that $F(t)$ vanishes in distant past, which is fulfilled here, because, according to the Bloch equations, $F(t)$ is proportional to the vector potential. Furthermore, the integration of (3.25) and (3.26) requires initial conditions for $\tilde{\rho}_{b'b}$ and $\tilde{\rho}_{ab}$. It is reasonable to consider the situation with no coherence (or microscopic polarization) between different bands before the electromagnetic fields are switched on. The initial occupation of the eliminated off-resonant bands is however given by the carrier distributions $\tilde{\rho}^{(0)}_{bb}$ which can be non-zero, especially for valence bands. More formally, we assume the initial conditions

$$\lim_{t\to-\infty} \tilde{\rho}_{ab}(t) = 0 \tag{3.29}$$

$$\lim_{t\to-\infty} \tilde{\rho}_{bb'}(t) = \delta_{bb'} \tilde{\rho}^{(0)}_{bb}\,. \tag{3.30}$$

After lengthy calculations where we keep only the terms up to the third order in the electromagnetic fields, we are finally left with the effective multi-band Bloch equations

$$\partial_t \tilde{\rho}_{AA'} = \left[\partial_t \tilde{\rho}_{AA'}\right]^{(1)} + \left[\partial_t \tilde{\rho}_{AA'}\right]^{(2)} + \left[\partial_t \tilde{\rho}_{AA'}\right]^{(3)}. \tag{3.31}$$

The three terms on the r.h.s. contain the effective interaction terms that are respectively linear, quadratic and cubic in the fields $\boldsymbol{A}_j$. The linear and quadratic terms read

$$\begin{aligned}\left[\partial_t \tilde{\rho}_{AA'}\right]^{(1)} = -i \sum_j \sum_\alpha A^\alpha_j/\hbar \sum_N \\ \times \Bigg[+ \sum_{a \neq A'} \tilde{\rho}_{Aa} \Pi^\alpha_{aA'} \mathcal{G}^j_{aA'}(N)\, e^{i(\Omega_{aA'} - N\circ\omega)t - iN\circ\phi} \\ - \sum_{a\neq A} \Pi^\alpha_{Aa} \tilde{\rho}_{aA'} \mathcal{G}^j_{Aa}(N)\, e^{i(\Omega_{Aa} - N\circ\omega)t - iN\circ\phi} \Bigg]\end{aligned} \tag{3.32}$$

and

$$
\begin{aligned}
&\big[\partial_t \tilde{\rho}_{AA'}\big]^{(2)} = \\
&\quad +i \sum_{j,k} \sum_{\alpha,\beta} A_j^\alpha A_k^\beta / \hbar^2 \sum_a \sum_b \sum_{N,N'} \\
&\qquad \times \Bigg[+ \tilde{\rho}_{Aa} \Pi_{ab}^\alpha \Pi_{bA'}^\beta \mathcal{G}_{ab}^j(N) \mathcal{G}_{bA'}^k(N') \, \frac{e^{i\left(\Omega_{aA'} - (N+N')\circ\omega\right)t - i(N+N')\circ\phi}}{\Omega_{ab} - N\circ\omega} \\
&\qquad\quad + \Pi_{Ab}^\beta \Pi_{ba}^\alpha \tilde{\rho}_{aA'} \mathcal{G}_{Ab}^k(N') \mathcal{G}_{ba}^j(N) \, \frac{e^{i\left(\Omega_{Aa} - (N+N')\circ\omega\right)t - i(N+N')\circ\phi}}{\Omega_{ba} - N\circ\omega} \Bigg] \qquad (3.33) \\
&\quad -i \sum_{j,k} \sum_{\alpha,\beta} A_j^\alpha A_k^\beta / \hbar^2 \sum_b \sum_{N,N'} \\
&\qquad \times \Bigg[+ \Pi_{Ab}^\alpha \tilde{\rho}_{bb}^{(0)} \Pi_{bA'}^\beta \mathcal{G}_{Ab}^j(N) \mathcal{G}_{bA'}^k(N') \, \frac{e^{i\left(\Omega_{AA'} - (N+N')\circ\omega\right)t - i(N+N')\circ\phi}}{\Omega_{Ab} - N\circ\omega} \\
&\qquad\quad + \Pi_{Ab}^\beta \tilde{\rho}_{bb}^{(0)} \Pi_{bA'}^\alpha \mathcal{G}_{Ab}^k(N') \mathcal{G}_{bA'}^j(N) \, \frac{e^{i\left(\Omega_{AA'} - (N+N')\circ\omega\right)t - i(N+N')\circ\phi}}{\Omega_{bA'} - N\circ\omega} \Bigg] .
\end{aligned}
$$

The terms that are cubic in the fields are given in appendix C. The sums over α and β correspond to the polarization of the electromagnetic fields $\boldsymbol{A}_j = (A_j^x \, A_j^y \, A_j^z)^T$ and are taken over the spatial directions x, y and z. The indices j and k label the quasi-monochromatic waves $\boldsymbol{A}_j \cos(\omega_j t + \phi_j)$ of (3.12) and range from 1 to s. Remind that a wavevector label $\boldsymbol{k}$ must be added to each pair of band indices.

The first term on the r.h.s. of the multi-band Bloch equations (3.31) includes all multi-photon processes, *i.e.* to any order in the fields, involving only resonant bands. The second term (respectively, third term) describes the contribution of the eliminated off-resonant bands as intermediate states to the multi-photon interactions up to the second order (respectively, third order) in the fields. The diagonal momentum matrix elements of the resonant bands are contained in the $\mathcal{G}$-functions.

The second term on the r.h.s. of (3.33) contains the initial carrier distributions $\tilde{\rho}_{bb}^{(0)}$ of the far off-resonant bands, stemming from the integration of (3.26). This reflects the presence of electrons in the eliminated bands and their effect on multi-photon transitions. These states can not in general be considered as unoccupied in the distant past, especially in the valence bands. Their contribution can however be neglected in practice, as we now show. First we remind that we consider only quasi-resonant optical transitions between bands in $\mathbb{A}$. In other words, we shall keep only the dominant slowly varying part of the Bloch equations *i.e.* the terms with small detunings $\Omega_{AA'} - (N + N') \circ \omega$ compared to the optical frequencies. Second, we note that the term that contains $\tilde{\rho}^{(0)}_{bb}$ in (3.33) can be written as

$$\begin{aligned} -\, i \sum_{j,k} \sum_{\alpha,\beta} A^{\alpha}_{j} A^{\beta}_{k} / \hbar^2 \sum_{b} \sum_{N,N'} \Pi^{\alpha}_{Ab} \tilde{\rho}^{(0)}_{bb} \Pi^{\beta}_{bA'} \mathcal{G}^{j}_{Ab}(N) \mathcal{G}^{k}_{bA'}(N') \\ \times \left[\frac{\Omega_{AA'} - (N + N') \circ \omega}{(\Omega_{Ab} - N \circ \omega)(\Omega_{bA'} - N' \circ \omega)} \right] e^{i\left(\Omega_{AA'} - (N+N') \circ \omega\right) t - i (N+N') \circ \phi} \end{aligned} \tag{3.34}$$

by exchanging the dummy indices (j, α, N) and (k, β, N') in its second part. The expression within the brackets clearly indicates that (3.34) can be safely neglected for quasi-resonant processes, *i.e.* for small detunings $\Omega_{AA'} - (N + N') \circ \omega$.

The multi-band Bloch equations give the dynamics of a reduced number of states taking into account the contribution of the eliminated off-resonant bands in a perturbative way. However, the remaining terms are not yet necessarily all slowly varying in time. The final selection of the dominant processes has still to be done and will depend on the optical frequencies and on the band structure of the crystal.

3.7 Effective multi-band Bloch equations for one- and two-photon transitions

We are now considering the case of one- and two-photon transitions between conduction and valence bands in a semiconductor. The ensemble $\mathbb{A}$ of resonant bands is divided into two sets of subbands: the conduction bands $\{c\}$ and the valence bands $\{v\}$. Physical quantities and processes will be designated by the adjectives *intra-band* if they involve only subbands from the same set and by *inter-band* if they concern subbands from both sets. We assume that the intra-band energy spacings are much smaller than the inter-band energy differences. This condition is well fulfilled by the lowest conduction subbands and the highest valence subbands of a semiconductor quantum well or quantum wire, for which the model will be applied in chapters 5–7. In the following, the conduction bands are labeled by c, c', c'', ..., and the valence bands by v, v', v'', ... Such a distinction is not relevant for the eliminated off-resonant bands and we continue to designate them by the subscript b.

3.7.1 Specialization to the case of two quasi-monochromatic fields

As we are interested in one- and two-photon inter-band transitions, the effective Bloch equations (3.31) are specialized to the case of two quasi-monochromatic electromagnetic fields

$$\boldsymbol{A} = \boldsymbol{A}_1 \cos(\omega_1 t + \phi_1) + \boldsymbol{A}_2 \cos(\omega_2 t + \phi_2) \tag{3.35}$$

of frequency $\omega_1 \simeq E_g$ and $\omega_2 \simeq E_g/2$ where E_g is the inter-band energy gap. Furthermore, the sum over $N = (N_1, N_2)$ is limited to $(\pm 1, 0)$, $(0, \pm 1)$ and $(0, \pm 2)$, and the functions $\mathcal{G}^j_{mn}(N) \equiv \mathcal{G}^j_{mn}(N_1, N_2)$ are expanded to the lowest order in Z^k_{mn}:

$$\mathcal{G}^1_{mn}(\pm 1, 0) \simeq \frac{1}{2} \qquad \mathcal{G}^2_{mn}(\pm 1, 0) = 0 \tag{3.36}$$

$$\mathcal{G}^1_{mn}(0, \pm 1) = 0 \qquad \mathcal{G}^2_{mn}(0, \pm 1) \simeq \frac{1}{2} \tag{3.37}$$

$$\mathcal{G}^1_{mn}(0, \pm 2) = 0 \qquad \mathcal{G}^2_{mn}(0, \pm 2) \simeq \pm(\boldsymbol{\Pi}_{mm} - \boldsymbol{\Pi}_{nn}) \frac{\boldsymbol{A}_2}{4\hbar\omega_2} \,. \tag{3.38}$$

In a first step, we drop the off-resonant contributions involving the eliminated bands $\mathbb{B}$. Thus, among the terms of second-order in the fields, those displaying rapid oscillations in time are now neglected with respect to the slowly varying contributions, in the spirit of the rotating wave approximation. As discussed above, the optical frequencies ω_1 and $2\omega_2$ are close to the inter-band frequencies Ω_{cv}, whereas the intra-band frequencies $\Omega_{cc'}$ and $\Omega_{vv'}$ are much smaller. As a consequence, we can restrict ourselves to the dominant contributions oscillating with the *low* frequencies $\Omega_{cc'}$, $\Omega_{vv'}$, $\Omega_{cv} - \omega_1$ and $\Omega_{cv} - 2\omega_2$. By keeping the corresponding terms of second order in the field envelopes $\boldsymbol{A}_1$ and $\boldsymbol{A}_2$, the effective Bloch equations become

$$\partial_t \tilde{\rho} = -i \, [\tilde{H} \, \tilde{\rho} - \tilde{\rho} \, \tilde{H}^\dagger] \tag{3.39}$$

with the non-hermitian Hamiltonian

$$\begin{aligned} \tilde{H}_{cc'} = &- (2\hbar)^{-1} \sum_j \sum_{\sigma=\pm 1} \sum_\alpha A^\alpha_j \Pi^\alpha_{cc'} \, e^{i(\Omega_{cc'} - \sigma\omega_j)t - i\sigma\phi_j} \, (1 - \delta_{cc'}) \\ &- (2\hbar)^{-2} \sum_j \sum_{\alpha,\beta} A^\alpha_j A^\beta_j \, e^{i\Omega_{cc'} t} \\ &\times \Big[\sum_b \frac{\Pi^\alpha_{cb} \Pi^\beta_{bc'}}{\Omega_{bc'} - \omega_j} + \sum_b \frac{\Pi^\alpha_{cb} \Pi^\beta_{bc'}}{\Omega_{bc'} + \omega_j} \Big] \,, \end{aligned} \tag{3.40}$$

$$\begin{aligned} \tilde{H}_{vv'} = &- (2\hbar)^{-1} \sum_j \sum_{\sigma=\pm 1} \sum_\alpha A^\alpha_j \Pi^\alpha_{vv'} \, e^{i(\Omega_{vv'} - \sigma\omega_j)t - i\sigma\phi_j} \, (1 - \delta_{vv'}) \\ &- (2\hbar)^{-2} \sum_j \sum_{\alpha,\beta} A^\alpha_j A^\beta_j \, e^{i\Omega_{vv'} t} \\ &\times \Big[\sum_b \frac{\Pi^\alpha_{vb} \Pi^\beta_{bv'}}{\Omega_{bv'} - \omega_j} + \sum_b \frac{\Pi^\alpha_{vb} \Pi^\beta_{bv'}}{\Omega_{bv'} + \omega_j} \Big] \,, \end{aligned} \tag{3.41}$$

$$\begin{aligned}\tilde{H}_{cv} = & -(2\hbar)^{-1} \sum_j \sum_{\sigma=\pm 1} \sum_\alpha A_j^\alpha \Pi_{cv}^\alpha \, e^{i(\Omega_{cv}-\sigma\omega_j)t - i\sigma\phi_j} \\ & -(2\hbar)^{-2} \sum_{\alpha,\beta} A_2^\alpha A_2^\beta \, e^{i(\Omega_{cv}-2\omega_2)t - i2\phi_2} \\ & \times \Big[\Pi_{cv}^\alpha (\Pi_{cc}^\beta - \Pi_{vv}^\beta)/\omega_2 + \sum_b \frac{\Pi_{cb}^\alpha \Pi_{bv}^\beta}{\Omega_{bv}-\omega_2} \Big] ,\end{aligned} \tag{3.42}$$

and

$$\begin{aligned}\tilde{H}_{vc} = & -(2\hbar)^{-1} \sum_j \sum_{\sigma=\pm 1} \sum_\alpha A_j^\alpha \Pi_{vc}^\alpha \, e^{i(\Omega_{vc}-\sigma\omega_j)t - i\sigma\phi_j} \\ & +(2\hbar)^{-2} \sum_{\alpha,\beta} A_2^\alpha A_2^\beta \, e^{i(\Omega_{vc}+2\omega_2)t + i2\phi_2} \\ & \times \Big[\Pi_{vc}^\alpha (\Pi_{vv}^\beta - \Pi_{cc}^\beta)/\omega_2 + \sum_b \frac{\Pi_{vb}^\alpha \Pi_{bc}^\beta}{\Omega_{cb}-\omega_2} \Big] .\end{aligned} \tag{3.43}$$

The non-hermiticity of $\tilde{H}$ will be discussed in section 3.7.3. Remind that a wavevector label $\boldsymbol{k}$ must be added to each pair of band indices *e.g.* $\Omega_{cv} \to \Omega_{cv,\boldsymbol{k}}$.

The r.h.s. of the transformed equation of motion (3.39) contains only driving terms which are linear or quadratic in the fields. The slowly varying linear driving terms (referred to as quasi-resonant terms) give the dominant contribution to the one-photon transitions whereas the ones displaying rapid oscillations (off-resonant terms) do not contribute significantly. As they may however be important for the resonant higher-order processes of interest to us (two-photon transitions, Stark shift, ...), we can not simply discard them. To treat these terms, we have developed a consistent scheme which amounts to use the same perturbative approach for rapidly oscillating terms as in the first step where we eliminated the far off-resonant bands and reduced the density matrix. As a result, we obtain an additional set of quasi-resonant quadratic terms. This reflects the fact that the bands of group $\mathbb{A}$ participate also to higher-order transitions as intermediate states. In the effective Bloch equations (3.39), the linear terms oscillating with central frequencies $\Omega_{cc'} \pm \omega_j$ or $\Omega_{vv'} \pm \omega_j$ contribute to the resonant second-order processes in $\tilde{H}_{cc'}$ or $\tilde{H}_{vv'}$ respectively, and those of frequency $\Omega_{cv} - \omega_2$ are important for the two-photon transition in $\tilde{H}_{cv}$. Thus, the sums

$$\sum_b \frac{\Pi_{ab}^\alpha \Pi_{ba'}^\beta}{\Omega_{ab} \pm \omega_j} \tag{3.44}$$

in (3.40) to (3.43), taken over the eliminated off-resonant bands $b \in \mathbb{B}$, have to be replaced by the sums

$$\sum_{n\neq a,a'} \frac{\Pi^{\alpha}_{an}\Pi^{\beta}_{na'}}{\Omega_{an} \pm \omega_j}\,, \tag{3.45}$$

taken over all bands n for which the corresponding denominator $\Omega_{an} \pm \omega_j$ is large enough. In other words, the sum over n includes all bands of $\mathbb{B}$, *and* some bands of $\mathbb{A}$. This procedure is similar to the one used to eliminate the off-resonant bands (group $\mathbb{B}$) and is depicted in appendix D. Note that the diagonal momentum matrix elements must be excluded from the sum over n. Indeed, they did not appear in the linear terms of $\tilde{H}_{cc'}$ and $\tilde{H}_{vv'}$, because they were already removed by the transformation to the rotating frame (§ 3.4). However, their resonant contribution to the second order processes, *i.e.* transitions where the intermediate state is either the initial or the final state, was taken into account by the expansion into Bessel functions (see § 3.5) which led to the expression

$$\Pi^{\alpha}_{vc}(\Pi^{\beta}_{vv} - \Pi^{\beta}_{cc})/\omega_2 \tag{3.46}$$

in the second term on the r.h.s. of (3.42) and (3.43). Note that (3.46) has not exactly the same structure than the expressions in the sum (3.45). Therefore, these two quadratic terms can not be put together in a more compact form.

3.7.2 Discussion of the band-diagonal momentum matrix elements

One may wonder why in (3.42) and (3.43) the second-order terms involving diagonal momentum matrix elements dot not have exactly the same form as those including only off-diagonal elements. One might indeed expect the expression

$$\sum_{a=c,v} \frac{\Pi_{ca}\Pi_{av}}{\Omega_{av} - \omega_2} = \frac{\Pi_{cv}\Pi_{vv}}{\Omega_{vv} - \omega_2} + \frac{\Pi_{cc}\Pi_{cv}}{\Omega_{cv} - \omega_2} \tag{3.47}$$

instead of the actual

$$\Pi_{cv}(\Pi_{cc} - \Pi_{vv})/\omega_2 = \frac{\Pi_{cv}\Pi_{vv}}{\Omega_{vv} - \omega_2} - \frac{\Pi_{cc}\Pi_{cv}}{\Omega_{cc} - \omega_2}\,. \tag{3.48}$$

First we note that the difference between the two is proportional to

$$\frac{\Omega_{cv} - 2\omega_2}{\omega_2\left(\Omega_{cv} - \omega_2\right)}\,, \tag{3.49}$$

and is therefore comparable to the small contribution (D.9) neglected while extending the intermediate states to the bands of group $\mathbb{A}$ in the quadratic terms (3.45) (see Appendix D). Second it appears that, if for the processes involving the diagonal momentum matrix elements one uses the procedure outlined in the appendix D instead of the expansion in Bessel functions, one obtains the second-order expression

$$\sum_{a=c,v}\left[\frac{\Pi_{ca}\Pi_{av}\rho_{vv}}{\Omega_{av}-\omega_2}-\frac{\rho_{cc}\Pi_{ca}\Pi_{av}}{\Omega_{ac}+\omega_2}+\frac{\Pi_{ca}\rho_{aa}\Pi_{av}}{\Omega_{va}+\omega_2}-\frac{\Pi_{ca}\rho_{aa}\Pi_{av}}{\Omega_{ca}-\omega_2}\right]. \tag{3.50}$$

If, following Appendix D, one neglects the small corrections given by the last two terms, one finds the expected transition amplitude (3.47). However, in the special case of diagonal momentum matrix elements, this approximation is not necessary, because some of the terms in (3.50) cancel exactly, and one recovers (3.48). We thus keep the specific form (3.48) rather than (3.47), because it is the natural one.

3.7.3 Discussion of hermiticity: symmetrized effective Hamiltonian

We emphasize that the perturbative approach described above does not preserve hermiticity, as can be seen from the Bloch equations (3.39) to (3.43). This is related to the second-order interaction terms with energy mismatch. Indeed, the denominators $(\Omega_{nv}-\omega_2)$ and $-(\Omega_{cn}-\omega_2)$ in $\tilde{H}_{cv}$ and $\tilde{H}_{vc}$ are not equal if $\Omega_{cv}\neq 2\omega_2$. The same problem appears for the denominators in $\tilde{H}_{cc'}$ and $\tilde{H}_{vv'}$ if $\Omega_{cc'}\neq 0$ and $\Omega_{vv'}\neq 0$. The departure from hermiticity is however *of the order of the terms neglected when making the far-off-resonance approximation* for the intermediate levels. Therefore it is justified to symmetrize the effective Hamiltonian. A crucial benefit is to ensure accurately the total charge conservation in the crystal during calculation.

Finally, among all quadratic terms obtained, we retain consistently the slowly varying ones (generalized rotating wave approximation). The resulting multi-band Bloch equations for the symmetrized effective Hamiltonian $\bar{H}_{aa'}=(\tilde{H}_{aa'}+\tilde{H}^{*}_{a'a})/2$ can be written as

$$\boxed{\partial_t\bar{\rho}=-i\big[\bar{H}\,,\bar{\rho}\big]} \tag{3.51}$$

with

$$\boxed{\begin{aligned}\bar{H}_{cc'}=&-(2\hbar)^{-2}\sum_j\sum_{\alpha,\beta}A_j^{\alpha}A_j^{\beta}\,e^{i\Omega_{cc'}t}\\&\times\frac{1}{2}\sum_{\sigma=\pm1}\sum_{n\neq c,c'}\left[\frac{\Pi^{\alpha}_{cn}\Pi^{\beta}_{nc'}}{\Omega_{nc}-\sigma\omega_j}+\frac{\Pi^{\alpha}_{cn}\Pi^{\beta}_{nc'}}{\Omega_{nc'}-\sigma\omega_j}\right]\end{aligned}} \tag{3.52}$$

$$\boxed{\begin{aligned}\bar{H}_{vv'} =& -(2\hbar)^{-2}\sum_{j}\sum_{\alpha,\beta} A_j^{\alpha}A_j^{\beta}\,e^{i\Omega_{vv'}t}\\ &\times\frac{1}{2}\sum_{\sigma=\pm1}\sum_{n\neq v,v'}\Big[\frac{\Pi^{\alpha}_{vn}\Pi^{\beta}_{nv'}}{\Omega_{nv}-\sigma\omega_j}+\frac{\Pi^{\alpha}_{vn}\Pi^{\beta}_{nv'}}{\Omega_{nv'}-\sigma\omega_j}\Big]\end{aligned}} \tag{3.53}$$

and

$$\boxed{\begin{aligned}\bar{H}_{cv} =& -(2\hbar)^{-1}\sum_{\alpha} A_1^{\alpha}\Pi^{\alpha}_{cv}\,e^{i(\Omega_{cv}-\omega_1)t-i\phi_1}\\ &-(2\hbar)^{-2}\sum_{\alpha,\beta} A_2^{\alpha}A_2^{\beta}\,e^{i(\Omega_{cv}-2\omega_2)t-i2\phi_2}\\ &\times\Big[\Pi^{\alpha}_{cv}(\Pi^{\beta}_{cc}-\Pi^{\beta}_{vv})/\omega_2+\frac{1}{2}\sum_{n\neq c,v}\big(\frac{\Pi^{\alpha}_{cn}\Pi^{\beta}_{nv}}{\Omega_{nv}-\omega_2}-\frac{\Pi^{\alpha}_{cn}\Pi^{\beta}_{nv}}{\Omega_{cn}-\omega_2}\big)\Big]\,.\end{aligned}} \tag{3.54}$$

The reduced density matrix $\tilde{\rho}$ in the rotating frame has been replaced by the new symbol $\bar{\rho}$ in order to stress that all rapid oscillations have been suppressed. Also keep in mind that a wavevector label $\boldsymbol{k}$ must be added to each pair of band indices *e.g.* $\Omega_{cv}\rightarrow\Omega_{cv,\boldsymbol{k}}$. To be precise, the Heisenberg equation (3.51) reads

$$\partial_t\bar{\rho}_{mm',\boldsymbol{k}} = -i\sum_{\boldsymbol{k}}\sum_{n}(\bar{H}_{mn,\boldsymbol{k}}\bar{\rho}_{nm',\boldsymbol{k}}-\bar{\rho}_{mn,\boldsymbol{k}}\bar{H}_{nm',\boldsymbol{k}})\,. \tag{3.55}$$

It must be reminded that all sums over the intermediate states n do not cover the same bands. Indeed, as discussed above, the sums over n include all far off-resonant bands eliminated from the equation of motion (set $\mathbb{B}$), as well as the bands of the *reduced* density matrix (set $\mathbb{A}$) for which the corresponding frequency denominator $\Omega\pm\omega_j$ is large. By contrast, the quadratic contributions from the transitions with small detuning $\Omega\pm\omega_j$ are automatically contained in the resonant linear interaction of $\bar{H}_{cv}$. Thus, the terms in $\bar{H}_{cc'}$ (respectively $\bar{H}_{vv'}$) containing ω_2 include all resonant and off-resonant states, whereas for ω_1 one has to exclude the valence bands (respectively, the conduction bands) of group $\mathbb{A}$ in the sum related to the denominators $\Omega_{nc}+\omega_1$ (respectively, $\Omega_{nv}-\omega_1$). The sum over n in $\bar{H}_{cv}$ refers to all bands in $\mathbb{A}$ and $\mathbb{B}$. Finally, the bands leading to diagonal momentum matrix elements have to be excluded from all sums over n, as indicated explicitly.

In the inter-band elements $\bar{H}_{cv}$ of the effective Hamiltonian, one can identify the one- and two-photon transition amplitudes between valence and conduction bands, involving respectively the electromagnetic fields $\boldsymbol{A}_1$ and $\boldsymbol{A}_2$. The one-photon transitions induced by the field of frequency ω_2 have been completely neglected. The field of frequency ω_1 can however still induce inter-band two-photon transitions, but with a large energy mismatch. The associated probability is therefore extremely weak compared to the resonant first-order process.

The diagonal part of $\bar{H}_{cc'}$ and $\bar{H}_{vv'}$ contains the AC Stark shifts, and the off-diagonal elements describe intra-band two-photon transitions where one photon is absorbed and one photon emitted. Both frequencies ω_1 and ω_2 contribute to these resonant processes. Further details on the various nonlinear phenomena described by the above equations can be found in section 3.10.

The effective equations (3.51) differ from the well-known Semiconductor Bloch Equations [108, 109] because we keep all intra-band momentum matrix elements (including the band-diagonal ones) and all quasi-resonant contributions of *both* frequencies. In the rotating frame, this was achieved by replacing the rapidly oscillating linear interaction terms by *effective* interactions which are quadratic in the field and eventually keeping only the slowly varying ones among them (generalized rotating wave approximation). This is well justified close to resonance and leads to a Schrödinger equation with all interaction terms (one- *and* two-photon processes) varying on the same time-scale (the pulse duration), which makes the numerical integration much more efficient.

3.8 Restrictions due to the slowly varying envelope approximation

Let us consider more in detail the limitations, that the main approximation (3.28) imposes on the slowly varying envelopes $\boldsymbol{A}_j$. In the case where the equations are restricted to interaction terms of first- and second-order in the electromagnetic field, the function $F(t)$ in the integral of (3.28) is simply proportional to $\boldsymbol{A}_j$ (see (3.36) and (3.37)). Thus, integrating by part leads to

$$\begin{aligned} i\int_0^\infty dt'\, e^{i(\Omega-\omega_j)(t-t')}\, A_j^\alpha(t-t')\,\bar{\rho}(t-t') &= \frac{e^{i(\Omega-\omega_j)t}}{\Omega-\omega_j}\, A_j^\alpha(t)\,\bar{\rho}(t) \\ - \int_0^\infty dt'\, \frac{e^{i(\Omega-\omega_j)(t-t')}}{\Omega-\omega_j} & \left[\dot{A}_j^\alpha(t-t')\,\bar{\rho}(t-t') + A_j^\alpha(t-t')\,\dot{\bar{\rho}}(t-t')\right], \quad (3.56) \end{aligned}$$

where the dots on A_j^α and $\bar{\rho}$ denote the time derivative. Neglecting the second term on the r.h.s. is justified only if the corresponding integrand is much smaller than the integrand on the l.h.s.. In other words, the vector potential and the density matrix element must satisfy

$$|\dot{A}_j^\alpha(t)/A_j^\alpha(t)| \ll |\Omega-\omega_j| \quad (3.57)$$

and

$$|\dot{\bar{\rho}}(t)/\bar{\rho}(t)| \ll |\Omega - \omega_j| \,. \tag{3.58}$$

For the field envelope of a typical (sech-) laser pulse $\boldsymbol{A}_j(t) \propto [\cosh(t/T)]^{-1}$, the condition (3.57) reduces to

$$\frac{1}{T} \ll |\Omega - \omega_j| \,. \tag{3.59}$$

Let us illustrate this with the one-photon transitions of frequency $\omega_2 \simeq \Omega_{cv}/2$ neglected in section 3.7. For a pulse duration of 100 fs at half-maximum of intensity and a band gap[5] $\hbar\Omega_{cv}$ of 1.5 eV, the inequality (3.59) is well satisfied, as it becomes $T = 56.7$ fs $\gg 2/\Omega_{cv} = 0.88$ fs.

3.9 Polarization current

In the previous sections, we set up effective multi-band Bloch equations governing the time evolution of the system. We now want to rely the reduced density matrix, solution of these equations, to a macroscopic observable. In the following, we thus derive an expression for an effective polarization current that must be consistent with the previous approximations.

The density of polarization current is obtained from the density matrix by

$$\boldsymbol{j} = \frac{1}{V}\mathrm{Tr}[-e\,\boldsymbol{v}\,\rho] \,, \tag{3.60}$$

where the velocity operator $\boldsymbol{v}$ is related to the momentum operator $\boldsymbol{\pi}$ by

$$\boldsymbol{v} = (\boldsymbol{\pi} + e\boldsymbol{A})/m_0 \,. \tag{3.61}$$

The symbol V denotes the dimension of the crystal in the unconfined directions, namely the volume of the bulk, the surface of the quantum well or the length of the quantum wire. Keeping the same notation (3.5), the density of current can be written as

$$\boldsymbol{j}(t) = \frac{1}{V}\sum_{\boldsymbol{k}}\sum_{mn}(\boldsymbol{\Pi}_{mn,\boldsymbol{k}} - \frac{e^2}{m_0}\boldsymbol{A}(t)\,\delta_{mn})\,\rho_{nm,\boldsymbol{k}}(t) \,. \tag{3.62}$$

This expression has to be put in a form containing only the *reduced* density matrix *i.e.* the bands for which the time evolution is calculated. This can be done by the same perturbative approach as above. In accordance with the approximations

---

[5] typical GaAs/AlGaAs quantum well

made to derive the effective multi-band Bloch equations (3.51), the polarization current has to be calculated to the next order in the fields, to properly include the two-photon transitions.

First, the reduced density matrix $\rho_{aa',\boldsymbol{k}}$ is expressed in the rotating frame introduced in section 3.4. Expanded to the first order in the field, the transformation (3.10) becomes

$$\begin{aligned}\rho_{aa'} \simeq &+ \tilde{\rho}_{aa'}\, e^{-i\Omega_{aa'}t} + (2\hbar)^{-1} \sum_j \sum_\alpha A_j^\alpha \tilde{\rho}_{aa'} (\Pi^\alpha_{aa} - \Pi^\alpha_{a'a'}) \\ &\times \sum_{\sigma=\pm 1} \frac{e^{-i(\Omega_{aa'}-\sigma\omega_j)t + i\sigma\phi_j}}{\sigma\omega_j} .\end{aligned} \tag{3.63}$$

The obvious $\boldsymbol{k}$ indices have been dropped.

Second, the rapidly varying density matrix elements $\rho_{ab,\boldsymbol{k}}$ and $\rho_{ba,\boldsymbol{k}}$ are also expressed in the rotating frame, and then approximated by the integrated r.h.s. of (3.25) and its complex conjugate. To the first order in the fields, we find

$$\begin{aligned}\rho_{ab} \simeq &- (2\hbar)^{-1} \sum_j \sum_\alpha A_j^\alpha \sum_{a'} \left[\tilde{\rho}_{aa'} \Pi^\alpha_{a'b} - \delta_{aa'} \Pi^\alpha_{a'b} \tilde{\rho}^{(0)}_{bb}\right] \\ &\times \sum_{\sigma=\pm 1} \frac{e^{-i(\Omega_{aa'}+\sigma\omega_j)t - i\sigma\phi_j}}{\Omega_{a'b} - \sigma\omega_j} .\end{aligned} \tag{3.64}$$

Note that, in this approximation, the rotating frame transformation is restricted to the zeroth order in the field: $\rho_{ab,\boldsymbol{k}} = \tilde{\rho}_{ab,\boldsymbol{k}}\, e^{-i\Omega_{ab,\boldsymbol{k}}t}$. This is consistent with our goal to derive an effective polarization current up to the first order in the field.

Finally, the remaining density matrix elements $\rho_{bb',\boldsymbol{k}}$ in (3.62) must be replaced by the integrated r.h.s. of (3.26). However, the equation of motion (3.26) does not contain any element of the *reduced* density matrix $\tilde{\rho}_{aa',\boldsymbol{k}}$, but exclusively $\tilde{\rho}_{ab,\boldsymbol{k}}$ and $\tilde{\rho}_{bb',\boldsymbol{k}}$. Thus, the latter must again be substituted by the formal solution of (3.25) and (3.26), in order to obtain an expression involving the reduced density matrix. In the polarization current, this would lead to terms of the *second* order in the field. Therefore, we can consistently neglect the contribution of $\rho_{bb',\boldsymbol{k}}$.

To summarize the above procedure, the polarization current (3.62) is restricted to

$$\begin{aligned}\boldsymbol{j} = &\frac{1}{V} \sum_{\boldsymbol{k}} \sum_{aa'} (\boldsymbol{\Pi}_{aa',\boldsymbol{k}} - \frac{e^2}{m_0} \boldsymbol{A}\, \delta_{aa'})\, \rho_{a'a,\boldsymbol{k}} \\ &+ \frac{1}{V} \sum_{\boldsymbol{k}} \sum_{ab} (\boldsymbol{\Pi}_{ab,\boldsymbol{k}}\, \rho_{ba,\boldsymbol{k}} + \rho_{ab,\boldsymbol{k}}\, \boldsymbol{\Pi}_{ba,\boldsymbol{k}}) ,\end{aligned} \tag{3.65}$$

with $\rho_{aa',\boldsymbol{k}}$ and $\rho_{ab,\boldsymbol{k}}$ approximated by (3.63) and (3.64). Keeping only the terms oscillating with frequency close to ω_1, ω_2 and 0, the polarization current becomes

$$\boxed{\boldsymbol{j} = \boldsymbol{j}_{\mathbb{AA}} + \boldsymbol{j}_{\mathbb{AB}} + \boldsymbol{j}_0\,.} \tag{3.66}$$

The three terms on the r.h.s. are detailed in what follows. Among them, only the first one depends on the reduced density matrix.

The main contribution $\boldsymbol{j}_{\mathbb{AA}}$ can be written as

$$\boxed{\boldsymbol{j}_{\mathbb{AA}} = \frac{1}{V}\mathrm{Tr}[\boldsymbol{J}_{\mathbb{AA}}\bar{\rho}]} \tag{3.67}$$

where the effective current operator $\boldsymbol{J}_{\mathbb{AA}}$ is defined by the sub-blocks

$$\boxed{\begin{aligned} J^{\beta}_{cc'} &= +\,\Pi^{\beta}_{cc'}\,e^{i\Omega_{cc'}t} \\ &\quad+(2\hbar)^{-1}\sum_{j}\sum_{\alpha}\sum_{\sigma=\pm1} A^{\alpha}_{j}\,e^{i(\Omega_{cc'}-\sigma\omega_j)t-i\sigma\phi_j} \\ &\quad\times\Big[\sum_{n}\frac{\Pi^{\beta}_{cn}\Pi^{\alpha}_{nc'}}{\Omega_{nc'}-\sigma\omega_j}+\sum_{n}\frac{\Pi^{\alpha}_{cn}\Pi^{\beta}_{nc'}}{\Omega_{nc}+\sigma\omega_j}\Big]\end{aligned}} \tag{3.68}$$

$$\boxed{\begin{aligned} J^{\beta}_{vv'} &= +\,\Pi^{\beta}_{vv'}\,e^{i\Omega_{vv'}t} \\ &\quad+(2\hbar)^{-1}\sum_{j}\sum_{\alpha}\sum_{\sigma=\pm1} A^{\alpha}_{j}\,e^{i(\Omega_{vv'}-\sigma\omega_j)t-i\sigma\phi_j} \\ &\quad\times\Big[\sum_{n}\frac{\Pi^{\beta}_{vn}\Pi^{\alpha}_{nv'}}{\Omega_{nv'}-\sigma\omega_j}+\sum_{n}\frac{\Pi^{\alpha}_{vn}\Pi^{\beta}_{nv'}}{\Omega_{nv}+\sigma\omega_j}\Big]\end{aligned}} \tag{3.69}$$

$$\boxed{\begin{aligned} J^{\beta}_{cv} &= +\,\Pi^{\beta}_{cv}\,e^{i\Omega_{cv}t} \\ &\quad+(2\hbar)^{-1}\sum_{\alpha} A^{\alpha}_{2}\,e^{i(\Omega_{cv}-\omega_2)t-i\phi_2} \\ &\quad\times\Big[\sum_{n}\frac{\Pi^{\beta}_{cn}\Pi^{\alpha}_{nv}}{\Omega_{nv}-\omega_2}-\sum_{n}\frac{\Pi^{\alpha}_{cn}\Pi^{\beta}_{nv}}{\Omega_{cn}-\omega_2}\Big]\,.\end{aligned}} \tag{3.70}$$

The symbol $\tilde{\rho}$ was replaced by $\bar{\rho}$ to emphasize the restriction to the dominant contribution resulting from the effective multi-band Bloch equations (3.51). Remind that a wavevector label $\boldsymbol{k}$ must be added to each pair of band indices *e.g.* $\Omega_{cv} \to \Omega_{cv,\boldsymbol{k}}$. To be precise, the trace on the r.h.s. of (3.67) reads $\sum_{\boldsymbol{k}}\sum_{mn}\boldsymbol{J}_{mn,\boldsymbol{k}}\bar{\rho}_{nm,\boldsymbol{k}}$. As in the preceding section (§ 3.7), the contribution of the off-resonant first-order processes to the resonant second-order transitions has been taken into account by extending the sum over the eliminated bands b to all intermediate states n leading to large denominators $\Omega \pm \omega_i$ (see Appendix D). Notice that the diagonal momentum matrix elements are not excluded from these sums. Finally, we point out that, unlike for the Hamiltonian, it is not necessary to symmetrize the effective current operator $\boldsymbol{J}$, because it is already hermitian.

The two remaining contributions to the polarization current (3.66) do not depend on the dynamics of the reduced density matrix. They are given by

$$j_0^\beta = -\frac{e^2}{m_0} A^\beta \frac{1}{V} \sum_{\boldsymbol{k}} \sum_a \bar{\rho}_{aa,\boldsymbol{k}} \tag{3.71}$$

and

$$\begin{aligned} j_{\mathbb{AB}}^\beta = &-(2\hbar)^{-1} \sum_j \sum_\alpha \sum_{\sigma=\pm 1} A_j^\alpha \, e^{-i\sigma\omega_j t - i\sigma\phi_j} \\ &\times \frac{1}{V} \sum_{\boldsymbol{k}} \sum_a \sum_b \bar{\rho}_{bb,\boldsymbol{k}}^{(0)} \left[\frac{\Pi_{ab,\boldsymbol{k}}^\beta \Pi_{ba,\boldsymbol{k}}^\alpha}{\Omega_{ba,\boldsymbol{k}} - \sigma\omega_j} + \frac{\Pi_{ab,\boldsymbol{k}}^\alpha \Pi_{ba,\boldsymbol{k}}^\beta}{\Omega_{ba,\boldsymbol{k}} + \sigma\omega_j} \right] . \end{aligned} \tag{3.72}$$

Due to the carrier conservation, the sum in (3.71) can be replaced by

$$\varrho = \frac{1}{V} \sum_{\boldsymbol{k}} \sum_a \bar{\rho}_{aa,\boldsymbol{k}} \, , \tag{3.73}$$

the *constant* density of electrons in the bands of group $\mathbb{A}$. The density of current (3.71) becomes

$$\boxed{j_0^\beta = -\frac{e^2 \varrho}{m_0} A^\beta \, .} \tag{3.74}$$

On the other hand, the time-reversal symmetry[6] ensures that the momentum matrix elements involving conjugate bands n and $\bar{n}$ (or m and $\bar{m}$) satisfy

$$\Pi_{mn,+\boldsymbol{k}}^\alpha \Pi_{nm,+\boldsymbol{k}}^\beta = \left[\Pi_{\bar{m}\bar{n},-\boldsymbol{k}}^\alpha \Pi_{\bar{n}\bar{m},-\boldsymbol{k}}^\beta \right]^* , \tag{3.75}$$

and that the energies are related by

$$E_{n,\boldsymbol{k}} = E_{\bar{n},-\boldsymbol{k}} . \tag{3.76}$$

Furthermore, we assume that in distant past the system was at thermal equilibrium, which implies that

$$\bar{\rho}_{nn,+\boldsymbol{k}}^{(0)} = \bar{\rho}_{\bar{n}\bar{n},-\boldsymbol{k}}^{(0)} \, . \tag{3.77}$$

---

[6] see also § 4.4.1

As a consequence of the symmetry properties (3.75) to (3.77), the sum

$$\frac{1}{V}\sum_{\boldsymbol{k}}\sum_{a}\sum_{b}\bar{\rho}^{(0)}_{bb,\boldsymbol{k}}\left[\frac{\Pi^{\beta}_{ab,\boldsymbol{k}}\Pi^{\alpha}_{ba,\boldsymbol{k}}}{\Omega_{ba,\boldsymbol{k}}-\sigma\omega_j}+\frac{\Pi^{\alpha}_{ab,\boldsymbol{k}}\Pi^{\beta}_{ba,\boldsymbol{k}}}{\Omega_{ba,\boldsymbol{k}}+\sigma\omega_j}\right] \tag{3.78}$$

is real and the current $\boldsymbol{j}_{\mathbb{AB}}$ can be expressed as

$$\boxed{\begin{aligned} j^{\beta}_{\mathbb{AB}} = &-\sum_{j}\sum_{\alpha}A^{\alpha}_{j}\,\cos(\omega_j t-\phi_j)\\ &\times\frac{1}{\hbar V}\sum_{\boldsymbol{k}}\sum_{a}\sum_{b}\bar{\rho}^{(0)}_{bb,\boldsymbol{k}}\left[\frac{\Pi^{\beta}_{ab,\boldsymbol{k}}\Pi^{\alpha}_{ba,\boldsymbol{k}}}{\Omega_{ba,\boldsymbol{k}}-\omega_j}+\frac{\Pi^{\alpha}_{ab,\boldsymbol{k}}\Pi^{\beta}_{ba,\boldsymbol{k}}}{\Omega_{ba,\boldsymbol{k}}+\omega_j}\right].\end{aligned}} \tag{3.79}$$

In order to highlight the physical origin of $\boldsymbol{j}_0$ and $\boldsymbol{j}_{\mathbb{AB}}$, let us change to the frequency domain and replace the density of current by the corresponding polarization $\boldsymbol{P}(\omega) = (i\omega)^{-1}\,\boldsymbol{j}(\omega)$, and the vector potential by the electric field $\boldsymbol{E}(\omega) = -i\omega\,\boldsymbol{A}(\omega)$. The relations (3.74) and (3.79) can then be expressed as

$$P^{\beta}_{0}(\omega) = \epsilon_0\sum_{\alpha}\chi^{\beta\alpha}_{0}(\omega)\,E^{\alpha}(\omega) \tag{3.80}$$

$$P^{\beta}_{\mathbb{AB}}(\omega) = \epsilon_0\sum_{\alpha}\chi^{\beta\alpha}_{\mathbb{AB}}(\omega)\,E^{\alpha}(\omega) \tag{3.81}$$

with

$$\chi^{\beta\alpha}_{0}(\omega) = -\,\omega^{-2}\,\frac{e^2\varrho}{\epsilon_0 m_0}\,\delta_{\beta\alpha} \tag{3.82}$$

$$\chi^{\beta\alpha}_{\mathbb{AB}}(\omega) = -\,\omega^{-2}\,\frac{1}{\epsilon_0\hbar V}\sum_{\boldsymbol{k}}\sum_{a}\sum_{b}\bar{\rho}^{(0)}_{bb,\boldsymbol{k}}\left[\frac{\Pi^{\beta}_{ab,\boldsymbol{k}}\Pi^{\alpha}_{ba,\boldsymbol{k}}}{\Omega_{ba,\boldsymbol{k}}-\omega}+\frac{\Pi^{\alpha}_{ab,\boldsymbol{k}}\Pi^{\beta}_{ba,\boldsymbol{k}}}{\Omega_{ba,\boldsymbol{k}}+\omega}\right]. \tag{3.83}$$

One recognizes respectively the (real) first-order susceptibility related to the constant electronic density ϱ, and the (real) first-order susceptibility due to the optical coupling between the principal bands (group $\mathbb{A}$) and the eliminated bands (group $\mathbb{B}$).

In the next chapters, we mainly focus on the “low frequency” part of the polarization current. The contributions $\boldsymbol{j}_0$ and $\boldsymbol{j}_{\mathbb{AB}}$ as well as the higher order terms in $\boldsymbol{j}_{\mathbb{AA}}$ oscillate with frequencies around ω_1 or ω_2. The slowly varying part of the current is therefore given by

$$\boxed{\boldsymbol{j} = \frac{1}{V}\sum_{\boldsymbol{k}}\Big[\sum_{cc'}\boldsymbol{\Pi}_{cc',\boldsymbol{k}}\,e^{i\Omega_{cc',\boldsymbol{k}}t}\,\bar{\rho}_{c'c,\boldsymbol{k}}+\sum_{vv'}\boldsymbol{\Pi}_{vv',\boldsymbol{k}}\,e^{i\Omega_{vv',\boldsymbol{k}}t}\,\bar{\rho}_{v'v,\boldsymbol{k}}\Big].} \tag{3.84}$$

3.10 Linear and nonlinear optical processes described by the model

The effective multi-band Bloch equations (3.51), and the related polarization current (3.66), describe the dynamics of the electrons in a crystal excited by two electromagnetic fields $\boldsymbol{A}_1$ and $\boldsymbol{A}_2$ of frequency ω_1 and ω_2 with $\hbar\omega_1$ and $2\hbar\omega_2$ *close to the inter-band transition energies*. This restriction on the frequencies reflects the underlying approximations: we neglected the off-resonant processes (generalized rotating wave approximation). In this context, the model accounts for the various nonlinear optical phenomena that are strongly enhanced when certain frequencies fall in the vicinity of transition frequencies of the medium ("resonance enhancement"). They can be classified in two categories according to the involved resonance: nonlinearities enhanced by i) quasi-resonant *inter-band* transitions, or ii) quasi-resonant *intra-band* transitions.

The first category implies real or virtual quasi-resonant inter-band transitions: first-order processes with detuning $\Omega_{cv} - \omega_1$ for the field $\boldsymbol{A}_1$, and second-order processes with detuning $\Omega_{cv} - 2\omega_2$ for the field $\boldsymbol{A}_2$. These nonlinearities involve, respectively, the linear and quadratic interaction terms in the inter-band matrix elements $\bar{H}_{cv}$ of the effective Hamiltonian (equation (3.54)).

The second category implies real or virtual quasi-resonant intra-band transitions: second-order processes with detuning $\Omega_{cc'}$ or $\Omega_{vv'}$ for both fields. These processes involve the quadratic interaction terms in the intra-band matrix elements $\bar{H}_{cc'}$ and $\bar{H}_{vv'}$ (equations (3.52) and (3.53)).

In the following, we list several optical nonlinear phenomena that are included in the present model, and give the corresponding first-, second- or third-order susceptibilities.

i) Inter-band resonance enhancement

One-photon absorption	$\chi^{(1)}(-\omega_1; \omega_1)$
Second-harmonic generation	$\chi^{(2)}(-2\omega_2; \omega_2, \omega_2)$
Second-order difference frequency mixing	$\chi^{(2)}(\omega_2 - \omega_1; -\omega_2, \omega_1)$
Two-photon absorption	$\chi^{(3)}(-\omega_2; -\omega_2, \omega_2, \omega_2)$
Third-order difference frequency mixing	$\chi^{(3)}(\omega_1 - 2\omega_2; -\omega_1, \omega_2, \omega_2)$
Injection of photocurrent	$\chi^{(3)}(0; -2\omega_2, \omega_2, \omega_2)$

ii) Intra-band resonance enhancement

Optical rectification	$\chi^{(2)}(0; -\omega_2, \omega_2)$
AC Stark effect	$\chi^{(3)}(-\omega_2; \omega_2, -\omega_2, \omega_2)$

We emphasize that these various processes are not independent, but take place simultaneously and interfere. Thus, the theory developed in this chapter is well adapted to the study of the *interplay* between these competing processes when the optical frequencies are close to resonance.

3.11 One- and two-photon absorption coefficient

In this section, we detail how to extract the one- and two-photon absorption coefficients from the time-dependent polarization current (3.67) obtained after solving the effective multi-band Bloch equations (3.51). For this purpose, we separately consider the case where the system is excited by one- or two-photon transitions only. In the framework of the present model, this corresponds respectively to $\boldsymbol{A}_1 = 0$ or $\boldsymbol{A}_2 = 0$ in the total field $\boldsymbol{A}$ (equation (3.35)).

As the following chapters will focus on nonlinear optical processes in symmetric AlGaAs/GaAs quantum wells and V-shaped AlGaAs/GaAs quantum wires, we restrict the main results of this section to the corresponding crystal classes[7] (respectively, $\mathbf{D}_{4h}$ and $\mathbf{C}_{2v}$).

3.11.1 Two-photon absorption and third-order susceptibility

The polarization current related to the two-photon transitions induced by the optical field $\boldsymbol{A}(t)$ is given by

$$j^{\mu}(t) = \epsilon_0 \int_{-\infty}^{+\infty} d\tau_3 \int_{-\infty}^{+\infty} d\tau_2 \int_{-\infty}^{+\infty} d\tau_1 \sum_{\gamma\beta\alpha} R^{\mu\gamma\beta\alpha}(t-\tau_3, t-\tau_2, t-\tau_1) \times A^{\gamma}(\tau_3) A^{\beta}(\tau_2) A^{\alpha}(\tau_1) \tag{3.85}$$

$$= \epsilon_0 \int_{-\infty}^{+\infty} d\omega_3 \int_{-\infty}^{+\infty} d\omega_2 \int_{-\infty}^{+\infty} d\omega_1 \sum_{\gamma\beta\alpha} Q^{\mu\gamma\beta\alpha}(\omega_3, \omega_2, \omega_1) \times A^{\gamma}(\omega_3) A^{\beta}(\omega_2) A^{\alpha}(\omega_1)\, e^{i(\omega_3+\omega_2+\omega_1)t} \tag{3.86}$$

where

$$\boldsymbol{A}(\omega) = \frac{1}{2\pi} \int_{-\infty}^{+\infty} d\tau \boldsymbol{A}(\tau)\, e^{-i\omega\tau} \tag{3.87}$$

and

$$Q^{\mu\gamma\beta\alpha}(\omega_3, \omega_2, \omega_1) = \int_{-\infty}^{+\infty} d\tau_3 \int_{-\infty}^{+\infty} d\tau_2 \int_{-\infty}^{+\infty} d\tau_1\, Q^{\mu\gamma\beta\alpha}(\tau_3, \tau_2, \tau_1)\, e^{-i(\omega_3\tau_3+\omega_2\tau_2+\omega_1\tau_1)} \tag{3.88}$$

---

[7] We neglect the small inversion asymmetry of GaAs.

are the Fourier transforms of the field and of the response function of the medium. Before going further, let us replace the density of current by the corresponding polarization $\partial_t \boldsymbol{P}(t) = \boldsymbol{j}(t)$, and the vector potential by the electric field $\boldsymbol{E}(t) = -\partial_t \boldsymbol{A}(t)$. Equation (3.86) then becomes

$$P^\mu(t) = \epsilon_0 \int_{-\infty}^{+\infty} d\omega_3 \int_{-\infty}^{+\infty} d\omega_2 \int_{-\infty}^{+\infty} d\omega_1 \sum_{\gamma\beta\alpha} \chi^{\mu\gamma\beta\alpha}(-\omega_\sigma; \omega_3, \omega_2, \omega_1) \\ \times E^\gamma(\omega_3) E^\beta(\omega_2) E^\alpha(\omega_1)\, e^{i(\omega_3+\omega_2+\omega_1)t} \tag{3.89}$$

where the third-order susceptibility $\chi^{\mu\gamma\beta\alpha}$ is related to the response function $Q^{\mu\gamma\beta\alpha}$ by[8]

$$\chi^{\mu\gamma\beta\alpha}(-\omega_\sigma; \omega_3, \omega_2, \omega_1) = -\frac{Q^{\mu\gamma\beta\alpha}(\omega_3, \omega_2, \omega_1)}{\omega_\sigma \omega_3 \omega_2 \omega_1} \tag{3.90}$$

with $\omega_\sigma = \omega_3 + \omega_2 + \omega_1$. The nonlinear polarization (3.89) is now inserted in Maxwell's vectorial wave equation

$$\boldsymbol{\nabla} \wedge \big(\boldsymbol{\nabla} \wedge \boldsymbol{E}(\boldsymbol{r}, t)\big) = -(\frac{n_r}{c})^2\, \partial_t^2 \boldsymbol{E}(\boldsymbol{r}, t) - \mu_0 \partial_t^2 \boldsymbol{P}(\boldsymbol{r}, t)\,, \tag{3.91}$$

where n_r is the refractive index, and specialized to the case of a monochromatic wave

$$\boldsymbol{E}(\boldsymbol{r}, t) = \boldsymbol{E}(\boldsymbol{r})\, e^{i\omega t} + \text{c.c.} = \boldsymbol{E}_0\, e^{-i\boldsymbol{k}\boldsymbol{r} + i\omega t} + \text{c.c.}\,. \tag{3.92}$$

The wavevector is related to the frequency by $\boldsymbol{k} = (n_r\omega/c)\hat{\boldsymbol{n}}$ with $\hat{\boldsymbol{n}}$ a unit vector. One is left with

$$-\nabla^2 E^\mu(\boldsymbol{r}) = (\frac{n_r\omega}{c})^2 E^\mu(\boldsymbol{r}) + 3(\frac{\omega}{c})^2 \sum_{\gamma\beta\alpha} \chi^{\mu\gamma\beta\alpha} E^\gamma(\boldsymbol{r})^* E^\beta(\boldsymbol{r}) E^\alpha(\boldsymbol{r})\,, \tag{3.93}$$

where we made use of $\boldsymbol{\nabla}\boldsymbol{E} = 0$ and introduced the shorthand notation $\chi^{\mu\gamma\beta\alpha} = \chi^{\mu\gamma\beta\alpha}(-\omega; -\omega, \omega, \omega)$. The factor 3 comes from the intrinsic permutation symmetry [21]

$$\chi^{\mu\gamma\beta\alpha}(-\omega; -\omega, \omega, \omega) = \chi^{\mu\beta\gamma\alpha}(-\omega; \omega, -\omega, \omega) = \chi^{\mu\beta\alpha\gamma}(-\omega; \omega, \omega, -\omega)\,.$$

Note that the wave envelope $\boldsymbol{E}_0$ varies with position inside the medium, due to the nonlinear susceptibility. However, we assume that this variation is sufficiently slow

---

[8] if $\omega_1 \neq 0$, $\omega_2 \neq 0$, $\omega_3 \neq 0$, and $\omega_\sigma \neq 0$

to approximate the second derivative of the field by

$$-\nabla^2 E^\mu(\boldsymbol{r}) \simeq 2i(\boldsymbol{k}\cdot\boldsymbol{\nabla})E^\mu(\boldsymbol{r}) - k^2 E^\mu(\boldsymbol{r})\,. \tag{3.94}$$

Let us now multiply equation (3.93) by $E^\mu(\boldsymbol{r})^*$ and take (twice) the imaginary part:

$$\begin{aligned} 2(\hat{\boldsymbol{n}}\cdot\boldsymbol{\nabla})|E^\mu(\boldsymbol{r})|^2 = &+\frac{3\omega}{n_r c}\sum_{\gamma\beta\alpha}(-i\chi^{\mu\gamma\beta\alpha})E^\mu(\boldsymbol{r})^* E^\gamma(\boldsymbol{r})^* E^\beta(\boldsymbol{r})E^\alpha(\boldsymbol{r}) \\ &+\frac{3\omega}{n_r c}\sum_{\gamma\beta\alpha}(-i\chi^{\mu\gamma\beta\alpha})^* E^\mu(\boldsymbol{r})E^\gamma(\boldsymbol{r})E^\beta(\boldsymbol{r})^* E^\alpha(\boldsymbol{r})^*\,. \end{aligned} \tag{3.95}$$

The following chapters will focus on nonlinear optical processes in symmetric AlGaAs/GaAs quantum wells and V-shaped AlGaAs/GaAs quantum wires (crystal class $\mathbf{D}_{4h}$ or $\mathbf{C}_{2v}$ respectively[9]). For these specific symmetries, the only nonzero susceptibility tensor elements are those with suffixes all equal or equal in pairs [21]. The previous equation then reduces to

$$\begin{aligned} (\hat{\boldsymbol{n}}\cdot\boldsymbol{\nabla})|E^\mu|^2 = &+\frac{3\omega}{n_r c}\mathrm{Im}(\chi^{\mu\mu\mu\mu})\,|E^\mu|^4 \\ &+\frac{3\omega}{n_r c}\sum_{\nu\neq\mu}\mathrm{Im}(2\chi^{\mu\nu\nu\mu})\,|E^\mu|^2|E^\nu|^2 \\ &+\frac{3\omega}{n_r c}\sum_{\nu\neq\mu}\mathrm{Im}(\chi^{\mu\mu\nu\nu}\,(E^{\mu*})^2(E^\nu)^2)\,, \end{aligned} \tag{3.96}$$

where the factor 2 in the second line comes from the intrinsic permutation symmetry [21]. Note that the last two terms may describe a linear-circular dichroism. However, in this work we restrict ourselves to linearly polarized light, *i.e.* $\boldsymbol{E} = E\hat{\boldsymbol{e}}$ with $\hat{\boldsymbol{e}} \in \mathbb{R}^3$, and we have thus $(E^{\mu*})^2(E^\nu)^2 = |E^\mu|^2|E^\nu|^2$. With the field intensity given by $I_\mu = 2c\epsilon_0 n_r|E^\mu|^2$ and the notation $\chi_i \equiv \mathrm{Im}(\chi)$, equation (3.96) becomes

$$(\hat{\boldsymbol{n}}\cdot\boldsymbol{\nabla})I_\mu = \frac{3}{2}\frac{\omega}{\epsilon_0 {n_r}^2 c^2}\big[\chi_i^{\mu\mu\mu\mu}\,{I_\mu}^2 + \sum_{\nu\neq\mu}(2\chi_i^{\mu\nu\nu\mu}+\chi_i^{\mu\mu\nu\nu})\,I_\mu I_\nu\big]\,. \tag{3.97}$$

The two-photon absorption tensor $\beta^{\mu\nu}$ is defined by

$$(\hat{\boldsymbol{n}}\cdot\boldsymbol{\nabla})I_\mu = -\sum_\nu \beta^{\mu\nu}\,I_\mu I_\nu\,, \tag{3.98}$$

---

[9] We neglect the small inversion asymmetry of GaAs.

and equation (3.97) thus leads to

$$\boxed{\beta^{\mu\nu} = -\frac{3}{2}\frac{\omega}{\epsilon_0 {n_r}^2 c^2}\left[2\chi_i^{\mu\nu\nu\mu} + \chi_i^{\mu\mu\nu\nu} - 2\chi_i^{\mu\mu\mu\mu}\delta_{\mu\nu}\right].} \tag{3.99}$$

Note that from the experimental point of view, it is difficult to distinguish between the different contributions $\beta^{\mu\nu}$ to the absorption. Photo-Luminescence Excitation (PLE) measurements usually give access only to the (polarization dependent) total absorption coefficient

$$\beta = \sum_{\mu\nu} \beta^{\mu\nu} {\hat{e}_\mu}^2 {\hat{e}_\nu}^2 . \tag{3.100}$$

Furthermore, in order to obtain an unambiguous definition of an absorption quantity in a system of reduced dimensionality, the volume V in the density of current (3.62) has to be replaced by L (the length of the wire) or S (the surface of the quantum well) [110]. The ill-defined lengths in the confined directions are absorbed in the definitions of the one-photon absorption coefficient α in units of m^{-1}, 1 and m for 3D, 2D and 1D respectively, and in the two-photon absorption coefficient β in units of m/W, m^2/W and m^3/W for 3D, 2D and 1D respectively.

3.11.2 Connection to the effective multi-band Bloch equations

Now that we have related the two-photon absorption coefficient to the third-order susceptibility, we need a formula to calculate the latter from the time-dependent density matrix.

In the special case where the reduced density matrix is obtained by solving the effective multi-band Bloch equations (3.51), the polarization current (3.67) corresponding to two-photon inter-band transitions can be written as

$$j^{\mu}(t) = \sum_{\gamma} j^{\mu\gamma}(t) A^{\gamma}(t) \tag{3.101}$$

with (see (3.70))

$$\begin{aligned} & j^{\mu\gamma}(t) = \\ & \frac{1}{\hbar V}\sum_{\boldsymbol{k}}\sum_{cv}\left[\sum_{n}\frac{\Pi^{\mu}_{cn,\boldsymbol{k}}\Pi^{\gamma}_{nv,\boldsymbol{k}}}{\Omega_{nv,\boldsymbol{k}}-\omega} - \sum_{n}\frac{\Pi^{\gamma}_{cn,\boldsymbol{k}}\Pi^{\mu}_{nv,\boldsymbol{k}}}{\Omega_{cn,\boldsymbol{k}}-\omega}\right] e^{i\Omega_{cv,\boldsymbol{k}}t}\bar{\rho}_{vc,\boldsymbol{k}}(t) + \text{c.c.}. \end{aligned} \tag{3.102}$$

Note that the additional contributions of frequency $\Omega_{cv,\boldsymbol{k}} + \omega$ appearing in (3.101) are neglected in (3.70). In fact, they correspond to strongly off-resonant two-photon processes.

On the other hand, the response function reduces to

$$R^{\mu\gamma\beta\alpha}(\tau_3,\tau_2,\tau_1) = \delta(\tau_3)\,\delta(\tau_2-\tau_1)\,\bar{R}^{\mu\gamma\beta\alpha}(\tau_1)\,. \tag{3.103}$$

The first delta-function accounts for the fact that the expression (3.70) for the current induced by inter-band two-photon transitions is directly proportional to the time-dependent field. The second delta-function reflects the coupling between the electrons and the *squared* field in the effective two-photon part of the Hamiltonian (3.54). The response function in the frequency domain thus becomes

$$Q^{\mu\alpha\beta\gamma}(\omega_3,\omega_2,\omega_1) = \int_{-\infty}^{+\infty} d\tau_1 \bar{R}^{\mu\gamma\beta\alpha}(\tau_1) e^{-i(\omega_2+\omega_1)\tau_1} \equiv \bar{Q}^{\mu\gamma\beta\alpha}(\omega_1+\omega_2)\,, \tag{3.104}$$

and the third-order susceptibility describing the two-photon absorption is given by

$$\chi^{\mu\gamma\beta\alpha}(-\omega;-\omega,\omega,\omega) = -\omega^{-4}\,\bar{Q}^{\mu\gamma\beta\alpha}(2\omega) \equiv \bar{\chi}^{\mu\gamma\beta\alpha}(-2\omega;2\omega)\,. \tag{3.105}$$

By using the equations (3.101) to (3.105) in (3.86), one finally obtains the main result

$$\boxed{\sum_{\beta\alpha} \hat{e}_\beta \hat{e}_\alpha\, \bar{\chi}^{\mu\gamma\beta\alpha}(-2\omega;2\omega) = -\frac{j^{\mu\gamma}(2\omega)}{\epsilon_0\,\omega^4\,[A^2](2\omega)}\,,} \tag{3.106}$$

where $[A^2](\omega)$ and $j^{\mu\gamma}(\omega)$ are the Fourier transforms of $A(t)^2$ and $j^{\mu\gamma}(t)$ respectively. Thanks to this relation, combined to equation (3.99), we are now able to extract the absorption spectrum from the polarization current, itself given by the time-dependent reduced density matrix.

Before closing this subject, we note that the expression (3.102) for the current implies that $j^{\mu\gamma} \simeq j^{\gamma\mu}$. Consequently, the third-order susceptibility displays the additional symmetry property

$$\sum_{\beta\alpha} \hat{e}_\beta \hat{e}_\alpha\, \bar{\chi}^{\mu\gamma\beta\alpha}(-2\omega;2\omega) \simeq \sum_{\beta\alpha} \hat{e}_\beta \hat{e}_\alpha\, \bar{\chi}^{\gamma\mu\beta\alpha}(-2\omega;2\omega)\,. \tag{3.107}$$

The small discrepancy is of the order of $(\Omega_{cv}-2\omega_2)/(\Omega_{cn}-\omega_2)^2$ and could be eliminated by symmetrizing the current operator (3.70) in the same way as it has been done for the Hamiltonian (3.54).

3.11.3 One-photon absorption and first-order susceptibility

To complete this discussion on absorption coefficients, let us briefly introduce similar equations for the one-photon case. First, we note that for the $\mathbf{D}_{4h}$ and $\mathbf{C}_{2v}$ symmetry all first order susceptibilities $\chi^{\mu\nu}$ with different superscripts vanish. The one-photon absorption coefficient $\alpha = \sum_\mu \alpha^\mu \hat{e}_\mu^{\,2}$ is thus given by

$$\boxed{\alpha^\mu = -\frac{\omega}{n_r c}\chi_i^{\mu\mu}\,.} \tag{3.108}$$

The first-order susceptibility can then be extracted from the polarization current (3.67) induced by one-photon transitions only (*i.e.* $\boldsymbol{A}_2 = 0$). The same procedure as for the above two-photon case leads to the formula

$$\boxed{\chi^{\mu\mu}(-\omega;\omega) = \frac{j^\mu(\omega)}{\epsilon_0\,\omega^2\,A^\mu(\omega)}\,,} \tag{3.109}$$

where $A^\mu(\omega)$ is the Fourier transform of the component μ of the field $\boldsymbol{A}(t)$.

3.12 Coulomb interaction within the Hartree-Fock approximation

In this section, we add first-order corrections due to the Coulomb interaction to the effective multi-band Bloch equations. Thus, we reproduce a derivation of the coherent part of the semiconductor Bloch equations [108], where the Coulomb contribution is taken into account within the time-dependent Hartree-Fock approximation.

Here we need an equation for the time evolution of the density matrix, including both the quasi-resonant effective two-photon transitions discussed above and the Coulomb repulsion. However, we neglect the cross terms between the electromagnetic field and the Coulomb interaction that result from the perturbative expansion. Each interaction is thus treated separately and the resulting effective interaction Hamiltonians are finally added.

Disregarding the electromagnetic field, the many-body Hamiltonian with Coulomb interaction can be written as

$$\begin{aligned} H = {} & \sum_n \sum_{\boldsymbol{k}} E_{n,\boldsymbol{k}} c^\dagger_{n,\boldsymbol{k}} c_{n,\boldsymbol{k}} \\ & + \frac{1}{2}\sum_{mm'}\sum_{nn'}\sum_{\boldsymbol{k}\boldsymbol{k}'}\sum_{\boldsymbol{q}} [V_q]^{m,n;m',n'}_{\boldsymbol{k}-\boldsymbol{q},\boldsymbol{k};\boldsymbol{k}'+\boldsymbol{q},\boldsymbol{k}'} c^\dagger_{m,\boldsymbol{k}-\boldsymbol{q}} c^\dagger_{m',\boldsymbol{k}'+\boldsymbol{q}} c_{n',\boldsymbol{k}'} c_{n,\boldsymbol{k}} \end{aligned} \tag{3.110}$$

where $c^\dagger_{n,\boldsymbol{k}}$ and $c_{n,\boldsymbol{k}}$ are respectively the creation and annihilation operators for the state $|n,\boldsymbol{k}\rangle$ introduced in (3.1). The Coulomb matrix elements are given by

$$[V_q]^{m,n;m',n'}_{\boldsymbol{k}-\boldsymbol{q},\boldsymbol{k};\boldsymbol{k}'+\boldsymbol{q},\boldsymbol{k}'} = \int d^3\boldsymbol{r}\, d^3\boldsymbol{r}'\, \psi^m_{\boldsymbol{k}-\boldsymbol{q}}(\boldsymbol{r})^\dagger\, \psi^n_{\boldsymbol{k}}(\boldsymbol{r})\, G_q(\boldsymbol{r},\boldsymbol{r}')\, \psi^{m'}_{\boldsymbol{k}'+\boldsymbol{q}}(\boldsymbol{r}')^\dagger\, \psi^{n'}_{\boldsymbol{k}'}(\boldsymbol{r}')\,, \tag{3.111}$$

where $G_q(\boldsymbol{r},\boldsymbol{r}')$ is the real Green's function of the Fourier transformed Poisson equation

$$\big[\boldsymbol{\nabla}\big(\epsilon(\boldsymbol{r})\boldsymbol{\nabla}\big)-q^2\epsilon(\boldsymbol{r})\big]G_q(\boldsymbol{r},\boldsymbol{r}')=\delta(\boldsymbol{r}-\boldsymbol{r}') \tag{3.112}$$

accounting for the position dependent dielectric function of the crystal $\epsilon(\boldsymbol{r})$. Note that the symmetry $G_q(\boldsymbol{r},\boldsymbol{r}')=G_q(\boldsymbol{r}',\boldsymbol{r})$ of the Green's function implies

$$[V_q]^{m,n;m',n'}_{\boldsymbol{k}-\boldsymbol{q},\boldsymbol{k};\boldsymbol{k}'+\boldsymbol{q},\boldsymbol{k}'}=[V_q]^{m',n';m,n}_{\boldsymbol{k}'+\boldsymbol{q},\boldsymbol{k}';\boldsymbol{k}-\boldsymbol{q},\boldsymbol{k}} \tag{3.113}$$

$$[V_q]^{m,n;m',n'}_{\boldsymbol{k}-\boldsymbol{q},\boldsymbol{k};\boldsymbol{k}'+\boldsymbol{q},\boldsymbol{k}'}=\big([V_q]^{n,m;n',m'}_{\boldsymbol{k},\boldsymbol{k}-\boldsymbol{q};\boldsymbol{k}',\boldsymbol{k}'+\boldsymbol{q}}\big)^*\,. \tag{3.114}$$

The Heisenberg equation $-i\hbar\,\partial_t c=[H,c]$, which gives the time-evolution of the annihilation and creation operators, leads to differential equations connecting the two-particle operators to four-particle operators:

$$\begin{aligned}\partial_t(c^\dagger_{m',\boldsymbol{k}}c_{m,\boldsymbol{k}})&=+i\Omega_{m'm,\boldsymbol{k}}c^\dagger_{m',\boldsymbol{k}}c_{m,\boldsymbol{k}}\\&+\frac{i}{\hbar}\sum_{nn'n''}\sum_{\boldsymbol{k}'}\sum_{\boldsymbol{q}}[V_q]^{n,n';n'',m'}_{\boldsymbol{k}'+\boldsymbol{q},\boldsymbol{k}';\boldsymbol{k}-\boldsymbol{q},\boldsymbol{k}}c^\dagger_{n'',\boldsymbol{k}-\boldsymbol{q}}c^\dagger_{n,\boldsymbol{k}'+\boldsymbol{q}}c_{n',\boldsymbol{k}'}c_{m,\boldsymbol{k}}\\&-\frac{i}{\hbar}\sum_{nn'n''}\sum_{\boldsymbol{k}'}\sum_{\boldsymbol{q}}[V_q]^{m,n'';n',n}_{\boldsymbol{k},\boldsymbol{k}-\boldsymbol{q};\boldsymbol{k}',\boldsymbol{k}'+\boldsymbol{q}}c^\dagger_{m',\boldsymbol{k}}c^\dagger_{n',\boldsymbol{k}'}c_{n,\boldsymbol{k}'+\boldsymbol{q}}c_{n'',\boldsymbol{k}-\boldsymbol{q}}\,.\end{aligned} \tag{3.115}$$

These equations for $c^\dagger c$ are not self-consistent, as they involve also four-particle operators. To complete the system, one can write down the time derivative of the four-particle products, which then introduce six-particle operators. This procedure can be repeated up to the correlation order one decides to include. But at some point, further approximations are necessary to express the highest correlation in function of the lower ones, and close the set of equations.

Here we restrict ourselves to differential equations involving expectation values of two-particle operators that are diagonal in wavevector indices. In the time-dependent Hartree-Fock approximation [111], the expectation values of the four-particle operators are thus simply replaced by products of density matrix elements:

$$\langle c^\dagger_{n'',\boldsymbol{k}-\boldsymbol{q}}c^\dagger_{n,\boldsymbol{k}'+\boldsymbol{q}}c_{n',\boldsymbol{k}'}c_{m,\boldsymbol{k}}\rangle\simeq\rho_{mn'',\boldsymbol{k}}\rho_{n'n,\boldsymbol{k}'}\,\delta_{\boldsymbol{q},0}-\rho_{mn,\boldsymbol{k}}\rho_{n'n'',\boldsymbol{k}'}\,\delta_{\boldsymbol{k}',\boldsymbol{k}-\boldsymbol{q}} \tag{3.116}$$

with

$$\rho_{mn,\boldsymbol{k}}=\langle c^\dagger_{m,\boldsymbol{k}}c_{n,\boldsymbol{k}}\rangle^*\,. \tag{3.117}$$

One is left with the following closed set of differential equations for the density matrix ρ.

$$\begin{aligned}\partial_t \rho_{mm',\boldsymbol{k}} = &-i\Omega_{mm',\boldsymbol{k}}\rho_{mm',\boldsymbol{k}}\\ &-\frac{i}{\hbar}\sum_{nn'n''}\sum_{\boldsymbol{k}'}\Big([V_{q=0}]^{m,n'';n',n}_{\boldsymbol{k},\boldsymbol{k};\boldsymbol{k}',\boldsymbol{k}'}\rho_{nn',\boldsymbol{k}'}\rho_{n''m',\boldsymbol{k}} - \rho_{mn'',\boldsymbol{k}}\rho_{n'n,\boldsymbol{k}'}[V_{q=0}]^{n,n';n'',m'}_{\boldsymbol{k}',\boldsymbol{k}';\boldsymbol{k},\boldsymbol{k}}\Big)\\ &+\frac{i}{\hbar}\sum_{nn'n''}\sum_{\boldsymbol{k}'}\Big([V_{|\boldsymbol{k}-\boldsymbol{k}'|}]^{m,n'';n',n}_{\boldsymbol{k},\boldsymbol{k}';\boldsymbol{k}',\boldsymbol{k}}\rho_{n''n',\boldsymbol{k}'}\rho_{nm',\boldsymbol{k}} - \rho_{mn,\boldsymbol{k}}\rho_{n'n'',\boldsymbol{k}'}[V_{|\boldsymbol{k}-\boldsymbol{k}'|}]^{n,n';n'',m'}_{\boldsymbol{k},\boldsymbol{k}';\boldsymbol{k}',\boldsymbol{k}}\Big).\end{aligned}$$

The first parenthesis on the r.h.s. is the direct or Hartree term, the second one the exchange or Fock term. We disregard the direct term. Notice that it cancels exactly [112] if one neglects the Coulomb-induced transitions between different bands and the wave function dependence of the Coulomb matrix element, *i.e.* $[V_q]^{m,m';n,n'}_{\cdots} = V_q\,\delta_{mm'}\delta_{nn'}$. We are left with

$$\begin{aligned}\partial_t \rho_{mm',\boldsymbol{k}} = &-i\Omega_{mm',\boldsymbol{k}}\rho_{mm',\boldsymbol{k}}\\ &+\frac{i}{\hbar}\sum_{nn'n''}\sum_{\boldsymbol{q}}[V_q]^{m,n'';n',n}_{\boldsymbol{k},\boldsymbol{k}-\boldsymbol{q};\boldsymbol{k}-\boldsymbol{q},\boldsymbol{k}}\rho_{n''n',\boldsymbol{k}-\boldsymbol{q}}\rho_{nm',\boldsymbol{k}}\\ &-\frac{i}{\hbar}\sum_{nn'n''}\sum_{\boldsymbol{q}}\rho_{mn,\boldsymbol{k}}\rho_{n'n'',\boldsymbol{k}-\boldsymbol{q}}[V_q]^{n,n';n'',m'}_{\boldsymbol{k},\boldsymbol{k}-\boldsymbol{q};\boldsymbol{k}-\boldsymbol{q},\boldsymbol{k}}\,.\end{aligned} \tag{3.118}$$

On the other hand, we limit the model to the Coulomb interaction between the quasi-resonant bands of the finite set $\mathbb{A}$ (see § 3.6), and denote the conduction and valence bands by the usual band indices c and v respectively. The inter-band[10] transitions induced by Coulomb scattering are neglected. In other words, only the matrix elements

$$[V_q]^{c,c';c'',c'''} \qquad [V_q]^{v,v';v'',v'''} \qquad [V_q]^{c,c';v,v'} \qquad [V_q]^{v,v';c,c'} \tag{3.119}$$

are considered. Furthermore it is reasonable to assume that the Coulomb contribution of filled bands is already taken into account by the effective bulk parameters (band energies, effective masses, ...). The occupation numbers $\rho_{vv,\boldsymbol{k}}$ of the electrons in the valence bands can thus be replaced by $\rho_{vv,\boldsymbol{k}} - 1$ in the Coulomb terms.

---

[10] between conduction and valence bands

The equations of motion finally read

$$
\begin{aligned}
\partial_t \rho_{cv,\boldsymbol{k}} = &- i\Omega_{cv,\boldsymbol{k}} \rho_{cv,\boldsymbol{k}} \\
&+ \frac{i}{\hbar} \sum_{c'c''} \sum_{c'''\neq c''} \sum_{\boldsymbol{q}} [V_q]^{c,c''';c'',c'}_{\boldsymbol{k},\boldsymbol{k}-\boldsymbol{q};\boldsymbol{k}-\boldsymbol{q},\boldsymbol{k}} \rho_{c'''c'',\boldsymbol{k}-\boldsymbol{q}} \rho_{c'v,\boldsymbol{k}} \\
&- \frac{i}{\hbar} \sum_{v'v''} \sum_{v'''\neq v''} \sum_{\boldsymbol{q}} \rho_{cv',\boldsymbol{k}} \rho_{v''v''',\boldsymbol{k}-\boldsymbol{q}} [V_q]^{v',v'';v''',v}_{\boldsymbol{k},\boldsymbol{k}-\boldsymbol{q};\boldsymbol{k}-\boldsymbol{q},\boldsymbol{k}} \\
&+ \frac{i}{\hbar} \sum_{c'v'v''} \sum_{\boldsymbol{q}} [V_q]^{c,c';v'',v'}_{\boldsymbol{k},\boldsymbol{k}-\boldsymbol{q};\boldsymbol{k}-\boldsymbol{q},\boldsymbol{k}} \rho_{c'v'',\boldsymbol{k}-\boldsymbol{q}} \rho_{v'v,\boldsymbol{k}} \\
&- \frac{i}{\hbar} \sum_{c'c''v'} \sum_{\boldsymbol{q}} \rho_{cc',\boldsymbol{k}} \rho_{c''v',\boldsymbol{k}-\boldsymbol{q}} [V_q]^{c',c'';v',v}_{\boldsymbol{k},\boldsymbol{k}-\boldsymbol{q};\boldsymbol{k}-\boldsymbol{q},\boldsymbol{k}} \\
&+ \frac{i}{\hbar} \sum_{c'c''} \sum_{\boldsymbol{q}} [V_q]^{c,c'';c'',c'}_{\boldsymbol{k},\boldsymbol{k}-\boldsymbol{q};\boldsymbol{k}-\boldsymbol{q},\boldsymbol{k}} \rho_{c''c'',\boldsymbol{k}-\boldsymbol{q}} \rho_{c'v,\boldsymbol{k}} \\
&- \frac{i}{\hbar} \sum_{v'v''} \sum_{\boldsymbol{q}} \rho_{cv',\boldsymbol{k}} (\rho_{v''v'',\boldsymbol{k}-\boldsymbol{q}} - 1) [V_q]^{v',v'';v'',v}_{\boldsymbol{k},\boldsymbol{k}-\boldsymbol{q};\boldsymbol{k}-\boldsymbol{q},\boldsymbol{k}} \,,
\end{aligned}
\tag{3.120}
$$

$$
\begin{aligned}
\partial_t \rho_{cc',\boldsymbol{k}} = &- i\Omega_{cc',\boldsymbol{k}} \rho_{cc',\boldsymbol{k}} \\
&+ \frac{i}{\hbar} \sum_{c''c'''} \sum_{c''''\neq c'''} \sum_{\boldsymbol{q}} [V_q]^{c,c'''';c''',c''}_{\boldsymbol{k},\boldsymbol{k}-\boldsymbol{q};\boldsymbol{k}-\boldsymbol{q},\boldsymbol{k}} \rho_{c''''c''',\boldsymbol{k}-\boldsymbol{q}} \rho_{c''c',\boldsymbol{k}} \\
&- \frac{i}{\hbar} \sum_{c''c'''} \sum_{c''''\neq c'''} \sum_{\boldsymbol{q}} \rho_{cc'',\boldsymbol{k}} \rho_{c'''c'''',\boldsymbol{k}-\boldsymbol{q}} [V_q]^{c'',c''';c'''',c'}_{\boldsymbol{k},\boldsymbol{k}-\boldsymbol{q};\boldsymbol{k}-\boldsymbol{q},\boldsymbol{k}} \\
&+ \frac{i}{\hbar} \sum_{c''vv'} \sum_{\boldsymbol{q}} [V_q]^{c,c'';v',v}_{\boldsymbol{k},\boldsymbol{k}-\boldsymbol{q};\boldsymbol{k}-\boldsymbol{q},\boldsymbol{k}} \rho_{c''v',\boldsymbol{k}-\boldsymbol{q}} \rho_{vc',\boldsymbol{k}} \\
&- \frac{i}{\hbar} \sum_{c''vv'} \sum_{\boldsymbol{q}} \rho_{cv,\boldsymbol{k}} \rho_{v'c'',\boldsymbol{k}-\boldsymbol{q}} [V_q]^{v,v';c'',c'}_{\boldsymbol{k},\boldsymbol{k}-\boldsymbol{q};\boldsymbol{k}-\boldsymbol{q},\boldsymbol{k}} \\
&+ \frac{i}{\hbar} \sum_{c''c'''} \sum_{\boldsymbol{q}} [V_q]^{c,c''';c''',c''}_{\boldsymbol{k},\boldsymbol{k}-\boldsymbol{q};\boldsymbol{k}-\boldsymbol{q},\boldsymbol{k}} \rho_{c'''c''',\boldsymbol{k}-\boldsymbol{q}} \rho_{c''c',\boldsymbol{k}} \\
&- \frac{i}{\hbar} \sum_{c''c'''} \sum_{\boldsymbol{q}} \rho_{cc'',\boldsymbol{k}} \rho_{c'''c''',\boldsymbol{k}-\boldsymbol{q}} [V_q]^{c'',c''';c''',c'}_{\boldsymbol{k},\boldsymbol{k}-\boldsymbol{q};\boldsymbol{k}-\boldsymbol{q},\boldsymbol{k}}
\end{aligned}
\tag{3.121}
$$

and

$$
\begin{aligned}
\partial_t \rho_{vv',\boldsymbol{k}} =& - i\Omega_{vv',\boldsymbol{k}}\rho_{vv',\boldsymbol{k}} \\
&+ \frac{i}{\hbar}\sum_{v''v'''}\sum_{v''''\neq v'''}\sum_{\boldsymbol{q}}[V_q]^{v,v'''';v''',v''}_{\boldsymbol{k},\boldsymbol{k}-\boldsymbol{q};\boldsymbol{k}-\boldsymbol{q},\boldsymbol{k}}\rho_{v''''v''',\boldsymbol{k}-\boldsymbol{q}}\rho_{v''v',\boldsymbol{k}} \\
&- \frac{i}{\hbar}\sum_{v''v'''}\sum_{v''''\neq v'''}\sum_{\boldsymbol{q}}\rho_{vv'',\boldsymbol{k}}\rho_{v'''v'''',\boldsymbol{k}-\boldsymbol{q}}[V_q]^{v'',v''';v'''',v'}_{\boldsymbol{k},\boldsymbol{k}-\boldsymbol{q};\boldsymbol{k}-\boldsymbol{q},\boldsymbol{k}} \\
&+ \frac{i}{\hbar}\sum_{v''cc'}\sum_{\boldsymbol{q}}[V_q]^{v,v'';c',c}_{\boldsymbol{k},\boldsymbol{k}-\boldsymbol{q};\boldsymbol{k}-\boldsymbol{q},\boldsymbol{k}}\rho_{v''c',\boldsymbol{k}-\boldsymbol{q}}\rho_{cv',\boldsymbol{k}} \\
&- \frac{i}{\hbar}\sum_{v''cc'}\sum_{\boldsymbol{q}}\rho_{vc,\boldsymbol{k}}\rho_{c'v'',\boldsymbol{k}-\boldsymbol{q}}[V_q]^{c,c';v'',v'}_{\boldsymbol{k},\boldsymbol{k}-\boldsymbol{q};\boldsymbol{k}-\boldsymbol{q},\boldsymbol{k}} \\
&+ \frac{i}{\hbar}\sum_{v''v'''}\sum_{\boldsymbol{q}}[V_q]^{v,v''';v''',v''}_{\boldsymbol{k},\boldsymbol{k}-\boldsymbol{q};\boldsymbol{k}-\boldsymbol{q},\boldsymbol{k}}(\rho_{v'''v''',\boldsymbol{k}-\boldsymbol{q}}-1)\rho_{v''v',\boldsymbol{k}} \\
&- \frac{i}{\hbar}\sum_{v''v'''}\sum_{\boldsymbol{q}}\rho_{vv'',\boldsymbol{k}}(\rho_{v'''v''',\boldsymbol{k}-\boldsymbol{q}}-1)[V_q]^{v'',v''';v''',v'}_{\boldsymbol{k},\boldsymbol{k}-\boldsymbol{q};\boldsymbol{k}-\boldsymbol{q},\boldsymbol{k}}\,.
\end{aligned}
\tag{3.122}
$$

The Coulomb interaction terms in the equations (3.120) to (3.122) can now be added to the effective multi-band Bloch equations (3.51). However, they must both be expressed *in the same rotating frame.* This amounts to replace the density matrix elements $\rho_{mn,\boldsymbol{k}}$ by $\bar{\rho}_{mn,\boldsymbol{k}}\, e^{i\Omega_{mn,\boldsymbol{k}}t}$ in the above equations. Remind that the cross-terms between the dipole interaction and the Coulomb coupling are neglected.

Note that the transformation to the rotating frame (3.10), introduced to derive general slowly varying Bloch equations, displays a strong subband and wavevector dependence. As a consequence, several exponential functions $e^{i\Omega_{mn,\boldsymbol{k}}t}$ appear in the effective multi-band Bloch equations. This might not be adequate for the numerical integration, especially in case one desires to include the Coulomb interaction. To avoid this, one may perform the additional transformation

$$
\hat{\rho}_{cc',\boldsymbol{k}} = \bar{\rho}_{cc',\boldsymbol{k}}\, e^{-i\Omega_{cc',\boldsymbol{k}}t} \tag{3.123}
$$

$$
\hat{\rho}_{vv',\boldsymbol{k}} = \bar{\rho}_{vv',\boldsymbol{k}}\, e^{-i\Omega_{vv',\boldsymbol{k}}t} \tag{3.124}
$$

$$
\hat{\rho}_{cv,\boldsymbol{k}} = \bar{\rho}_{cv,\boldsymbol{k}}\, e^{-i(\Omega_{cv,\boldsymbol{k}}-E_g)t}\,, \tag{3.125}
$$

where E_g is the energy gap ($\Omega_{cv,\boldsymbol{k}} \simeq E_g$). The transformed density matrix $\hat{\rho}$ remains slowly varying in time. This procedure removes the exponentials $e^{i\Omega_{cc',\boldsymbol{k}}t}$ and $e^{i\Omega_{vv',\boldsymbol{k}}t}$, and replaces $e^{i\Omega_{cv,\boldsymbol{k}}t}$ by e^{iE_gt}, in the effective Hamiltonian (3.52)–(3.54) and in the polarization current (3.68)–(3.70). However, additional terms $-i\Omega_{cc',\boldsymbol{k}}\hat{\rho}_{cc',\boldsymbol{k}}$, $-i\Omega_{vv',\boldsymbol{k}}\hat{\rho}_{vv',\boldsymbol{k}}$ and $-i(\Omega_{cv,\boldsymbol{k}}-E_g)\hat{\rho}_{cv,\boldsymbol{k}}$ appear on the r.h.s. of the equation of motion for $\hat{\rho}$.

3.13 Comments on the electron-hole picture

For convenience, we worked in a pure electron picture to derive the multi-band Bloch equations. An important advantage is that one does not have to specify the nature of the bands in the derivation of the general effective equations (3.31). However, the electron-hole picture may be preferred in some circumstances. In this section, we outline the procedure to follow to express the equations in a properly defined electron-hole basis.

For particles with half-integer spin, the time-reversal operator K satisfies the property $K^2 = -1$ [113]. This symmetry is responsible for the Kramers degeneracy of the $\pm\boldsymbol{k}$ states (the symmetry of the dispersion curve around $\boldsymbol{k} = 0$). A second consequence is the existence of bands that are mutually conjugate by time reversal. We denote them by n and $\bar{n}$. In other words, the creation operators $c^\dagger_{n,\boldsymbol{k}}$ and $c^\dagger_{\bar{n},\boldsymbol{k}}$ associated to the electronic states $|n,\boldsymbol{k}\rangle$ and $|\bar{n},\boldsymbol{k}\rangle$ satisfy the standard time-reversal conditions

$$\begin{aligned} K c^\dagger_{n,\boldsymbol{k}} K^{-1} &= +c^\dagger_{\bar{n},-\boldsymbol{k}} \\ K c^\dagger_{\bar{n},\boldsymbol{k}} K^{-1} &= -c^\dagger_{n,-\boldsymbol{k}} \,. \end{aligned} \tag{3.126}$$

Note that such a definition for mutually conjugate bands implies that the band indices can not be permuted. The irreducible representations to which the states $|n,\boldsymbol{k}\rangle$ and $|\bar{n},\boldsymbol{k}\rangle$ belong depend of course on the corresponding little group of $\boldsymbol{k}$. For instance, in the case of $\mathbf{C}_s$ symmetry, the states of the conjugate bands n and $\bar{n}$ would belong to ${}^1E_{1/2}$ and ${}^2E_{1/2}$ respectively. In this section, mutually conjugate valence bands (respectively, conduction bands) satisfying (3.126) are *exceptionally* designated by v and $\bar{v}$ (respectively, c and $\bar{c}$). We emphasize that, in all other sections of this chapter, v and c denote *any* valence band and conduction band.

To define properly the holes, we require that the creation operators for holes and electrons with identical quantum numbers satisfy the same group transformation-laws and the same convention (3.126), as discussed in [114, 115]. For mutually conjugate valence bands v and $\bar{v}$, we thus introduce the creation operators for holes

$$\begin{aligned} b^\dagger_{v,\boldsymbol{k}} &= +c_{\bar{v},-\boldsymbol{k}} \\ b^\dagger_{\bar{v},\boldsymbol{k}} &= -c_{v,-\boldsymbol{k}} \,. \end{aligned} \tag{3.127}$$

The hole related to the absence of an electron in the valence band v (respectively, $\bar{v}$) is thus labeled by the corresponding conjugate band $\bar{v}$ (respectively, v). This expresses the fact that the hole and the electron related by (3.127) belong to mutually conjugate representations. As outlined by Fetter and Walecka [116], this definition for holes, including the choice of phase, ensures that the creation operator $b^\dagger_{v,\boldsymbol{k}}$ (respectively, $b^\dagger_{\bar{v},\boldsymbol{k}}$) transforms according to the irreducible representation denoted by $v, \boldsymbol{k}$ (respectively, $\bar{v}, \boldsymbol{k}$).

Let $\mathbb{C}_b$ and $\mathbb{V}_b$ be the ensemble of all conduction bands and all valence bands respectively, independently of their properties under time-reversal. The occupation number for electrons (e) and holes (h) are then defined by

$$\begin{aligned} n^e_{\mu,\boldsymbol{k}} &= \langle c^\dagger_{\mu,\boldsymbol{k}} c_{\mu,\boldsymbol{k}} \rangle \qquad && \mu \in \mathbb{C}_b \\ n^h_{\nu,\boldsymbol{k}} &= \langle b^\dagger_{\nu,\boldsymbol{k}} b_{\nu,\boldsymbol{k}} \rangle \qquad && \nu \in \mathbb{V}_b \,. \end{aligned} \tag{3.128}$$

The electron-electron (e), hole-hole (h) and electron-hole (x) microscopic polarizations can be written as

$$\begin{aligned} p^e_{\mu\mu',\boldsymbol{k}} &= \langle c^\dagger_{\mu,\boldsymbol{k}} c_{\mu',\boldsymbol{k}} \rangle^* \qquad && \forall \mu, \mu' \in \mathbb{C}_b \\ p^h_{\nu\nu',\boldsymbol{k}} &= \langle b^\dagger_{\nu,\boldsymbol{k}} b_{\nu',\boldsymbol{k}} \rangle^* \qquad && \forall \nu, \nu' \in \mathbb{V}_b \\ p^x_{\mu\nu,\boldsymbol{k}} &= \langle c^\dagger_{\mu,\boldsymbol{k}} b^\dagger_{\nu,-\boldsymbol{k}} \rangle^* \qquad && \forall \mu \in \mathbb{C}_b,\ \forall \nu \in \mathbb{V}_b \,. \end{aligned} \tag{3.129}$$

Consequently, the transformation relating the density matrix used throughout this chapter to the occupation numbers (3.128) and microscopic polarization (3.129) in the electron-hole picture reads

$$\begin{aligned} n^e_{c,\boldsymbol{k}} &= \rho_{cc,\boldsymbol{k}} \qquad\qquad && n^h_{v,\boldsymbol{k}} = 1 - \rho_{\bar{v}\bar{v},-\boldsymbol{k}} \\ n^e_{\bar{c},\boldsymbol{k}} &= \rho_{\bar{c}\bar{c},\boldsymbol{k}} && n^h_{\bar{v},\boldsymbol{k}} = 1 - \rho_{vv,-\boldsymbol{k}} \,, \end{aligned}$$

and

$$\begin{aligned} p^e_{cc',\boldsymbol{k}} &= +\rho_{cc',\boldsymbol{k}} \qquad && p^h_{vv',\boldsymbol{k}} = -\rho_{\bar{v}'\bar{v},-\boldsymbol{k}} \qquad && p^x_{cv,\boldsymbol{k}} = +\rho_{c\bar{v},\boldsymbol{k}} \\ p^e_{\bar{c}\bar{c}',\boldsymbol{k}} &= +\rho_{\bar{c}\bar{c}',\boldsymbol{k}} && p^h_{\bar{v}\bar{v}',\boldsymbol{k}} = -\rho_{v'v,-\boldsymbol{k}} && p^x_{\bar{c}\bar{v},\boldsymbol{k}} = -\rho_{\bar{c}v,\boldsymbol{k}} \\ p^e_{c\bar{c}',\boldsymbol{k}} &= +\rho_{c\bar{c}',\boldsymbol{k}} && p^h_{\bar{v}v',\boldsymbol{k}} = +\rho_{v'\bar{v},-\boldsymbol{k}} && p^x_{\bar{c}v,\boldsymbol{k}} = +\rho_{\bar{c}\bar{v},\boldsymbol{k}} \\ p^e_{\bar{c}c',\boldsymbol{k}} &= +\rho_{\bar{c}c',\boldsymbol{k}} && p^h_{v\bar{v}',\boldsymbol{k}} = +\rho_{\bar{v}'v,-\boldsymbol{k}} && p^x_{c\bar{v},\boldsymbol{k}} = -\rho_{cv,\boldsymbol{k}} \,. \end{aligned}$$

The density matrix in the effective multi-band Bloch equations can now be reformulated in terms of the above quantities. However, note that the energy, momentum and Coulomb matrix elements are then still defined in terms of electronic wave functions. In order to work consistently in the electron-hole picture, one may also express the matrix elements of these operators in the same electron-hole basis. This is achieved by introducing a hole wave function that is the image of the corresponding electron wave function through the time reversal operator K. Note that in this case, the phase factors of (3.127) cancel with those appearing in the hole wave functions.

Nevertheless, in this thesis we choose to work in a pure electron basis, without the above hole concept. This has the following advantage. As we work with one type of particles only (electrons), we do not have to specify the nature of the bands in the derivation of the general equations (see for instance equation (3.31)). Thus, it is not necessary to distinguish notationally[11] between the microscopic polarizations (3.129) involving valence and/or conduction bands, and we can use a much more compact notation.

However, as the states in the valence bands are in general occupied, the valence-band occupation number $\rho_{vv,\boldsymbol{k}}$ is not always an adequate quantity. For practical purpose, we thus replace $\rho_{vv,\boldsymbol{k}}$ by $1-\rho_{vv,\boldsymbol{k}}$ when required (and allowed). In particular, this substitution is convenient for the description of the thermal equilibrium in the valence bands (see section 3.14). Strictly speaking, $1-\rho_{vv,\boldsymbol{k}}$ is not the distribution of properly defined hole-particles in the valence band v, but describes the absence of electrons.

3.14 Phenomenological thermalization and decoherence

In this section, we introduce phenomenological relaxation times to describe the thermalization and decoherence in the multi-band Bloch equations.

The loss of coherence between the states of the bands m and n is described by

$$\partial_t \bar{\rho}_{mn,\boldsymbol{k}} = -\bar{\rho}_{mn,\boldsymbol{k}}/\tau_{mn}\,, \qquad m \neq n\,, \tag{3.130}$$

with τ_{mn} the decoherence time. As a consequence, the off-diagonal elements of the density matrix vanish exponentially. The carrier distribution $n_{\nu,\boldsymbol{k}}$, defined by

$$n_{c,\boldsymbol{k}} = \bar{\rho}_{cc,\boldsymbol{k}} \qquad \text{for conduction bands } (\nu = c), \tag{3.131}$$

$$n_{v,\boldsymbol{k}} = 1 - \bar{\rho}_{vv,\boldsymbol{k}} \qquad \text{for valence bands } (\nu = v), \tag{3.132}$$

relaxes with characteristic time $\tau_{\nu\nu}$ to the thermalized Fermi distribution

$$f_{\nu,\boldsymbol{k}} = \frac{1}{e^{\beta_\nu(\epsilon_{\nu,\boldsymbol{k}}-\mu_\nu)}+1}\,, \tag{3.133}$$

and is thus modeled by

$$\partial_t n_{\nu,\boldsymbol{k}} = -(n_{\nu,\boldsymbol{k}} - f_{\nu,\boldsymbol{k}})/\tau_{\nu\nu}\,. \tag{3.134}$$

---

[11] besides the electronic band labels

The energy dispersion $\epsilon_{\nu,\boldsymbol{k}}$ is defined by

$$\epsilon_{c,\boldsymbol{k}} = +E_{c,\boldsymbol{k}} \qquad \text{for conduction bands,} \tag{3.135}$$

$$\epsilon_{v,\boldsymbol{k}} = -E_{v,\boldsymbol{k}} \qquad \text{for valence bands,} \tag{3.136}$$

and the chemical potential μ_ν and temperature T_ν ($k_B T_\nu = 1/\beta_\nu$) of the particle distribution in band ν are given by the solution of the equations

$$\sum_{\boldsymbol{k}} \epsilon_{\nu,\boldsymbol{k}}\, n_{\nu,\boldsymbol{k}} = \sum_{\boldsymbol{k}} \epsilon_{\nu,\boldsymbol{k}}\, f_{\nu,\boldsymbol{k}} \tag{3.137}$$

$$\sum_{\boldsymbol{k}} n_{\nu,\boldsymbol{k}} = \sum_{\boldsymbol{k}} f_{\nu,\boldsymbol{k}}\,. \tag{3.138}$$

This thermalization mechanism conserves the density of energy and density of particles in each band. However, both densities evolve in time, due to the electronic transitions induced by the electromagnetic field. Also note that the relaxation (3.134) leads to a quasi-equilibrium with a different temperature in each band. Finally, we emphasize that the above relaxation can not be related to elastic scattering only, despite the energy is conserved, because the total momentum vanishes exponentially.

This model based on phenomenological relaxation times is easy to implement, but has several limitations. First, the total density of energy and carriers is not conserved during the time evolution, despite the fact that the distribution in the band tends to the correct thermal equilibrium. Second, the scattering is not weighted by the exchange of momentum and energy between the involved particles. The in- or out-scattering rate depends only on the instantaneous occupation of the considered state, and not on the detailed distribution in the band.

Overcoming these limitations would require a much more complex model describing many-body effects. Let us mention two of them. First, the microscopic carrier-carrier scattering can be taken into account by expanding the Coulomb interaction beyond the Hartree-Fock approximation [108]. Second, the evolution to thermal equilibrium with the lattice can be modeled by the Fröhlich interaction between electrons and LO-phonons [117]. A detailed treatment of the so-called quantum kinetics in semiconductors, using nonequilibrium Green's function techniques, can be found in Haug and Jauho's book [118].

3.15 Conclusion

In this chapter, we detailed a general procedure to derive effective equations of motion for electrons in a crystal, interacting with several quasi-monochromatic waves. The key point of this theory is that the final effective equations describe the time evolution of a *reduced* density matrix accounting only for a limited set of significative bands (depending of the situation). However, the withdrawn bands, which have to be far off-resonant with respect to the optical transitions, are included as a perturbation up to the first order in the frequency detuning. A second important feature of the model is that all remaining quantities vary on a same time-scale, namely the pulse durations, which makes the numerical integration much more efficient. For this purpose, the equations of motion for the density matrix, expressed in the rotating frame, were restricted to the slowly varying dominant contribution, in the spirit of the rotating wave approximation.

These effective equations of motion were specialized to the case of semiconductors with several conduction bands and valence bands, interacting with two electromagnetic fields of frequency respectively close to the band-gap energy, and to the half of the band-gap energy. The final effective multi-band Bloch equations (3.51) take consistently into account all quasi-resonant interaction terms up to the second order in the optical fields. They include various linear and nonlinear optical processes, such as inter-band one- and two-photon absorption, coherent control of photocurrent, second-harmonic generation, difference-frequency mixing, or the AC Stark shifts.

Once the effective multi-band Bloch equations were established, we also derived and discussed an expression for an effective macroscopic polarization current (3.66) that is consistent with the previous approximations. From this time-dependent current, we then extracted the one- and two-photon absorption coefficients (equations (3.109) and (3.106) respectively). Finally, we outlined how the Coulomb interaction can be included within the Hartree-Fock approximation.

In the following, the effective multi-band Bloch equations (3.51) will be applied to optical processes in different semiconductor heterostructures. In chapter 5, we calculate the charge and spin current injected in a symmetric quantum well, by interference between one- and two-photon transitions. Then we focus on nonlinear optical phenomena in a V-shaped quantum wire, taking into account the Coulomb interaction within the Hartree-Fock approximation. First, the two-photon absorption coefficient of the quantum wire is calculated in chapter 6. Second, in chapter 7, we show that the interferences between excitonic coherences result in an oscillating charge current, when the quantum wire is excited slightly below the band gap by two laser pulses of frequency ω and 2ω.

4 Band structure of the quantum well

4.1 Introduction

An accurate description of optical transitions in semiconductors requires the use of a detailed band structure. Indeed, the resonant transition energies are set by the inter-(sub)band frequencies. The oscillator strengths associated to the various excitation channels depend upon the momentum matrix elements between the involved bands. Furthermore, to account correctly for the polarization anisotropy [29, 31], one has to include the strong valence-band mixing. The band structure is particularly rich in heterostructures, due to the splitting into subbands induced by the confinement, and can also be engineered to some extent. To illustrate its importance, let us mention the complex inter-subband dynamics induced by an optical excitation, which may significantly affect the macroscopic polarization, as it will be shown in chapter 5.

In this chapter, we introduce the well-known $\boldsymbol{k}\cdot\boldsymbol{p}$ method to calculate the realistic band structure of a typical GaAs/AlGaAs quantum well. The results will be used in the next chapter, together with the effective multi-band Bloch equations derived in chapter 3.

In section 4.2, the $\boldsymbol{k}\cdot\boldsymbol{p}$ envelope function method is derived in detail. In section 4.3, we outline the numerical method using finite elements. Finally, section 4.4 is devoted to the band structure of a specific symmetric quantum well, and to the related symmetry properties of the states.

4.2 $\boldsymbol{k}\cdot\boldsymbol{p}$ envelope function method

In this section, we give an overview of Burt's "exact" envelope function formulation. The reader interested in more details is advised to refer to the review paper by Burt [47] and the citations therein.

The main idea of the $\boldsymbol{k}\cdot\boldsymbol{p}$ envelope function method is to replace the microscopic details of the Hamiltonian (§ 4.2.1) by a limited number of bulk parameters in order to obtain an effective eigenvalue equation for the macroscopic heterostructure. This is achieved by expanding the wave functions into an infinite sum of periodic Bloch functions multiplying slowly varying envelope functions (§ 4.2.2). The former can be eliminated by projecting the equation onto them and one is left with a differential equation for the latter only. The infinite number of envelope functions required by this expansion is then restricted to those expected to give the dominant contribution. The eliminated part is however replaced by effective bulk parameters resulting from a perturbative approach (§ 4.2.3). This procedure leads to an effective mass equation. In a similar way, the resulting eigensolutions are used to calculate effective momentum matrix elements (§ 4.2.4).

4.2.1 Schrödinger equation

As a starting point, we consider the Schrödinger equation

$$H\,\psi(\boldsymbol{r}) = E\,\psi(\boldsymbol{r}) \tag{4.1}$$

for an electron in an arbitrary crystalline nanostructure defined by the Hamiltonian

$$H = \frac{\boldsymbol{p}^2}{2m_0} + V(\boldsymbol{r}) + \frac{\hbar}{4{m_0}^2c^2}\big(\boldsymbol{\nabla}V(\boldsymbol{r}) \wedge \boldsymbol{p}\big)\cdot\boldsymbol{\sigma} \tag{4.2}$$

where $V(\boldsymbol{r})$ is the microscopic potential of the heterostructure and $\boldsymbol{\sigma}$ is the vector $(\sigma_x\ \sigma_y\ \sigma_z)$ with the Pauli matrices as components. Note that $V(\boldsymbol{r})$ includes the macroscopic potential modulation of the heterostructure as well as the underlying crystal periodicity (Figure 4.1). Far from the interfaces, $V(\boldsymbol{r})$ thus recovers the full crystal periodicity. Before going further, let us define the notation

$$T = \frac{\boldsymbol{p}^2}{2m_0} \tag{4.3}$$

for the kinetic energy and

$$\boldsymbol{\pi} = \boldsymbol{p} + \frac{\hbar}{4m_0c^2}\,\boldsymbol{\sigma}\wedge\boldsymbol{\nabla}V(\boldsymbol{r}) \tag{4.4}$$

for the momentum. The latter is related to the position operator $\boldsymbol{r}$ by

$$\boldsymbol{\pi} = i\,\frac{m_0}{\hbar}\,[H,\boldsymbol{r}]\,. \tag{4.5}$$

Thus, in the Heisenberg picture, $\boldsymbol{\pi}/m_0$ represents the velocity operator $\boldsymbol{v} = \dot{\boldsymbol{r}}$.

4.2.2 Envelope expansion

We consider a complete set of functions $U_n(\boldsymbol{r})$ that are periodic with respect to a Bravais lattice. The envelope functions $F_n(\boldsymbol{r})$ for an arbitrary wave function $\psi(\boldsymbol{r})$

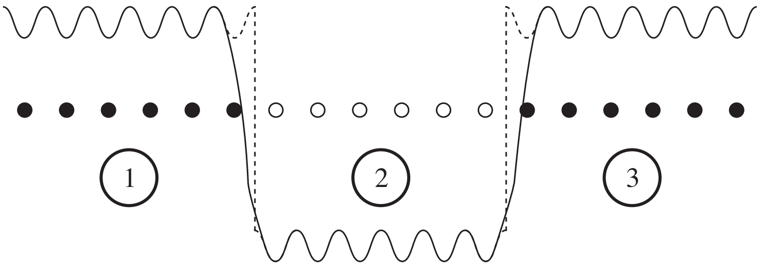

Figure 4.1: Microscopic potential $V(\boldsymbol{r})$ of a quantum well (full line). The heterostructure is modeled by three regions (1,2 and 3) with abrupt interfaces (dashed line).

are then defined by the unique and exact expansion

$$\psi(\boldsymbol{r}) = \sum_n F_n(\boldsymbol{r})\, U_n(\boldsymbol{r}) \tag{4.6}$$

where the plane wave expansions

$$F(\boldsymbol{r}) = \sum_{\boldsymbol{k}} F_{\boldsymbol{k}}\, e^{i\boldsymbol{kr}} \tag{4.7}$$

$$U(\boldsymbol{r}) = \sum_{\boldsymbol{G}} U_{\boldsymbol{G}}\, e^{i\boldsymbol{Gr}} \tag{4.8}$$

are limited to wavevectors $\boldsymbol{k}$ in the first Brillouin zone for F_n and to the reciprocal-lattice vectors $\boldsymbol{G}$ for U_n. For a given basis, the wave functions are therefore completely determined by their coefficients F_n. These envelope functions are necessarily slowly varying in the sense that their Fourier transforms are restricted to the first Brillouin zone. This implies, together with the periodicity of the basis functions U_n, that the orthonormality relation between two eigenstates states $\psi^{(i)}$ and $\psi^{(j)}$ can be written as

$$\langle \psi^{(i)} | \psi^{(j)} \rangle = \sum_{nn'} \langle F_n^{(i)} | F_{n'}^{(j)} \rangle \langle U_n | U_{n'} \rangle_0 = \delta_{ij}\,. \tag{4.9}$$

The above scalar products are defined by

$$\langle f | g \rangle \equiv \int_\Omega d^3\boldsymbol{r}\, f(\boldsymbol{r})^* g(\boldsymbol{r}) \tag{4.10}$$

$$\langle f | g \rangle_0 \equiv \frac{1}{\Omega_0} \int_{\Omega_0} d^3\boldsymbol{r}\, f(\boldsymbol{r})^* g(\boldsymbol{r}) \tag{4.11}$$

where Ω is the crystal volume and Ω_0 the unit cell volume of the Bravais lattice. For practical purpose, the basis functions U_n are defined as the zone-center eigenfunctions of the *bulk* Hamiltonian of a selected region in the heterostructure (usually the confined region). The important point is to use the same basis functions throughout the entire crystal, even if they are not everywhere eigenstates of the local Hamiltonian. Nevertheless, we assume an unique Bravais lattice for the whole heterostructure. As a consequence, the crystal potential at large distance from the interfaces has the periodicity of the basis functions. Moreover, as the bulk eigenfunctions are orthonormal, the relation (4.9) becomes

$$\sum_n \langle F_n^{(i)} | F_n^{(j)} \rangle = \delta_{ij} \,. \tag{4.12}$$

The basic idea of the method is to bring both sides of the Schrödinger equation (4.1) into the envelope expansion form (4.6) and project the resulting equation onto the basis functions U_n. The expansion is easily performed for the kinetic energy term and we obtain

$$T\psi = \sum_n \Big(-\frac{\hbar^2}{2m_0}\Delta F_n - \frac{i\hbar}{m_0}\sum_{n'} \boldsymbol{\pi}_{nn'} \cdot \boldsymbol{\nabla} F_{n'} + \sum_{n'} T_{nn'} F_{n'} \Big) U_n \tag{4.13}$$

where

$$\boldsymbol{\pi}_{nn'} = \langle U_n | \boldsymbol{\pi} | U_{n'} \rangle_0 \tag{4.14}$$

$$T_{nn'} = \langle U_n | T | U_{n'} \rangle_0 \,. \tag{4.15}$$

The expansion of $V\psi$ is however more tricky, as the potential V of the heterostructure does not have the full periodicity of U_n. The Fourier transform of V involves all wavevectors $\boldsymbol{k} + \boldsymbol{G}$ and its envelope expansion therefore leads to non-local expressions of the form[1]

$$\sum_{n'} \int V_{nn'}(\boldsymbol{r}, \boldsymbol{r}') F_{n'}(\boldsymbol{r}')\, d^3\boldsymbol{r}' \,. \tag{4.16}$$

However, at large distances from any interface, the potential $V(\boldsymbol{r})$ reduces to the local periodic bulk potential $V^{(b)}(\boldsymbol{r})$, which can be expanded as

$$V^{(b)}(\boldsymbol{r}) = \sum_{\boldsymbol{G}} V_{\boldsymbol{G}}^{(b)}\, e^{i\boldsymbol{G}\boldsymbol{r}} \,. \tag{4.17}$$

The details of the potential variation at the interfaces are now neglected and the

---

[1] For the definition of $V_{nn'}(\boldsymbol{r}, \boldsymbol{r}')$, refer to [47].

heterostructure is modeled by different regions i with abrupt interfaces (Figure 4.1). The corresponding potential is given by

$$V(\boldsymbol{r}) = \sum_i \theta^{(i)}(\boldsymbol{r})\, V^{(i)}(\boldsymbol{r})\,, \tag{4.18}$$

where $\theta^{(i)}$ equals one in the region i and zero elsewhere, and $V^{(i)}$ is the appropriate local bulk potential. For slowly varying envelope functions on the scale of the lattice period, only small $\boldsymbol{k}$ vectors are of importance. Thus, restricting the Fourier expansion of (4.18) to small wavevectors is expected to be a good approximation and one is left with [119]

$$V(\boldsymbol{r})\psi(\boldsymbol{r}) = \sum_i \theta^{(i)}(\boldsymbol{r}) \sum_{nn'} U_n(\boldsymbol{r}) V^{(i)}_{nn'} F_{n'}(\boldsymbol{r})\,. \tag{4.19}$$

where

$$V^{(i)}_{nn'} = \langle U_n | V^{(i)} | U_{n'} \rangle_0\,. \tag{4.20}$$

With the expansions (4.13) and (4.19), the projection of the Schrödinger equation (4.1) on the basis functions U_n finally leads to the equation for envelope functions

$$-\frac{\hbar^2}{2m_0}\Delta F_n(\boldsymbol{r}) - \frac{i\hbar}{m_0}\sum_{n'} \boldsymbol{\pi}_{nn'}(\boldsymbol{r})\cdot\boldsymbol{\nabla} F_{n'}(\boldsymbol{r}) + \sum_{n'} H_{nn'}(\boldsymbol{r}) F_{n'}(\boldsymbol{r}) = E\, F_n(\boldsymbol{r}) \tag{4.21}$$

where

$$\boldsymbol{\pi}_{nn'}(\boldsymbol{r}) = \langle U_n | \boldsymbol{\pi} | U_{n'} \rangle_0 \tag{4.22}$$
$$H_{nn'}(\boldsymbol{r}) = \langle U_n | H | U_{n'} \rangle_0 \tag{4.23}$$

take the local bulk value at the position $\boldsymbol{r}$.

4.2.3 Effective-mass equation for heterostructures

Let us now consider a heterostructure with a d-dimensional confinement of electronic states ($d = 1, 2, 3$). The corresponding envelope functions can be expressed as

$$F_n(\boldsymbol{r}) = \frac{1}{\sqrt{\Omega_{\shortparallel}}} e^{i\boldsymbol{k}_{\shortparallel}\boldsymbol{r}_{\shortparallel}} f_{n,\boldsymbol{k}_{\shortparallel}}(\boldsymbol{r}_\perp) \tag{4.24}$$

where $\boldsymbol{r}_\perp$ and $\boldsymbol{r}_{\shortparallel}$ are the space coordinates in the confined and unconfined directions respectively ($\boldsymbol{r} = \boldsymbol{r}_\perp + \boldsymbol{r}_{\shortparallel}$ and $\boldsymbol{r}_\perp \cdot \boldsymbol{r}_{\shortparallel} = 0$). $\Omega_{\shortparallel}$ is the volume of the unconfined

$(3-d)$-dimensional subspace[2] and $\boldsymbol{k}_{\shortparallel}$ the related wavevector. In what follows, we omit the wavevector label of the envelope functions, except when explicitly required. The envelope function equation (4.21) becomes

$$\begin{aligned} &-\frac{\hbar^2}{2m_0}\Delta_{\perp} f_n(\boldsymbol{r}_{\perp}) - \frac{i\hbar}{m_0}\sum_{n'} \boldsymbol{\pi}_{nn'}(\boldsymbol{r}_{\perp}) \cdot \boldsymbol{\nabla}_{\perp} f_{n'}(\boldsymbol{r}_{\perp}) + \frac{\hbar^2 k_{\shortparallel}^2}{2m_0} f_n(\boldsymbol{r}_{\perp}) \\ &\qquad + \frac{\hbar}{m_0}\sum_{n'} \boldsymbol{k}_{\shortparallel} \cdot \boldsymbol{\pi}_{nn'}(\boldsymbol{r}_{\perp}) f_{n'}(\boldsymbol{r}_{\perp}) + \sum_{n'} H_{nn'}(\boldsymbol{r}_{\perp}) f_{n'}(\boldsymbol{r}_{\perp}) = E\, f_n(\boldsymbol{r}_{\perp}) \end{aligned} \tag{4.25}$$

where $\boldsymbol{\nabla}_{\perp}$ and $\Delta_{\perp}$ denote respectively the gradient and the Laplacian restricted to the coordinate $\boldsymbol{r}_{\perp}$.

The infinite number of electronic bands is now divided into two sets $\mathbb{A}$ and $\mathbb{B}$. The N_A envelope functions in group $\mathbb{A}$, labeled by a, a', …, are dominant while the remaining functions in group $\mathbb{B}$, labeled by b, b', …, are small and are eliminated in a perturbative way. Note that this procedure is similar to the one used in chapter 4, for the elimination of the far off-resonant bands in the effective multi-band Bloch equations. In the spirit of the effective mass equation, the bulk energy of the bands to eliminate is usually far from the considered eigenenergy E. For slowly varying envelope functions, the term

$$\frac{1}{2m_0}\left[\hbar^2(-\Delta_{\perp} + k_{\shortparallel}^2) + \hbar \boldsymbol{\pi}_{bb} \cdot (-i\,\boldsymbol{\nabla}_{\perp} + \boldsymbol{k}_{\shortparallel})\right] f_b$$

can thus be safely neglected with respect to $(E - H_{bb})f_b$, and the equation for f_b can be approximated by

$$f_b \simeq (E - H_{bb})^{-1} \sum_{a'} \left[\frac{\hbar}{m_0}\boldsymbol{\pi}_{ba'} \cdot (-i\,\boldsymbol{\nabla}_{\perp} + \boldsymbol{k}_{\shortparallel}) f_{a'} + H_{ba'} f_{a'}\right]. \tag{4.26}$$

If one replaces f_b in equation (4.25) for $n = a$ by the expression (4.26), one is finally left[3] with the effective mass equation

$$\begin{aligned} &\sum_{a'} \Big\{ \frac{1}{2m_0}(\boldsymbol{p}_{\perp} + \hbar\boldsymbol{k}_{\shortparallel}) \boldsymbol{\gamma}_{aa'} (\boldsymbol{p}_{\perp} + \hbar\boldsymbol{k}_{\shortparallel}) + \frac{1}{2m_0}(\boldsymbol{p}_{\perp} + \hbar\boldsymbol{k}_{\shortparallel})(\boldsymbol{\pi}_{aa'} + \delta\hat{\boldsymbol{\pi}}_{aa'}) \\ &\qquad + \frac{1}{2m_0}(\boldsymbol{\pi}_{aa'} + \delta\check{\boldsymbol{\pi}}_{aa'})(\boldsymbol{p}_{\perp} + \hbar\boldsymbol{k}_{\shortparallel}) + H_{aa'} + \delta H_{aa'} \Big\} f_{a'}(\boldsymbol{r}_{\perp}) = E\, f_a(\boldsymbol{r}_{\perp}). \end{aligned} \tag{4.27}$$

For each pair of band subscripts aa', $\boldsymbol{\gamma}_{aa'}$ is a 3-by-3 matrix, $\delta\hat{\boldsymbol{\pi}}_{aa'}$ and $\delta\check{\boldsymbol{\pi}}_{aa'}$ are

---

[2] for $d = 3$, $\Omega_{\shortparallel} = 1$

[3] after further approximations not detailed here

real-space vectors, and $\delta h_{aa'}$ is a scalar. They are given by their elements

$$\gamma^{\alpha\beta}_{aa'} = \delta^{\alpha\beta} + \frac{2}{m_0}\sum_b \frac{\pi^{\alpha}_{ab}\pi^{\beta}_{ba'}}{E - H_{bb}}\,, \tag{4.28}$$

$$\delta\hat{\pi}^{\alpha}_{aa'} = 2\sum_b \frac{\pi^{\alpha}_{ab}H_{ba'}}{E - H_{bb}}\,, \tag{4.29}$$

$$\delta\check{\pi}^{\alpha}_{aa'} = 2\sum_b \frac{H_{ab}\pi^{\alpha}_{ba'}}{E - H_{bb}}\,, \tag{4.30}$$

and

$$\delta h_{aa'} = \sum_b \frac{H_{ab}H_{ba'}}{E - H_{bb}}\,. \tag{4.31}$$

The vector-matrix-vector product appearing in the first term on the r.h.s. of (4.27) is defined by

$$\boldsymbol{v}\boldsymbol{M}\boldsymbol{v} \equiv \sum_{\alpha\beta} v^{\alpha}M^{\alpha\beta}v^{\beta}\,, \tag{4.32}$$

and the superscripts α and β label the three spatial directions x, y and z.

In the following, $\gamma^{\beta\alpha}$, $\delta\hat{\pi}^{\alpha}$ and $\delta\check{\pi}^{\alpha}$ refer to the corresponding N_A-by-N_A matrices associated to the directions α and/or β whereas γ, $\delta\hat{\pi}$, $\delta\check{\pi}$ and δh denote the full tensors. According to the above expressions, they satisfy the relations $(\gamma^{\alpha\beta})^{\dagger} = \gamma^{\beta\alpha}$, $(\delta\hat{\pi}^{\alpha})^{\dagger} = \delta\check{\pi}^{\alpha}$ and $\delta h^{\dagger} = \delta h$. The tensor γ represents the (inverse) effective mass due to the eliminated bands, and $\delta\pi$ and δh are first-order corrections to momentum and energy respectively. The influence of $\delta\hat{\pi}$ and $\delta\check{\pi}$ was discussed in [120] by Foreman. They are neglected here (as in most works), together with δh.

The zone-center Bloch functions of the confined region (*e.g.* a quantum well or quantum wire) are chosen as the periodic basis function U_n. In the confined region, $H_{aa'}$ reduces thus exactly to the zero wavevector bulk energies E_a of the remaining bands $a \in \mathbb{A}$ (the off-diagonal elements are all zero) and $\boldsymbol{\gamma}_{aa'}$ and $\boldsymbol{\pi}_{aa'}$ are the appropriate local bulk tensors. Out of the confined region, U_n are no more eigenfunctions of the corresponding bulk Hamiltonian, and $H_{aa'}$ and $\boldsymbol{\gamma}_{aa'}$ will differ slightly from the bulk values. This divergence is however neglected, as is generally done. Moreover, $\boldsymbol{\pi}_{aa'}$ depends on position only through the potential gradient in the spin-orbit part. We disregard this material dependence and replace the momentum matrix in the entire heterostructure by its value in the confined region. The effective mass equation finally becomes

$$\sum_{a'} \Big\{ \frac{1}{2m_0} (\boldsymbol{p}_\perp + \hbar\boldsymbol{k}_\parallel) \boldsymbol{\gamma}_{aa'} (\boldsymbol{p}_\perp + \hbar\boldsymbol{k}_\parallel) + \frac{1}{m_0} \boldsymbol{\pi}_{aa'} (\boldsymbol{p}_\perp + \hbar\boldsymbol{k}_\parallel) + E_a \delta_{aa'} \Big\} f_{a'}(\boldsymbol{r}_\perp) = E\, f_a(\boldsymbol{r}_\perp) \quad (4.33)$$

where the piecewise constant functions $\boldsymbol{\gamma}_{aa'}(\boldsymbol{r}_\perp)$ and $E_a(\boldsymbol{r}_\perp)$ take the local bulk value. Remind that the eigensolution E and $f_a(\boldsymbol{r}_\perp)$ depend on $\boldsymbol{k}_\parallel$. We denote them by $E^{(i)}_{\boldsymbol{k}_\parallel}$ and $f^{(i)}_{a,\boldsymbol{k}_\parallel}(\boldsymbol{r}_\perp)$, where i is the subband label.

The envelope functions $f_a(\boldsymbol{r}_\perp)$ have to be continuous at the interfaces. Integrating over an infinitesimal volume about the interface, one finds that

$$\sum_{a'} \boldsymbol{\gamma}_{aa'} (\boldsymbol{p}_\perp + \hbar\boldsymbol{k}_\parallel)\, f_{a'}(\boldsymbol{r}_\perp) \quad (4.34)$$

is also continuous. The effective mass tensor $\boldsymbol{\gamma}$ is discontinuous at interfaces and so are the derivatives of f_a. Foreman gives a detailed discussion on these boundary conditions in [121]. They are similar to the one given by Bastard [46]. However, note the absence of the bulk momentum. This is due to the fact that we have disregarded the material dependence of its spin-orbit part. The matrix elements $\boldsymbol{\pi}_{aa'}$ are thus constant over the entire heterostructure.

4.2.4 Momentum matrix elements

The momentum matrix element between two eigenstates of (4.2) is given by

$$\langle \psi^{(i)}_{\boldsymbol{k}_\parallel} | \boldsymbol{\pi} | \psi^{(j)}_{\boldsymbol{k}_\parallel{}'} \rangle = \sum_{nn'} \Big[\langle f^{(i)}_{n,\boldsymbol{k}_\parallel} | (\boldsymbol{p}_\perp + \hbar\boldsymbol{k}_\parallel) | f^{(j)}_{n',\boldsymbol{k}_\parallel} \rangle_\perp \, \delta_{nn'} + \langle f^{(i)}_{n,\boldsymbol{k}_\parallel} | f^{(j)}_{n',\boldsymbol{k}_\parallel} \rangle_\perp \, \boldsymbol{\pi}_{nn'} \Big] \, \delta_{\boldsymbol{k}_\parallel \boldsymbol{k}_\parallel{}'}$$

where the scalar product in the confined subspace is defined by

$$\langle f | g \rangle_\perp \equiv \int_{\Omega_\perp} d\boldsymbol{r}_\perp \, f(\boldsymbol{r}_\perp)^* g(\boldsymbol{r}_\perp) \, . \quad (4.35)$$

By using the same perturbative scheme to eliminate the remote bands $\mathbb{B}$ as for the effective envelope function equation, the momentum becomes

$$\begin{aligned} \langle \psi^{(i)}_{\boldsymbol{k}_\parallel} | \boldsymbol{\epsilon\pi} | \psi^{(j)}_{\boldsymbol{k}_\parallel} \rangle = {} & \sum_{aa'} \langle f^{(i)}_{a,\boldsymbol{k}_\parallel} | \frac{1}{2} \big[(\boldsymbol{p}_\perp + \hbar\boldsymbol{k}_\parallel) \boldsymbol{\gamma}_{aa'} \boldsymbol{\epsilon} + \boldsymbol{\epsilon} \boldsymbol{\gamma}_{aa'} (\boldsymbol{p}_\perp + \hbar\boldsymbol{k}_\parallel) \big] | f^{(j)}_{a',\boldsymbol{k}_\parallel} \rangle_\perp \\ & + \sum_{aa'} \langle f^{(i)}_{a,\boldsymbol{k}_\parallel} | \boldsymbol{\epsilon\pi}_{aa'} | f^{(j)}_{a',\boldsymbol{k}_\parallel} \rangle_\perp \, . \end{aligned} \quad (4.36)$$

The momentum matrix elements between two states with different wavevectors $\boldsymbol{k}_{\shortparallel}$ are zero. The effective mass tensors and momentum matrix elements of the bulk ($\boldsymbol{\gamma}_{aa'}$ and $\boldsymbol{\pi}_{aa'}$ respectively) are the same as in the effective mass equation (4.33).

Note that if we define the effective envelope function Hamiltonian $\tilde{H}$ and effective momentum operator $\tilde{\boldsymbol{\pi}}$ as

$$\sum_{a'} \tilde{H}_{aa'} f^{(j)}_{a',\boldsymbol{k}_{\shortparallel}} = E^{(j)}_{\boldsymbol{k}_{\shortparallel}} f^{(j)}_{a,\boldsymbol{k}_{\shortparallel}} \tag{4.37}$$

and

$$\langle \psi^{(i)}_{\boldsymbol{k}_{\shortparallel}} | \boldsymbol{\epsilon\pi} | \psi^{(j)}_{\boldsymbol{k}_{\shortparallel}'} \rangle = \sum_{aa'} \langle f^{(i)}_{a,\boldsymbol{k}_{\shortparallel}} | \boldsymbol{\epsilon} \tilde{\boldsymbol{\pi}}_{aa'} | f^{(j)}_{a',\boldsymbol{k}_{\shortparallel}} \rangle_{\perp} \, \delta_{\boldsymbol{k}_{\shortparallel}\boldsymbol{k}_{\shortparallel}'} \,, \tag{4.38}$$

then the relation (4.5) remains valid for the effective operators in the confined direction $\boldsymbol{\epsilon}_{\perp}$:

$$\boldsymbol{\epsilon}_{\perp} \tilde{\boldsymbol{\pi}}_{aa'} = i \, \frac{m_0}{\hbar} \, [\tilde{H}_{aa'}, \boldsymbol{\epsilon}_{\perp} \boldsymbol{r}] \,. \tag{4.39}$$

In the unconfined direction, the matrix element of the position operator $\boldsymbol{r}_{\shortparallel}$ is however not well defined.

As it can be seen from the effective mass equation (4.33), the complex microscopic potential of the heterostructure is replaced by a limited number of *bulk* parameters at zone center: effective mass $\boldsymbol{\gamma}_{aa'}$, energy E_a and momentum $\boldsymbol{\pi}_{aa'}$. Note that the effective mass is defined by the formal second-order expression (4.28). However, the structure of this tensor is equivalent to the general form resulting from the theory of invariants [122], based only on the spatial symmetry of the bulk crystal. The values of these parameters are usually fitted to experimental results. Once the envelope functions and eigenenergies have been obtained by solving the effective mass equation (4.33), the momentum matrix elements can be calculated with formula (4.36). This is done in section 4.4.4 for the symmetric AlGaAs/GaAs quantum well used in chapter 5. The numerical method using finite elements is outlined in the next section for the one-dimensional case.

4.3 Finite element method

In this section, we introduce the finite element method used to solve the effective mass equation (4.33). This numerical method will be applied to the band structure calculation of the quantum well used in chapter 5. For this reason, we consider here the case of a one-dimensional confinement, *i.e.* a quantum well with planar interfaces. The position vectors in the unconfined and confined directions, $\boldsymbol{r}_{\shortparallel}$ and $\boldsymbol{r}_{\perp}$, correspond to the coordinates (x, y) and z respectively. To solve the differential eigenvalue equation (4.33) for the envelope functions, we use the finite element method outlined in what follows (see *e.g.* [123] for a good introduction).

In section 4.3.1, the equations to be solved are first expressed in appropriate units. In section 4.3.2, the problem is then discretized for the simplest case of piecewise linear basis functions. The corresponding generalized eigenvalue problem is detailed in section 4.3.3. In section 4.3.4, we introduce the mapping onto a master element, which simplifies the numerical integration. The piecewise linear basis functions are explicitly given in section 4.3.5. Finally, in section 4.3.6, we outline how the method can be generalized to higher order basis functions.

4.3.1 1D effective mass equation in appropriate units

We first introduce dimensionless quantities by expressing length, energy and momentum in the new units l_u, e_u and π_u respectively, where l_u is a characteristic length, and e_u and π_u are defined by

$$e_u = \frac{\hbar^2}{2m_0 l_u^2} \qquad\qquad \pi_u = \frac{\hbar}{2l_u}\,. \tag{4.40}$$

After the substitution

$$\begin{aligned} &z \to z\, l_u && H \to H\, e_u && \pi \to \pi\, \pi_u \\ &k \to k/l_u && E \to E\, e_u && \end{aligned}$$

the one-dimensional effective mass equation becomes

$$\begin{aligned} \Big\{ -\frac{d}{dz}\gamma^{zz}\frac{d}{dz} - i\sum_{\mu}\big[\frac{d}{dz}\gamma^{z\mu} + \gamma^{\mu z}\frac{d}{dz}\big]k_\mu - i\pi^z\frac{d}{dz} + \pi^\mu k_\mu \\ + H + \sum_{\mu\nu}\gamma^{\mu\nu}k_\mu k_\nu\Big\} f(z) = E\, f(z)\,, \end{aligned} \tag{4.41}$$

where H is the diagonal bulk Hamiltonian at zone center ($H_{aa'} = E_a\delta_{aa'}$). The symbols are commented below. The momentum matrix elements are given by

$$\begin{aligned} &\langle\psi^{(n)}_{\boldsymbol{k}_{\shortparallel}}|\boldsymbol{\epsilon}_\alpha\boldsymbol{\pi}|\psi^{(m)}_{\boldsymbol{k}_{\shortparallel}}\rangle = \\ &\qquad \langle f^{(n)}|\Big\{ -i\big[\frac{d}{dz}\gamma^{z\alpha} + \gamma^{\alpha z}\frac{d}{dz}\big] + \sum_{\mu}\big[\gamma^{\mu\alpha} + \gamma^{\alpha\mu}\big]k_\mu + \pi^\alpha\Big\}|f^{(m)}\rangle_\perp\,, \end{aligned} \tag{4.42}$$

where $\boldsymbol{\epsilon}_\alpha$ is the unit vector in the direction $\alpha = x, y, z$. The sums over μ and ν cover the unconfined directions x and y.

The effective mass tensors $\gamma^{\mu\nu}$, the momentum π^μ and the bulk Hamiltonian H

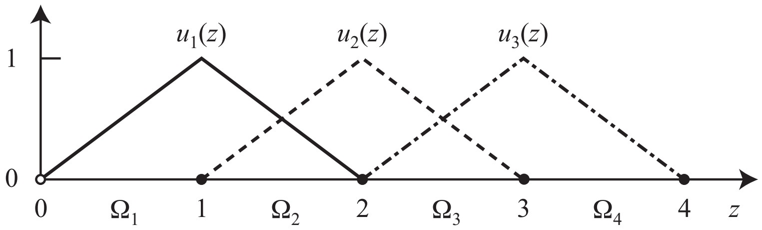

Figure 4.2: Piecewise linear basis functions u_i for a 4-element mesh.

are $N_A \times N_A$ matrices, where N_A is the number of bands in group $\mathbb{A}$ (see section 4.2.3). They multiply the envelope function $f(z)$, which is a vector with N_A components. We dropped the band indices and the explicit summation for the matrix-vector products. For the sake of simplicity, the vectorial nature of these quantities is ignored in the following derivation. This is not restrictive, and the eigenvalue equation to solve will be generalized at the end of section 4.3.3.

4.3.2 Discretization

The finite discretization volume $[0, L]$ within the one-dimensional real space $\Omega_\perp$ is divided into $N_e = N_n + 1$ cells or elements Ω_e defining a grid with N_n internal nodes (Figure 4.2). The elements and the internal nodes are labeled by $e = 1, \dots, N_e$ and $j = 1, \dots, N_n$ respectively. The node j with coordinate z_j is therefore shared by the two cells Ω_j and Ω_{j+1}. To each internal node j, we associate a function $u_j(z)$ taking the value 1 at z_j and 0 outside the two adjacent elements Ω_j and Ω_{j+1}. The set $\{u_j(z)\}_{j=1}^{N_n}$ of N_n basis functions generates a subspace $\mathcal{L}$ of $L^2(\mathbb{R})$, and the eigenfunction $f \in L^2(\mathbb{R})$ can be approximated by

$$\tilde{f}(z) = \sum_{j=1}^{N_n} f_j \, u_j(z) \tag{4.43}$$

with $f_j = f(z_j)$. The function $\tilde{f}(z) \in \mathcal{L}$ is therefore equal to $f(z)$ at the nodes of the grid.

For bound states, the envelope functions $f(z)$ have to vanish at large distance of the quantum well. In the finite element formulation, these boundary conditions become $\tilde{f}(0) = \tilde{f}(L) = 0$. In the present case, they are already naturally included in the expansion (4.43), as the basis functions centered on the nodes 0 and $N_n + 1$ on the border of the domain $[0, L]$ have been omitted, and $u_1(0) = u_{N_n}(L) = 0$.

4.3.3 Generalized eigenvalue problem

The envelope function in the effective mass equation (4.41) is now replaced by the approximate expansion (4.43), where we take care that any material interface coincide with a node. The resulting equation is then multiplied by the basis functions u_j and integrated over $[0, L]$. The differential equation reduces to the generalized eigenvalue problem

$$K \cdot v = \lambda\, M \cdot v \tag{4.44}$$

where v is the column vector

$$v = \begin{pmatrix} f_1 & f_2 & \ldots & f_{N_n} \end{pmatrix}^T , \tag{4.45}$$

and K and M are hermitian N_n-by-N_n matrices. The *stiffness* matrix K can be expressed as

$$K = K^{\gamma_\perp} + K^{\gamma_\times} + K^{\gamma_\parallel} + K^{\pi_\perp} + K^{\pi_\parallel} + K^H \tag{4.46}$$

with

$$K^{\gamma_\perp}_{ij} = \int dz\, u'_i \gamma^{zz} u'_j \tag{4.47}$$

$$K^{\gamma_\times}_{ij} = \int dz \sum_\mu \left[u'_i \gamma^{z\mu} u_j - u_i \gamma^{\mu z} u'_j \right] ik_\mu \tag{4.48}$$

$$K^{\gamma_\parallel}_{ij} = \int dz\, u_i \sum_{\mu\nu} (k_\mu \gamma^{\mu\nu} k_\nu)\, u_j \tag{4.49}$$

$$K^{\pi_\perp}_{ij} = \int dz\, u_i\, (-i\pi^z)\, u'_j \tag{4.50}$$

$$K^{\pi_\parallel}_{ij} = \int dz\, u_i \sum_\mu (\pi^\mu k_\mu)\, u_j \tag{4.51}$$

$$K^H_{ij} = \int dz\, u_i\, H\, u_j \tag{4.52}$$

and the *mass* matrix M is given by

$$M_{ij} = \int dz\, u_i u_j\,. \tag{4.53}$$

The indices μ and ν in the sums take the value x and y, and u' is a shorthand notation for the derivative du/dz. Once the eigenvalue problem is solved, the momentum matrix elements between two states approximated by the vectors $v^{(n)}$ and

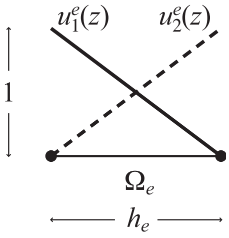

Figure 4.3: A generic finite element Ω_e with linear shape functions.

$v^{(m)}$ can be obtained by

$$\langle\psi_{\boldsymbol{k}_{\shortparallel}}^{(n)}|\boldsymbol{\epsilon}_\alpha\boldsymbol{\pi}|\psi_{\boldsymbol{k}_{\shortparallel}}^{(m)}\rangle = v^{(n)\dagger} P\, v^{(m)} \tag{4.54}$$

where the hermitian matrix P is given by

$$P_{ij} = P_{ij}^{\gamma_\perp} + P_{ij}^{\gamma_{\shortparallel}} + P_{ij}^{\pi} \tag{4.55}$$

with

$$P_{ij}^{\gamma_\perp} = i\int dz\,\left[u_i'\gamma^{z\alpha}u_j - u_i\gamma^{\alpha z}u_j'\right] \tag{4.56}$$

$$P_{ij}^{\gamma_{\shortparallel}} = \int dz\,u_i\left[\gamma^{\mu\alpha}+\gamma^{\alpha\mu}\right]k_\mu\,u_j \tag{4.57}$$

$$P_{ij}^{\pi} = \int dz\,u_i\,\pi^\alpha\,u_j\,. \tag{4.58}$$

The derivatives of the discontinuous effective mass tensors γ in (4.47), (4.48) and (4.56) have been eliminated by integrating by parts. Note that all quantities in (4.41), except $f(z)$, are constant within any element Ω_e. To construct the matrices K and M, one has therefore to integrate only products of basis functions and/or their first derivatives.

For practical purpose, the basis functions u_j are divided into *element shape functions* u_ν^e, defined locally over each element e (Figure 4.3). Let us illustrate this with the mass matrix M, whose element (i,j) is defined by

$$M_{ij} = \int dz\,u_iu_j = \sum_{(e,\mu)_i}\sum_{(e,\nu)_j}\int_{\Omega_e} dz\,u_\mu^e u_\nu^e\,. \tag{4.59}$$

The symbol $(e,\nu)_j$ denotes all shape functions u_ν^e composing the basis function u_j. Piecewise linear basis functions are constructed by two shape functions ($\nu = 1,\,2$), and the band matrix M is thus given by

$$\begin{bmatrix} m_{22}^1+m_{11}^2 & m_{12}^2 & & & & \\ m_{21}^2 & m_{22}^2+m_{11}^3 & m_{12}^3 & & 0 & \\ & m_{21}^3 & m_{22}^3+m_{11}^4 & m_{12}^4 & & \\ & & \cdots & \cdots & \cdots & \\ & 0 & & m_{21}^{N_e-2} & m_{22}^{N_e-2}+m_{11}^{N_e-1} & m_{12}^{N_e-1} \\ & & & & m_{21}^{N_e-1} & m_{22}^{N_e-1}+m_{11}^{N_e} \end{bmatrix}$$

where

$$m_{\mu\nu}^e = \int_{\Omega_e} dz\, u_\mu^e(z) u_\nu^e(z)\,. \tag{4.60}$$

Note that the mass matrix carries the non-orthogonality of the basis. This is expressed by the non-diagonal nature of the matrix.

The generalization of (4.44) and (4.54) to the multi-band case where $\gamma^{\mu\nu}$, π^μ and H are $N_A \times N_A$ matrices is straightforward. The elements K_{ij}, M_{ij} and P_{ij} become $N_A \times N_A$ matrices. Note that the elements M_{ij} (and $m_{\mu\nu}^e$) are replaced by diagonal matrices with equal elements. Each element f_i of the vector v (equation (4.45)) becomes itself a vector of N_A components. Consequently, K, M and P stand for $N_n N_A \times N_n N_A$ hermitian matrices, and v for a vector of $N_n N_A$ components.

4.3.4 Master element

The master element is the interval $\hat{\Omega} = [-1, 1]$ with coordinate $\xi \in \hat{\Omega}$. Inside each element Ω_e, we introduce the bijective mapping

$$\begin{aligned} T_e : \hat{\Omega} &\rightarrow \Omega_e \\ \xi &\mapsto z\,. \end{aligned} \tag{4.61}$$

This transformation has to be “smooth” in the sense that it corresponds to a deformation of the master element $\hat{\Omega}$ into Ω_e. In the one-dimensional case, T_e is given by

$$z(\xi) = z_{e-1} + \frac{h_e}{2}(1+\xi)\,, \tag{4.62}$$

where $h_e = z_e - z_{e-1}$ is the length of the element Ω_e. The mapping T_e transforms the shape function $u_\nu^e(z)$ defined over the element Ω_e into the master shape function $\hat{u}_\nu(\xi)$ defined over $\hat{\Omega}$.

To construct the matrices K and M, one has to integrate products of shape functions and/or their first derivatives only. Using the mapping on the master element, the integrals to calculate become

$$\int_{\Omega_e} dz\, g(z) = \frac{h_e}{2} \int_{-1}^{1} d\xi\, \hat{g}(\xi)\,, \tag{4.63}$$

where $\hat{g}(\xi)$ has to be replaced by $\hat{u}_\mu(\xi)\hat{u}_\nu(\xi)$, $\hat{u}'_\mu(\xi)\hat{u}_\nu(\xi)$ or $\hat{u}'_\mu(\xi)\hat{u}'_\nu(\xi)$. The prime denotes the derivative with respect to ξ. As one usually uses polynomial basis functions, the integrals are computed most efficiently with a N_g-point Gauss-Legendre integration

$$\int_{\Omega_e} dz\, g(z) = \frac{h_e}{2} \sum_{l=1}^{N_g} w_l\, \hat{g}(\xi_l)\,, \tag{4.64}$$

where w_l is the weight of the integration point ξ_l. This method is simple, reliable, and *exact* for a polynomial of degree ${N_g}^2 - 1$. For piecewise linear basis functions, $N_g = 2$ is therefore sufficient.

4.3.5 Piecewise linear basis functions

We give here the explicit form of the piecewise linear basis functions and the corresponding master shape functions.

Basis functions

$$u_j(z) = \begin{cases} +(z - z_{j-1})/h_j & z \in \Omega_j \\ -(z - z_{j+1})/h_{j+1} & z \in \Omega_{j+1} \\ 0 & \text{elsewhere} \end{cases} \tag{4.65}$$

Shape functions

$$u_1^e(z) = -(z - z_e)/h_e \qquad z \in \Omega_e \tag{4.66}$$

$$u_2^e(z) = +(z - z_{e-1})/h_e \qquad z \in \Omega_e \tag{4.67}$$

Master shape functions

$$\hat{u}_1(\xi) = \frac{1}{2}(1 - \xi) \qquad \xi \in [-1, 1] \tag{4.68}$$

$$\hat{u}_2(\xi) = \frac{1}{2}(1 + \xi) \qquad \xi \in [-1, 1] \tag{4.69}$$

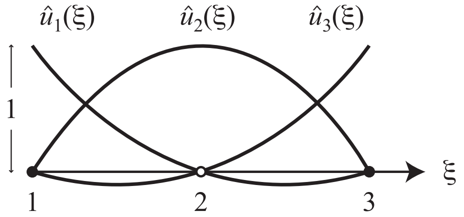

Figure 4.4: A master element with 3 nodes and piecewise quadratic shape functions.

4.3.6 Higher order element shape functions

The previous discussion focused on linear shape functions. The solution of the differential eigenvalue problem was thus approximated by piecewise linear functions. The method can however be easily extended to polynomial basis functions of higher degree. For shape functions of degree k, we identify $k+1$ nodes (including the endpoints) which divide the element into k segments. To every element, one associates $k+1$ shape functions (one per node). For each node j, the shape function $\hat{u}_j(\xi)$ defined on the master element is zero at all nodes except j where it takes the value 1. This is illustrated for $k=2$ in Figure 4.4. The expansion (4.43) remains the same, but the number of internal nodes N_n is related to the number of elements N_e by $N_n = k\,N_e - 1$. The eigenfunction is now approximated by piecewise polynomials of degree k. Because the overlap region between two shape functions can include up to $k+1$ nodes, the stiffness matrix K and mass matrix M have k non-zero upper/lower diagonals.

4.4 Symmetric quantum well

In the following, we consider a symmetric GaAs/AlGaAs quantum well with growth direction along [001]. The Bravais lattice of the corresponding bulk crystal is zinc blende, which is not invariant under spatial inversion. The inversion asymmetry in GaAs has however very small effects on the valence band structure and is therefore neglected. Thus, the heterostructure we are interested in reduces to the centrosymmetric case.

First we derive general properties of the eigenstates and the momentum matrix elements, following from the spatial inversion and time reversal symmetries (§ 4.4.1). Then, we give the zone-center wave function of the bulk and the related effective parameters we use (§ 4.4.2), and discuss the constraints on the envelope functions they impose (§ 4.4.3). Finally, we show the calculated energy bands and momentum matrix elements of the quantum well (§ 4.4.4).

4.4.1 Symmetry related properties

Let K and I be the anti-unitary time-reversal operator and the unitary spatial inversion operator respectively. For a system with half-integer spin they have the properties $K^2 = -1$ and $I^2 = 1$ [113, 122].

Let $\psi_{\boldsymbol{k}}$ be an eigenstate of the Hamiltonian $H(\boldsymbol{k})$ with energy $E_{\boldsymbol{k}}$ and wavevector $\boldsymbol{k}$. We show now that $KI\psi_{\boldsymbol{k}}$ is not only an *eigenstate* of $H(\boldsymbol{k})$ but also *orthogonal* to $\psi_{\boldsymbol{k}}$. In other words, the eigenspace of $H(\boldsymbol{k})$ associated to the energy $E_{\boldsymbol{k}}$ and wavevector $\boldsymbol{k}$ is at least of dimension 2. First, we note that the operator KI is antiunitary with $(KI)^2 = -1$. Second we compute the scalar product

$$\langle\psi_{\boldsymbol{k}}|KI\psi_{\boldsymbol{k}}\rangle = \langle(KI)^2\psi_{\boldsymbol{k}}|KI\psi_{\boldsymbol{k}}\rangle = -\langle\psi_{\boldsymbol{k}}|KI\psi_{\boldsymbol{k}}\rangle\,, \tag{4.70}$$

where we have used the anti-unitary property of KI. It follows that

$$\langle\psi_{\boldsymbol{k}}|KI\psi_{\boldsymbol{k}}\rangle = 0\,, \tag{4.71}$$

and the band structure is at least twice-degenerate.

Let us now denote the two states with same energy and wavevector by $|n,\boldsymbol{k}\rangle$ and $|\bar{n},\boldsymbol{k}\rangle$ where n and $\bar{n}$ label the two degenerate bands. The four eigenstates of the Hamiltonian with same energy $|n,+\boldsymbol{k}\rangle$, $|\bar{n},+\boldsymbol{k}\rangle$, $|n,-\boldsymbol{k}\rangle$ and $|\bar{n},-\boldsymbol{k}\rangle$ for $\boldsymbol{k}\neq 0$ are generally related to each other by

$$I|n,+\boldsymbol{k}\rangle = +e^{i\phi}\,|n,-\boldsymbol{k}\rangle \tag{4.72}$$

$$I|\bar{n},+\boldsymbol{k}\rangle = +e^{i\bar{\phi}}\,|\bar{n},-\boldsymbol{k}\rangle \tag{4.73}$$

$$K|n,+\boldsymbol{k}\rangle = +e^{i\theta}\,|\bar{n},-\boldsymbol{k}\rangle \tag{4.74}$$

$$K|\bar{n},+\boldsymbol{k}\rangle = -e^{i\bar{\theta}}\,|n,-\boldsymbol{k}\rangle\,. \tag{4.75}$$

One easily shows that

$$(KI)^2|n,+\boldsymbol{k}\rangle = -e^{i(\phi+\theta-\bar{\phi}-\bar{\theta})}|n,+\boldsymbol{k}\rangle\,, \tag{4.76}$$

and with $(KI)^2 = -1$, one gets

$$e^{i(\phi+\theta)/2} = \pm e^{i(\bar{\phi}+\bar{\theta})/2}\,. \tag{4.77}$$

By choosing the phases of the wave functions like

$$|n,\pm\boldsymbol{k}\rangle' = e^{i(\theta\mp\phi)/2}\,|n,\pm\boldsymbol{k}\rangle \tag{4.78}$$

$$|\bar{n},\pm\boldsymbol{k}\rangle' = e^{i(\bar{\theta}\mp\bar{\phi})/2}\,|\bar{n},\pm\boldsymbol{k}\rangle \tag{4.79}$$

with

$$e^{i(\phi+\theta)/2} = +e^{i(\bar{\phi}+\bar{\theta})/2} \tag{4.80}$$

for gerade wave functions, and

$$|n, \pm\boldsymbol{k}\rangle' = e^{i(\theta\mp\phi\mp\pi)/2}\,|n, \pm\boldsymbol{k}\rangle \tag{4.81}$$

$$|\bar{n}, \pm\boldsymbol{k}\rangle' = e^{i(\bar{\theta}\mp\bar{\phi}\mp\pi)/2}\,|\bar{n}, \pm\boldsymbol{k}\rangle \tag{4.82}$$

with

$$e^{i(\phi+\theta)/2} = -e^{i(\bar{\phi}+\bar{\theta})/2} \tag{4.83}$$

for ungerade wave functions, one finds respectively

$$I|n, +\boldsymbol{k}\rangle' = +|n, -\boldsymbol{k}\rangle' \tag{4.84}$$

$$I|\bar{n}, +\boldsymbol{k}\rangle' = +|\bar{n}, -\boldsymbol{k}\rangle' \tag{4.85}$$

$$K|n, +\boldsymbol{k}\rangle' = +|\bar{n}, -\boldsymbol{k}\rangle' \tag{4.86}$$

$$K|\bar{n}, +\boldsymbol{k}\rangle' = -|n, -\boldsymbol{k}\rangle' \tag{4.87}$$

and

$$I|n, +\boldsymbol{k}\rangle' = -|n, -\boldsymbol{k}\rangle' \tag{4.88}$$

$$I|\bar{n}, +\boldsymbol{k}\rangle' = -|\bar{n}, -\boldsymbol{k}\rangle' \tag{4.89}$$

$$K|n, +\boldsymbol{k}\rangle' = -|\bar{n}, -\boldsymbol{k}\rangle' \tag{4.90}$$

$$K|\bar{n}, +\boldsymbol{k}\rangle' = +|n, -\boldsymbol{k}\rangle'\,. \tag{4.91}$$

The choice of (4.80) and (4.83) ensures that $KI|n, +\boldsymbol{k}\rangle' = |\bar{n}, +\boldsymbol{k}\rangle'$ in both cases. The symmetry relations $I\boldsymbol{\pi}I = -\boldsymbol{\pi}$ and $K\boldsymbol{\pi}K = -\boldsymbol{\pi}$ thus imply

$$\boldsymbol{\pi}_{mn,+\boldsymbol{k}} = -\boldsymbol{\pi}_{mn,-\boldsymbol{k}} = +\boldsymbol{\pi}_{\bar{n}\bar{m},+\boldsymbol{k}} = -\boldsymbol{\pi}_{\bar{n}\bar{m},-\boldsymbol{k}} \tag{4.92}$$

$$\boldsymbol{\pi}_{m\bar{n},+\boldsymbol{k}} = -\boldsymbol{\pi}_{m\bar{n},-\boldsymbol{k}} = -\boldsymbol{\pi}_{n\bar{m},+\boldsymbol{k}} = +\boldsymbol{\pi}_{n\bar{m},-\boldsymbol{k}} \tag{4.93}$$

for states with same parity, and

$$\boldsymbol{\pi}_{mn,+\boldsymbol{k}} = +\boldsymbol{\pi}_{mn,-\boldsymbol{k}} = +\boldsymbol{\pi}_{\bar{n}\bar{m},+\boldsymbol{k}} = +\boldsymbol{\pi}_{\bar{n}\bar{m},-\boldsymbol{k}} \tag{4.94}$$

$$\boldsymbol{\pi}_{m\bar{n},+\boldsymbol{k}} = +\boldsymbol{\pi}_{m\bar{n},-\boldsymbol{k}} = -\boldsymbol{\pi}_{n\bar{m},+\boldsymbol{k}} = -\boldsymbol{\pi}_{n\bar{m},-\boldsymbol{k}} \tag{4.95}$$

for states with opposite parity.

Note that the noncompulsory choice of different phases according to parity ensures that the above relations remain valid for $\boldsymbol{k} = 0$. Indeed, equations (4.84) and (4.88) must be seen as the *definition* of the band label n in the two-dimensional subspace associated to $-\boldsymbol{k}$, with respect to n in the subspace associated to $+\boldsymbol{k}$. This is not possible at zero wavevector, as there are no more two distinct subspaces, and the behavior under the inversion operation is necessarily dictated by parity.

For a quantum well oriented along a principal axis (*e.g.* [001]), the only symmetry which leaves $\boldsymbol{k}$ invariant besides the identity is the in-plane reflection. The little group of $\boldsymbol{k}$ is therefore $\mathbf{C}_s$. Group theory tables [124] show that both irreducible representations[4] (irreps) ${}^1E_{1/2}$ and ${}^2E_{1/2}$ of the double group $\mathbf{C}_s$ are one-dimensional and related to each other by the time-reversal operation. In other words, the states labeled with the band index n and $\bar{n}$ belong to ${}^1E_{1/2}$ and ${}^2E_{1/2}$ respectively. The momentum operators $\boldsymbol{\epsilon}_{\shortparallel} \cdot \boldsymbol{\pi}$ and $\boldsymbol{\epsilon}_{\perp} \cdot \boldsymbol{\pi}$, parallel and perpendicular to the quantum well, belong respectively to the irreps A' and A''. Therefore, the representation products

$$
\begin{aligned}
&A' \otimes {}^1E_{1/2} = {}^1E_{1/2} && A'' \otimes {}^1E_{1/2} = {}^2E_{1/2} \\
&A' \otimes {}^2E_{1/2} = {}^2E_{1/2} && A'' \otimes {}^2E_{1/2} = {}^1E_{1/2} \qquad (4.96)
\end{aligned}
$$

imply the important result

$$\boldsymbol{\epsilon}_{\perp} \cdot \boldsymbol{\pi}_{nm,\boldsymbol{k}} = 0 \qquad (4.97)$$

$$\boldsymbol{\epsilon}_{\shortparallel} \cdot \boldsymbol{\pi}_{n\bar{m},\boldsymbol{k}} = 0\,. \qquad (4.98)$$

These properties are used in section 5.2.

4.4.2 Effective mass and momentum tensors

As basis for the envelope function expansion, we take the zone center Bloch states of the lowest conduction band and of the highest valence band. At zero wavevector, the former is doubly degenerate and belongs to $E_{1/2}$ (or Γ_6 according to the notation of Koster [125]), whereas the latter is four times degenerate and belongs to $F_{3/2}$ (or Γ_8).

The crystallographic point group of GaAs is $\mathbf{T}_d$, which does not contain the spatial inversion operation. It follows that the partner functions of the irreps are not necessary gerade or ungerade. However, the departure of the inversion symmetry is small and will be neglected here. The basis can therefore be approximated by either gerade or ungerade functions, depending on the state. As the conduction band and valence band wave functions are strongly s-like and p-like respectively,

---

[4] We follow the notation of Altmann and Herzig [124] for the irreducible representations.

one uses the basis functions

$$|\tfrac{1}{2}\,\tfrac{1}{2}\rangle = |\mathrm{S}\rangle \otimes |+\rangle \tag{4.99}$$

$$|\tfrac{1}{2}\,\tfrac{\bar{1}}{2}\rangle = |\mathrm{S}\rangle \otimes |-\rangle \tag{4.100}$$

and

$$|\tfrac{3}{2}\,\tfrac{3}{2}\rangle = +\frac{1}{\sqrt{2}}\left(|\mathrm{X}\rangle + i\,|\mathrm{Y}\rangle\right) \otimes |+\rangle \tag{4.101}$$

$$|\tfrac{3}{2}\,\tfrac{1}{2}\rangle = +\frac{1}{\sqrt{6}}\left\{\left(|\mathrm{X}\rangle + i\,|\mathrm{Y}\rangle\right) \otimes |-\rangle - 2|\mathrm{Z}\rangle \otimes |+\rangle\right\} \tag{4.102}$$

$$|\tfrac{3}{2}\,\tfrac{\bar{1}}{2}\rangle = -\frac{1}{\sqrt{6}}\left\{\left(|\mathrm{X}\rangle - i\,|\mathrm{Y}\rangle\right) \otimes |+\rangle + 2|\mathrm{Z}\rangle \otimes |-\rangle\right\} \tag{4.103}$$

$$|\tfrac{3}{2}\,\tfrac{\bar{3}}{2}\rangle = -\frac{1}{\sqrt{2}}\left(|\mathrm{X}\rangle - i\,|\mathrm{Y}\rangle\right) \otimes |-\rangle \tag{4.104}$$

for $E_{1/2}$ and $F_{3/2}$ respectively[5]. They are arranged as follows:

$$\{|\tfrac{1}{2}\,\tfrac{1}{2}\rangle, |\tfrac{1}{2}\,\tfrac{\bar{1}}{2}\rangle\} \qquad \text{for } E_{1/2} \tag{4.105}$$

$$\{|\tfrac{3}{2}\,\tfrac{3}{2}\rangle, |\tfrac{3}{2}\,\tfrac{1}{2}\rangle, |\tfrac{3}{2}\,\tfrac{\bar{1}}{2}\rangle, |\tfrac{3}{2}\,\tfrac{\bar{3}}{2}\rangle\} \qquad \text{for } F_{3/2}\,. \tag{4.106}$$

In the band structure model we use here, the equation (4.33) does not couple the conduction bands to the valence bands. The effective envelope function equation (4.33) is solved independently for the conduction subbands and the valence subbands of the quantum well, using only the basis of $E_{1/2}$ and $F_{3/2}$ respectively.

The doubly degenerate conduction band is described by the isotropic effective-mass m_c *i.e.*

$$\gamma^{\alpha\beta}_{cc'} = \delta_{\alpha\beta}\,\delta_{cc'}\,\frac{m_0}{m_c}\,. \tag{4.107}$$

The two degenerate conduction bands are thus independent and the corresponding effective envelope function equation (4.33) reduces to two (equivalent) one-dimensional equations. For the valence bands, the effective Hamiltonian reduces to the four-by-four Luttinger Hamiltonian. The valence-band mixing is given by

---

[5] Altmann and Herzig [124] use the two notations $|j\ m\rangle$ and $|j\ m\rangle^{\bullet}$ to distinguish between basis vectors which are respectively gerade and ungerade under spatial inversion. In the present work, the vectors $|\tfrac{3}{2}\ m\rangle$ of $F_{3/2}$ correspond actually to $|\tfrac{3}{2}\ m\rangle^{\bullet}$ in their tables. We dropped the bullets for the sake of legibility.

the effective-mass tensors [46, 126]

$$\gamma^{xx} = -\begin{bmatrix} \gamma_1+\gamma_2 & 0 & -\sqrt{3}\gamma_2 & 0 \\ 0 & \gamma_1-\gamma_2 & 0 & -\sqrt{3}\gamma_2 \\ -\sqrt{3}\gamma_2 & 0 & \gamma_1-\gamma_2 & 0 \\ 0 & -\sqrt{3}\gamma_2 & 0 & \gamma_1+\gamma_2 \end{bmatrix} \tag{4.108}$$

$$\gamma^{yy} = -\begin{bmatrix} \gamma_1+\gamma_2 & 0 & \sqrt{3}\gamma_2 & 0 \\ 0 & \gamma_1-\gamma_2 & 0 & \sqrt{3}\gamma_2 \\ \sqrt{3}\gamma_2 & 0 & \gamma_1-\gamma_2 & 0 \\ 0 & \sqrt{3}\gamma_2 & 0 & \gamma_1+\gamma_2 \end{bmatrix} \tag{4.109}$$

$$\gamma^{zz} = -\begin{bmatrix} \gamma_1-2\gamma_2 & 0 & 0 & 0 \\ 0 & \gamma_1+2\gamma_2 & 0 & 0 \\ 0 & 0 & \gamma_1+2\gamma_2 & 0 \\ 0 & 0 & 0 & \gamma_1-2\gamma_2 \end{bmatrix} \tag{4.110}$$

and

$$\gamma^{xy} = -\begin{bmatrix} 0 & 0 & +i\sqrt{3}\gamma_3 & 0 \\ 0 & 0 & 0 & +i\sqrt{3}\gamma_3 \\ -i\sqrt{3}\gamma_3 & 0 & 0 & 0 \\ 0 & -i\sqrt{3}\gamma_3 & 0 & 0 \end{bmatrix} \tag{4.111}$$

$$\gamma^{yz} = -\begin{bmatrix} 0 & +i\sqrt{3}\gamma_3 & 0 & 0 \\ -i\sqrt{3}\gamma_3 & 0 & 0 & 0 \\ 0 & 0 & 0 & -i\sqrt{3}\gamma_3 \\ 0 & 0 & +i\sqrt{3}\gamma_3 & 0 \end{bmatrix} \tag{4.112}$$

$$\gamma^{zx} = -\begin{bmatrix} 0 & -\sqrt{3}\gamma_3 & 0 & 0 \\ -\sqrt{3}\gamma_3 & 0 & 0 & 0 \\ 0 & 0 & 0 & +\sqrt{3}\gamma_3 \\ 0 & 0 & +\sqrt{3}\gamma_3 & 0 \end{bmatrix} \tag{4.113}$$

where γ_1, γ_2 and γ_3 are the usual Luttinger parameters. The minus sign in front of the matrices comes from our choice to work with electrons only, instead of holes.

In this model, the momentum matrix elements $\boldsymbol{\pi}_{cv}$ between the conduction bands and valence bands of the bulk are not explicitly used for the eigenstate calculation. Their contribution is however taken into account in the effective masses. On the other hand, the momentum matrix elements $\boldsymbol{\pi}_{cc'}$ between the two conduction bands or $\boldsymbol{\pi}_{vv'}$ between the four valence bands of the bulk vanish by symmetry.

Nevertheless, the inter-band bulk momentum $\boldsymbol{\pi}_{cv}$ is still required in equation (4.36) for the calculation of the momentum matrix elements between subbands of the quantum well. It is given by the two-by-four Kane matrices [46]

$$\pi_P^x = P \begin{bmatrix} \frac{1}{\sqrt{2}} & 0 & -\frac{1}{\sqrt{6}} & 0 \\ 0 & \frac{1}{\sqrt{6}} & 0 & -\frac{1}{\sqrt{2}} \end{bmatrix} \tag{4.114}$$

$$\pi_P^y = P \begin{bmatrix} \frac{i}{\sqrt{2}} & 0 & \frac{i}{\sqrt{6}} & 0 \\ 0 & \frac{i}{\sqrt{6}} & 0 & \frac{i}{\sqrt{2}} \end{bmatrix} \tag{4.115}$$

$$\pi_P^z = P \begin{bmatrix} 0 & -\sqrt{\frac{2}{3}} & 0 & 0 \\ 0 & 0 & -\sqrt{\frac{2}{3}} & 0 \end{bmatrix} \tag{4.116}$$

where the parameter P is related to the Kane energy E_P by

$$P = \sqrt{m_0 E_P/2}\,. \tag{4.117}$$

Once the bulk parameters m_c, γ_1, γ_2, γ_3, E_P and E_g (the band-gap energy) are known for all materials composing the heterostructure, the envelope function equation can be solved and the momentum matrix elements calculated.

4.4.3 Symmetries of the envelope functions

In the following, we give the symmetry properties of the envelope functions due to the invariance of the Hamiltonian under spatial inversion and time-reversal. The basis vectors of $E_{1/2}$ and $F_{3/2}$ are respectively gerade and ungerade under spatial inversion *i.e.*

$$I\,|\tfrac{1}{2}\;m\rangle = +|\tfrac{1}{2}\;m\rangle \qquad m = \tfrac{\bar{1}}{2}, \tfrac{1}{2} \tag{4.118}$$

$$I\,|\tfrac{3}{2}\;m\rangle = -|\tfrac{3}{2}\;m\rangle \qquad m = \tfrac{\bar{3}}{2}, \tfrac{\bar{1}}{2}, \tfrac{1}{2}, \tfrac{3}{2} \tag{4.119}$$

and the time-reversal operation acts like

$$K\,|\tfrac{1}{2}\;\tfrac{\bar{1}}{2}\rangle = +|\tfrac{1}{2}\;\tfrac{1}{2}\rangle \tag{4.120}$$

$$K\,|\tfrac{3}{2}\;\tfrac{1}{2}\rangle = -|\tfrac{3}{2}\;\tfrac{\bar{1}}{2}\rangle \tag{4.121}$$

$$K\,|\tfrac{3}{2}\;\tfrac{\bar{3}}{2}\rangle = -|\tfrac{3}{2}\;\tfrac{3}{2}\rangle\,. \tag{4.122}$$

The reciprocal relations are obtained with $K^2 = -1$. It follows that

$$KI\,|\tfrac{1}{2}\;\tfrac{\bar{1}}{2}\rangle = |\tfrac{1}{2}\;\tfrac{1}{2}\rangle \tag{4.123}$$

$$KI\,|\tfrac{3}{2}\;\tfrac{1}{2}\rangle = |\tfrac{3}{2}\;\tfrac{\bar{1}}{2}\rangle \tag{4.124}$$

$$KI\,|\tfrac{3}{2}\;\tfrac{\bar{3}}{2}\rangle = |\tfrac{3}{2}\;\tfrac{3}{2}\rangle\,. \tag{4.125}$$

As mentioned above, the eigenfunctions of the present symmetric quantum well belong to the two irreps ${}^1E_{1/2}$ and ${}^2E_{1/2}$ of $\mathbf{C}_s$, the corresponding little group of $\boldsymbol{k}$. With respect to this group, the basis function $|\tfrac{1}{2}\;\tfrac{\bar{1}}{2}\rangle$, $|\tfrac{3}{2}\;\tfrac{1}{2}\rangle$ and $|\tfrac{3}{2}\;\tfrac{\bar{3}}{2}\rangle$ belong to ${}^1E_{1/2}$ whereas $|\tfrac{1}{2}\;\tfrac{1}{2}\rangle$, $|\tfrac{3}{2}\;\tfrac{3}{2}\rangle$ and $|\tfrac{3}{2}\;\tfrac{\bar{1}}{2}\rangle$ belong to ${}^2E_{1/2}$. On the other hand, any envelope function $f(z)$ can be written as

$$f(z) = f_+(z) + f_-(z) \tag{4.126}$$

where $f_+(z)$ and $f_-(z)$ are gerade and ungerade under the in-plane reflection, and therefore belong to the irreps A' and A'' of $\mathbf{C}_s$ respectively. The representation products (4.96) thus imply that any eigenfunction ${}^1\psi$ or ${}^2\psi$ belonging to ${}^1E_{1/2}$ or ${}^2E_{1/2}$ respectively can be written as

$$\begin{aligned} {}^1\psi = &+ {}^1f_-^{(\frac{1}{2}\,\frac{1}{2})}|\tfrac{1}{2}\;\tfrac{1}{2}\rangle + {}^1f_-^{(\frac{3}{2}\,\frac{3}{2})}|\tfrac{3}{2}\;\tfrac{3}{2}\rangle + {}^1f_-^{(\frac{3}{2}\,\frac{\bar{1}}{2})}|\tfrac{3}{2}\;\tfrac{\bar{1}}{2}\rangle \\ &+ {}^1f_+^{(\frac{1}{2}\,\frac{\bar{1}}{2})}|\tfrac{1}{2}\;\tfrac{\bar{1}}{2}\rangle + {}^1f_+^{(\frac{3}{2}\,\frac{1}{2})}|\tfrac{3}{2}\;\tfrac{1}{2}\rangle + {}^1f_+^{(\frac{3}{2}\,\frac{\bar{3}}{2})}|\tfrac{3}{2}\;\tfrac{\bar{3}}{2}\rangle \end{aligned} \tag{4.127}$$

or

$$\begin{aligned} {}^2\psi = &+ {}^2f_+^{(\frac{1}{2}\,\frac{1}{2})}|\tfrac{1}{2}\;\tfrac{1}{2}\rangle + {}^2f_+^{(\frac{3}{2}\,\frac{3}{2})}|\tfrac{3}{2}\;\tfrac{3}{2}\rangle + {}^2f_+^{(\frac{3}{2}\,\frac{\bar{1}}{2})}|\tfrac{3}{2}\;\tfrac{\bar{1}}{2}\rangle \\ &+ {}^2f_-^{(\frac{1}{2}\,\frac{\bar{1}}{2})}|\tfrac{1}{2}\;\tfrac{\bar{1}}{2}\rangle + {}^2f_-^{(\frac{3}{2}\,\frac{1}{2})}|\tfrac{3}{2}\;\tfrac{1}{2}\rangle + {}^2f_-^{(\frac{3}{2}\,\frac{\bar{3}}{2})}|\tfrac{3}{2}\;\tfrac{\bar{3}}{2}\rangle \end{aligned} \tag{4.128}$$

where the envelope functions labeled by the subscript "+" and "−" are respectively gerade and ungerade. If ${}^1\psi$ and ${}^2\psi$ represent the two degenerate states with same energy and same wavevector, they are related by ${}^2\psi = KI\,{}^1\psi$ modulo an arbitrary phase factor. It follows from (4.123)–(4.125) that their envelope functions satisfy

$${}^2f_\pm^{(j\;m)} = \left[{}^1f_\pm^{(j\;\bar{m})}\right]^*. \tag{4.129}$$

In the specific case described in section 4.4.3, where the coupling between the conduction bands and the valence bands is neglected, the envelope functions related to the bases (4.105) or (4.106) are respectively zero for the valence subbands or zero for the conduction subbands. Furthermore, the two degenerate conduction bands are independent, because the effective mass tensor (4.107) is band-diagonal. The

Symbol	Parameter	$Al_xGa_{1-x}As$	Unit
m_c	Effective mass of the conduction band	$0.0665 + 0.0835x$	$[m_0]$
γ_1	Luttinger parameter	$6.790 - 3.000x$	[–]
γ_2	Luttinger parameter	$1.924 - 0.694x$	[–]
γ_3	Luttinger parameter	$2.681 - 1.286x$	[–]
E_P	Kane parameter	28.8	[eV]
E_g	Energy gap	$1.423 + 1.247x$	[eV]
$\Delta E_c/\Delta E_v$	Band offsets	68/32	[–]

Table 4.1: Bulk band structure parameters [127] of $Al_xGa_{1-x}As$ used in this study. The energy gap is shifted to the room temperature value.

wave functions describing the states of the valence subbands can thus be written as

$$ {}^1\psi_v = {}^1f_-^{(\frac{3}{2}\ \frac{3}{2})}|\tfrac{3}{2}\ \tfrac{3}{2}\rangle + {}^1f_+^{(\frac{3}{2}\ \frac{1}{2})}|\tfrac{3}{2}\ \tfrac{1}{2}\rangle + {}^1f_-^{(\frac{3}{2}\ \frac{\bar{1}}{2})}|\tfrac{3}{2}\ \tfrac{\bar{1}}{2}\rangle + {}^1f_+^{(\frac{3}{2}\ \frac{\bar{3}}{2})}|\tfrac{3}{2}\ \tfrac{\bar{3}}{2}\rangle \tag{4.130} $$

$$ {}^2\psi_v = {}^2f_+^{(\frac{3}{2}\ \frac{3}{2})}|\tfrac{3}{2}\ \tfrac{3}{2}\rangle + {}^2f_-^{(\frac{3}{2}\ \frac{1}{2})}|\tfrac{3}{2}\ \tfrac{1}{2}\rangle + {}^2f_+^{(\frac{3}{2}\ \frac{\bar{1}}{2})}|\tfrac{3}{2}\ \tfrac{\bar{1}}{2}\rangle + {}^2f_-^{(\frac{3}{2}\ \frac{\bar{3}}{2})}|\tfrac{3}{2}\ \tfrac{\bar{3}}{2}\rangle\,. \tag{4.131} $$

Those corresponding to the conduction subbands are given by either

$$ {}^1\psi_c = {}^1f_-^{(\frac{1}{2}\ \frac{1}{2})}|\tfrac{1}{2}\ \tfrac{1}{2}\rangle \tag{4.132} $$

$$ {}^2\psi_c = {}^2f_-^{(\frac{1}{2}\ \frac{\bar{1}}{2})}|\tfrac{1}{2}\ \tfrac{\bar{1}}{2}\rangle \tag{4.133} $$

or

$$ {}^1\psi_c = {}^1f_+^{(\frac{1}{2}\ \frac{\bar{1}}{2})}|\tfrac{1}{2}\ \tfrac{\bar{1}}{2}\rangle \tag{4.134} $$

$$ {}^2\psi_c = {}^2f_+^{(\frac{1}{2}\ \frac{1}{2})}|\tfrac{1}{2}\ \tfrac{1}{2}\rangle\,, \tag{4.135} $$

depending on the state.

4.4.4 Specific band structure

In this section, we give the band structure of a 70 Å thick GaAs/$Al_{0.4}Ga_{0.6}As$ symmetric quantum well with growth direction along [001], calculated with the bulk parameters in Table 4.1 [127].

The energy bands of the quantum well are shown in Figure 4.5. All bands are doubly degenerate[6] and related by the time reversal times spatial inversion operation

---

[6] belonging respectively to the irreps ${}^1E_{1/2}$ and ${}^2E_{1/2}$ of the point group $\mathbf{C}_s$

(KI). The Figures 4.6–4.13 display the corresponding in-plane momentum matrix elements (4.36) for the lowest conduction band c_1 and the three highest valence bands v_1, v_2 and v_3. We show only the matrix elements between bands belonging to ${}^2E_{1/2}$. The elements between ${}^1E_{1/2}$-bands are related to the former by KI and thus given by complex conjugation (see (4.92) and (4.94)). According to (4.97), the in-plane momentum elements involving both ${}^1E_{1/2}$ and ${}^2E_{1/2}$ states are all zero. The phase factors of the eigenfunctions are chosen in order to fulfill (4.129). These eigenenergies and momentum matrix elements will be used in chapter 5.

4.5 Conclusion

This chapter was devoted to the band structure of a typical quantum well. First, we detailed Burt's $\boldsymbol{k} \cdot \boldsymbol{p}$ envelope function method yielding an effective mass equation for the heterostructure. Second, we outlined the finite element method used to numerically solve this eigenvalue problem. Finally, we explicitly calculated the band structure of a symmetric AlGaAs/GaAs quantum well, and discussed general symmetry properties of the corresponding eigenstates. The computed eigenenergies and momentum matrix elements are required in chapter 5.

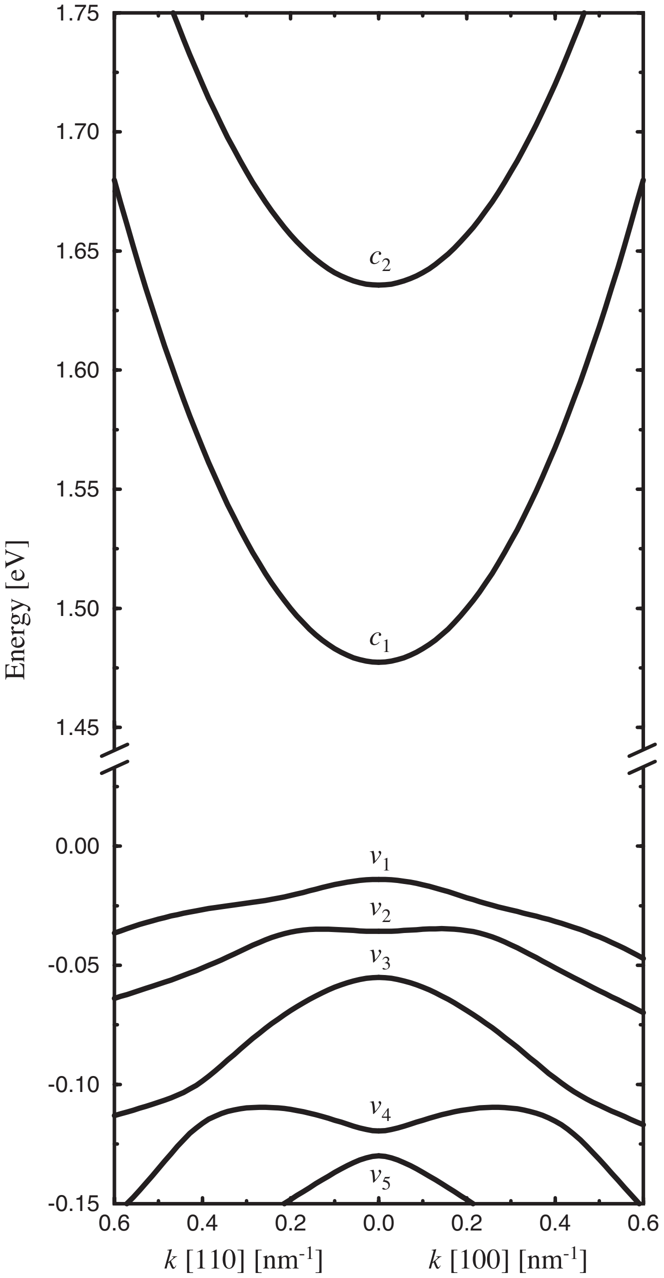

Figure 4.5: Band structure of a 70 Å thick GaAs/$Al_{0.4}Ga_{0.6}As$ quantum well calculated with the bulk parameters in Table 4.1.

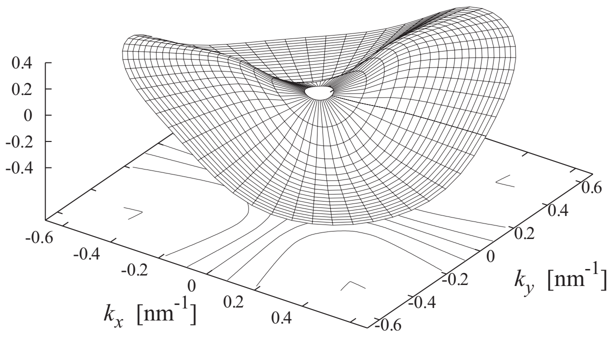

(a) $\mathrm{Re}(\pi^x_{v_1c_1})$

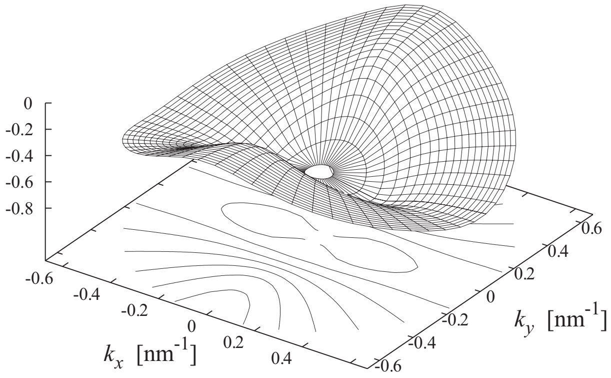

(b) $\mathrm{Im}(\pi^x_{v_1c_1})$

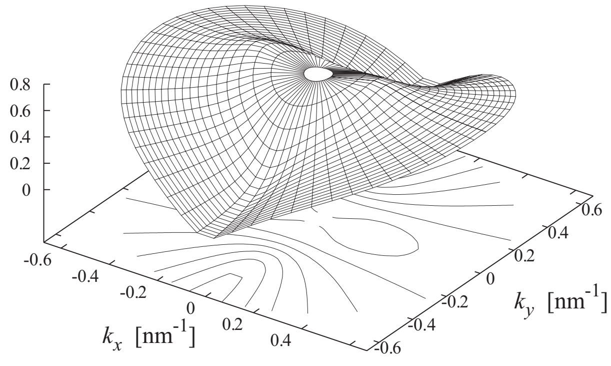

(c) $|\pi^x_{v_1c_1}|$

Figure 4.6: Inter-band momentum matrix element $\pi^x_{v_1c_1}$ between the ${}^2E_{1/2}$ valence band v_1 and the ${}^2E_{1/2}$ conduction band c_1 in units of $\sqrt{m_0E_P/2}$.

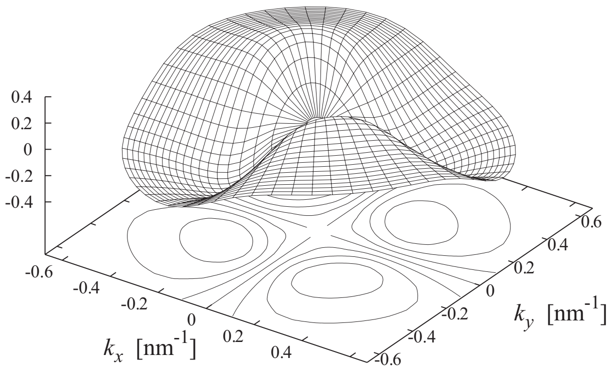

(a) $\mathrm{Re}(\pi^x_{v_2c_1})$

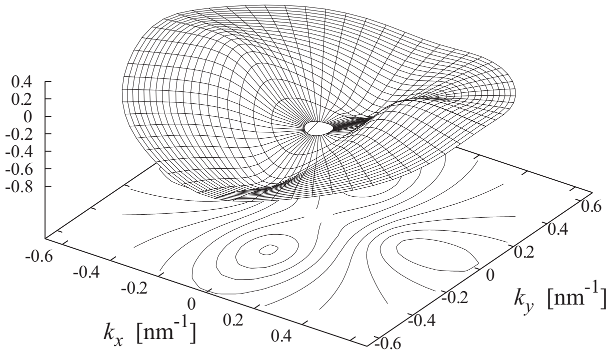

(b) $\mathrm{Im}(\pi^x_{v_2c_1})$

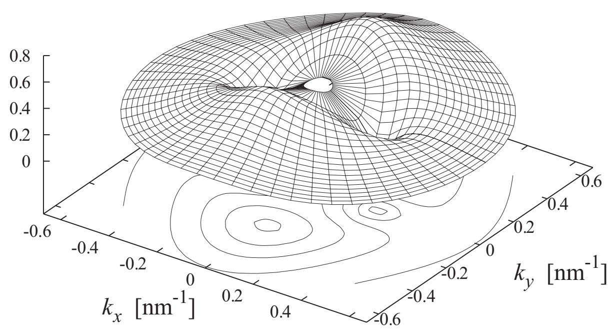

(c) $|\pi^x_{v_2c_1}|$

Figure 4.7: Inter-band momentum matrix element $\pi^x_{v_2c_1}$ between the ${}^2E_{1/2}$ valence band v_2 and the ${}^2E_{1/2}$ conduction band c_1 in units of $\sqrt{m_0E_P/2}$.

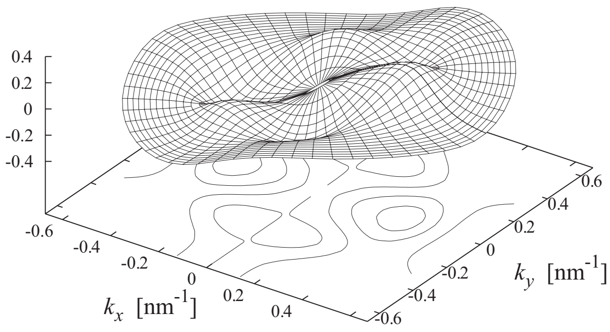

(a) $\mathrm{Re}(\pi^x_{v_3c_1})$

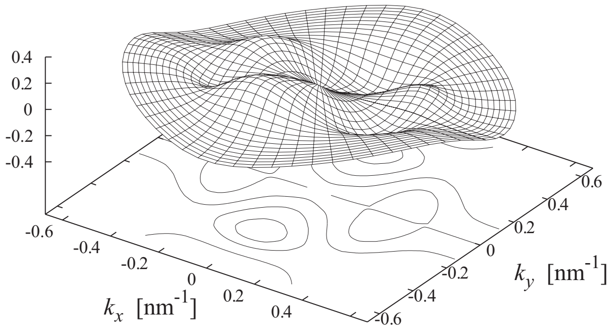

(b) $\mathrm{Im}(\pi^x_{v_3c_1})$

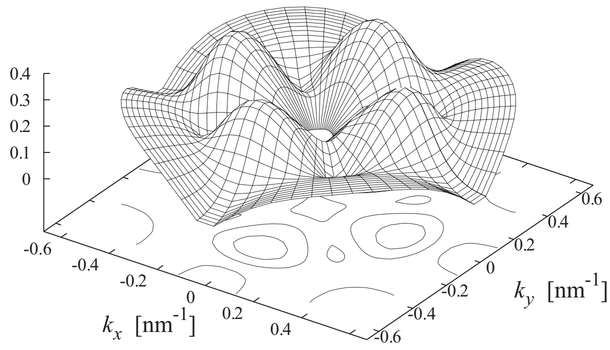

(c) $|\pi^x_{v_3c_1}|$

Figure 4.8: Inter-band momentum matrix element $\pi^x_{v_3c_1}$ between the ${}^2E_{1/2}$ valence band v_3 and the ${}^2E_{1/2}$ conduction band c_1 in units of $\sqrt{m_0E_P/2}$.

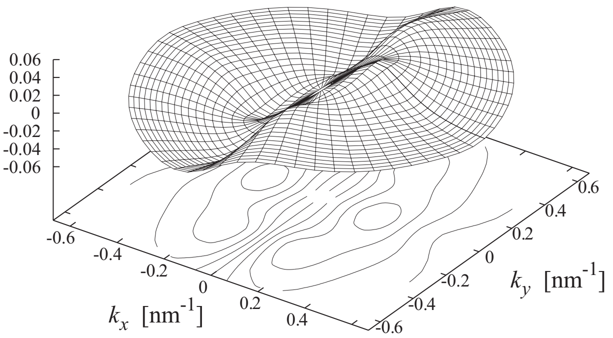

(a) $\mathrm{Re}(\pi^x_{v_2 v_1})$

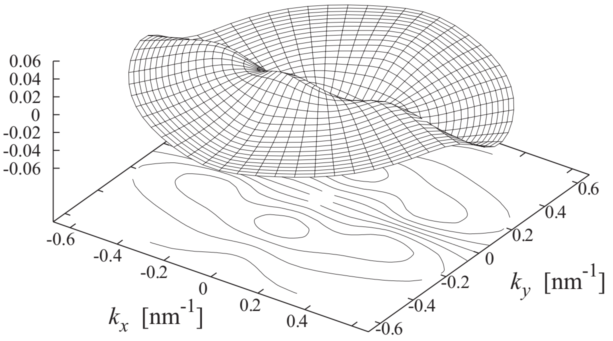

(b) $\mathrm{Im}(\pi^x_{v_2 v_1})$

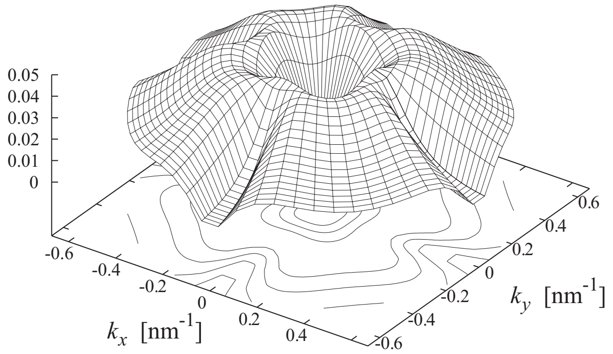

(c) $|\pi^x_{v_2 v_1}|$

Figure 4.9: Intra-valence-band momentum matrix element $\pi^x_{v_2 v_1}$ between the ${}^2E_{1/2}$ valence band v_2 and the ${}^2E_{1/2}$ valence band v_1 in units of $\sqrt{m_0 E_P/2}$.

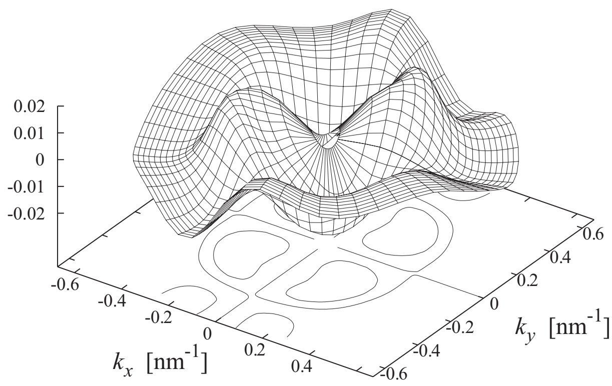

(a) $\mathrm{Re}(\pi^x_{v_3 v_1})$

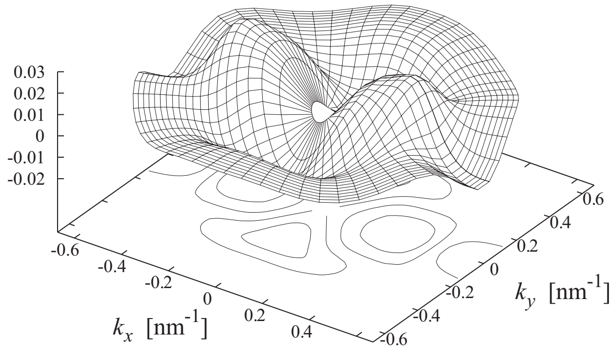

(b) $\mathrm{Im}(\pi^x_{v_3 v_1})$

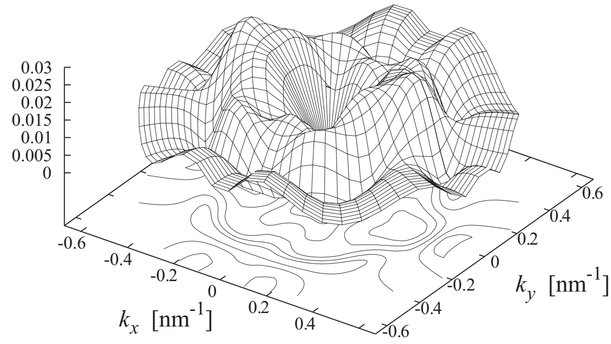

(c) $|\pi^x_{v_3 v_1}|$

Figure 4.10: Intra-valence-band momentum matrix element $\pi^x_{v_3 v_1}$ between the ${}^2E_{1/2}$ valence band v_3 and the ${}^2E_{1/2}$ valence band v_1 in units of $\sqrt{m_0 E_P/2}$.

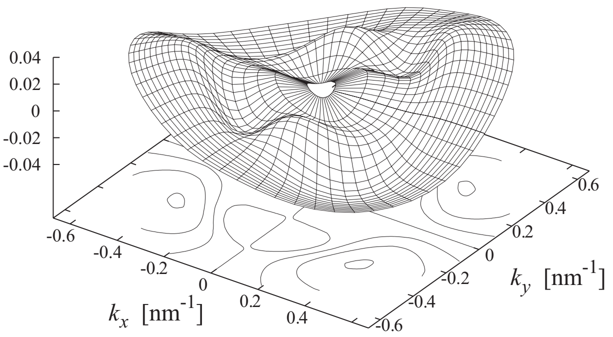

(a) $\mathrm{Re}(\pi^x_{v_3 v_2})$

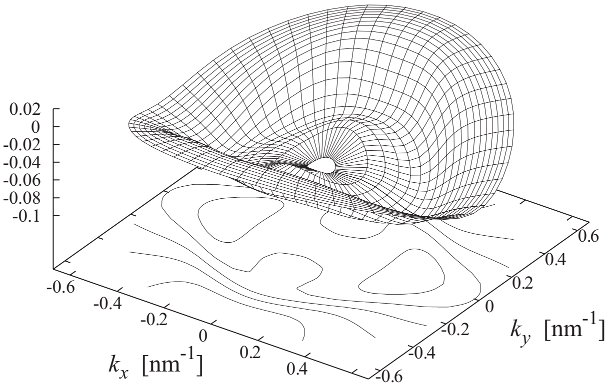

(b) $\mathrm{Im}(\pi^x_{v_3 v_2})$

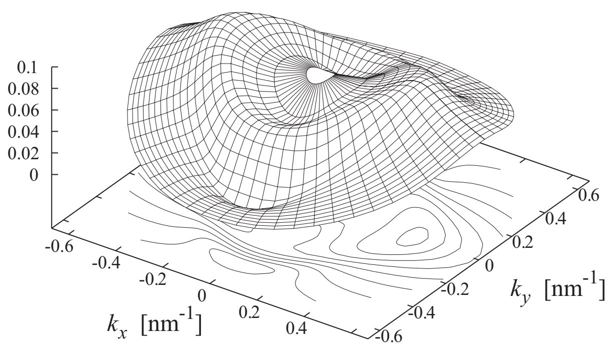

(c) $|\pi^x_{v_3 v_2}|$

Figure 4.11: Intra-valence-band momentum matrix element $\pi^x_{v_3 v_2}$ between the ${}^2E_{1/2}$ valence band v_3 and the ${}^2E_{1/2}$ valence band v_2 in units of $\sqrt{m_0 E_P/2}$.

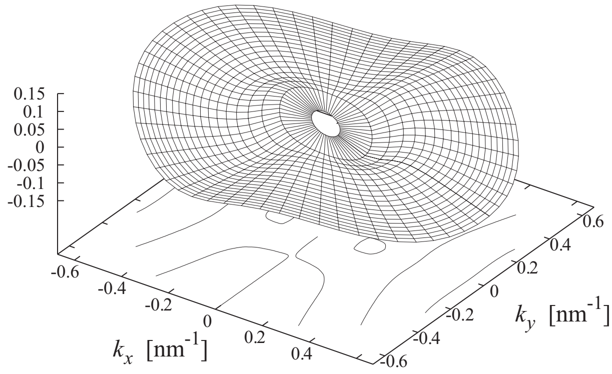

(a) $\pi^x_{v_1 v_1}$

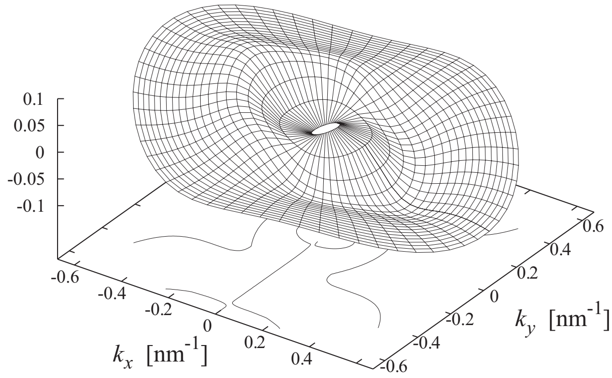

(b) $\pi^x_{v_2 v_2}$

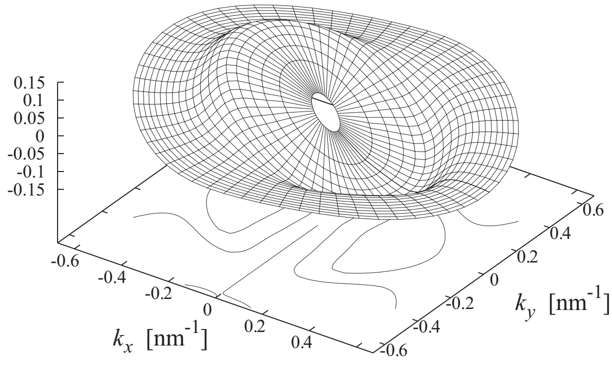

(c) $\pi^x_{v_3 v_3}$

Figure 4.12: Band-diagonal intra-valence-band momentum matrix elements π^x_{vv} of the ${}^2E_{1/2}$ valence bands v_1, v_2 and v_3 in units of $\sqrt{m_0 E_P/2}$.

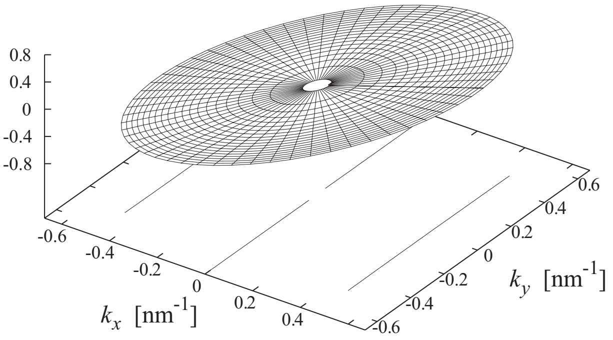

(a) $\pi^x_{c_1 c_1}$

Figure 4.13: Band-diagonal intra-conduction-band momentum matrix element $\pi^x_{c_1 c_1}$ of the ${}^2E_{1/2}$ conduction band c_1 in units of $\sqrt{m_0 E_P/2}$.

5 Optical injection of charge and spin current in quantum wells

5.1 Introduction

In the following, we illustrate the general theory developed in chapter 3, with a first application involving simultaneous one- and two-photon transitions induced by ultra-short laser pulses, namely optical injection of current by quantum interference. In recent years, this process has attracted considerable interest in semiconductors.

It has been demonstrated that quantum interference between one- and two-photon absorption leads to measurable directional photocurrent in bulk for inter-band excitation [16, 128] and in quantum wells (QWs) in the case of conduction band to continuum transitions [129]. Two coherent electromagnetic fields of frequency ω and 2ω, with ω below and 2ω above the band gap, couple the same initial and final states and induce a polar asymmetry in the momentum space distribution of the carriers, which can be controlled by the relative phase of the beams. One can also show that this directional photocurrent is a manifestation of the third-order nonlinearity $\chi^{(3)}(0; -2\omega, \omega, \omega)$ [130]. Such optical injection of current by femtosecond pulses has for instance been used for terahertz wave generation [131], or proposed for demonstration of current echoes [132]. With the same interference scheme, it is also possible to generate directional spin current, as shown by Bhat and Sipe [133], which can be of great interest in future spintronic applications. Optically injected charge current that, according to the theory, should be spin-polarized, was measured in bulk-GaAs [134]. Recently, pure spin current (*without* an accompanying charge current) was injected in bulk [135] and quantum wells [136]. Current relaxation by scattering with LO phonons was also included in the theoretical description by a Green's functions formalism [97]. Finally, we note that the research is now extended to other materials than GaAs, like GaN [137] and ZnSe [135].

To the best of our knowledge, all work published in this field concerns bulk semiconductors, excepted the early measurements by Dupont *et al.* [129] who considered conduction band to continuum transitions, and the very recent measurement of pure spin current by Stevens *et al.* [136]. Both of them concerned AlGaAs/GaAs multiple quantum wells. In this chapter, we study the dynamics of charge and spin current injection by quantum interference between one- and two-photon inter-band transitions, essentially for the case of quantum wells. The investigation of these processes in heterostructures is of great interest as the latter introduce new degrees of freedom and tunability. In order to study the temporal behavior, we use the specific multi-band semiconductor Bloch equations derived in chapter 3, which go beyond Fermi's golden rule used by most authors. Our model treats the whole dynamic of the lowest conduction band and the three highest valence bands, quasi-resonantly coupled by two slowly-varying monochromatic electromagnetic fields. The contribution of the far off-resonant intermediate states to the second order processes (Stark shifts and two-photon transitions) is taken into account within a perturbative approach and the carrier thermalization is included by phenomenological relaxation times. The calculation of the two-photon transitions requires the inter-subband momentum matrix elements, especially the band-diagonal part [74]. They are obtained with a $\boldsymbol{k} \cdot \boldsymbol{p}$ envelope function method [47] accounting for the non-parabolic band structure (chapter 4). We also calculate the far field THz emission taking into account the radiation from the charge current related to the coherence between the subbands, and show that they may contribute significantly to the emission. Finally, the influence of the AC Stark shifts and inter-valence-band two-photon transitions on the charge current is evaluated and discussed.

The chapter is organized as follows. In section 5.2, we start with a simple introduction to the core phenomenon of current generation by quantum interference between single and two-photon transitions. Then, in section 5.3, we summarize the equations used throughout this chapter. Section 5.4 is devoted to the numerical study and the discussion of the results obtained with the multi-band semiconductor Bloch equations including all the relevant terms. Finally, the conclusions are drawn in section 5.5.

5.2 Quantum interferences between one- and two photon transitions

The interferences between one- and two-photon transitions can lead to different transition probabilities for states with opposite wavevectors $\boldsymbol{k}$ and -$\boldsymbol{k}$ (Figure 5.1). This generates an asymmetric carrier distribution in reciprocal space, resulting in a net charge or spin current. In this section, we give a short insight into the physics behind this process in the case of a centro-symmetric crystal, by using simple group theoretical arguments. One has to emphasize that the spatial inversion symmetry is not mandatory for the subject discussed here, but it is convenient. Together with time-reversal symmetry it implies that all energy bands are doubly degenerate.

The dipole interaction $\boldsymbol{A} \cdot \boldsymbol{\Pi}$ between the carriers and electromagnetic fields is expressed in the velocity gauge where

$$\boldsymbol{A}(t) = \boldsymbol{A}_1 \cos(2\omega t + \phi_1) + \boldsymbol{A}_2 \cos(\omega t + \phi_2) \tag{5.1}$$

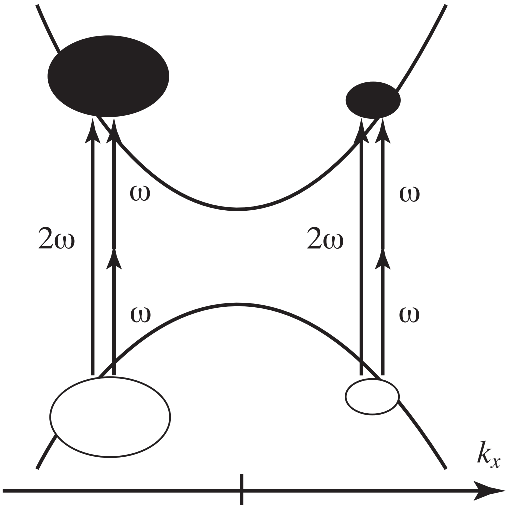

Figure 5.1: Asymmetric inter-band excitation due to the interference between one- and two-photon transition.

is the vector potential describing the two monochromatic waves, and

$$\mathbf{\Pi} = \frac{-e}{m_0}\boldsymbol{\pi} = \frac{-e}{m_0}\big[\boldsymbol{p} + \frac{\hbar}{4m_0c^2}\boldsymbol{\sigma}\wedge\nabla V\big] \tag{5.2}$$

is proportional to the momentum operator $\boldsymbol{\pi}$.

For each pair of degenerate bands $(n,\bar{n})$, it is sufficient for our purpose to consider the four eigenstates of the Hamiltonian with same energy: $|n,+\boldsymbol{k}\rangle$, $|\bar{n},+\boldsymbol{k}\rangle$, $|n,-\boldsymbol{k}\rangle$ and $|\bar{n},-\boldsymbol{k}\rangle$ $(\boldsymbol{k}\neq 0)$. They can be chosen so that the momentum matrix elements display the symmetry properties

$$\mathbf{\Pi}_{mn,+\boldsymbol{k}} = -\mathbf{\Pi}_{mn,-\boldsymbol{k}} = +\mathbf{\Pi}_{\bar{n}\bar{m},+\boldsymbol{k}} = -\mathbf{\Pi}_{\bar{n}\bar{m},-\boldsymbol{k}} \tag{5.3}$$
$$\mathbf{\Pi}_{m\bar{n},+\boldsymbol{k}} = -\mathbf{\Pi}_{m\bar{n},-\boldsymbol{k}} = -\mathbf{\Pi}_{n\bar{m},+\boldsymbol{k}} = +\mathbf{\Pi}_{n\bar{m},-\boldsymbol{k}} \tag{5.4}$$

between two states with same parity, and

$$\mathbf{\Pi}_{mn,+\boldsymbol{k}} = +\mathbf{\Pi}_{mn,-\boldsymbol{k}} = +\mathbf{\Pi}_{\bar{n}\bar{m},+\boldsymbol{k}} = +\mathbf{\Pi}_{\bar{n}\bar{m},-\boldsymbol{k}} \tag{5.5}$$
$$\mathbf{\Pi}_{m\bar{n},+\boldsymbol{k}} = +\mathbf{\Pi}_{m\bar{n},-\boldsymbol{k}} = -\mathbf{\Pi}_{n\bar{m},+\boldsymbol{k}} = -\mathbf{\Pi}_{n\bar{m},-\boldsymbol{k}} \tag{5.6}$$

between two states with opposite parity (see § 4.4.1). Furthermore, for a quantum well oriented along a principal axis (*e.g.* [001]), the in-plane reflection symmetry ensures that $\boldsymbol{\epsilon}_{\perp}\cdot\mathbf{\Pi}_{mn,k} = 0$ and $\boldsymbol{\epsilon}_{\shortparallel}\cdot\mathbf{\Pi}_{m\bar{n},k} = 0$, where $\boldsymbol{\epsilon}_{\perp}$ and $\boldsymbol{\epsilon}_{\shortparallel}$ are respectively perpendicular and parallel to the quantum well. For an optical field polarized in the plane of the quantum well, the $n \to \bar{m}$ transitions are therefore forbidden, and we can restrict ourselves to the cases $n \to m$ and $\bar{n} \to \bar{m}$.

We now consider resonant one- and two-photon transitions from two degenerate valence bands v and $\bar{v}$ to two degenerate conduction bands c and $\bar{c}$. The $v \to c$ transition amplitudes at wavevector $\boldsymbol{k}$ are given by $a_{1,\boldsymbol{k}} = b_{1,\boldsymbol{k}}\, e^{-i\phi_1}$ and $a_{2,\boldsymbol{k}} = b_{2,\boldsymbol{k}}\, e^{-i2\phi_2}$ with

$$b_{1,\boldsymbol{k}} = (2\hbar)^{-1} \sum_{\alpha} A_1^{\alpha} \Pi^{\alpha}_{cv,\boldsymbol{k}} \tag{5.7}$$

$$b_{2,\boldsymbol{k}} = (2\hbar)^{-2} \sum_{\alpha\beta} A_2^{\alpha} A_2^{\beta} \sum_{n} \frac{\Pi^{\alpha}_{cn,\boldsymbol{k}} \Pi^{\beta}_{nv,\boldsymbol{k}}}{\Omega_{cn,\boldsymbol{k}} - \omega}\,. \tag{5.8}$$

The sum $\sum_n$ is taken over all energy bands, and $\Omega_{cn,\boldsymbol{k}}$ is the inter-band frequency. The total transition probability is given by

$$|a_{1,\boldsymbol{k}} + a_{2,\boldsymbol{k}}|^2 = |a_{1,\boldsymbol{k}}|^2 + |a_{2,\boldsymbol{k}}|^2 + 2\,\mathrm{Re}(a_{1,\boldsymbol{k}}{}^{*} a_{2,\boldsymbol{k}})\,. \tag{5.9}$$

The first two terms on the right-hand side are phase-independent and can not generate asymmetric carrier distributions with respect to the inversion. Thus, the current is only injected by the interference term

$$I_{\boldsymbol{k}} = 2\,\mathrm{Re}(a_{1,\boldsymbol{k}}{}^{*} a_{2,\boldsymbol{k}})\,. \tag{5.10}$$

The amplitudes $\bar{a}_{j,\boldsymbol{k}}$ (and $\bar{b}_{j,\boldsymbol{k}}$) for the $\bar{v} \to \bar{c}$ transitions are obtained by replacing c by $\bar{c}$ and v by $\bar{v}$ in the above expressions. Let us define

$$\eta_{\boldsymbol{k}} = 2 b^{*}_{1,\boldsymbol{k}} b_{2,\boldsymbol{k}} \tag{5.11}$$

$$\bar{\eta}_{\boldsymbol{k}} = 2 \bar{b}^{*}_{1,\boldsymbol{k}} \bar{b}_{2,\boldsymbol{k}} \tag{5.12}$$

with the properties $\eta_{\boldsymbol{k}} = -\eta_{-\boldsymbol{k}}$ and $\eta_{\boldsymbol{k}} = \bar{\eta}^{*}_{\boldsymbol{k}}$. The interference terms $I_{\boldsymbol{k}}$ and $\bar{I}_{\boldsymbol{k}}$ for the $v \to c$ and $\bar{v} \to \bar{c}$ transitions respectively become

$$I_{\boldsymbol{k}} = \mathrm{Re}(\eta_{\boldsymbol{k}})\, \cos(2\phi_2 - \phi_1) + \mathrm{Im}(\eta_{\boldsymbol{k}})\, \sin(2\phi_2 - \phi_1) \tag{5.13}$$

$$\bar{I}_{\boldsymbol{k}} = \mathrm{Re}(\eta_{\boldsymbol{k}})\, \cos(2\phi_2 - \phi_1) - \mathrm{Im}(\eta_{\boldsymbol{k}})\, \sin(2\phi_2 - \phi_1)\,. \tag{5.14}$$

The velocity of an injected electron $|n, \boldsymbol{k}\rangle$ is given by $-\boldsymbol{\Pi}_{nn,\boldsymbol{k}}/e$, and the expectation value of its spin perpendicular to the quantum well is

$$\frac{\hbar}{2}\sigma_{nn,\boldsymbol{k}} = \frac{\hbar}{2}\langle n, \boldsymbol{k}|\sigma_z|n, \boldsymbol{k}\rangle\,, \tag{5.15}$$

with the symmetry properties

$$\sigma_{nn,\boldsymbol{k}} = \sigma_{nn,-\boldsymbol{k}} = -\sigma_{\bar{n}\bar{n},\boldsymbol{k}} = -\sigma_{\bar{n}\bar{n},-\boldsymbol{k}} \,. \tag{5.16}$$

The contribution of the state $|n, \boldsymbol{k}\rangle$ to the charge and spin current is given by $\boldsymbol{j}_{n,\boldsymbol{k}} = \boldsymbol{\Pi}_{nn,\boldsymbol{k}} I_{\boldsymbol{k}}$ and $\boldsymbol{s}_{n,\boldsymbol{k}} = -\sigma_{nn,\boldsymbol{k}} \boldsymbol{\Pi}_{nn,\boldsymbol{k}} I_{\boldsymbol{k}}$ respectively. The spin has been multiplied by $2e/\hbar$ to be expressed in the same units than the charge. The symmetry properties (5.3) involve $I_{\boldsymbol{k}} = -I_{-\boldsymbol{k}}$ and $\bar{I}_{\boldsymbol{k}} = -\bar{I}_{-\boldsymbol{k}}$. Thus, the net charge current j and spin current s obtained by summing over the four states in the same doubly degenerate band are given by

$$j \propto 4\,\mathrm{Re}(\eta_{\boldsymbol{k}})\,\cos(2\phi_2 - \phi_1) \tag{5.17}$$

$$s \propto 4\,\mathrm{Im}(\eta_{\boldsymbol{k}})\,\sin(2\phi_2 - \phi_1)\,. \tag{5.18}$$

Note that these expressions are valid for single independent (degenerate) bands. In case of multiple subbands, the currents must be generalized to account for the subband-mixing (see § 5.3.3).

The total injected current is obtained by adding the contributions of all states. Yet each set of four resonantly excited states related by time reversal and spatial inversion will contribute in the same way to the current. Thus, the equations (5.17) and (5.18) show that the charge and spin currents are related respectively to the real and imaginary part of the same tensor η describing the interference between one- and two-photon transitions. Both current amplitudes can be controlled by the relative phase between the two electromagnetic waves, but not through the same dependence. Therefore, two linearly polarized beams can be used to inject either pure charge or pure spin current by tuning the phase difference to 0 or $\pi/2$ respectively. This is illustrated by Figure 5.2 and Figure 5.3 showing the carrier distribution in the lowest (doubly degenerate) conduction band of the symmetric GaAs/AlGaAs quantum well described in section 4.4.4 (Figure 5.4). In both bands, the electron distributions generated by only one beam (one- *or* two-photon transitions) are symmetric with respect to the spatial inversion. This symmetry can be suppressed if the two electromagnetic fields interfere. For zero phase difference (Figure 5.2), the two asymmetric distributions are equal and lead to a (spin-*un*polarized) charge current. When the phase difference corresponds to $\pi/2$ (Figure 5.3), the two distributions are no more identical but related to each other by spatial inversion, which results in a pure spin current.

In this chapter we focus on the photocurrent generated by femtosecond pulses in quantum wells through inter-band transitions. In such structures, the inter-valence-band frequencies are comparable to the spectral width of the pulses, and one can no longer use a simple two-band model. As we shall see in the next sections, the inter-subband coherence plays a significant role in this study, especially concerning the THz emission. Furthermore, to obtain the proper polarization dependence, one has to take into account the valence-band mixing.

In the following, we use adequate multi-band semiconductor Bloch equations (§ 3.7) for the description of the optical current injection. They are applied to the specific case of a quantum well with realistic band structure (§ 4.4.4), as well as to bulk GaAs. Yet, the above model based on Fermi's golden rule highlights the underlying physical process, especially the phase dependence, which is somewhat hidden in the Bloch equations.

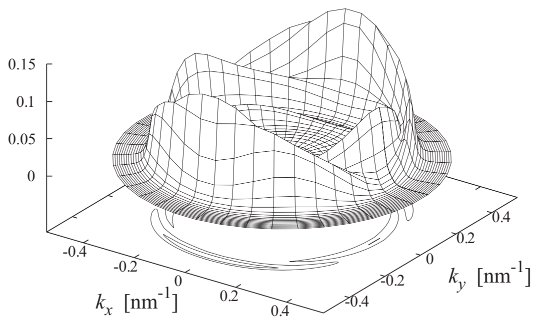

(a) One-photon transitions induced by the $\boldsymbol{A}_1$ laser pulse polarized along the x axis.

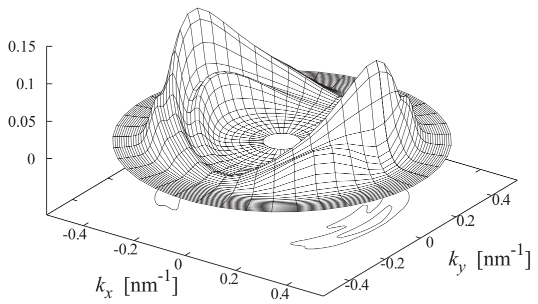

(b) Two-photon transitions induced by the $\boldsymbol{A}_2$ laser pulse polarized along the x axis.

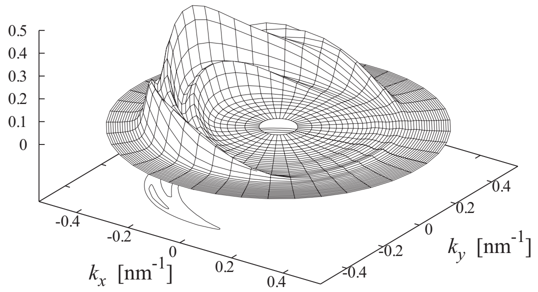

(c) One and two-photon transitions induced by the $\boldsymbol{A}_1$ and $\boldsymbol{A}_2$ laser pulses co-polarized along the x axis, with a phase difference $\phi_1 - 2\phi_2 = 0$.

Figure 5.2: Carrier distributions in the ${}^1E_{1/2}$ conduction band generated by (a) one-photon transitions (b) two-photon transitions (c) one- and two-photon transitions. The carrier distributions in the conjugate ${}^2E_{1/2}$ conduction band are identical.

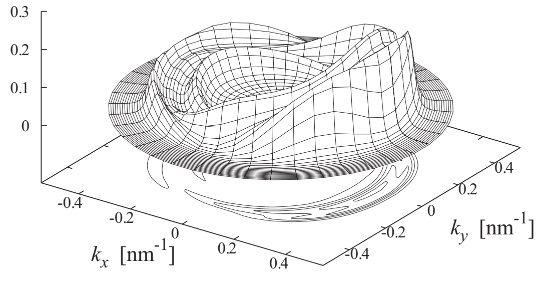

(a) $^1E_{1/2}$

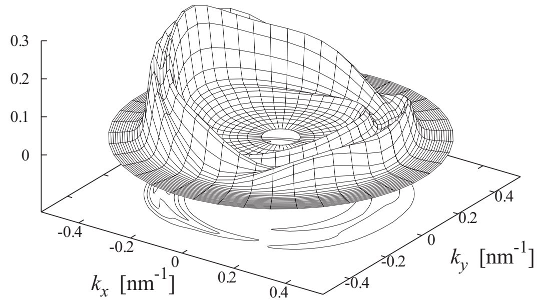

(b) $^2E_{1/2}$

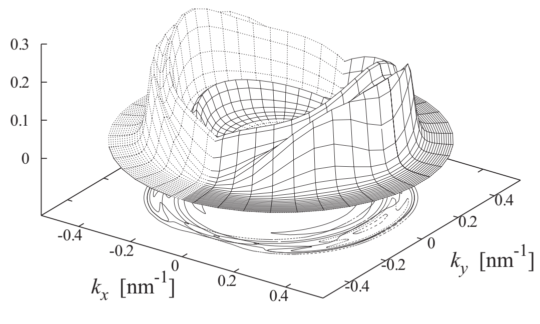

(c) $^1E_{1/2}$ (full line) and $^2E_{1/2}$ (dashed line)

Figure 5.3: Carrier distributions in the doubly degenerate conduction bands $^1E_{1/2}$ and $^2E_{1/2}$ induced by the $\boldsymbol{A}_1$ and $\boldsymbol{A}_2$ laser pulses (cross-) polarized along the y and x axes respectively, with a phase difference $\phi_1 - 2\phi_2 = \pi/2$.

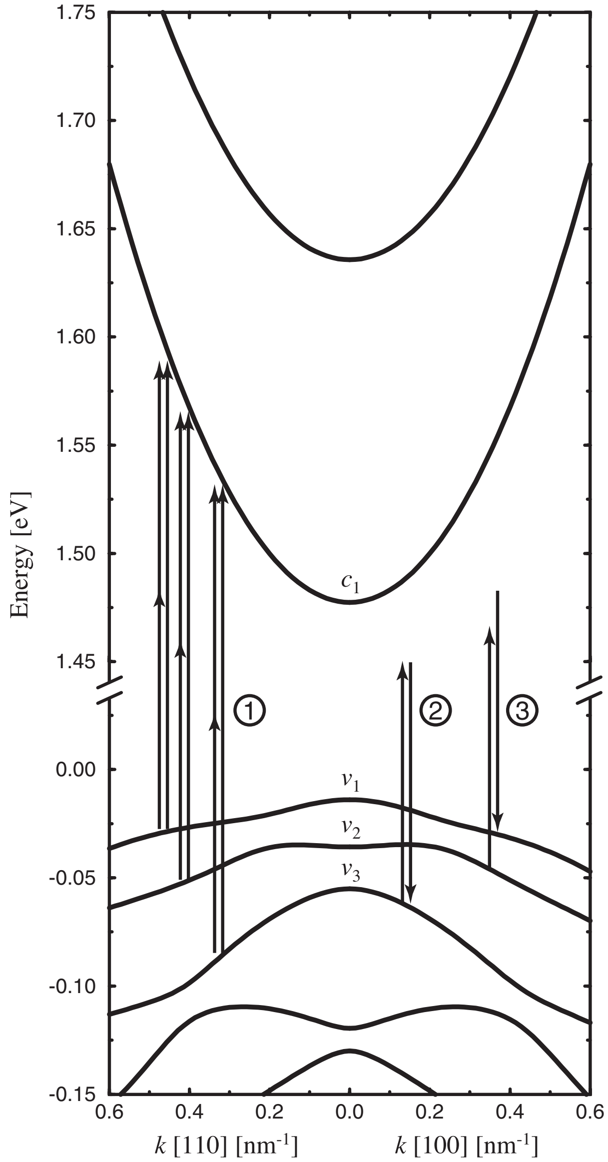

Figure 5.4: Band structure of a 70 Å thick GaAs/$Al_{0.4}Ga_{0.6}As$ quantum well (QW) used in the calculations (band gap: 1.491 eV). The barriers of the QW correspond approximatively to the upper and lower border of the frame. The arrows indicate the optical transitions included in the model: (1) one- and two-photon transition between valence and conduction bands, (2) AC Stark shift, (3) inter-valence band two-photon transitions.

5.3 Model

Before discussing the numerical results, let us briefly summarize the equations derived in chapter 3 and used throughout this chapter.

5.3.1 Optical pulses

The linearly polarized electromagnetic laser pulses are given by

$$\boldsymbol{A}(t) = \boldsymbol{A}_1(t)\cos(\omega_1 t + \phi_1) + \boldsymbol{A}_2(t)\cos(\omega_2 t + \phi_2) \tag{5.19}$$

with the slowly varying envelopes

$$\boldsymbol{A}_j(t) = \begin{pmatrix} A_j^x(t) & A_j^y(t) & A_j^z(t) \end{pmatrix}^T \tag{5.20}$$

$$A_j^\alpha(t) \propto [\cosh(t/T)]^{-1}, \qquad \alpha = x, y, z\,. \tag{5.21}$$

The pulse durations at half maximum of intensity correspond to $1.76T$. The optical frequencies must satisfy $\omega_1 \simeq 2\omega_2 \simeq E_g/\hbar$ where E_g is the energy gap. For the calculations in this chapter, we use $\omega_1 = 2\omega_2$.

5.3.2 Effective multi-band Bloch equations

In the rotating frame, the time evolution of the reduced density matrix

$$\bar{\rho}_{mn}(t) = \rho_{mn}(t)\,\exp\big[i\Omega_{mn}t - i(\boldsymbol{\Pi}_{mm} - \boldsymbol{\Pi}_{nn})\sum_{j=1,2}\frac{\boldsymbol{A}_j(t)}{\hbar\omega_j}\sin(\omega_j t + \phi_j)\big] \tag{5.22}$$

is given by the effective Schrödinger equation

$$\partial_t\bar{\rho} = -i\big[\bar{H}\,,\bar{\rho}\big] \tag{5.23}$$

with

$$\begin{aligned}\bar{H}_{cc'} = &-(2\hbar)^{-2}\sum_j\sum_{\alpha,\beta}A_j^\alpha A_j^\beta\, e^{i\Omega_{cc'}t}\\ &\times\frac{1}{2}\sum_{\sigma=\pm1}\sum_{n\neq c,c'}\Big[\frac{\Pi_{cn}^\alpha\Pi_{nc'}^\beta}{\Omega_{nc}-\sigma\omega_j}+\frac{\Pi_{cn}^\alpha\Pi_{nc'}^\beta}{\Omega_{nc'}-\sigma\omega_j}\Big]\,,\end{aligned} \tag{5.24}$$

$$\begin{aligned}\bar{H}_{vv'} = &-(2\hbar)^{-2}\sum_j\sum_{\alpha,\beta}A_j^\alpha A_j^\beta\, e^{i\Omega_{vv'}t}\\ &\times\frac{1}{2}\sum_{\sigma=\pm1}\sum_{n\neq v,v'}\Big[\frac{\Pi_{vn}^\alpha\Pi_{nv'}^\beta}{\Omega_{nv}-\sigma\omega_j}+\frac{\Pi_{vn}^\alpha\Pi_{nv'}^\beta}{\Omega_{nv'}-\sigma\omega_j}\Big]\,,\end{aligned} \tag{5.25}$$

and

$$
\begin{aligned}
\bar{H}_{cv} = & - (2\hbar)^{-1} \sum_{\alpha} A_1^{\alpha} \Pi_{cv}^{\alpha} \, e^{i(\Omega_{cv}-\omega_1)t - i\phi_1} \\
& - (2\hbar)^{-2} \sum_{\alpha,\beta} A_2^{\alpha} A_2^{\beta} \, e^{i(\Omega_{cv}-2\omega_2)t - i2\phi_2} \\
& \times \Big[\Pi_{cv}^{\alpha} (\Pi_{cc}^{\beta} - \Pi_{vv}^{\beta})/\omega_2 + \frac{1}{2} \sum_{n \neq c,v} \big(\frac{\Pi_{cn}^{\alpha} \Pi_{nv}^{\beta}}{\Omega_{nv} - \omega_2} - \frac{\Pi_{cn}^{\alpha} \Pi_{nv}^{\beta}}{\Omega_{cn} - \omega_2} \big) \Big] \, .
\end{aligned}
\tag{5.26}
$$

For the sake of simplicity, the $\boldsymbol{k}$-vector indices have been omitted but should be added after each couple of band subscripts. The superscripts α and β label the spatial directions x, y and z.

In the above expressions, the sums over n include all far off-resonant bands eliminated from the equation of motion, as well as the bands of the *reduced* density matrix, for which the corresponding denominator $\Omega \pm \omega_j$ is large. By contrast, the quadratic contributions from the transitions with small detuning $\Omega \pm \omega_j$ are automatically contained in the resonant linear interaction of $\bar{H}_{cv'}$.

These effective multi-band Bloch equations take consistently into account all quasi-resonant interaction terms up to the second order in the optical fields. They include the interference between various nonlinear optical phenomena, such as interband one- and two-photon absorption, coherent control of photocurrent, second-harmonic generation, difference-frequency mixing, or the AC Stark shifts. Because the optical frequencies lie in the vicinity of transition frequencies of the medium, these nonlinear processes are strongly enhanced by quasi-resonant real or virtual transitions.

In the following, we consider a symmetric AlGaAs/AlAs quantum well with growth direction along [001]. The small inversion asymmetry of GaAs is neglected. The heterostructure reduces to the centro-symmetric case, for which the second-order susceptibility is zero [21]. Therefore, all dominant optical processes are related to first-order and third-order susceptibilities. The dominant quasi-resonant transitions we are left with are detailed below and sketched in Figure 5.4.

The matrix elements $\bar{H}_{cv}$ describe the one- and two-photon transitions between valence and conduction bands. They also account for the generation of photocurrent. The off-diagonal Hamiltonian matrix elements $\bar{H}_{cc'}$ and $\bar{H}_{vv'}$ describe Raman-like inter-subband two-photon transitions, whereas the diagonal part contains the AC Stark shifts.

The relaxation of the system is described by the phenomenological model discussed in section 3.14. We use a unique characteristic time τ for the thermalization of the carrier distribution and for the decoherence. This corresponds to $\tau_{mn} = \tau$ in (3.130) and $\tau_{\nu\nu} = \tau$ in (3.134).

5.3.3 Polarization current

The differentiation between charge and displacement current is somewhat arbitrary, as the whole polarization current is related to carrier movement. We will distinguish them in the frequency domain. Direct measurements of the electric current, *e.g.* through the voltage associated with charge accumulation [16], are sensitive only to the low frequencies as the higher (optical) frequencies can not be time-resolved and vanish through the time-integration. On the other hand, the high-frequency part of the current affects the optical properties of the medium and can be well described by optical susceptibilities. The low-frequency polarization current describing the injected charge current can be written as

$$\boldsymbol{j} = \frac{1}{S} \sum_{\boldsymbol{k}} \Big[\sum_{cc'} \boldsymbol{\Pi}_{cc',\boldsymbol{k}}\, \rho_{c'c,\boldsymbol{k}} + \sum_{vv'} \boldsymbol{\Pi}_{vv',\boldsymbol{k}}\, \rho_{v'v,\boldsymbol{k}} \Big] . \tag{5.27}$$

In what follows, we distinguish between two contributions. First, the diagonal elements of ρ (the populations) lead to the charge current $\boldsymbol{j}_{\text{pop}} = \sum_n \boldsymbol{j}_n$, where

$$\boldsymbol{j}_n = \frac{1}{S} \sum_{\boldsymbol{k}} \boldsymbol{\Pi}_{nn,\boldsymbol{k}}\, \rho_{nn,\boldsymbol{k}} \tag{5.28}$$

is the current associated to the band n. The sum $\sum_n$ is taken over the conduction bands and valence bands. Second, the off-diagonal terms give rise to a charge current related to the inter-subband coherence, whose low frequency part can be written as

$$\boldsymbol{j}_{\text{coh}} = \frac{1}{S} \sum_{\boldsymbol{k}} \Big[\sum_{c \neq c'} \boldsymbol{\Pi}_{cc',\boldsymbol{k}}\, \rho_{c'c,\boldsymbol{k}} + \sum_{v \neq v'} \boldsymbol{\Pi}_{vv',\boldsymbol{k}}\, \rho_{v'v,\boldsymbol{k}} \Big] . \tag{5.29}$$

The sums $\sum_{c \neq c'}$ and $\sum_{v \neq v'}$ are taken over all pairs of different conduction bands and valence bands respectively. Note that the presence of coherence means that the quantum states of the carriers are not given by the occupation of the bands only.

The theoretical works published up to now concern two-band models and/or focus on the electronic transition probabilities using Fermi's golden rule. Such models do not take into account the inter-subband coherence and give only access to the charge current associated to the carrier distribution in the band. However, as mentioned above, the charge current that can be experimentally measured includes both contributions, and it will be shown in section 5.4 that the part related to the coherence may indeed be important.

Note that the rapidly oscillating inter-band coherences ρ_{cv} do not explicitly appear in the low-frequency part of the current but indeed contribute to the inter-subband coherence and populations through the semiconductor Bloch equations.

One expects that the current related to the coherence oscillates with the inter-subband frequencies and its contribution may therefore vanish in a time-integrated measurement. However it also affects the electromagnetic radiation due to the variation in time of the current. Indeed, the power of the far-field THz emission originating from a finite volume V is given by

$$P(t) = \frac{1}{6\pi\epsilon_0 c^3}\Big[\int_V \partial_t\big[\boldsymbol{j}_{\mathrm{pop}}(\boldsymbol{r}', t) + \boldsymbol{j}_{\mathrm{coh}}(\boldsymbol{r}', t)\big]\, d^3\boldsymbol{r}'\Big]^2 \tag{5.30}$$

(see Appendix E), and the corresponding power spectrum reads

$$P(\nu) \propto \Big|\int_{-\infty}^{+\infty} \partial_t\big(\boldsymbol{j}_{\mathrm{pop}} + \boldsymbol{j}_{\mathrm{coh}}\big)\, e^{-i2\pi\nu t}\, dt\Big|^2 . \tag{5.31}$$

Therefore, one can also distinguish between the two contributions $P = P_{\mathrm{pop}} + P_{\mathrm{coh}}$ related to the coherence and population respectively. As we will see, the inter-subband coherence may significantly contribute to the radiated power.

By analogy to the charge current, we define the current of spins aligned along β and moving along α as [133]

$$s^{\alpha\beta} = \frac{1}{S}\mathrm{Tr}[(\hbar/2)v^{\alpha}\sigma^{\beta}\rho]\,, \tag{5.32}$$

where σ^{β} are the Pauli matrices and v^{α} the velocity operator. The superscripts α and β denote cartesian components.

5.4 Results

5.4.1 Introduction

In the following, we discuss numerical results obtained with our model for two interfering femtosecond laser pulses. First, the optically injected charge current, related to the asymmetric carrier distribution in the bands (see Figure 5.2), and the corresponding far-field THz emission are calculated for a symmetric 70 Å wide GaAs/AlGaAs quantum well (QW). The latter is detailed in section 4.4.4, and its band structure is shown in Figure 5.4. Especially the contribution of the inter-valence-band coherence will be emphasized. We also give a quantitative comparison to bulk values. Then, using other beam polarizations, the generated pure spin current in the QW is computed. Finally, the influence of the AC Stark shifts and the inter-valence-band two-photon transitions are calculated and discussed.

For the calculations discussed in what follows, eight energy bands have been used in the reduced density matrix: the lowest conduction band and the three highest valence bands, all of them being doubly degenerate. However, in order to estimate the contribution of the other bands shown in Figure 5.4, we have also performed calculations where we included them i) in the reduced density matrix, or ii) as far off-resonant states (*i.e.* states that are not described by the reduced density matrix but nevertheless used as intermediate states in the quadratic interaction terms). First, it turns out that for the optical frequencies used in this study the neglected bands are almost not excited by the pulses and the results are not affected qualitatively. Therefore, the corresponding inter-band transitions can be considered as off-resonant. Second, the two-photon transition amplitude is modified when these additional bands are taken into account. Nevertheless, this increases the injected current by only 10-15% in our typical conditions.

All subsequent results were obtained with two laser pulses ($\boldsymbol{A}_1$ and $\boldsymbol{A}_2$ in (5.19)) polarized along principal axes in the plane of the quantum well (TE mode). Both have a duration of 100 fs at half maximum (of intensity). The peak intensities of the two pulses are chosen to lead separately to the same carrier injection in order to obtain a high contrast in the interference. Two pairs of frequencies ω_1/ω_2 were used: 1.54/0.77 eV and 1.60/0.80 eV for the one-photon/two-photon beams, which corresponds to excitation ∼50 meV and ∼110 meV above the band gap of the quantum well (1.491 eV). In both cases, the peak intensity of the two-photon pulse $\boldsymbol{A}_2$ is taken to be 10 GW/cm^2. The corresponding peak intensities of the one-photon pulse $\boldsymbol{A}_1$ are 18 MW/cm^2 and 42 MW/cm^2 for the lower and higher frequencies respectively. These values lead to injected carrier densities in the quantum well of 0.8 10^{11} cm^{-2} and 1.6 10^{11} cm^{-2} when both beams are present.

The current decay is related to the thermalization of the carrier distributions, and more specifically to the relaxation of the total crystal momentum in each band. Let us consider the two main mechanisms which govern electron scattering: emission of LO-phonons and carrier-carrier Coulomb interaction. The latter can further be divided into intra-band (electron-electron) and inter-band (electron-hole) scattering. Král and Sipe [97] already considered the emission of LO-phonons in bulk GaAs for carriers excited at high energy (600 meV above the band gap), and obtained a current decay time of 50 fs. In the present work, the excitation energy is much lower (50 and 110 eV above the band gap) and the corresponding relaxation is thus expected to be slower [138] (∼200 fs). At high density, carrier-carrier scattering may however become dominant. But by contrast to the former mechanism, the Coulomb interaction conserves the total momentum of the carrier distribution. The fast intra-band scattering alone is thus not sufficient for the current to vanish but needs the interplay with inter-band scattering and/or phonon emission. Usual thermalization times due to carrier-carrier Coulomb interaction (about 100 fs and 1 ps for the intra- and inter-band contributions respectively) are in general related to *symmetric* out-of-equilibrium distributions and may therefore not be appropriate in the context of current injection. A detailed description of the current decay is difficult because of the asymmetric distributions, and we finally use the phenomenological relaxation time $\tau = 200$ fs for both the thermalization of the carrier distributions and the decoherence.

In the following, we focus exclusively on results obtained for two EM pulses with TE polarization (in the plane of the QW). The beams are always polarized along principal axes af the crystal. Note that the charge current injected with one beam in TM polarization is more than one order of magnitude smaller, and there is even no current generated when both fields are polarized perpendicular to the QW.

5.4.2 Charge current

Figure 5.5 shows the calculated charge current burst $\boldsymbol{j}(t)$ (equation (5.27)) injected by beams co-polarized along a principal axis and with zero phase difference ($\phi_1 - 2\phi_2 = 0$). The current flows parallel to the one-photon polarization (there is no current injection perpendicular to the polarizations). Notice that due to the lateral confinement of the quantum well it corresponds to a current per *length* unit (A/m). The exponential decay is directly related to the phenomenological thermalization of the carrier distribution. As there is no low-frequency inter-band coherence, the charge current (thick line) can be separated into the currents in the conduction bands (thin dashed line) and in the valence bands (thin full line). The main contribution comes from the carrier motion in the conduction band because of the higher band-diagonal momentum matrix element *i.e.* the higher velocity of the electrons. The oscillation of the current in the valence bands is due to the inter-subband coherence (Figure 5.6). As discussed above, the charge current $\boldsymbol{j}$ can be divided into two parts, $\boldsymbol{j}_{\text{pop}}$ and $\boldsymbol{j}_{\text{coh}}$, related to the populations and the coherences respectively. The oscillations appear only in $\boldsymbol{j}_{\text{coh}}$ and correspond to the inter-valence-band frequencies.

It is interesting to note that only $\boldsymbol{j}_{\text{pop}}$ contributes to the *time-integrated* current that is usually measured. Indeed, for 1.54 eV (respectively 1.60 eV), $\int \boldsymbol{j}_{\text{coh}} dt$ represents only 0.54% (-0.13%) of the total charge current and 3.9% (-0.76%) of the current in the valence bands. The negative sign for 1.60 eV means that the time-integrated contribution of $\boldsymbol{j}_{\text{coh}}$ diminishes the total integrated current.

The charge current $\boldsymbol{j}_{\text{pop}}$ in the valence bands can further be divided into the current in the different subbands (Figure 5.7). Their relative contributions depend on the photon energy because of the complicated dispersion of the momentum matrix elements due to the valence-band mixing.

The multi-band Bloch equations include also correctly the saturation effects due to the time-evolving phase space filling. However, our results indicate that the high field intensities (10 GW/cm^2 for the two-photon pulse) used in this study are not sufficient for the saturation to become important. The decoherence time is also too short to allow Rabi flopping.

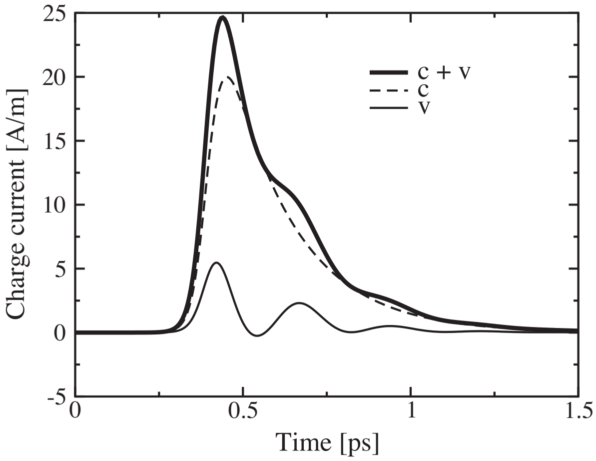

(a) $\hbar\omega_1 = 2\hbar\omega_2 = 1.54$ eV

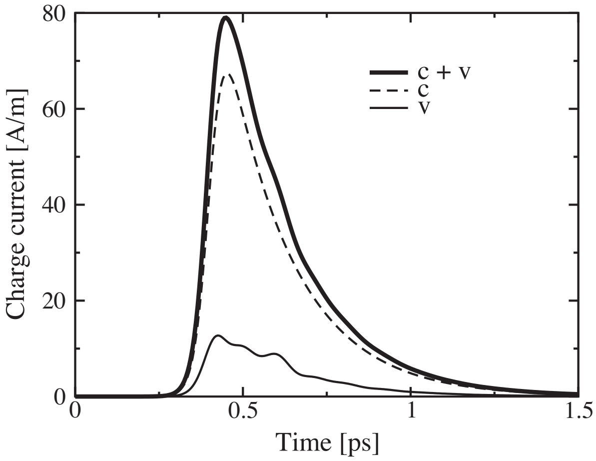

(b) $\hbar\omega_1 = 2\hbar\omega_2 = 1.60$ eV

Figure 5.5: Injected charge current along the one-photon polarization for (a) $\hbar\omega_1 = 2\hbar\omega_2 = 1.54$ eV and (b) $\hbar\omega_1 = 2\hbar\omega_2 = 1.60$ eV. Thin lines: charge current in the conduction bands (c) and in the valence bands (v). Thick line: total charge current (c + v).

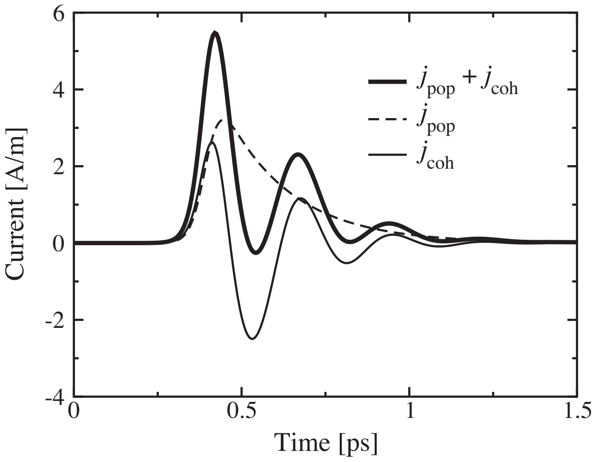

(a) $\hbar\omega_1 = 2\hbar\omega_2 = 1.54$ eV

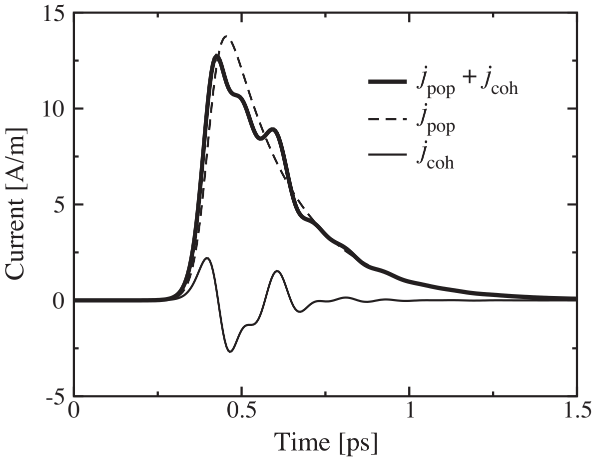

(b) $\hbar\omega_1 = 2\hbar\omega_2 = 1.60$ eV

Figure 5.6: Injected charge current in the valence bands along the one-photon polarization for (a) $\hbar\omega_1 = 2\hbar\omega_2 = 1.54$ eV and (b) $\hbar\omega_1 = 2\hbar\omega_2 = 1.60$ eV. Thick line: total charge current in the valence bands ($\boldsymbol{j} = \boldsymbol{j}_{\text{pop}} + \boldsymbol{j}_{\text{coh}}$). Thin lines: charge current related to the populations ($\boldsymbol{j}_{\text{pop}}$) and to the coherences ($\boldsymbol{j}_{\text{coh}}$).

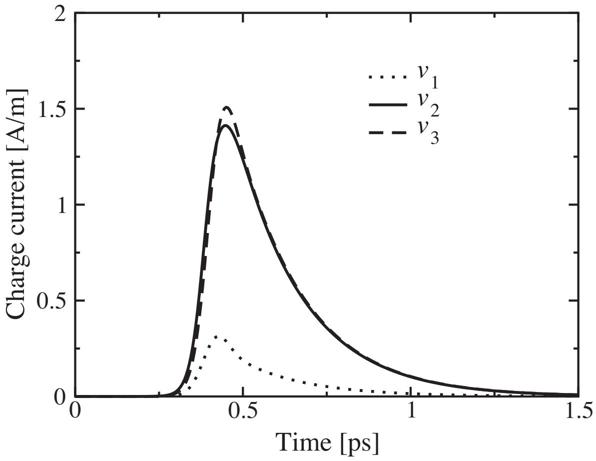

(a) $\hbar\omega_1 = 2\hbar\omega_2 = 1.54$ eV

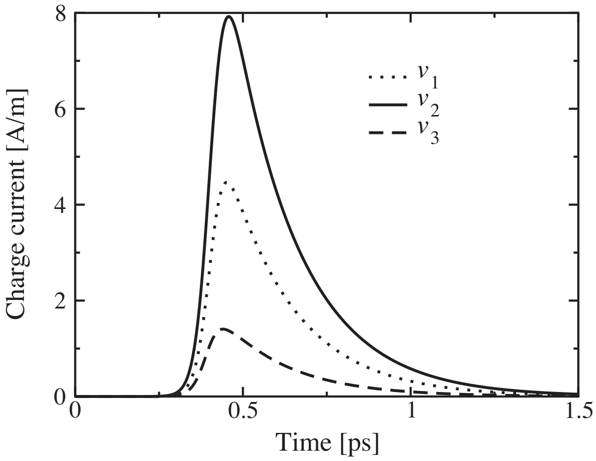

(b) $\hbar\omega_1 = 2\hbar\omega_2 = 1.60$ eV

Figure 5.7: Injected charge current $\boldsymbol{j}_{\text{pop}}$ related to the populations in the valence bands along the one-photon polarization for (a) $\hbar\omega_1 = 2\hbar\omega_2 = 1.54$ eV and (b) $\hbar\omega_1 = 2\hbar\omega_2 = 1.60$ eV. For each band label v_1, v_2 and v_3, the current is summed over the corresponding pair of degenerate subbands.

5.4.3 Comparison with current injection in bulk

The calculated peak intensities of the density of current in the QW (25 A/m for 1.54 eV and 79 A/m for 1.60 eV) are certainly much higher than to be expected in a real measurement. Indeed, it has been shown [139] that some effects that have been neglected, like frequency chirp in the pulses or spatial variation of the phase due to the frequency dependence of the refractive index, can strongly reduce the current injection. Yet it is useful to compare current intensities in QWs to bulk values obtained with the same model and in a similar configuration. The structure of the multi-band Bloch equations (3.51) remains the same except that the $\boldsymbol{k}$-vectors become *three-dimensional*. The electronic energies and dipole matrix elements for the bulk are the values corresponding to the (doubly degenerate) conduction band and to the four-valence-band Luttinger Hamiltonian used for the band structure calculation of the well. The density of current (3.84) relates to a volume unit (the surface of the quantum well is replaced by the crystal volume).

As the band gap for the QW (1.491 eV) and the bulk (1.423 eV) are different, we do not compare the injected currents for equal beam frequencies, but for equal energy differences with respect to the band gap. Thus we calculate the current generated in a GaAs bulk crystal by two pulses of frequency 1.47 eV and 0.735 eV (50 meV above the band gap) and co-polarized along a principal axis. The used peak intensities of 16 MW/cm^2 and 10 GW/cm^2 for the one- and two-photon beam respectively excite independently a carrier density of $1.6 \cdot 10^{16}$ cm^{-3} in the conduction band. The model gives a maximal injected current of 1900 μA/μm^2 in the bulk, which has to be compared to the 25 A/m obtained in the QW for the frequency 1.54 eV (also 50 meV above the QW band gap). The bulk value is therefore comparable to the current expected by approximatively 77 QWs per μm, insofar as the wells can be taken as independent. Indeed, these QWs would be separated by barriers of only 60 Å. We have to mention here that, for numerical reasons, the calculation for the bulk case was done with a lower discretization of $\boldsymbol{k}$-space than for the quantum well, and the convergence was not completely achieved.

5.4.4 Far-field THz emission

The power spectrum (5.31) of the far-field THz emission from the QW is plotted in Figure 5.8 and Figure 5.9 for the photon energy 1.54 eV and 1.60 eV respectively. The dashed lines show the power P_{pop} radiated only by the charge current pulse $\boldsymbol{j}_{\text{pop}}$ whereas the full lines represent the total THz emission $P = P_{\text{pop}} + P_{\text{coh}}$ originating from $\boldsymbol{j}_{\text{pop}} + \boldsymbol{j}_{\text{coh}}$. One can clearly see the contributions from the field emitted by the current $\boldsymbol{j}_{\text{coh}}$ due to the inter-subband coherences. The additional peaks around 5 and 10 THz are related to the coherences between the pairs of valence subbands v_1-v_2 and v_2-v_3 respectively. The polarization between v_2 and v_3 for 1.54 eV, as well as between v_1 and v_3 for both energies, are too small to be visible on this scale. The positions of these peaks are given by the inter-subband frequencies and are therefore *specific to the quantum well geometry.* The radiated power for 1.60 eV is about 10 times higher than for 1.54 eV, but the relative contribution of the inter-valence-band coherences to the total THz emission is much more important for the smaller injection energy. This can be explained by the dependence of the momentum matrix element between v_1 and v_2 on the wave vector $\boldsymbol{k}$ (Figure 5.10). The lasers with frequency 1.54/0.77 eV and 1.60/0.80 eV excite mainly the states of the two highest valence bands with $\boldsymbol{k}$-vector around 0.25 nm^{-1} and 0.4 nm^{-1} respectively. The v_1-v_2 momentum matrix element is maximal in the first case, and then decreases with increasing wavevector. The related polarization is expected to follow the same trend. On the other hand, the contribution $\boldsymbol{j}_{\text{pop}}$ to the injected charge current is about 3-4 times higher at 1.60 eV than at 1.54 eV. The related radiation P_{pop} becomes therefore dominant at higher laser frequencies. Figure 5.8 also shows the effect of a shorter thermalization and decoherence time of 100 fs on the spectrum. The contribution P_{pop} from the populations is shifted to higher frequencies because of its faster decay, and the different peaks of P_{coh} are no longer well resolved.

It is important to emphasize that the low frequency part of the current $\boldsymbol{j}_{\text{coh}}$ discussed above is also related to the interferences between the two fields, as is the current $\boldsymbol{j}_{\text{pop}}$ generated by the asymmetric population distribution. Indeed, there is almost no THz emission when only one beam is present.

5.4.5 Spin current

As the spin current is also dominated by the carriers in the degenerate conduction band, we restrict ourselves to these two bands. Furthermore, laser pulses polarized in the TE mode do not generate any coherence between bands m and $\bar{n}$ which do not belong to the same irreducible representation ${}^1E_{1/2}$ or ${}^2E_{1/2}$ of $\mathbf{C}_s$, the little group of $\boldsymbol{k}$. Indeed, the involved momentum matrix elements $\mathbf{\Pi}_{m\bar{n}}$ are equal to zero in the plane of the quantum well (see § 4.4.1). Therefore, with the band structure model described in section 4.4.4, the spin current in the conduction bands reduces to

$$s^{z\beta} = -\frac{1}{S}\sum_c \sigma^z_{cc} \sum_{\boldsymbol{k}} \Pi^\beta_{cc,\boldsymbol{k}}\, \rho_{cc,\boldsymbol{k}} \tag{5.33}$$

and $s^{x\beta} = s^{y\beta} = s^{\alpha z} = 0$. The left sum has to be taken over the two degenerate conduction bands with spin $\sigma = +1$ and $\sigma = -1$ pointing along the confinement direction z. The spin current is expressed in the same units as the charge current, and $\frac{\hbar}{2}$ was therefore replaced by $-e$ in (5.33).

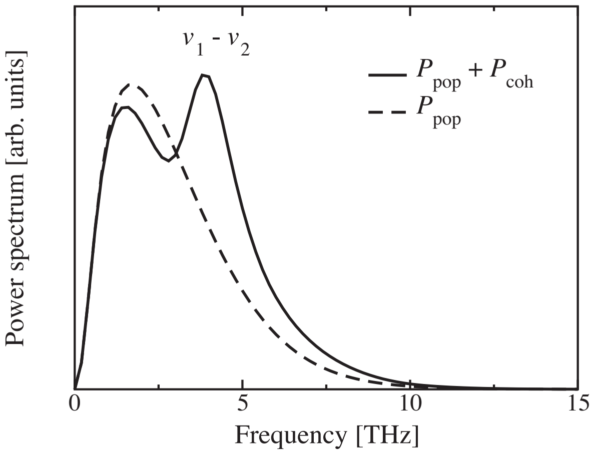

(a) $\tau = 200$ fs

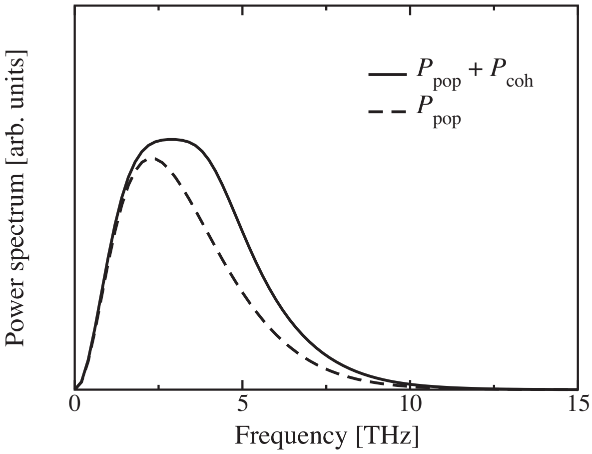

(b) $\tau = 100$ fs

Figure 5.8: Power spectrum of the far-field THz emission for $\hbar\omega_1 = 2\hbar\omega_2 = 1.54$ eV calculated with two different thermalization and decoherence times: (a) $\tau = 200$ fs and (b) $\tau = 100$ fs. Full line: total THz emission $P = P_{\text{pop}} + P_{\text{coh}}$ due to the total charge current $\boldsymbol{j} = \boldsymbol{j}_{\text{pop}} + \boldsymbol{j}_{\text{coh}}$. Dashed line: THz emission P_{pop} due to the charge current $\boldsymbol{j}_{\text{pop}}$ only. Both figures are plotted on the same scale.

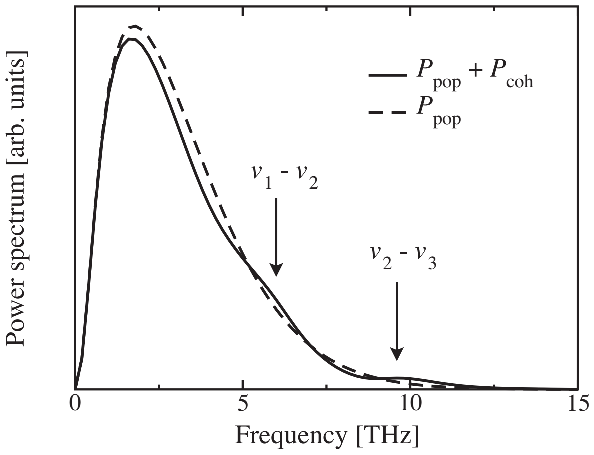

(a) $\tau = 200$ fs

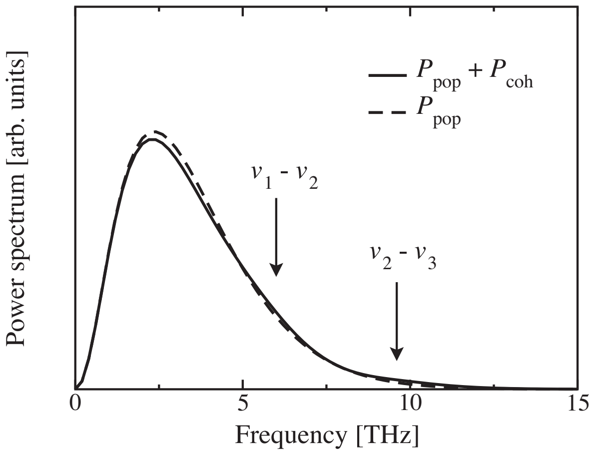

(b) $\tau = 100$ fs

Figure 5.9: Power spectrum of the far-field THz emission for $\hbar\omega_1 = 2\hbar\omega_2 = 1.60$ eV calculated with two different thermalization and decoherence times: (a) $\tau = 200$ fs and (b) $\tau = 100$ fs. Full line: total THz emission $P = P_{\text{pop}} + P_{\text{coh}}$ due to the total charge current $\boldsymbol{j} = \boldsymbol{j}_{\text{pop}} + \boldsymbol{j}_{\text{coh}}$. Dashed line: THz emission P_{pop} due to the charge current $\boldsymbol{j}_{\text{pop}}$ only. Both figures are plotted on the same scale.

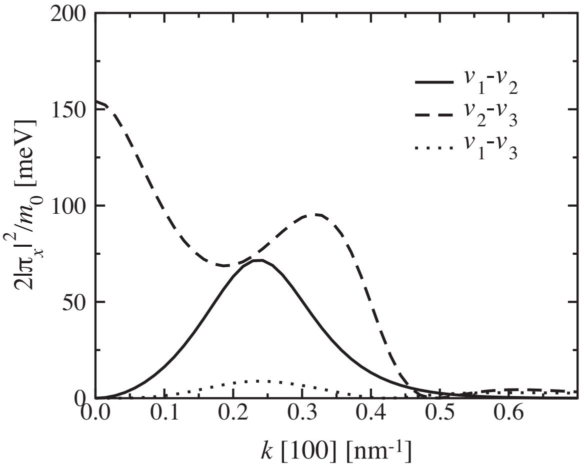

Figure 5.10: Inter-valence band momentum matrix elements $2|\pi_x|^2/m_0$.

The pure spin current (5.33) injected by cross-polarized laser beams with a phase difference $\phi_1 - 2\phi_2 = \pi/2$ is shown in Figure 5.11. The frequencies and intensities are the same as in the case of the charge current injection discussed above. The pulses are polarized along two principal axes, and the spin current flows parallel to the two-photon polarization *without* any net charge flow. However, a small charge current due to the off-resonant states subsists in the orthogonal in-plane direction (along the one-photon polarization). There is no THz emission polarized along the spin current direction and only a small radiation polarized perpendicularly to it (Figure 5.12). The latter is essentially due to $\boldsymbol{j}_{\text{coh}}$ parallel to the one-photon polarization. The charge current and the THz emission are respectively about one and two orders of magnitude weaker than for the preceding configuration with co-polarized beams and no phase difference.

5.4.6 AC Stark shifts and inter-valence-band transitions

The multi-band semiconductor Bloch equations (5.23) include all processes described by quasi-resonant interaction terms up to the second-order in the EM fields, but only the inter-band transitions contribute directly to the current injection. Nevertheless, the influence of the inter-subband transitions on the charge current generation remains an interesting issue.

Figure 5.13 displays the time-integrated charge current $\int \boldsymbol{j}(t)\, dt$ versus the photon energies, in the cases where the Stark shifts (ACSS) and/or the inter-valence-band (IVB) transitions are neglected or not. The laser pulses are co-polarized along one

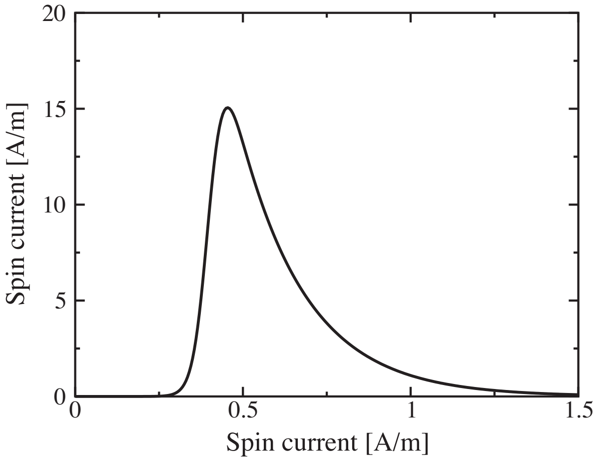

(a) $\hbar\omega_1 = 2\hbar\omega_2 = 1.54$ eV

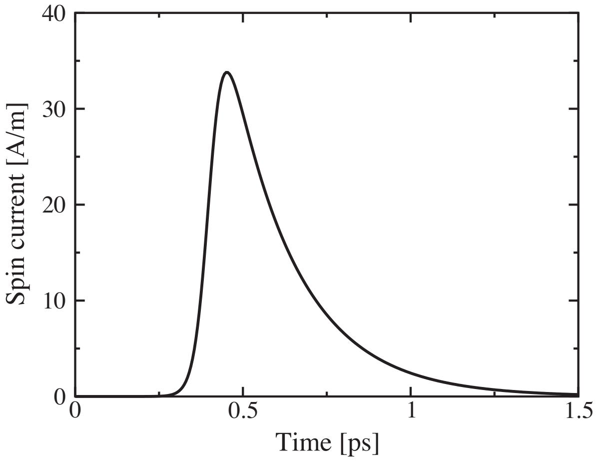

(b) $\hbar\omega_1 = 2\hbar\omega_2 = 1.60$ eV

Figure 5.11: Injected spin current in the conduction bands along the two-photon polarization for (a) $\hbar\omega_1 = 2\hbar\omega_2 = 1.54$ eV and (b) $\hbar\omega_1 = 2\hbar\omega_2 = 1.60$ eV.

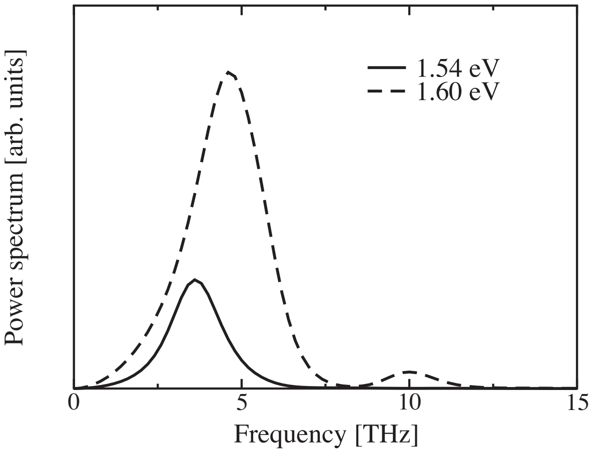

Figure 5.12: Power spectrum of the far-field THz emission along the one-photon polarization, in the configuration for spin current injection (cross-polarized beams with a phase difference of $\pi/2$). Full line: $\hbar\omega_1 = 2\hbar\omega_2 = 1.54$ eV. Dashed line: $\hbar\omega_1 = 2\hbar\omega_2 = 1.60$ eV.

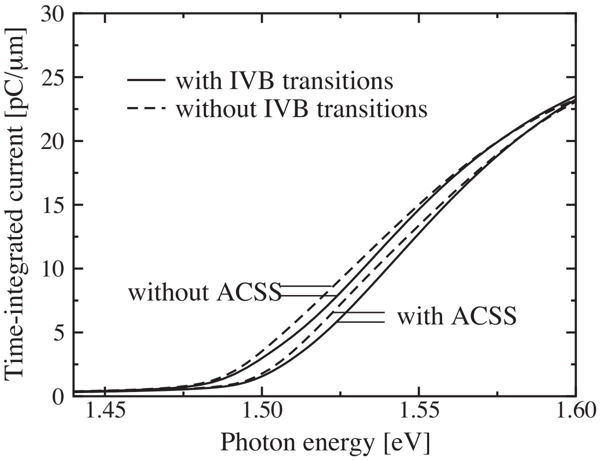

Figure 5.13: Time-integrated charge current versus the photon energy $\hbar\omega_1 = 2\hbar\omega_2$, with and without the AC Stark shifts (ACSS) and/or the inter-valence-band (IVB) transitions. The two lower/upper curves correspond to calculations with/without the AC Stark shifts. For both of these pairs, the full line includes the IVB transitions whereas for the dashed line they are neglected. Band gap of the quantum well: 1.491 eV.

of the principal axes, with no phase difference ($\phi_1 - 2\phi_2 = 0$) and constant peak intensities of 42 MW/cm^2 and 10 GW/cm^2 for the one- and two-photon beams respectively. The AC Stark effect mainly shifts the current curve to higher energies, in accordance with the field-induced band gap change. This results in weaker injected current for given optical frequencies, especially close to the band gap. At higher excitation energy, both computed currents become comparable, because the AC Stark shifts decrease for electronic states with higher $\boldsymbol{k}$-vector. The contribution of the IVB Raman-like two-photon transitions to the total charge current is rather weak. Indeed, they mainly affect the carrier distributions in the valence bands, whereas the charge current is dominated by carriers in the conduction band.

5.5 Conclusion

The model of multi-band Bloch equations including one- and two-photon interband transitions, the AC Stark shifts and inter-valence band two-photon transitions, developed in chapter 3, was used to calculate the injection of charge and spin current and the corresponding THz emission in a symmetric semiconductor quantum well. This allows us to evidence for the first time that the inter-subband coherences are important for the THz radiation (Figure 5.8 and 5.9). We also discussed the influence of the Stark shifts and the inter-valence-band transitions on the current injection.

The decay of the current has been included in the model by the mean of a phenomenological relaxation time. A microscopic description of the thermalization of the carrier distributions would therefore be an important improvement. Interaction with LO-phonons has already been considered by Král and Sipe [97]. *Intra*-band Coulomb scattering can not directly cause the decay of the current, as it conserves the total crystal momentum in the band, and its *inter*-band counterpart takes place on a longer time-scale.

6 Two-photon absorption in quantum wires with excitonic coherence

6.1 Introduction

In the previous chapter, we investigated the interplay between one- and two-photon transitions in a quantum well with realistic band structure, but neglected the Coulomb interaction. The latter can in principle easily be included in the effective multi-band Bloch equations, as outlined in section 3.12. In practice, the integration of these equations of motion is however limited by the computation time and the memory space. Therefore, in order to keep the complexity on a reasonable level, we focus our attention on a one-dimensional case. In this chapter, we calculate and discuss the two-photon absorption spectra of a realistic V-shaped quantum wire, including the Coulomb coupling within the Hartree-Fock approximation. Besides their physical relevance, these results also provide a good check of our numerical code in a more simple case. In this sense, the following study can be seen as a preliminary to further investigations of nonlinear optical processes. Indeed, in chapter 7, the same model is applied to the optical injection of current, taking into account excitonic effects.

Two-photon absorption has been looked at especially in quantum wells, both experimentally [94] and theoretically [35, 41], whereas it has received much less attention in quantum wires (QWRs). First measurements of two-photon absorption spectra were reported in rectangular [39] and V-shaped [40] QWRs, while Shimizu *et al.* [41] and Ogawa *et al.* [42] developed a simple effective-mass model with excitons included through an analytically solvable model for an electron-hole pair interacting with a modified Coulomb potential [43].

Recently [140], the influence of spatial symmetry and time-reversal symmetry was used to provide stringent conditions for the construction of excitons in QWRs with well-defined selection rules for one-photon transitions. In particular, it was shown that in V-shaped QWRs with $\mathbf{C}_s$ symmetry[1], the three possible linear polarizations of light interact with three classes of excitons (A_1, B_1 and B_2), whereas the forth class (A_2) can not be accessed (notations are changed with respect to [140]). However, two-photon spectroscopy involves alternate selection rules. Thus it becomes

---

[1] $\mathbf{C}_s$ will be extended to $\mathbf{C}_{2v}$ is section 6.2

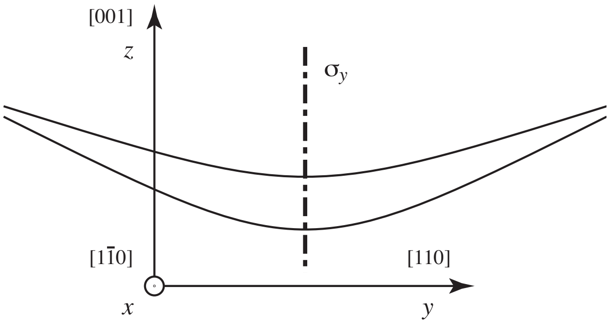

Figure 6.1: V-shaped quantum wire, orientated with respect to the bulk crystal axes.

interesting as a tool to collect complementary information.

In this chapter, we first calculate the anisotropic two-photon absorption spectra of an AlGaAs/GaAs V-shaped QWR with realistic band structure, and identify the various excitonic peaks with respect to the involved energy subbands and the symmetry properties. Then we show that the formerly dark A_2-excitons may become bright when the light is polarized along a direction that is *not* a symmetry axis.

The two-photon absorption coefficient is obtained by integrating the effective multi-band Bloch equations (§ 3.7) including the Coulomb interaction within the Hartree-Fock approximation (§ 3.12). The model treats the Coulomb interaction between five doubly-degenerate conduction subbands and eight doubly-degenerate valence subbands. Additional subbands that are important for the two-photon absorption are also taken into account as intermediate states in the transition amplitude.

In section 6.2, we detail the realistic V-shaped QWR we use in this chapter. Section 6.3 is dedicated to the symmetry properties of the excitons and to the related optical one- and two-photon selection rules. The calculated two-photon absorption spectra including excitonic effects are shown and discussed in section 6.4. Finally, the conclusions are drawn in section 6.5.

6.2 Band structure

In the following, we consider a V-shaped $\mathrm{Al}_x\mathrm{Ga}_{1-x}\mathrm{As}/\mathrm{GaAs}$ ($x = 0.337$) quantum wire (QWR) orientated with respect to the crystal main symmetry axes, as shown in Figure 6.1. The symmetry group of the underlying crystalline structure is T_d. Thus, the heterostrucruture exhibits the $\mathbf{C}_s$ symmetry, with unique symmetry plane σ_y. However, the inversion asymmetry in GaAs has only very small effects on the valence band structure. Therefore, it is neglected here. Within this approximation,

Symbol	Parameter	$\mathrm{Al}_x\mathrm{Ga}_{1-x}\mathrm{As}$	Unit
m_c	Effective mass of the conduction band	$0.0665 + 0.0835x$	$[m_0]$
γ_1	Luttinger parameter	$6.790 - 3.000x$	[–]
γ_2	Luttinger parameter	$1.924 - 0.694x$	[–]
γ_3	Luttinger parameter	$2.681 - 1.286x$	[–]
E_P	Kane parameter	28.8	[eV]
E_g	Energy gap	$1.519 + 1.247x$	[eV]
$\Delta E_c/\Delta E_v$	Band offsets	68/32	[–]

Table 6.1: Bulk band structure parameters [127] of $\mathrm{Al}_x\mathrm{Ga}_{1-x}\mathrm{As}$ used in this chapter.

the QWR possesses two symmetry planes σ_x and σ_y, defined by their normal axes x ([1$\bar{1}$0]) and y ([110]) respectively. Together with the identity E and the binary rotation $C_{2z} = \sigma_x\sigma_y$, they form the crystallographic point group $\mathbf{C}_{2v}$ that is considered here. In the following, $\boldsymbol{x}$, $\boldsymbol{y}$ and $\boldsymbol{z}$ denote unit vectors parallel to the axes.

For the band structure computations, the exact contour is extracted from a Transmission Electron Microscope (TEM) picture. The confined electronic states in the GaAs/AlGaAs QWR were calculated by Dupertuis [140, 141] with $\boldsymbol{k}\cdot\boldsymbol{p}$ theory: the bulk conduction band is a doubly degenerate S-like band, and the bulk valence band is described by the four-bands Luttinger Hamiltonian. The bulk band structure parameters are shown in Table 6.1, and the energy subbands of the QWR are displayed in Figure 6.2. This band structure already led to a one-photon absorption spectrum in good agreement with the experimental results [142]. The momentum matrix elements of the QWR are obtained by the formula (4.36). The bulk momentum matrix elements $\boldsymbol{\pi}_{aa'}$ between a conduction band and a valence band are given by the Kane matrices (4.114) to (4.116), whereas the elements between two conduction bands or two valence bands are equal to zero due to symmetry.

6.3 Excitons

The excitonic contributions are included in the effective Bloch equations through the Coulomb interaction within the Hartree-Fock approximation (§ 3.12). The required Coulomb matrix elements were calculated by Dupertuis [142], by solving the Poisson equation (3.112) with position dependent dielectric function. In the following, we classify the excitons with respect to the symmetry properties, and deduce well-defined optical selection rules for one- and two-photon transitions.

The electronic one-particle states with non-zero crystal momentum $\boldsymbol{k}$ do not belong to the irreducible representations (irreps) of the zone-center point group $\mathbf{C}_{2v}$.

Indeed, the only symmetry operation which leaves the associated energy subspace invariant, besides the identity E, is the reflection with respect to the symmetry plane σ_y. Thus, the corresponding little group of $\boldsymbol{k}$ is $\mathbf{C}_s$, which has two one-dimensional irreducible spinor representations, ${}^1E_{1/2}$ and ${}^2E_{1/2}$. Let us denote the eigenstates related to ${}^1E_{1/2}$ and ${}^2E_{1/2}$ by $|n,k\rangle$ and $|\bar{n},k\rangle$ respectively, where the pair n and $\bar{n}$ refers to the pair of subbands that are degenerate at zone-center. Taking into account the condition ${\sigma_x}^2 = {\sigma_y}^2 = K^2 = -E$, with K the time-reversal operator, the eigenstates can always be chosen to fulfill

$$\sigma_x\,|n,+k\rangle = +\,|\bar{n},-k\rangle\,, \qquad \sigma_x\,|\bar{n},+k\rangle = -\,|n,-k\rangle\,, \tag{6.1}$$

$$\sigma_y\,|n,+k\rangle = +i|n,+k\rangle\,, \qquad \sigma_y\,|\bar{n},+k\rangle = -i|\bar{n},+k\rangle\,, \tag{6.2}$$

$$C_{2z}\,|n,+k\rangle = +i|\bar{n},-k\rangle\,, \qquad C_{2z}\,|\bar{n},+k\rangle = +i|n,-k\rangle\,, \tag{6.3}$$

and

$$K\,|n,+k\rangle = +|\bar{n},-k\rangle\,, \qquad K\,|\bar{n},+k\rangle = -|n,-k\rangle\,. \tag{6.4}$$

The last equation reflects the fact that the subbands n and $\bar{n}$ are mutually conjugate by time-reversal.

Excitonic quantum numbers may be defined from the irreps of product states of single particles, since the Coulomb interaction always belongs to the invariant representation and thus mixes only product states with a given representation. Insofar as the wavevector of the electromagnetic field is neglected, only the excitons with center-of-mass wavevector equal to zero are optically active. As a consequence, all optically active excitons *exhibit the zone center symmetry* and can be labeled by the irreps of the point group of the QWR. Furthermore, excitons being product states of two particles with half-integer spin, their total spin is integer. By contrast to the single particle case, excitons therefore belong to the irreps of the *single* group. In QWRs with $\mathbf{C}_{2v}$ symmetry, the optically active excitons can consequently be classified according to the four one-dimensional irreps denoted by A_1, B_1, A_2 and B_2.

To go further, let us first describe the electronic states in terms of the single-particle creation operators

$$a^\dagger_{n,k}\,|0\rangle = |n,k\rangle \qquad a^\dagger_{\bar{n},k}\,|0\rangle = |\bar{n},k\rangle\,. \tag{6.5}$$

We then define a highly symmetrized basis for product states

$$B^{A_1\,\dagger}_{cv,k} = \frac{1}{\sqrt{2}}\,[a^\dagger_{c,k}a_{v,k} + a^\dagger_{\bar{c},-k}a_{\bar{v},-k}]\,, \tag{6.6}$$

$$B^{B_1\,\dagger}_{cv,k} = \frac{i}{\sqrt{2}}\,[a^\dagger_{c,k}a_{v,k} - a^\dagger_{\bar{c},-k}a_{\bar{v},-k}]\,, \tag{6.7}$$

	1-PA			$2_{\shortparallel}$-PA			$2_{\perp}$-PA		
$\mu/\mu\nu$	x	y	z	xx	yy	zz	xy	yz	zx
Γ	B_1	B_2	A_1	A_1	A_1	A_1	A_2	B_2	B_1

Table 6.2: Optical selection rules for different types Γ of excitons in a quantum wire with $\mathbf{C}_{2v}$ symmetry, for the absorption of one photon (1-PA), two co-polarized photons ($2_{\shortparallel}$-PA) and two cross-polarized photons ($2_{\perp}$-PA). The symbols μ and $\mu\nu$ refer to the superscripts of the linear and quadratic optical interactions Π^{μ}_{cv} and $\sum_n \Pi^{\mu}_{cn}\Pi^{\nu}_{nv}/(\Omega_{nv}-\omega)$. Only the allowed transitions are displayed. All other transitions are forbidden. Note that Γ also represents the irreps to which the interactions belong. Notations are changed with respect to [140].

$$B^{A_2}_{cv,k}{}^{\dagger} = \frac{i}{\sqrt{2}}\,[a^{\dagger}_{c,k}a_{\bar{v},k} + a^{\dagger}_{\bar{c},-k}a_{v,-k}]\,, \tag{6.8}$$

$$B^{B_2}_{cv,k}{}^{\dagger} = \frac{1}{\sqrt{2}}\,[a^{\dagger}_{c,k}a_{\bar{v},k} - a^{\dagger}_{\bar{c},-k}a_{v,-k}]\,. \tag{6.9}$$

Note that these states are self-conjugate under time-reversal, as shown by Koster *et al.* [143], and obey

$$K B^{\Gamma}_{cv,k}{}^{\dagger} K^{-1} = B^{\Gamma}_{cv,k}{}^{\dagger}\,, \qquad \forall\,\Gamma \in \{A_1,\, B_1,\, A_2,\, B_2,\}\,. \tag{6.10}$$

On the level of the Hartree-Fock approximation, the excitons are described in the effective Bloch equations only through the microscopic coherence $\langle B^{\Gamma}_{cv,k}{}^{\dagger}\rangle$. Nevertheless, they appear as excitonic resonances in the macroscopic polarization.

The optical excitation in the dipole approximation is described by the linear interaction

$$\Pi^{\mu}_{cv}\,, \qquad \mu \in \{x,y,z\} \tag{6.11}$$

for resonant one-photon transitions and by the effective quadratic interaction

$$\sum_n \frac{\Pi^{\mu}_{cn}\Pi^{\nu}_{nv}}{\Omega_{nv}-\omega}\,, \qquad \mu,\nu \in \{x,y,z\} \tag{6.12}$$

for resonant two-photon transitions. The matrix $\mathbf{\Pi}$ (proportional to the momentum) is defined by (3.5). Under the spatial symmetry operations, the linear interactions transform like the cartesian components $\mu \in \{x,y,z\}$, whereas the quadratic interactions transform like the product $\mu\nu$ of two cartesian components. The irreps of $\mathbf{C}_{2v}$ to which they belong are shown in Table 6.2. Taking into account these symmetries, the excitonic selection rules are derived and summarized in the same table. Only the allowed transitions are displayed. All other transitions are forbidden.

For one-photon excitation, as already discussed by Dupertuis [140], the three possible linear polarizations of light interact with three independent classes of excitons: A_1, B_1 and B_2. The fourth class A_2 appears to be dark.

By two-photon excitation with light polarized along a symmetry axis x, y or z, only excitons of the type A_1 can be accessed. A_2-excitons remain dark. This selection rule breaks down when the light is polarized along an arbitrary direction in the plane perpendicular to the QWR. It emerges from the last columns of Table 6.2, that the contribution of the two-photon interaction (6.12) mixing the x and y polarizations may indeed access the A_2-excitons.

Finally, when spin splitting is ignored in the conduction band, it can be shown [144] that the A_1 and B_1 excitons are degenerate, as well as A_2 and B_2.

6.4 One- and two-photon absorption spectra

6.4.1 Model

The absorption spectra are calculated by solving the time-dependent effective Bloch equations (3.51), taking into account the Coulomb interaction within the Hartree-Fock approximation (§ 3.12). The one- and two-photon absorption coefficients, $\alpha(\omega)$ and $\beta(\omega)$ respectively, are extracted from the time-dependent macroscopic polarization current by the procedure detailed in section 3.11. We restrict ourselves to the low density regime by exciting the system with sufficiently low optical intensity. As a consequence, the Coulomb interaction $[V_q]^{c,c';c'',c'''}$ and $[V_q]^{v,v';v'',v'''}$ between electrons in the conduction subbands or between electrons in the valence subbands respectively can be neglected and we keep only the inter-band matrix elements $[V_q]^{c,c';v,v'}$ and $[V_q]^{v,v';c,c'}$.

The calculations are performed with a reduced density matrix describing the 6 lowest pairs of conduction bands and the 8 highest pairs of valence bands. The two bands defining a pair are conjugate by time-reversal. A pair of conduction bands is completely degenerate and a pair of valence bands degenerate at zone center. The bands are labeled as follows: c_i denotes the i^{th} pair of conduction subbands, starting from the bottom, and v_i denotes the i^{th} pair of valence subbands, starting from the top. To correctly describe the two-photon transitions, one should in principle take into account a complete set of intermediate states. In practice however, we restrict ourselves to the 12 lowest pairs of conduction bands and the 24 highest pairs of valence bands. In terms of the notations introduced in chapter 3, this corresponds to 28 bands in group $\mathbb{A}$ and 44 bands in group $\mathbb{B}$. The decoherence is modeled by a unique characteristic relaxation time $\tau = 200$ fs leading to a broadening of ~3 meV. According to the notations used in section 3.14, this corresponds to $\tau_{mn} = \tau, \forall\, m, n$.

In order to obtain an unambiguous definition of an absorption quantity in a quasi-one-dimensional QWR, the volume V in the density of current (3.62) has to

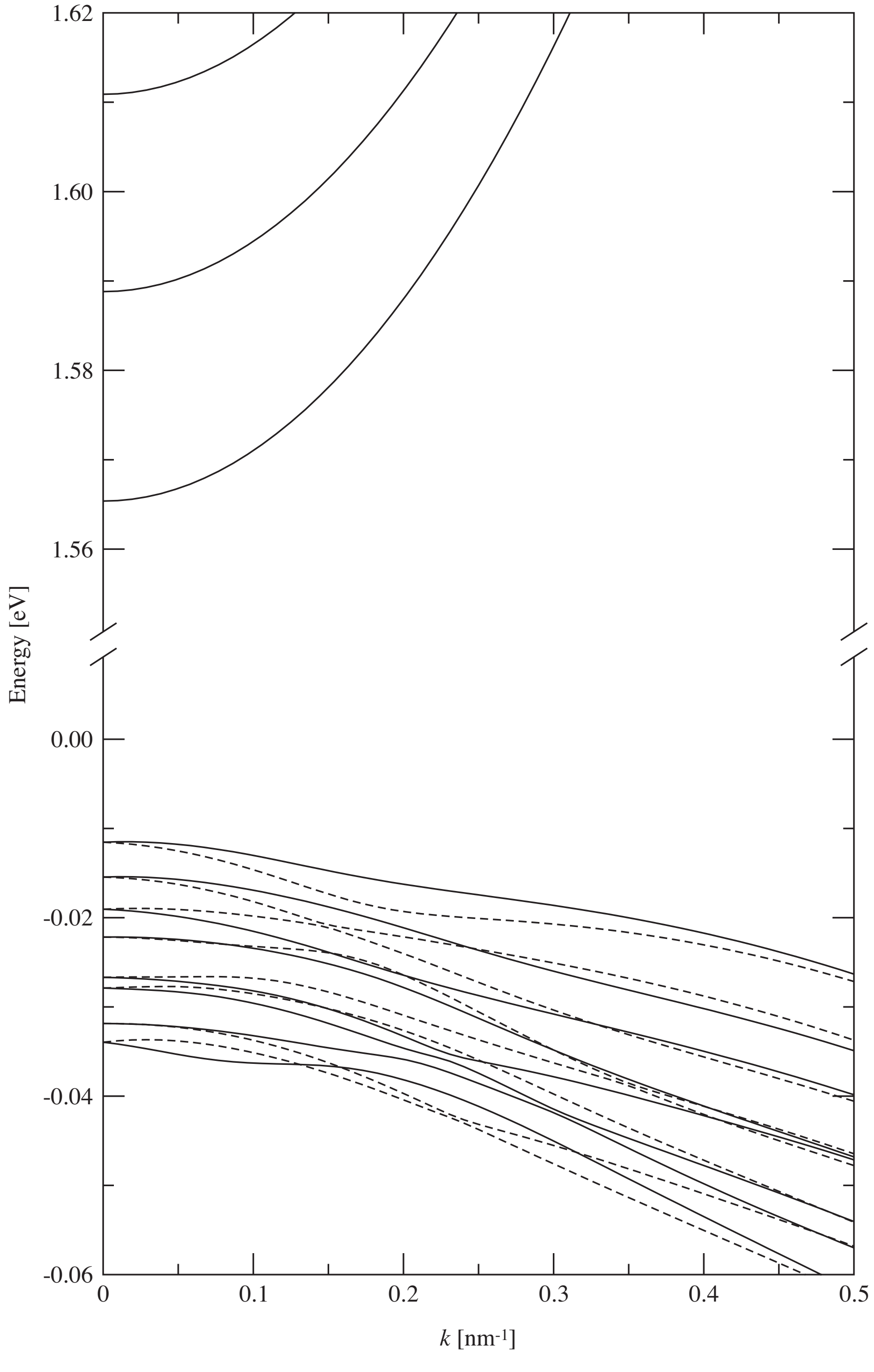

Figure 6.2: Band structure of a V-shaped AlGaAs/GaAs quantum wire. Two bands that are degenerate at zone center are mutually conjugate by time-reversal (full line and dashed line).

be replaced by the length of the wire [110]. The ill-defined lengths in the confined directions are absorbed in the definition of the one-photon absorption coefficient α in units of m instead of m^{-1}, and in the definition of the two-photon absorption coefficient β in units of m^3/W instead of m/W.

6.4.2 Results: light polarized along a symmetry axis

The two-photon absorption spectra for the three polarizations along the high symmetry axes x, y and z are displayed in Figure 6.3–6.5. With these specific polarizations, one accesses independently the components β^{xx}, β^{yy} and β^{zz} of the two-photon absorption tensor (3.100), which are related to the imaginary part of the third-order susceptibilities χ^{xxxx}, χ^{yyyy} and χ^{zzzz} respectively (equation (3.99)). For comparison, the calculated one-photon absorption spectra for the three independent polarizations are shown in Figure 6.6. Note that most of the periodic oscillations appearing in the part of the spectrum corresponding to the continuum, especially for the $\boldsymbol{x}$-polarization, are due to the finite discretization in reciprocal space, and are not physical.

These results require some comments on the numerical convergence. Two-photon transitions involve a complete set of intermediate states. Consequently, bands that are not, or only weakly, excited by the electromagnetic field may nevertheless strongly contribute to the transition probability between other bands. However, one expects that these contributions decrease with increasing distance in energy. As mentioned above, 12 pairs of conduction bands and 24 pairs of valence bands were used for the calculations in this chapter. For light polarized along the axis x or y, the same computations with only 6–9 pairs of conduction bands and 8–12 pairs of valence bands lead to very similar spectra with only *quantitative* differences (10%-20%). This suggests that the spectra for light polarized along the axis x or y have qualitatively converged. This may not be the case for light polarized parallel to the z axis. Indeed, the convergence with respect to the number of included bands seems to be slower in this case. For instance, a strong peak related to the c_2v_4 coherence appears at ~1.602 eV when only 9 pairs of conduction bands are used. This peak disappears only when the 10th pair of conduction bands is added.

Let us now analyze the two-photon absorption spectra more in detail. First, we emphasize that, according to the discussion in section 6.3, all excitonic peaks appearing in the three two-photon absorption spectra correspond to the same kind of excitons, namely the ones that belong to the irrep A_1. The subbands giving the dominant contribution to the main peaks have been identified and are displayed above the peaks. Second, we observe a strong polarization anisotropy, especially between the directions parallel and perpendicular to the QWR. Indeed, the associated excitons involve different combinations of conduction subbands and valence subbands. This polarization anisotropy was already predicted by Spector [33] and

Shimizu *et al.* [41]. Let us review their arguments in the framework of the present model.

Analysis without valence band mixing

We consider a simplified model where the valence band mixing is neglected. In this case, any electronic state is described by a wave function of the form $\psi_a^{(i)} = f_a^{(i)} U_a$, with U_a the zone-center Bloch function of the (bulk-) band a and $f_a^{(i)}$ the envelope function defining the subband i of the QWR (we dropped the wavevector label). First, we note that because the intermediate states for the higher-order transitions are the eigenstates of the QWR, any two-photon transition channel is given by the product of one inter-band[2] and one intra-band[3] momentum matrix element. Second, we calculate the effective momentum matrix elements given by equation (4.36). For isotropic parabolic bands, the effective mass tensor $\gamma_{aa'}^{\alpha\beta}$ is band-diagonal and isotropic, *i.e.* $\gamma_{aa'}^{\alpha\beta} = \gamma_{aa}\delta_{aa'}\delta_{\alpha\beta}$, and the band-diagonal elements of the bulk momentum $\boldsymbol{\pi}_{aa'}$ vanish. Thus, the inter-band momentum matrix elements in the direction $\boldsymbol{\epsilon}$ between a conduction subband i ($a = c$) and a valence subband j ($a = v$) are given by

$$\langle \psi_c^{(i)} | \boldsymbol{\epsilon\pi} | \psi_v^{(j)} \rangle = \boldsymbol{\epsilon\pi}_{cv} \, \langle f_c^{(i)} | f_v^{(j)} \rangle_\perp \, , \tag{6.13}$$

and the intra-band momentum matrix elements between two conduction subbands i and j ($a = c$) or two valence subbands i and j ($a = v$) are obtained by

$$\langle \psi_a^{(i)} | \boldsymbol{\epsilon\pi} | \psi_a^{(j)} \rangle = \gamma_{aa} \, \langle f_a^{(i)} | \boldsymbol{\epsilon}(\boldsymbol{p}_\perp + \hbar \boldsymbol{k}_{\shortparallel}) | f_a^{(j)} \rangle_\perp \, . \tag{6.14}$$

In the case of light polarized along an unconfined direction ($\boldsymbol{\epsilon}_{\shortparallel}$), the latter reduces to

$$\langle \psi_a^{(i)} | \boldsymbol{\epsilon}_{\shortparallel} \boldsymbol{\pi} | \psi_a^{(j)} \rangle = \gamma_{aa} \hbar \boldsymbol{\epsilon}_{\shortparallel} \boldsymbol{k}_{\shortparallel} \, \langle f_a^{(i)} | f_a^{(j)} \rangle_\perp \, , \tag{6.15}$$

whereas for light polarized along a confined direction ($\boldsymbol{\epsilon}_\perp$), it becomes

$$\langle \psi_a^{(i)} | \boldsymbol{\epsilon}_\perp \boldsymbol{\pi} | \psi_a^{(j)} \rangle = \gamma_{aa} \, \langle f_a^{(i)} | \boldsymbol{\epsilon}_\perp \boldsymbol{p}_\perp | f_a^{(j)} \rangle_\perp \, . \tag{6.16}$$

These results imply important selection rules with respect to the parity of the envelope functions under the spatial reflection σ_y. Equation (6.13) shows that inter-band momentum matrix elements between states described by envelope functions of opposite parity are equal to zero for any direction of polarization. By contrast, intra-band elements between envelope functions of opposite parity vanish for a polar-

---

[2] between a conduction subband and a valence subband

[3] between two conduction subbands or two valence subbands

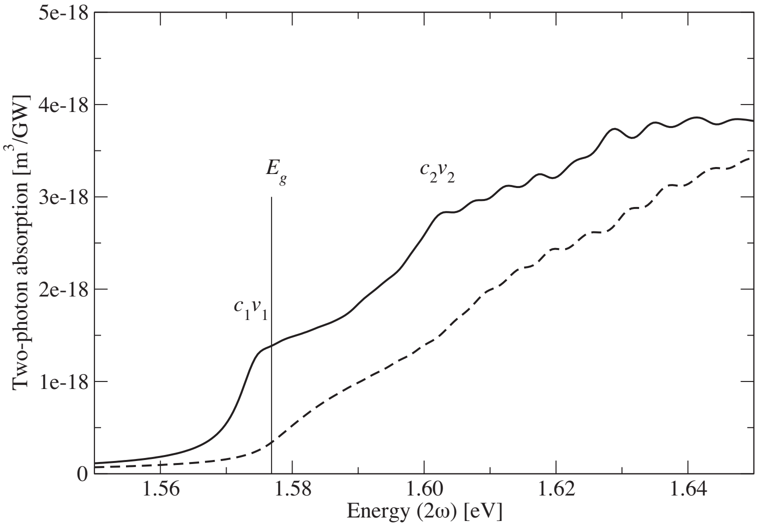

Figure 6.3: Two-photon absorption spectrum of the V-shaped quantum wire for light linearly polarized in the $\boldsymbol{x}$ direction (parallel to the QWR). Full line: Coulomb interaction included within the Hartree-Fock approximation. Dashed line: Coulomb interaction neglected. E_g: energy gap of the QWR.

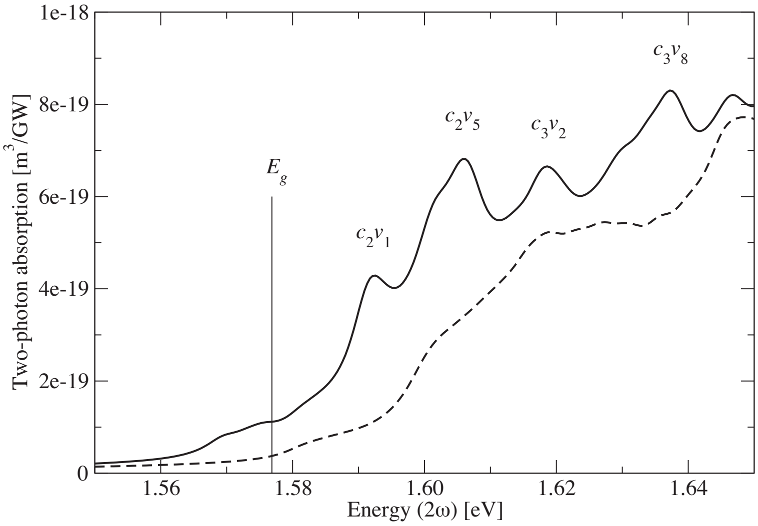

Figure 6.4: Two-photon absorption spectrum of the V-shaped quantum wire for light linearly polarized in the $\boldsymbol{y}$ direction (perpendicular to the QWR). Full line: Coulomb interaction included within the Hartree-Fock approximation. Dashed line: Coulomb interaction neglected. E_g: energy gap of the QWR.

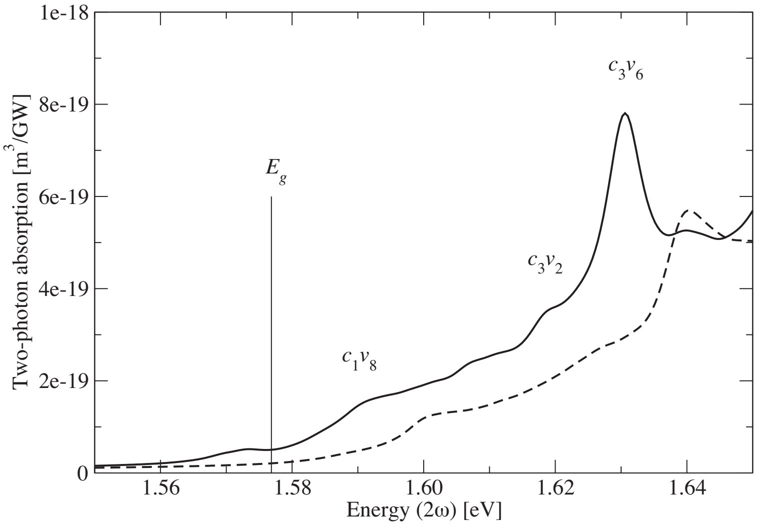

Figure 6.5: Two-photon absorption spectrum of the V-shaped quantum wire for light linearly polarized in the z direction (perpendicular to the QWR). Full line: Coulomb interaction included within the Hartree-Fock approximation. Dashed line: Coulomb interaction neglected. E_g: energy gap of the QWR.

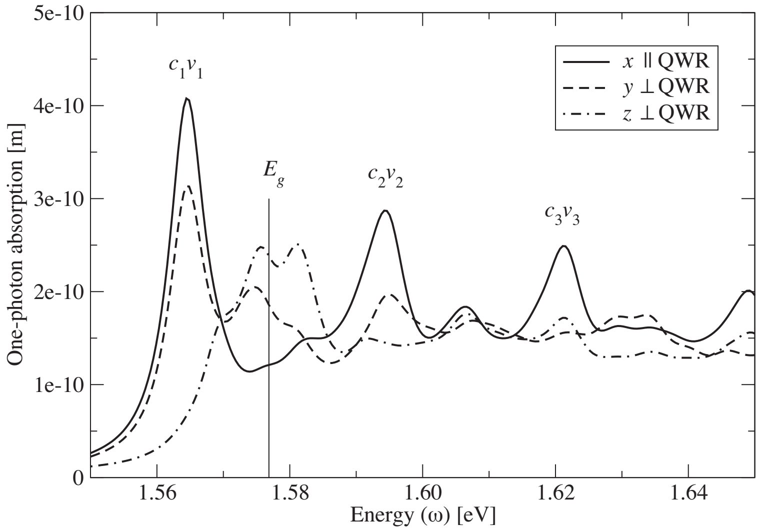

Figure 6.6: One-photon absorption spectrum of the V-shaped quantum wire for the three possible linear polarization of light. E_g: energy gap of the QWR.

ization vector $\boldsymbol{\epsilon} \parallel \boldsymbol{x}$ (equation (6.15)) or $\boldsymbol{\epsilon} \parallel \boldsymbol{z}$ (equation (6.16)), whereas intra-band elements between envelope functions of identical parity vanish for a polarization vector $\boldsymbol{\epsilon} \parallel \boldsymbol{y}$ (equation (6.16)). Therefore, the product between one inter-band and one intra-band element

$$\langle \psi_c^{(i)} | \boldsymbol{\epsilon\pi} | \psi_a^{(n)} \rangle \langle \psi_a^{(n)} | \boldsymbol{\epsilon\pi} | \psi_v^{(j)} \rangle \tag{6.17}$$

vanishes i) between states $\psi_c^{(i)}$ and $\psi_v^{(j)}$ with envelope functions of identical parity when the light is polarized along the confined direction $\boldsymbol{y}$, and ii) between states with envelope functions of opposite parity when the light is polarized along the unconfined direction $\boldsymbol{x}$ or along the confined direction $\boldsymbol{z}$. Consequently, in the framework of this simplified model, an electromagnetic field with frequency close to the half of the band gap and with a polarization vector $\boldsymbol{\epsilon} \parallel \boldsymbol{y}$ (respectively, $\boldsymbol{\epsilon} \perp \boldsymbol{y}$) can induce an inter-band coherence only between subbands of opposite (respectively, identical) parity.

A peculiarity of the *intra-band* momentum matrix elements is the strong polarization anisotropy *due to the quantum confinement* (compare equations (6.15) and (6.16)). By contrast, the anisotropy of the *inter-band* elements comes essentially from the underlying crystal symmetry. In the absence of valence-band mixing, the anisotropy of the inter-band elements (6.14) is even completely given by the bulk momentum matrix element $\boldsymbol{\pi}_{cv}$. As a consequence, the two-photon absorption displays a strong qualitative polarization anisotropy due to the quasi-one-dimensional quantum confinement.

In a *bulk* crystal modeled by isotropic bands, the two-photon inter-band transitions would excite P-like excitons oriented along the polarization vector of the light. Consider now the deformation of these states due to the confinement, when placed in V-shaped QWR (Figure 6.7). It is obvious that the P_x-exciton is much less affected by the QWR, than P_y and P_z. The strong absorption below the band gap, for the polarization parallel to the x axis (Figure 6.3), can thus be explained by the existence of bound P_x-like excitons. In the other directions, however, the confinement strongly affects the initial bulk excitons and the spectra can no more be interpreted in terms of P-like excitons. Also note that, because of the weaker lateral confinement (along the y axis), one may expect the spectrum for the polarization parallel to $\boldsymbol{y}$ to display some quantum-well-like features.

Analysis with valence band mixing

In our calculations involving a realistic band structure, the situation is more complex because of the valence band mixing. In fact, the conduction subbands still have a well defined parity under the spatial reflection σ_y, as they derive only from a single isotropic parabolic band. However, the valence subbands are based on the four-

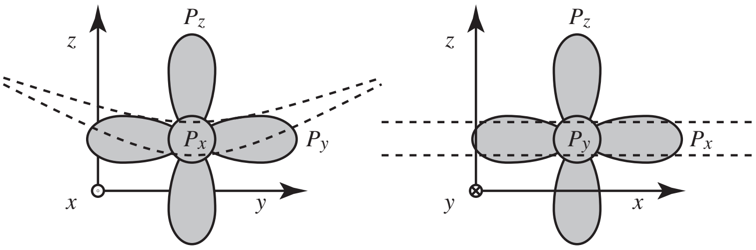

Figure 6.7: P-like bulk excitons. The dashed line shows the quasi-one-dimensional V-shaped quantum wire.

bands Luttinger Hamiltonian. Each eigenstate is thus described by four envelope functions. If the spin quantization axis is chosen parallel to $\boldsymbol{y}$, it follows from group theoretical arguments that these functions, which multiply the four basis states $|\frac{3}{2}, m\rangle_y$ with $-\frac{3}{2} \leq m \leq \frac{3}{2}$, are alternatively odd and even with increasing m.

Of course, the four envelope functions do not necessarily have the same weight, and a *dominant* parity may be associated to the eigenstate. However, with the band structure model used here, some states do not exhibit a clear dominant parity. This is what we observe in the calculated two-photon absorption spectra in Figure 6.4 and Figure 6.5, corresponding to the direction of polarization $\boldsymbol{y}$ and $\boldsymbol{z}$. The involved subbands satisfy only partially the above selection rules. Indeed, without valence-band mixing, an excitonic peak associated to a given set of subbands would never appear in *both* absorption spectra. For instance, the exciton peaks labeled by c_3v_2 show that the states in the valence subband v_2 are described by even *and* odd envelope functions.

Figure 6.3–6.5 also contain the TPA spectra without excitonic effects. We note an enhancement of the two-photon absorption due to the Coulomb interaction for the three linear polarizations.

6.4.3 Results: light polarized along the direction $\boldsymbol{x}+\boldsymbol{y}$

Let us now discuss the absorption of light polarized along a direction that is not a symmetry axis of the nanostructure. For this purpose, we consider an electromagnetic field with polarization vector $\boldsymbol{\epsilon}$ parallel to $\boldsymbol{x}+\boldsymbol{y}$. The corresponding two-photon absorption spectrum $\beta^{(x+y)}(\omega)$ is given in Figure 6.8. For comparison, we also show, in the same figure, the TPA spectra $\beta^{xx}(\omega)$ and $\beta^{yy}(\omega)$ for light polarized along the symmetry axes x and y. At least one additional peak, with respect to β^{xx} and β^{yy}, appears clearly in $\beta^{(x+y)}$. From the symmetry analysis in section 6.3, we know that the corresponding excitonic coherence must belong to the irreps A_1 or A_2. Nevertheless, to distinguish between the two types of excitons, a more detailed investigation is necessary.

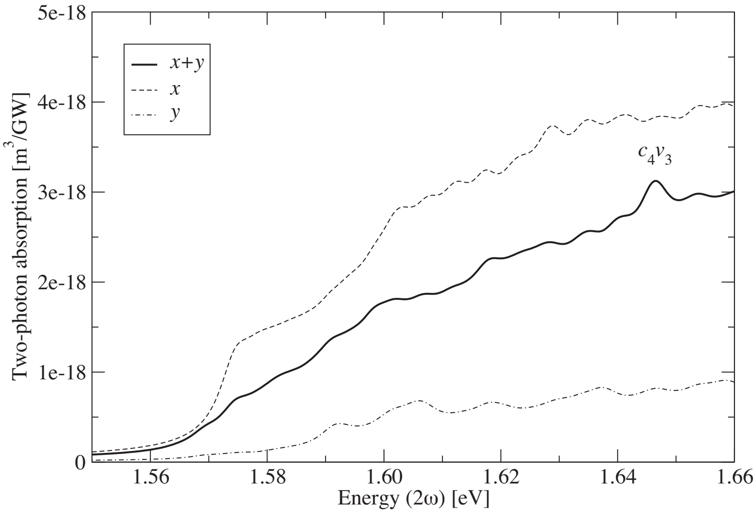

Figure 6.8: Two-photon absorption spectrum of the V-shaped quantum wire for light linearly polarized along $\boldsymbol{x}+\boldsymbol{y}$, $\boldsymbol{x}$ and $\boldsymbol{y}$.

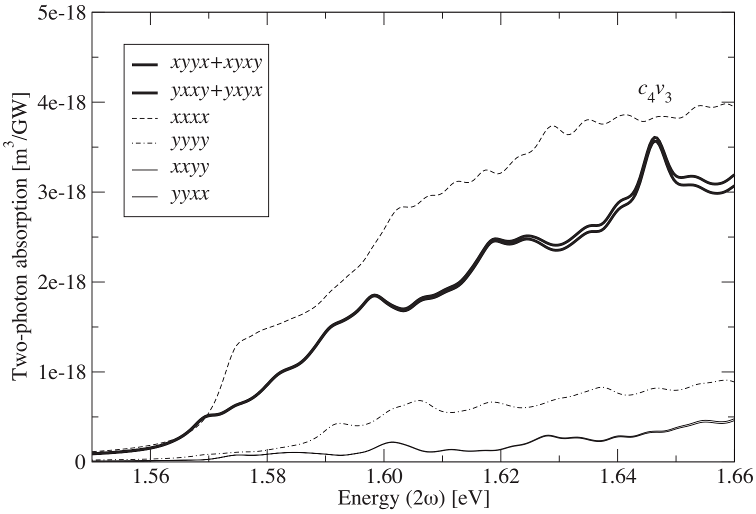

Figure 6.9: Contribution of the susceptibility tensor elements $\chi^{\kappa\lambda\mu\nu}$ to the two-photon absorption spectrum of the V-shaped quantum wire. The curve label $\kappa\lambda\mu\nu$ (respectively, $\mu\nu\nu\mu+\mu\nu\mu\nu$) designates the absorption related to the imaginary part of $\chi^{\kappa\lambda\mu\nu}$ (respectively, $\chi^{\mu\nu\nu\mu}+\chi^{\mu\nu\mu\nu}$).

According to (3.100), the total absorption coefficient for the direction of polarization $\boldsymbol{x}+\boldsymbol{y}$ can be expressed as

$$\beta^{(x+y)} = \frac{1}{4}(\beta^{xx} + \beta^{yy} + \beta^{xy} + \beta^{yx})\,. \tag{6.18}$$

We emphasize that from the experimental point of view it is difficult to measure directly the different contributions $\beta^{\mu\nu}$ to the total absorption coefficient. In fact, excitation with light polarized along $\boldsymbol{x}$, $\boldsymbol{y}$ or $\boldsymbol{x}+\boldsymbol{y}$ gives access to β^{xx}, β^{yy} or $\beta^{(x+y)}$ respectively. This information would be sufficient to extract $\beta^{xy} + \beta^{yx}$, which, according to (3.99), is related to the imaginary part of the susceptibility

$$\chi^{xxyy} + \chi^{yyxx} + \chi^{xyyx} + \chi^{xyxy} + \chi^{yxxy} + \chi^{yxyx}\,. \tag{6.19}$$

However, only the last four terms of (6.19) involve A_2-excitons, whereas the first two terms involve A_1-excitons. Thus, in order to determine the nature of the peaks appearing in the calculated spectrum $\beta^{(x+y)}$, we have to compare the contributions from the different elements of the third-order susceptibility tensor. The two-photon absorption related to imaginary part of these elements is shown in Figure 6.9. Note that $\chi^{xyxy} = \chi^{yxxy}$ and $\chi^{yxxy} = \chi^{yxyx}$, due to the intrinsic permutation symmetry.

First, we notice that the part of the two-photon absorption related to χ^{xxyy} and χ^{yyxx} is much smaller than the part described by χ^{yxxy} and χ^{xyyx}. Second, some of the additional peaks of $\beta^{(x+y)}$ clearly originate from χ^{yxxy} and χ^{xyyx}. The strongest one is labeled by the involved subbands c_4v_3. These peaks reflect the presence of A_2-excitons. Indeed, the corresponding susceptibilities derive from the transition amplitude (6.12) with $(\mu,\nu) = (x,y)$ and $(\mu,\nu) = (y,x)$. From a more physical point of view, they describe the microscopic process where two photons with different polarization ($\boldsymbol{x}$ and $\boldsymbol{y}$) are absorbed. Consequently, we argue that the formerly "dark" excitons A_2 might be observable in V-shaped QWRs by two-photon spectroscopy with light polarized perpendicularly to the growth direction $\boldsymbol{z}$, but not along one of the symmetry axes x and y.

Finally, we remark a small difference between the susceptibilities χ^{xyyx} and χ^{yxxy}. As discussed in section 3.11 (see equation (3.107)), this is due to the contribution of the slightly off-resonant two-photon transitions inherent to the band dispersion.

6.5 Conclusion

Using the multi-band effective Bloch equations derived in chapter 3, we calculated the two-photon absorption spectra of a V-shaped AlGaAs/GaAs QWR with a realistic band structure including the valence-band mixing. The Coulomb interaction was taken into account within the Hartree-Fock approximation. We discussed the strong polarization anisotropy and identified the dominant excitonic peaks for excitation by light polarized along the three principal symmetry axes.

Excitons that belong to the irreducible representation A_2 of the crystallographic point group $\mathbf{C}_{2v}$ are "dark" for one-photon spectroscopy *and* two-photon spectroscopy with light polarized along the symmetry axes x, y and z. We have shown that such A_2-excitons might however be observable with a polarization vector parallel to the direction $\boldsymbol{x}+\boldsymbol{y}$. One of them has clearly been identified on the calculated absorption spectrum.

7 Optical injection of current in quantum wires with excitonic effects

7.1 Introduction

In the following, the effective multi-band Bloch equations, derived in chapter 3, are applied to the optical injection of current *in the presence of excitonic effects.* Coherent control of charge current generated by quantum interference between one- and two-photon absorption has attracted considerable interest, since the first measurements in semiconductors [16, 129] (see chapter 5 for details). However, it has not yet been investigated how it may be affected by the Coulomb interaction. Nevertheless, new interesting phenomena may be expected, as it will be shown in this chapter.

This first investigation concentrates on a one-dimensional system: the realistic V-shaped AlGaAs/As quantum wire (QWR) studied in chapter 6. We give first results concerning the charge current generated in the QWR, and the associated terahertz emission, when the lowest B_1 and A_1 excitonic resonances are excited simultaneously by one- and two-photon transitions. Because of the different symmetry properties of the involved excitons, the injected charge current displays oscillations due to the quantum interference between the excitonic coherences. The oscillation frequency is given by the energy spacing between the excitons. This phenomenon has the same origin than the polarization interference between excitons with different energy, observed in quantum wells by four-wave mixing (see *e.g.* [145–147]). However, the excitation scheme described in this chapter makes the resulting modulation of the inter-band coherence also appear as oscillations in the charge current, which is directly related to the occupation of the bands.

7.2 Model

The dynamics is described by the effective multi-band Bloch equations, that include nonlinear processes such as two-photon transitions or AC Stark shifts. The model is detailed in chapter 3, and the important equations are summarized in section 5.3, so that we do not reproduce them here. However, note that the wavevector $\boldsymbol{k}$ is now one-dimensional and the surface S in the polarization current (5.27) is replaced by the length L of the QWR. The Coulomb interaction is treated within the Hartree-Fock approximation (see § 3.12). The Coulomb coupling $[V_q]^{c,c';c'',c'''}_{\cdots}$ and $[V_q]^{v,v';v'',v'''}_{\cdots}$ between electrons in the conduction subbands or between electrons in the valence subbands respectively are neglected, and we keep only the inter-band matrix elements $[V_q]^{c,c';v,v'}_{\cdots}$ and $[V_q]^{v,v';c,c'}_{\cdots}$.

The QWR described in section 6.2 is simultaneously excited by two laser pulses $\boldsymbol{A}_1 \cos(\omega t+\phi)$ and $\boldsymbol{A}_2 \cos(2\omega t)$, which induce respectively (quasi-) resonant one- and two-photon inter-band transitions. With respect to the notations used throughout this thesis, the frequencies and phases of these fields correspond to $\phi_1 = \phi$, $\phi_2 = 0$ and $\omega_1 = 2\omega_2 = 2\omega$ (see equation (5.19)). The two pulses have a duration of 100 fs at half maximum (of intensity) and are co-polarized along the quantum wire (x axis). The optical frequency $2\hbar\omega = 1.57$ eV corresponds to an excitation energy in the middle between the two lowest c_1v_1 excitonic resonances for light polarized along the x axis, namely the lowest B_1-exciton in the one-photon absorption spectrum (Figure 6.6) and the lowest A_1-exciton in the two-photon absorption spectrum (Figure 6.3). The spectral widths of the pulses are sufficiently large to cover both resonances. The peak intensities are chosen to get a high contrast in the interference: 7 MW/cm^2 and 10 GW/cm^2 for the $\boldsymbol{A}_1$- and $\boldsymbol{A}_2$-pulse respectively. The decoherence and the thermalization of the carrier distributions are modeled by a unique characteristic time τ. According to the notations in section 3.14, this corresponds to $\tau_{mn} = \tau$, $\forall\, m, n$. The calculations are essentially done for a long relaxation time $\tau = 1$ ps.

The equation of motion is solved for a reduced density matrix describing the three lowest pairs of conduction bands and the four highest pairs of valence bands (Figure 6.2). The two bands defining a pair are conjugate by time-reversal symmetry. In order to correctly describe the two-photon transitions, one should in principle take into account a complete set of intermediate states. In practice however, we restrict ourselves to the 12 lowest pairs of conduction bands and the 24 highest pairs of valence bands. In terms of the notations introduced in chapter 3, this corresponds to 14 bands in group $\mathbb{A}$ and 58 bands in group $\mathbb{B}$.

7.3 Results and discussion

In Figure 7.1, we show the charge current[1] (5.27) injected along the quantum wire for two values of the phase difference between the pulses: $\phi = 0$ and $\phi = \pi/2$. The results are displayed for a long relaxation time ($\tau = 1$ ps), and compared to the values obtained in the same configuration but without Coulomb interaction. The power spectrum of the associated terahertz emission (5.31) is displayed in Figure 7.2.

When the Coulomb interaction is taken into account within the Hartree-Fock approximation, a strongly oscillating charge current appears. First, we note that

---

[1] low-frequency part of the polarization current

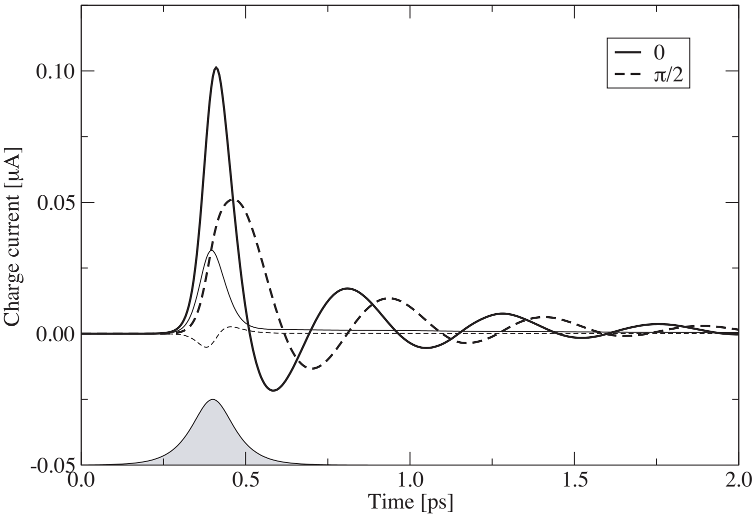

Figure 7.1: Charge current along the V-shaped quantum wire for two different optical phases: $\phi = 0$ (full line) and $\phi = \pi/2$ (dashed line). Thick lines: the Coulomb interaction is taken into account within the Hartree-Fock approximation. Thin lines: the Coulomb interaction is neglected. Relaxation time $\tau = 1$ ps. The shaded curve on the bottom of the figure shows the time-dependence of the optical pulses in the QWR.

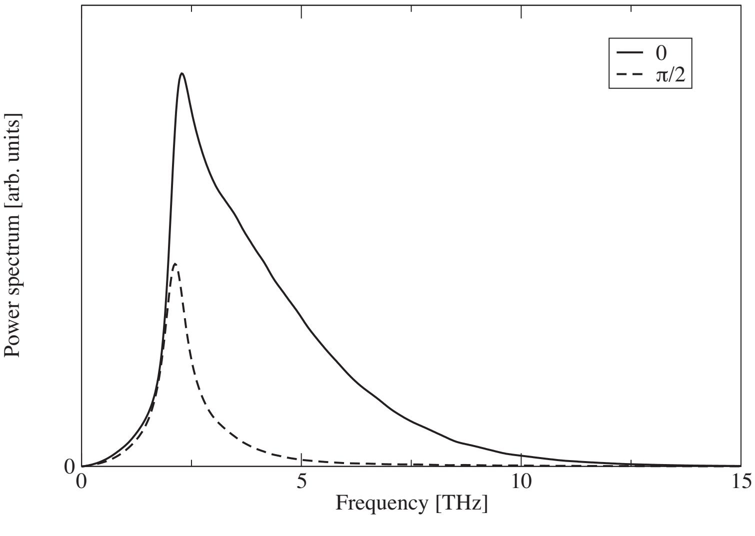

Figure 7.2: Power spectrum of the far-field THz emission for two different optical phases: $\phi = 0$ (full line) and $\phi = \pi/2$ (dashed line). Relaxation time $\tau = 1$ ps.

the current diminishes and the oscillations disappear, when the Coulomb interaction is neglected. This indicates that excitonic resonances are involved. Second, the oscillations subsist even after the optical pulses vanished. We also checked that the oscillation frequency does not depend on the pulse frequencies, insofar as the same resonances are excited. Finally, there is no current injected when only one beam is present.

7.3.1 Charge current injection: two contributions

The oscillating current is present in both phase configurations ($\phi = 0$ and $\phi = \pi/2$). However, as it can be seen from the terahertz spectra, an additional (broader) contribution appears for $\phi = 0$.

To investigate this phase dependence, let us first remind the phenomenon of current injection by interference between one- and two-photon transitions. As discussed in section 5.2, the same initial and final states are coupled by two coherent electromagnetic fields of frequency 2ω and ω. The interferences between the two processes induce a charge current, whose amplitude can be controlled by the relative phase between the two pulses: the current is maximal for the phase $\phi = 0$ and zero for the phase $\phi = \pi/2$.

The oscillating charge current in Figure 7.1 separates into two contributions. The amplitude of one part of the current can be controlled by the relative phase between the beams. In particular, it vanishes for $\phi = \pi/2$. By contrast, the rest of the current can not be switched of by tuning the phases of the pulses. The oscillations we are interested in appear in this second contribution. Figure 7.3 shows that the amplitude of the oscillating current (after the pulses vanished) is not affected by the optical phase ϕ. Nevertheless, the *phase* of the oscillations can still be controlled.

In the terahertz emission, the oscillations of the current appear in both spectra as a sharp peak centered around 2 THz. In the case where an additional current is injected by tuning the phase to $\phi = 0$, a broader contribution with higher frequency tail is superimposed on the peak.

We emphasize that in the present case, the optical frequencies are detuned with respect to the inter-band transition frequencies, as the QWR is excited slightly *below* the band gap. The injected charge current (and carrier densities) for $\phi = 0$ would be much higher, if the subbands of the QWR were excited resonantly. However, in this chapter, we focus on the excitonic contributions below the band gap.

In order to isolate and analyze the current oscillations, we concentrate now on the situation where no additional current is injected by interference between one- and two-photon transitions (*i.e.* $\phi = \pi/2$). In this case, the peak in the power spectrum of the far-field terahertz emission is centered at ~ 2.13 THz (or ~ 8.8 meV).

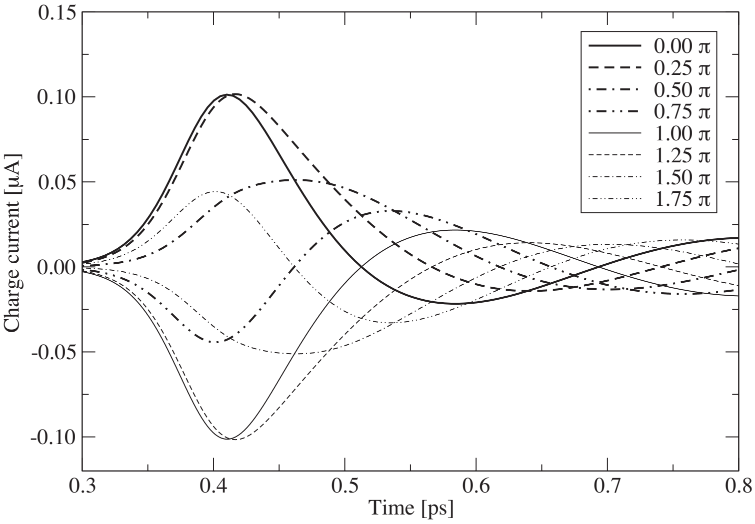

Figure 7.3: Charge current along the V-shaped quantum wire for different optical phases ϕ. Relaxation time $\tau = 1$ ps.

7.3.2 Analysis: interference between B_1 and A_1 excitonic coherences

The low-frequency oscillations in the polarization current are generated by interferences between B_1 and A_1 excitonic coherences stimulated respectively by the $\boldsymbol{A}_1$ and $\boldsymbol{A}_2$ electromagnetic fields. Indeed, the selection rules discussed in section 6.3 imply that the effective one- and two-photon interactions excite only excitons belonging to the irreps B_1 and A_1 respectively. The strong peak of the excitonic ground state in the one-photon absorption spectrum (Figure 6.6) indicates that the $\boldsymbol{A}_1$-pulse primarily builds up the lowest B_1 excitonic coherence related to the subbands c_1 and v_1. On the other hand, the $\boldsymbol{A}_2$-pulse stimulates the A_1 excitonic resonances associated to the same subbands, that appear close to the band edge in the two-photon absorption spectrum (Figure 6.3). The statement that this process involves mainly excitons related to the subbands c_1 and v_1 is confirmed by the small amount of current injected in the other subbands. Indeed, Figure 7.4 shows that the essential contribution to the charge current is given by the electrons in the subband pairs c_1 and v_1. The oscillatory motion of the electrons in the lowest conduction band c_1 is illustrated in Figure 7.5, where we have plotted the carrier distribution[2] in reciprocal space, at different times during the evolution.

To get a better insight into the underlying physical process, let us illustrate this phenomenon by a simple two-band model. For this purpose, we consider an undoped

---

[2] a diagonal element of the reduced density matrix

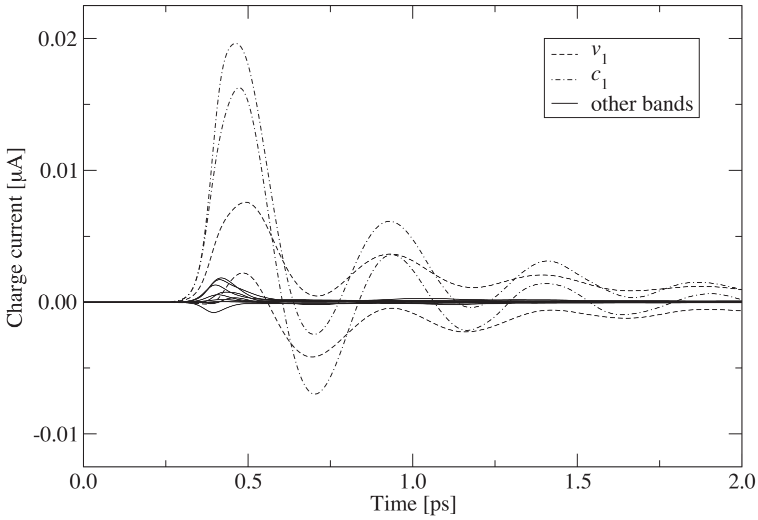

Figure 7.4: Charge current in the different subbands. Relaxation time: $\tau = 1$ ps. Optical phase: $\phi = \pi/2$.

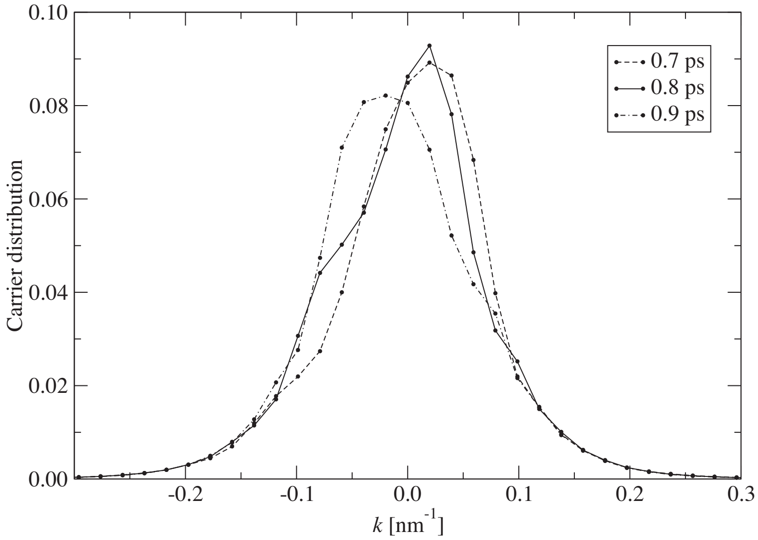

Figure 7.5: Carrier distribution in the lowest pair of conduction subbands c_1 at different times (0.7, 0.8 and 0.9 ps). The distribution is shown for the subband belonging to ${}^1E_{1/2}$. The distribution in the conjugate subband belonging to ${}^2E_{1/2}$ is similar. Optical phase: $\phi = \pi/2$.

semiconductor described by the occupation number $n_k = \rho_{cc,k} = 1 - \rho_{vv,k}$ and the inter-band coherence $p_k = \rho_{cv,k}$. The semiconductor Bloch equations (SBE) that govern the dynamics can be written as

$$\begin{aligned} \frac{d}{dt} n_k &= -\frac{2}{\hbar} \mathrm{Im}\big[(\boldsymbol{A\Pi}_k + \sum_q V_q p_{k+q}) {p_k}^*\big] \\ \frac{d}{dt} p_k &= -i\Omega_k p_k + \frac{i}{\hbar}(1-2n_k)(\boldsymbol{A\Pi}_k + \sum_q V_q p_{k+q})\,, \end{aligned} \tag{7.1}$$

where Ω_k is the inter-band frequency and $\mathbf{\Pi}_k$ the inter-band momentum matrix element. After mixing the two equations, one is left with

$$\frac{d}{dt}|p_k|^2 = (1-2n_k)\frac{d}{dt} n_k\,. \tag{7.2}$$

Let us assume initial conditions that correspond to an unexcited system: $n_k(0) = p_k(0) = 0$. One finds the relation

$$n_k = \frac{1}{2}\big(1 - \sqrt{1 - 4|p_k|^2}\big) \tag{7.3}$$

valid for all times. For weak excitation, it reduces to $n_k \simeq |p_k|^2$. Following the perturbative scheme developed in chapter 3, the dipole interaction in the SBE (7.1) can easily be replaced by effective first- and second-order interactions describing resonant one- and two-photon transitions. Thus, the relation (7.3) remains valid for the interference process we want to discuss here.

Let us now assume that we excite simultaneously two excitonic resonances at frequencies Ω_1 and Ω_2. The corresponding coherence is given by

$$p_k = \bar{p}_{1,k} e^{i\Omega_1 t} + \bar{p}_{2,k} e^{i\Omega_2 t}\,, \tag{7.4}$$

where, in the case of *quasi-resonant* optical excitation, the functions $\bar{p}_{i,k}$ are slowly varying in time. The squared module of this coherence becomes

$$|p_k|^2 = |\bar{p}_{1,k}|^2 + |\bar{p}_{2,k}|^2 + 2\mathrm{Re}\big[\bar{p}_{1,k}\,\bar{p}^*_{2,k}\,e^{i(\Omega_1-\Omega_2)t}\big]\,. \tag{7.5}$$

For weak excitation, this expression is almost equal to the carrier distribution n_k. As a consequence, the occupation number n_k oscillates with frequency $\Omega_1 - \Omega_2$. Now, if the coherences $\bar{p}_{1,k}$ and $\bar{p}_{2,k}$ are respectively even and odd as functions of the wavevector k, and of comparable magnitude, then the resulting carrier distribution is asymmetric in k-space, leading to a macroscopic charge current. The important point here, is that the excitonic frequencies do not depend on the wavevector k. Thus, all occupation numbers n_k oscillate in phase. It follows that the related

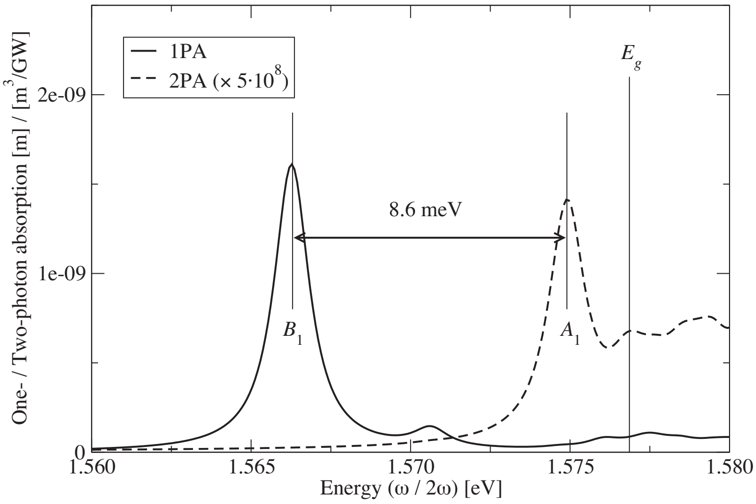

Figure 7.6: Lowest B_1 and A_1 excitonic resonances in the one-photon absorption (1PA) and two-photon absorption (2PA) respectively. The absorption spectra are calculated for thermalized carrier distributions that correspond approximatively to the carrier densities excited in the configuration for current injection. Decoherence time: $\tau = 1$ ps (note that the spectra in chapter 6 correspond to $\tau = 0.2$ ps). E_g: energy gap of the QWR.

charge current oscillates with frequency $\Omega_1 - \Omega_2$ given by the energy spacing between the involved excitonic resonances. This is what we observe in Figure 7.1–7.5. First, the lowest B_1 and A_1 excitonic coherences excited by the $\boldsymbol{A}_1$ and $\boldsymbol{A}_2$ pulses display respectively an (even) S-like and (odd) P-like shape in reciprocal space (not shown). Second, the central frequency of the peak in the THz power spectrum ($\sim$ 8.8 meV) corresponds approximatively to the energy spacing between the B_1- and A_1-excitons related to the bands c_1 and v_1 ($\sim$ 8.6 meV) shown in Figure 7.6. The small discrepancy is discussed in what follows.

First, the energies of the excitonic resonances shift with higher carrier density. At zero density, the lowest B_1 and A_1 excitons are separated by $\sim$ 9.7 meV. The absorption spectra shown in Figure 7.6 are calculated for finite *thermalized* carrier distributions corresponding to the densities of energy and densities of carriers that are injected by the two laser pulses in the configuration for current generation: $\sim 2 \times 2 \cdot 10^4$ electrons/cm at $\sim$ 75 K in the lowest pair of conduction bands and $\sim 2 \times 2 \cdot 10^4$ holes/cm at $\sim$ 18 K in the highest pair of valence bands (the temperatures are given by the average energy of the excited carriers). Nevertheless, these thermalized carrier distributions are not exactly equal to the optically injected distributions. The latter increase while the current is building up, and evolve during the subsequent oscillations and thermalization (see Figure 7.5). This affects the excitonic energies.

Second, the $\boldsymbol{A}_2$ laser pulse excites also excitonic resonances at higher energy. Indeed, the two-photon absorption spectra in Figure 7.6 shows that the absorption near the band gap and the one due to the lowest A_1 exciton are of comparable magnitude. These (bound or unbound) excitons also interfere with the B_1 exciton, and affect the current.

Finally, if one wishes to identify precisely the energy spacing between the excitons in the terahertz emission, then all contributions that come from the build-up and decay of the current should first be deconvoluted from the power spectrum.

To summarize, the two pulses of frequency 2ω and ω build up two inter-band coherences, which interfere. This results in an asymmetric carrier distribution in the bands. The key point is that the beams excite two excitonic resonances of *different* energies. As a consequence, the corresponding coherences oscillate with different frequencies. This leads to an injected current that oscillates with frequency given by the energy spacing between the excitons.

Concerning the coherent control of the injected current, we note that the optical phases of the beams can not be used to tune the amplitude of the oscillating current. This is related to the fact that, even in the stationary regime, there is no constant phase relation between the interfering coherences. However, one can modify the phase of the oscillations. By contrast, if the two beams excite two resonances with *identical* energies, then the associated coherences oscillate in phase (with same frequency). In such a case, the current does not oscillate. However, the *constant* relative phase between the coherences can be shifted by the optical phases of the beams, which allows to control the current injection rate *for all times.*

7.3.3 Dependence on the relaxation time

In Figure 7.7, we show the calculated time-evolution of the optically injected charge current for different relaxation times (1 ps, 0.5 ps and 0.2 ps) and $\phi = \pi/2$. The power spectrum of the corresponding terahertz emission is displayed in Figure 7.8. One sees that the relaxation time must be sufficiently long, for the current oscillations to be observable. This implies low carrier densities, and thus weak excitation. On the other hand, the oscillations appear in the charge current, which is directly related to carrier distribution in the bands. Therefore, from the experimental point of view, a stronger signal requires higher carrier densities, which accelerates the decay of the current. This issue deserves further investigations.

7.4 Conclusion

Using the effective multi-band Bloch equations including the Coulomb interaction within the Hartree-Fock approximation (chapter 3), we calculated the charge current injected in a V-shaped AlGaAs/GaAs QWR, when excited slightly below the band

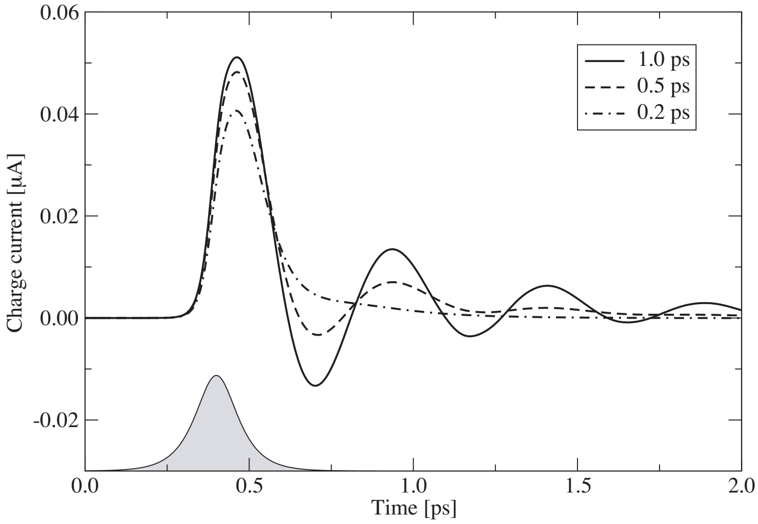

Figure 7.7: Charge current along the V-shaped quantum wire for different relaxation times τ (1 ps, 0.5 ps and 0.2 ps). Optical phase: $\phi = \pi/2$. The shaded curve on the bottom of the figure shows the time-dependence of the optical pulses in the QWR.

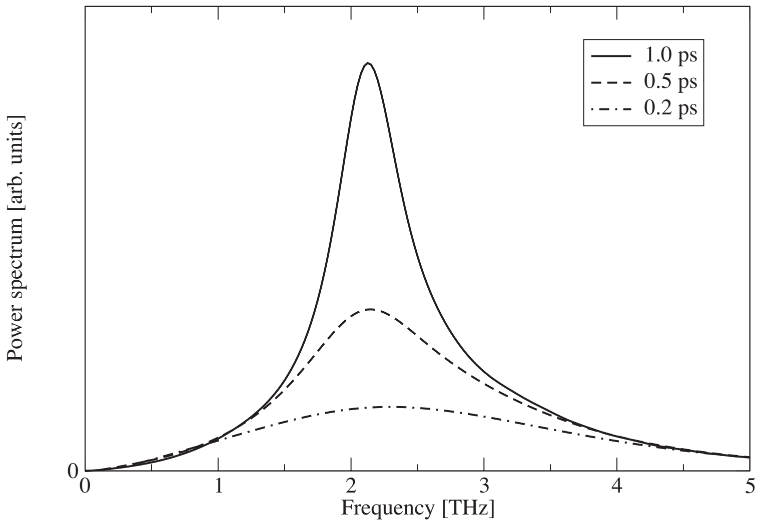

Figure 7.8: Power spectrum of the far-field THz emission for different relaxation times τ (1 ps, 0.5 ps and 0.2 ps). Optical phase: $\phi = \pi/2$.

gap by two phase-related femtosecond laser pulses of frequency ω and 2ω. The two optical beams excite independently the lowest B_1 and A_1 excitonic resonances. We have shown that the interferences between these excitonic coherences result in terahertz oscillations in the low-frequency polarization current, that subsist after the laser pulses vanished. For a long decoherence time (1 ps), these oscillations appear as a peak in the power spectrum of the far-field terahertz emission. By contrast to the current injected by resonant one- and two-photon inter-band transitions discussed in chapter 5, this oscillating current can not be switched of by tuning the relative phase between the two pulses.

8 Conclusions

In this thesis, we investigated the dynamics of two-photon transitions in semiconductors. The modeling of these processes was approached on different levels of complexity.

First we developed a rate equation model to study the feasibility of two-photon amplification in a semiconductor microcavity. We estimated the integrated two-photon gain that can be expected in a pump-probe measurement. Although two-photon absorption is an important process, the amplification predicted is fairly low ($\sim$2% for 11 imbedded quantum wells) because of the limiting intra-band relaxation and the very high pumping rate and optical intensities that are required. A better insight into the dependence of the gain on the various physical parameters was obtained by deriving an analytical formula resulting from various adequate approximations on the rate equations.

Second, we developed a new general theory of multi-band effective Bloch equations for quasi-resonant one- and two-photon transitions in semiconductors. This theory leads to equations of motions that consistently account for all quasi-resonant interaction terms up to the second order in the optical fields. They include various interfering linear and nonlinear optical processes, such as inter-band one- and two-photon absorption, coherent control of photocurrent, second-harmonic generation, difference-frequency mixing, or the AC Stark shifts. Since all electronic states do not participate to the same degree to the dynamics, we selected the important bands to define a reduced density matrix for which the time evolution is calculated. Yet the bands eliminated from the dynamics may contribute to the second-order transitions as intermediate states. They were thus included within a perturbative scheme in an effective dipole interaction. A similar approach was used to derive an effective expression for the macroscopic polarization current that is consistent with the physical information retained in the effective multi-band Bloch equations. We finally identified the different contributions to this current. Since this approach is new, the entire procedure and the involved approximations have been largely detailed.

We would like to emphasize that the various nonlinear phenomena described by the effective equations of motion may be strongly coupled, especially when the optical frequencies become equal to transition frequencies of the medium. In this context, an interesting issue that can be properly addressed by our model is, for instance, the interplay between two-photon absorption/gain and parametric amplification (a $\chi^{(3)}$ and $\chi^{(2)}$ process respectively), when the optical frequencies approach and eventually cross the band gap.

In this thesis, we focused on an important application of this model, namely the optical injection of charge and spin current originating from the interferences between one- and two-photon transitions induced by ultrashort pulses. We first investigated this time-dependent phenomenon in a symmetric AlGaAs/GaAs quantum well with realistic band structure. As an important result, the separate contributions of the populations and inter-valence-band coherences to the charge current and THz emission were identified for the first time. We also calculated and discussed the influence of the Stark shifts and Raman-like inter-valence-band transitions.

The carrier-carrier Coulomb interaction can be included in the effective multiband Bloch equations in a standard way. We solved them numerically within the Hartree-Fock approximation in a quasi-one-dimensional case, namely for a V-shaped AlGaAs/GaAs quantum wire. As a first result, we obtained the strongly anisotropic two-photon absorption spectra including excitonic effects. Furthermore, we showed that the excitons belonging to the irreducible representation A_2 of the crystallographic point group $\mathbf{C}_{2v}$, which are "dark" in one-photon spectroscopy, may be observable in two-photon spectroscopy with light polarized along a direction that is *not* a symmetry axis of the heterostructure.

With the same model, we calculated the charge current injected in a V-shaped AlGaAs/GaAs QWR, when excited slightly below the band gap by two phase-related femtosecond laser pulses of frequency ω and 2ω. The two optical beams excite independently the lowest B_1 and A_1 excitonic resonances. First results showed that the interference between these excitonic coherences induce terahertz oscillations in the low-frequency polarization current. For a long decoherence time (1 ps), these oscillations appear as a clear peak in the power spectrum of the far-field terahertz emission. The oscillation frequency corresponds to the energy spacing between the lowest B_1 and A_1 excitons.

The present work can be extended in many directions. Let us mention two of them. A first important task would be a more detailed investigation of the many-body effects. One could start with a study of the influence of Coulomb correlations at high density. A more challenging improvement of the model is the inclusion of Coulomb scattering beyond the Hartree-Fock approximation. This may lead to interesting physics especially because of the complicated asymmetric carrier distributions that can be generated by the one- and two-photon absorption interference scheme.

Another way that can be taken, is extending the present model to effective Maxwell-Bloch equations, that account for the propagation of the *emitted* light (the polarization) and its back-coupling to the carriers. An interesting application would be, for instance, the investigation of the time-dependent interaction between electromagnetic pulses and quantum wells in a Fabry-Pérot resonator.

A Confinement factor for two-photon transitions

This appendix is devoted to the relation between the confinement factors for one- and two-photon transitions. The following notations will be used.

S_i^{w}	Density of ω_i-photons in the quantum wells (QWs)
S_i^{c}	Density of ω_i-photons in the cavity (without the QWs)
$S_i^{\mathrm{c+w}}$	Density of ω_i-photons in the cavity and in the QWs ($S_i^{\mathrm{c}} + S_i^{\mathrm{w}}$)
n_{c}	Refractive index in the cavity
n_{w}	Refractive index in the quantum well
Γ_1	Confinement factor for one-photon transitions
Γ_2	Confinement factor for two-photon transitions
g_1	One-photon material gain coefficient
g_2	Two-photon material gain coefficient

The one- and two-photon confinement factors Γ_1 and Γ_2 are defined by the equations

$$\dot{S}_1^{\mathrm{c+w}} = \frac{c}{n_{\mathrm{w}}}\, S_1^{\mathrm{w}}\, g_1 = \left(\frac{c}{n_{\mathrm{w}}} S_1^{\mathrm{w}} + \frac{c}{n_{\mathrm{c}}} S_1^{\mathrm{c}}\right) \Gamma_1\, g_1\,, \tag{A.1}$$

$$\dot{S}_2^{\mathrm{c+w}} = \left(\frac{c}{n_{\mathrm{w}}}\, S_2^{\mathrm{w}}\right)^2 g_2 = \left\{ \left(\frac{c}{n_{\mathrm{w}}} S_2^{\mathrm{w}}\right)^2 + \left(\frac{c}{n_{\mathrm{c}}} S_2^{\mathrm{c}}\right)^2 \right\} {\Gamma_2}^2\, g_2\,. \tag{A.2}$$

The time-derivative $\dot{S}_i^{\mathrm{c+w}}$ expresses the photon density variation in the microcavity. The products $\Gamma_1\, g_1$ and ${\Gamma_2}^2\, g_2$ represent the gain coefficients for equivalent photon densities homogeneously distributed over the entire structure (cavity and QWs). It follows that

$$S_1^{\mathrm{c+w}} = \frac{\Gamma_1\, n_{\mathrm{w}} + (1 - \Gamma_1)\, n_{\mathrm{c}}}{\Gamma_1\, n_{\mathrm{w}}}\, S_1^{\mathrm{w}}\,, \tag{A.3}$$

$$S_2^{\mathrm{c+w}} = \frac{\Gamma_2\, n_{\mathrm{w}} + \sqrt{1 - {\Gamma_2}^2}\, n_{\mathrm{c}}}{\Gamma_2\, n_{\mathrm{w}}}\, S_2^{\mathrm{w}}\,. \tag{A.4}$$

If one assumes that the optically active region (*i.e.* the QWs) does not affect the cavity modes, then the ratios

$$S_1^{\mathrm{c+w}}/S_1^{\mathrm{w}} = 1 + \frac{(1-\Gamma_1)}{\Gamma_1}\frac{n_\mathrm{c}}{n_\mathrm{w}} \tag{A.5}$$

$$S_2^{\mathrm{c+w}}/S_2^{\mathrm{w}} = 1 + \frac{\sqrt{1-{\Gamma_2}^2}}{\Gamma_2}\frac{n_\mathrm{c}}{n_\mathrm{w}} \tag{A.6}$$

must be identical. The two-photon confinement factor Γ_2 is therefore related to the one-photon confinement factor Γ_1 by

$${\Gamma_2}^2 = \frac{{\Gamma_1}^2}{{\Gamma_1}^2 + (1-\Gamma_1)^2}\,. \tag{A.7}$$

B Bessel functions

Definition

$$\mathrm{J}_n(z) = \frac{1}{\pi}\int_0^\pi \cos(z\sin\theta - n\theta)\,d\theta \qquad n\in\mathbb{Z} \qquad z\in\mathbb{C} \tag{B.1}$$

Properties

$$\mathrm{J}_{-n}(z) = (-1)^n\mathrm{J}_n(z) = \mathrm{J}_n(-z) \tag{B.2}$$

$$\mathrm{J}_n(z) \simeq (z/2)^n/n! \qquad \text{for } \ n\in\mathbb{N} \ \text{ and } \ z\ll 1 \tag{B.3}$$

$$\lim_{z\to 0}\frac{n}{z}\mathrm{J}_n(z) = \frac{1}{2}\delta_{n,\pm 1} \tag{B.4}$$

Expansion

$$e^{iz\sin\theta} = \sum_{n\in\mathbb{Z}} \mathrm{J}_n(z)\,e^{in\theta} \tag{B.5}$$

C Third-order interaction terms

In the following, we give all interaction terms that are cubic in the electromagnetic fields. Up to the third order in the field, the effective multi-band Bloch equation can be written as

$$\partial_t \tilde{\rho}_{AA'} = \left[\partial_t \tilde{\rho}_{AA'}\right]^{(1)} + \left[\partial_t \tilde{\rho}_{AA'}\right]^{(2)} + \left[\partial_t \tilde{\rho}_{AA'}\right]^{(3)} . \tag{C.1}$$

The first- and second-order terms are detailed in chapter 3 (see (3.32) and (3.33)). The third order-term is given by

$$\begin{aligned}
&\left[\partial_t \tilde{\rho}_{AA'}\right]^{(3)} = \\
&\quad +i \sum_{j,k,l} \sum_{\alpha,\beta,\gamma} A_j^\alpha A_k^\beta A_l^\gamma / \hbar^3 \sum_a \sum_{a' \neq a} \sum_b \sum_{N,N',N''} \\
&\qquad \times \Bigg[+ \tilde{\rho}_{Aa'} \Pi^\alpha_{a'a} \Pi^\beta_{ab} \Pi^\gamma_{bA'} \mathcal{G}^j_{a'a}(N) \mathcal{G}^k_{ab}(N') \mathcal{G}^l_{bA'}(N'') \\
&\qquad\quad \times \frac{e^{i\left(\Omega_{a'A'} - (N+N'+N'')\circ\omega\right)t - i(N+N'+N'')\circ\phi}}{\left(\Omega_{ab} - N' \circ \omega\right)\left(\Omega_{a'b} - (N+N') \circ \omega\right)} \\
&\qquad\quad - \Pi^\gamma_{Ab} \Pi^\beta_{ba} \Pi^\alpha_{aa'} \tilde{\rho}_{a'A'} \mathcal{G}^l_{Ab}(N'') \mathcal{G}^k_{ba}(N') \mathcal{G}^j_{aa'}(N) \\
&\qquad\quad \times \frac{e^{i\left(\Omega_{Aa'} - (N+N'+N'')\circ\omega\right)t - i(N+N'+N'')\circ\phi}}{\left(\Omega_{ba} - N' \circ \omega\right)\left(\Omega_{ba'} - (N+N') \circ \omega\right)} \Bigg] \\
&\quad -i \sum_{j,k,l} \sum_{\alpha,\beta,\gamma} A_j^\alpha A_k^\beta A_l^\gamma / \hbar^3 \sum_a \sum_b \sum_{b' \neq b} \sum_{N,N',N''} \\
&\qquad \times \Bigg[+ \tilde{\rho}_{Aa} \Pi^\alpha_{ab'} \Pi^\beta_{b'b} \Pi^\gamma_{bA'} \mathcal{G}^j_{ab'}(N) \mathcal{G}^k_{b'b}(N') \mathcal{G}^l_{bA'}(N'') \\
&\qquad\quad \times \frac{e^{i\left(\Omega_{aA'} - (N+N'+N'')\circ\omega\right)t - i(N+N'+N'')\circ\phi}}{\left(\Omega_{ab'} - N \circ \omega\right)\left(\Omega_{ab} - (N+N') \circ \omega\right)} \\
&\qquad\quad - \Pi^\gamma_{Ab} \Pi^\beta_{bb'} \Pi^\alpha_{b'a} \tilde{\rho}_{aA'} \mathcal{G}^l_{Ab}(N'') \mathcal{G}^k_{bb'}(N') \mathcal{G}^j_{b'a}(N) \\
&\qquad\quad \times \frac{e^{i\left(\Omega_{Aa} - (N+N'+N'')\circ\omega\right)t - i(N+N'+N'')\circ\phi}}{\left(\Omega_{b'a} - N \circ \omega\right)\left(\Omega_{ba} - (N+N') \circ \omega\right)} \Bigg] .
\end{aligned} \tag{C.2}$$

D Second-order transitions with resonant bands as intermediate states

In this appendix, we detail how we include the bands defining the reduced density matrix (group $\mathbb{A}$), as intermediate states in the second-order terms of the effective Hamiltonian (§ D.1) and effective polarization current (§ D.2).

D.1 Effective multi-band Bloch equations

The (non-hermitian) effective Bloch equations (3.39) for the reduced density matrix have the general form

$$\partial_t \tilde{\rho} = -i\,[\tilde{H}\tilde{\rho} - \tilde{\rho}\tilde{H}^\dagger] \tag{D.1}$$

with

$$\tilde{H} = \sum_j \tilde{H}_j = \sum_j \hat{H}_j\, e^{i\Omega_j t}\,. \tag{D.2}$$

The square matrices $\hat{H}_j$ are slowly varying in time compared to the oscillations of frequency $\Omega_{j\neq 0}$. Furthermore we assume $\Omega_0 \simeq 0$, so that the only low-frequency term in the Hamiltonian $\tilde{H}$ is $\tilde{H}_0$. In the Bloch equations defined by (3.40) to (3.43), the slowly varying part $\tilde{H}_0$ contains the linear and quadratic terms of frequency $\Omega_{cv}-\omega_1$, $\Omega_{cv}-2\omega_2$, $\Omega_{cc'}$ and $\Omega_{vv'}$, whereas the high frequencies in $\tilde{H}_{j\neq 0}$ correspond to $\Omega_{cv}+\omega_1$, $\Omega_{cv}\pm\omega_2$, $\Omega_{cc'}\pm\omega_j$ and $\Omega_{vv'}\pm\omega_j$.

Because of the rapidly oscillating terms in $\tilde{H}$, the solution of (D.1) contains also a high frequency part besides its dominant slow part $\tilde{\rho}_0$. In general, the frequencies in $\tilde{\rho}$ cover all harmonics $\sum_j \sum_{n_j} n_j \Omega_j$ with integer n_j's. However, for our purpose, this set of frequencies is restricted to the Ω_j's appearing in the Hamiltonian (D.2). This is justified by the fact that we want to derive an effective equation of motion for $\tilde{\rho}_0$ up to the *second* order in the $\tilde{H}_j$'s. By contrast, the neglected harmonics would contribute only to a higher order, once approximated by an expression containing only $\tilde{\rho}_0$. Thus, the reduced density matrix is written as

$$\tilde{\rho} = \sum_k \tilde{\rho}_k = \sum_k \hat{\rho}_k \, e^{i\Omega_k t} \,, \tag{D.3}$$

where all matrices $\hat{\rho}_k$ are slowly varying in time. The differential equation (D.1) now becomes

$$\partial_t \tilde{\rho} = -i \, [\tilde{H}_0 \tilde{\rho}_0 - \tilde{\rho}_0 \tilde{H}_0^\dagger] - i \sum_{j \neq 0} \sum_{k \neq 0} [\tilde{H}_j \tilde{\rho}_k - \tilde{\rho}_k \tilde{H}_j^\dagger] \,. \tag{D.4}$$

In what follows, we isolate the dominant contributions in the Bloch equations and eliminate the terms displaying rapid oscillations. The latter may however contribute resonantly to higher orders and have therefore to be included in the corresponding effective transition amplitudes. In other words, the second term on the r.h.s. of (D.4) may contain a significant low-frequency part. This contribution is added to $\tilde{H}_0$ in order to get an effective equation of the form $\partial_t \tilde{\rho}_0 = -i \, [\bar{H}' \tilde{\rho}_0 - \tilde{\rho}_0 \bar{H}']$, where $\bar{H}'$ is slowly varying in time and includes all resonant second-order processes. This effective equation is finally symmetrized by introducing the hermitian Hamiltonian $\bar{H} = (\bar{H}' + \bar{H}'^\dagger)/2$, and becomes $\partial_t \tilde{\rho}_0 = -i \, [\bar{H}, \, \tilde{\rho}_0]$.

To start, let us write down the low-frequency part of the Bloch equation (D.4):

$$\partial_t \tilde{\rho}_0 = -i \, [\tilde{H}_0 \tilde{\rho}_0 - \tilde{\rho}_0 \tilde{H}_0^\dagger] - i \, \Big\{ \sum_{j \neq 0} \sum_{k \neq 0} [\tilde{H}_j \tilde{\rho}_k - \tilde{\rho}_k \tilde{H}_j^\dagger] \Big\}_0 \,. \tag{D.5}$$

The notation $\{...\}_l$ designates the restriction to the contribution of frequencies near Ω_l. The slowly varying second-order terms of the final effective Hamiltonian $\bar{H}$ are obtained by replacing $\tilde{\rho}_k$ in (D.5) by the solution of

$$\begin{aligned} \partial_t \tilde{\rho}_k &= -i \, \Big\{ \sum_{jl} [\tilde{H}_j \tilde{\rho}_l - \tilde{\rho}_l \tilde{H}_j^\dagger] \Big\}_k \\ &\simeq -i \, \Big\{ \sum_{j} [\tilde{H}_j \tilde{\rho}_0 - \tilde{\rho}_0 \tilde{H}_j^\dagger] \Big\}_k \\ &= -i \, [\hat{H}_k \tilde{\rho}_0 \, e^{i\Omega_k t} - \tilde{\rho}_0 \hat{H}_k^\dagger \, e^{-i\Omega_k t}] \,. \end{aligned} \tag{D.6}$$

The second line is commented below. By integrating this differential equation, we obtain

$$\tilde{\rho}_k \simeq {\Omega_k}^{-1} [\hat{H}_k \tilde{\rho}_0 \, e^{i\Omega_k t} + \tilde{\rho}_0 \hat{H}_k^\dagger \, e^{-i\Omega_k t}] \,, \tag{D.7}$$

where we have used the fact that $\hat{H}_k$ is slowly varying in time compared to the complex exponentials. Furthermore, in distant past, the fields were switched off and the system was at equilibrium *i.e.* $\hat{H}_k(t=-\infty)=0$ and $\tilde{\rho}_{k\neq 0}(t=-\infty)=0$. The matrices $\tilde{\rho}_{k\neq 0}$ have been neglected in the second line of (D.6), as they would contribute only to the next order in the $\tilde{H}_j$'s when replaced recursively by the solution of (D.7). The Bloch equation (D.5) now becomes

$$\begin{aligned}\partial_t\tilde{\rho}_0 =& -i\,[\tilde{H}_0\tilde{\rho}_0-\tilde{\rho}_0\tilde{H}_0^\dagger]\\ &-i\,\Big\{\sum_{j\neq 0}\sum_{k\neq 0}{\Omega_k}^{-1}[\hat{H}_j\hat{H}_k\tilde{\rho}_0\,e^{i(\Omega_j+\Omega_k)t}-\tilde{\rho}_0\hat{H}_k^\dagger\hat{H}_j^\dagger\,e^{-i(\Omega_j+\Omega_k)t}]\Big\}_0\\ &-i\,\Big\{\sum_{j\neq 0}\sum_{k\neq 0}{\Omega_k}^{-1}[\hat{H}_j\tilde{\rho}_0\hat{H}_k^\dagger\,e^{i(\Omega_j-\Omega_k)t}-\hat{H}_k\tilde{\rho}_0\hat{H}_j^\dagger\,e^{-i(\Omega_j-\Omega_k)t}]\Big\}_0\end{aligned} \tag{D.8}$$

where the second and third term on the r.h.s. are restricted to the frequency combinations satisfying $\Omega_j+\Omega_k\simeq 0$ and $\Omega_j-\Omega_k\simeq 0$ respectively. The last term can also be written as

$$-i\,\Big\{\sum_{j\neq 0}\sum_{k\neq 0}\frac{\Omega_j-\Omega_k}{\Omega_j\Omega_k}\,\hat{H}_j\tilde{\rho}_0\hat{H}_k^\dagger\,e^{i(\Omega_j-\Omega_k)t}\Big\}_0\,. \tag{D.9}$$

Thus it can be safely neglected, because $\Omega_j-\Omega_k\simeq 0$ due to the restriction to the low frequency part $\{\dots\}_0$.

Finally, the symmetrized effective Hamiltonian $\bar{H}$, restricted up to the second order in the fields (or first order in the inverse detuning ${\Omega_k}^{-1}$), becomes

$$\bar{H}=\frac{1}{2}\big[\tilde{H}_0+\tilde{H}_0^\dagger\big]+\frac{1}{2}\sum_{j\neq 0}\sum_{k\neq 0}{\Omega_k}^{-1}\big\{\tilde{H}_j\tilde{H}_k+\tilde{H}_k^\dagger\tilde{H}_j^\dagger\big\}_0\,. \tag{D.10}$$

We are left with the effective Bloch equations

$$\partial_t\bar{\rho}=-i\big[\bar{H}\,,\bar{\rho}\big] \tag{D.11}$$

for the density matrix $\bar{\rho}\equiv\tilde{\rho}_0$ expressed in the rotating frame, reduced to a finite number of resonant states, and restricted to all resonant processes up to the second order in the fields. This procedure, applied to the Hamiltonian defined by (3.40) to (3.43), leads to the effective Bloch equations (3.51) to (3.54).

D.2 Effective polarization current

In a similar way as for the effective Hamiltonian, one has to include the resonant second-order processes in the polarization current. Let $\mathbf{\Pi}$ be the momentum matrix restricted to the bands in group $\mathbb{A}$. To the first-order in the field, the polarization current can be written as

$$\boldsymbol{j} = \frac{1}{V}\mathrm{Tr}\big[\boldsymbol{\Pi}\tilde{\rho}\big] = \frac{1}{V}\sum_k \mathrm{Tr}\big[\boldsymbol{\Pi}\tilde{\rho}_k\big] \tag{D.12}$$

according to the expansion (D.3). After substituting the rapidly oscillating part $\rho_{k\neq 0}$ by its approximate expression (D.7), one finds

$$\begin{aligned} \boldsymbol{j} &= \frac{1}{V}\sum_k {\Omega_k}^{-1}\mathrm{Tr}\big[\boldsymbol{\Pi}\tilde{H}_k\tilde{\rho}_0\, e^{i\Omega_k t} + \boldsymbol{\Pi}\tilde{\rho}_0\tilde{H}_k^\dagger\, e^{-i\Omega_k t}\big] \\ &= \frac{1}{V}\mathrm{Tr}\big[\sum_k {\Omega_k}^{-1}(\boldsymbol{\Pi}\tilde{H}_k\, e^{i\Omega_k t} + \tilde{H}_k^\dagger\boldsymbol{\Pi}\, e^{-i\Omega_k t})\,\tilde{\rho}_0\big]\,. \end{aligned} \tag{D.13}$$

The cyclicity of the trace was used in the second line. Keeping only the frequencies of interest to us, we are left with the terms needed to extend the sum over the eliminated bands b in (3.68), (3.69) and (3.70) to all bands n leading to large denominators.

E Power spectrum of the far-field emission

The electromagnetic radiation emitted by a density of current $\boldsymbol{j}(\boldsymbol{r},t)$ in the finite volume V is described by the retarded vector potential

$$\boldsymbol{A}(\boldsymbol{r},t) = \frac{\mu_0}{4\pi}\int_V \frac{\boldsymbol{j}(\boldsymbol{r}',t-|\boldsymbol{r}-\boldsymbol{r}'|/c)}{|\boldsymbol{r}-\boldsymbol{r}'|}\,d^3\boldsymbol{r}' \tag{E.1}$$

(c is the speed of light). Far from the volume V, $|\boldsymbol{r}-\boldsymbol{r}'|$ can be approximated by the distance to the source $|\boldsymbol{r}| = r$, and the field (E.1) becomes

$$\boldsymbol{A}(r,t) = \frac{\mu_0}{4\pi r}\int_V \boldsymbol{j}(\boldsymbol{r}',t-r/c)\,d^3\boldsymbol{r}'\,. \tag{E.2}$$

The total power P radiated by the volume V at time t is given by the energy current leaving the sphere of radius r at time $t + r/c$. Let Σ_r be the spherical surface of radius r centered on the volume V, and

$$d\boldsymbol{\sigma} = r^2 \sin\theta\, d\theta d\phi\, \hat{\boldsymbol{e}}_r \tag{E.3}$$

the positively orientated surface element (in spherical coordinates). The radiated power can then be written as

$$P(t) = \int_{\Sigma_r} \boldsymbol{S}(\boldsymbol{r},t+r/c)\,d\boldsymbol{\sigma}\,, \tag{E.4}$$

where $\boldsymbol{S}$ is the Poynting vector defined by

$$\boldsymbol{S} = \boldsymbol{E}\wedge\boldsymbol{H} = -\frac{1}{\mu_0}\partial_t\boldsymbol{A}\wedge(\boldsymbol{\nabla}\wedge\boldsymbol{A})\,. \tag{E.5}$$

The spatial derivative in (E.5) is now replaced by a time derivative by using the following relation:

$$\partial_r\boldsymbol{j}(\boldsymbol{r}',t-r/c) = -\frac{1}{c}\partial_t\boldsymbol{j}(\boldsymbol{r}',t-r/c)\,. \tag{E.6}$$

Integrating over the surface, the radiated power becomes

$$P(t) = \frac{1}{6\pi\epsilon_0 c^3}\left[\int_V \partial_t \boldsymbol{j}(\boldsymbol{r}', t)\, d^3\boldsymbol{r}'\right]^2 . \tag{E.7}$$

Let us assume a homogeneous current density in the volume V. The power then reduces to

$$P(t) = \frac{V^2}{6\pi\epsilon_0 c^3}\left[\partial_t \boldsymbol{j}(t)\right]^2 , \tag{E.8}$$

and the corresponding power spectrum[1] is given by

$$P(\nu) = \frac{V^2}{12\pi^2\epsilon_0 c^3}\left|\int_{-\infty}^{+\infty} \partial_t \boldsymbol{j}(t)\, e^{-i2\pi\nu t}\, dt\right|^2 . \tag{E.9}$$

---

[1] Autocorrelation of the signal

References

[1] M. Göppert-Mayer, “Über Elementarakte mit zwei Quantensprüngen,” *Annalen der Physik*, vol. 9, p. 273, 1931.

[2] W. Kaiser and C. G. B. Garrett, “2-photon excitation in CaF_2:Eu^{2+},” *Physical Review Letters*, vol. 7, no. 6, p. 229, 1961.

[3] W. L. Peticolas, K. E. Rieckhoff, and J. P. Goldsborough, “Double photon excitation in organic crystals,” *Physical Review Letters*, vol. 10, no. 2, p. 43, 1963.

[4] P. P. Sorokin and N. Braslau, “Some theoretical aspects of proposed double quantum stimulated emission device,” *IBM Journal of Research and Development*, vol. 8, no. 2, p. 177, 1964.

[5] D. J. Gauthier, Q. L. Wu, S. E. Morin, and T. W. Mossberg, “Realization of a continuous-wave, 2-photon optical laser,” *Physical Review Letters*, vol. 68, no. 4, p. 464, 1992.

[6] F. Biraben, B. Cagnac, and G. Grynberg, “experimental evidence of 2-photon transition without Doppler broadening,” *Physical Review Letters*, vol. 32, no. 12, p. 643, 1974.

[7] M. Inoue and Y. Toyozawa, “2-photon absorption and energy band structure,” *Journal of the Physical Society of Japan*, vol. 20, no. 3, p. 363, 1965.

[8] T. R. Bader and A. Gold, “Polarization dependence of 2-photon absorption in solids,” *Physical Review*, vol. 171, no. 3, p. 997, 1968.

[9] M. M. Denisov and V. P. Makarov, “Polarization dependence of 2 photon absorption-coefficient in crystals,” *Journal of Physics Part C Solid State Physics*, vol. 5, no. 18, p. 2651, 1972.

[10] E. Doni, R. Girlanda, and G. P. Parravicini, “Note on polarization dependence of 2-photon absorption-coefficient in crystals,” *Physica Status Solidi B-Basic Research*, vol. 65, no. 1, p. 203, 1974.

[11] E. Doni, R. Girlanda, and G. P. Parravicini, "Selection-rules for direct creation of biexcitons by giant 2-photon absorption," *Solid State Communications*, vol. 17, no. 2, p. 189, 1975.

[12] E. Doni, R. Girlanda, and G. P. Parravicini, "Note on polarization dependence of 2-photon absorption-coefficient in crystals - extension to circularly polarized-light," *Physica Status Solidi B-Basic Research*, vol. 88, no. 2, p. 773, 1978.

[13] K. L. Hall, A. M. Darwish, E. P. Ippen, U. Koren, and G. Raybon, "Femtosecond index nonlinearities in InGaAsP optical amplifiers," *Applied Physics Letters*, vol. 62, no. 12, p. 1320, 1993.

[14] A. Villeneuve, C. C. Yang, P. G. J. Wigley, G. I. Stegeman, J. S. Aitchison, and C. N. Ironside, "Ultrafast all-optical switching in semiconductor nonlinear directional-couplers at half the band-gap," *Applied Physics Letters*, vol. 61, no. 2, p. 147, 1992.

[15] M. Dabbicco, A. M. Fox, G. von Plessen, and J. F. Ryan, "Role of $\chi^{(3)}$ anisotropy in the generation of squeezed light in semiconductors," *Physical Review B*, vol. 53, no. 8, p. 4479, 1996.

[16] A. Haché, Y. Kostoulas, R. Atanasov, J. L. P. Hughes, J. E. Sipe, and H. M. van Driel, "Observation of coherently controlled photocurrent in unbiased, bulk GaAs," *Physical Review Letters*, vol. 78, no. 2, p. 306, 1997.

[17] L. V. Keldysh, "Ionization in field of a strong electromagnetic wave," *Soviet Physics JETP-USSR*, vol. 20, no. 5, p. 1307, 1965.

[18] H. D. Jones and H. R. Reiss, "Intense-field effects in solids," *Physical Review B*, vol. 16, no. 6, p. 2466, 1977.

[19] H. S. Brandi and C. B. Dearaujo, "Multiphoton absorption-coefficients in solids - a universal curve," *Journal of Physics C-Solid State Physics*, vol. 16, no. 30, p. 5929, 1983.

[20] M. Sheik-Bahae, D. C. Hutchings, D. J. Hagan, and E. W. Van Stryland, "Dispersion of bound electronic nonlinear refraction in solids," *IEEE Journal of Quantum Electronics*, vol. 27, no. 6, p. 1296, 1991.

[21] P. N. Butcher and D. Cotter, *The elements of nonlinear optics.* Cambridge University Press, 1990.

[22] R. Loudon, "Theory of non-linear optical processes in semiconductors and insulators," *Proceedings of the Physical Society of London*, vol. 80, no. 516, p. 952, 1962.

[23] G. D. Mahan, “Theory of 2-photon spectroscopy in alkali halides,” *Physical Review Letters*, vol. 20, no. 7, p. 332, 1968.

[24] B. S. Wherrett, “Scaling rules for multiphoton interband absorption in semiconductors,” *Journal of the Optical Society of America B-Optical Physics*, vol. 1, no. 1, p. 67, 1984.

[25] R. Braunstein, “Nonlinear optical effects,” *Physical Review*, vol. 125, no. 2, p. 475, 1962.

[26] R. Braunstein and N. Ockman, “Optical double-photon absorption in CdS,” *Physical Review A-General Physics*, vol. 134, no. 2A, p. A499, 1964.

[27] C. R. Pidgeon, B. S. Wherrett, A. M. Johnston, J. Dempsey, and A. Miller, “2-photon absorption in zincblende semiconductors,” *Physical Review Letters*, vol. 42, no. 26, p. 1785, 1979.

[28] D. C. Hutchings and E. W. van Stryland, “Nondegenerate 2-photon absorption in zinc blende semiconductors,” *Journal of the Optical Society of America B-Optical Physics*, vol. 9, no. 11, p. 2065, 1992.

[29] M. I. Dykman and Y. G. Rubo, “Anisotropy of 2-photon absorption in cubic direct-band-gap semiconductors,” *Physical Review B*, vol. 45, no. 11, p. 5926, 1992.

[30] C. C. Lee and H. Y. Fan, “2-photon absorption with exciton effect for degenerate valence bands,” *Physical Review B*, vol. 9, no. 8, p. 3502, 1974.

[31] D. C. Hutchings and B. S. Wherrett, “Theory of anisotropy of 2-photon absorption in zincblende semiconductors,” *Physical Review B*, vol. 49, no. 4, p. 2418, 1994.

[32] E. Doni, G. P. Parravicini, and R. Girlanda, “Intensity of 2-photon excitonic absorption in 2-band and 3-band models,” *Solid State Communications*, vol. 14, no. 9, p. 873, 1974.

[33] H. N. Spector, “2-photon absorption in semiconducting quantum-well structures,” *Physical Review B*, vol. 35, no. 11, p. 5876, 1987.

[34] A. Pasquarello and A. Quattropani, “Gauge-invariant 2-photon transitions in quantum wells,” *Physical Review B*, vol. 38, no. 9, p. 6206, 1988.

[35] A. Pasquarello and A. Quattropani, “2-photon transitions to excitons in quantum-wells,” *Physical Review B*, vol. 42, no. 14, p. 9073, 1990.

[36] A. Shimizu, “2-photon absorption in quantum-well structures near half the direct band-gap,” *Physical Review B*, vol. 40, no. 2, p. 1403, 1989.

[37] A. Pasquarello and A. Quattropani, “Effect of continuum states on 2-photon absorption in quantum-wells,” *Physical Review B*, vol. 41, no. 18, p. 12728, 1990.

[38] A. Obeidat and J. Khurgin, “Excitonic enhancement of 2-photon absorption in semiconductor quantum-well structures,” *Journal of the Optical Society of America B-Optical Physics*, vol. 12, no. 7, p. 1222, 1995.

[39] R. Cingolani, M. Lepore, R. Tommasi, I. M. Catalano, H. Lage, D. Heitmann, K. Ploog, A. Shimizu, H. Sakaki, and T. Ogawa, “2-photon absorption in GaAs quantum wires,” *Physical Review Letters*, vol. 69, no. 8, p. 1276, 1992.

[40] R. Rinaldi, R. Cingolani, M. Lepore, M. Ferrara, I. M. Catalano, F. Rossi, L. Rota, E. Molinari, P. Lugli, U. Marti, D. Martin, F. Moriergemoud, P. Ruterana, and F. K. Reinhart, “Exciton binding-energy in GaAs V-shaped quantum wires,” *Physical Review Letters*, vol. 73, no. 21, p. 2899, 1994.

[41] A. Shimizu, T. Ogawa, and H. Sakaki, “2-photon absorption-spectra of quasi-low-dimensional exciton systems,” *Physical Review B*, vol. 45, no. 19, p. 11338, 1992.

[42] T. Ogawa and A. Shimizu, “Dimensional crossover of excitons in one-photon and 2-photon absorption processes,” *Physical Review B*, vol. 48, no. 7, p. 4910, 1993.

[43] T. Ogawa and T. Takagahara, “Optical-absorption and Sommerfeld factors of one-dimensional semiconductors - an exact treatment of excitonic effects,” *Physical Review B*, vol. 44, no. 15, p. 8138, 1991.

[44] J. B. Khurgin, “Nonlinear response of the semiconductor quantum-confined structures near and below the middle of the band-gap,” *Journal of the Optical Society of America B-Optical Physics*, vol. 11, no. 4, p. 624, 1994.

[45] J. M. Luttinger and W. Kohn, “Motion of electrons and holes in perturbed periodic fields,” *Physical Review*, vol. 97, no. 4, p. 869, 1955.

[46] G. Bastard, *Wave mechanics applied to semiconductor heterostructures.* Les Ulis (France): Les éditions de physique, 1990.

[47] M. G. Burt, “The justification for applying the effective-mass approximation to microstructures,” *Journal of Physics-Condensed Matter*, vol. 4, no. 32, p. 6651, 1992.

[48] A. Vaidyanathan, A. H. Guenther, and S. S. Mitra, "Band-structure calculations of the 2-photon absorption- coefficients of GaAs, InP, CdTe, and ZnSe," *Physical Review B*, vol. 24, no. 4, p. 2259, 1981.

[49] M. Murayama and T. Nakayama, "2-photon-absorption spectra originating from higher-energy transitions," *Physical Review B*, vol. 49, no. 8, p. 5737, 1994.

[50] M. Murayama and T. Nakayama, "Ab-initio calculations of 2-photon absorption-spectra in semiconductors," *Physical Review B*, vol. 52, no. 7, p. 4986, 1995.

[51] S. Krishnamurthy, A. Sher, and A. B. Chen, "Below band-gap optical absorption in semiconductor alloys," *Journal of Applied Physics*, vol. 88, no. 1, p. 260, 2000.

[52] J. E. Sipe and A. I. Shkrebtii, "Second-order optical response in semiconductors," *Physical Review B*, vol. 61, no. 8, p. 5337, 2000.

[53] T. I. Park, G. Gumbs, and Y. C. Chen, "Properties of the second-order nonlinear optical susceptibility $\chi^{(2)}$ in asymmetric undoped AlGaAs InGaAs double quantum wells," *Journal of Applied Physics*, vol. 86, no. 3, p. 1467, 1999.

[54] D. C. Hutchings and J. M. Arnold, "Determination of second-order nonlinear coefficients in semiconductors using pseudospin equations for three-level systems," *Physical Review B*, vol. 56, no. 7, p. 4056, 1997.

[55] A. Fiore, E. Rosencher, B. Vinter, D. Weill, and V. Berger, "2nd-order optical susceptibility of biased quantum-wells in the interband regime," *Physical Review B*, vol. 51, no. 19, p. 13192, 1995.

[56] C. Kelaidis, D. C. Hutchings, and J. M. Arnold, "Asymmetric 2-step GaAlAs quantum-well for cascaded 2nd-order processes," *IEEE Journal of Quantum Electronics*, vol. 30, no. 12, p. 2998, 1994.

[57] R. Atanasov, F. Bassani, and V. M. Agranovich, "2nd-order nonlinear-optical susceptibility of asymmetric quantum-wells," *Physical Review B*, vol. 50, no. 11, p. 7809, 1994.

[58] H. Kuwatsuka and H. Ishikawa, "Calculation of the 2nd-order optical nonlinear susceptibilities in biased $\mathrm{Al}_x\mathrm{Ga}_{1-x}\mathrm{As}$ quantum-wells," *Physical Review B*, vol. 50, no. 8, p. 5323, 1994.

[59] P. J. Harshman and S. Wang, "Asymmetric AlGaAs quantum-wells for 2nd-harmonic generation and quasiphase matching of visible-light in surface emitting wave- guides," *Applied Physics Letters*, vol. 60, no. 11, p. 1277, 1992.

[60] L. Tsang, S. L. Chuang, and S. M. Lee, "2nd-order nonlinear optical susceptibility of a quantum-well with an applied electric-field," *Physical Review B*, vol. 41, no. 9, p. 5942, 1990.

[61] L. Tsang and S. L. Chuang, "Exciton effects on 2nd-order nonlinear susceptibility in a quantum-well with an applied electric-field," *Physical Review B*, vol. 42, no. 8, p. 5229, 1990.

[62] J. Khurgin, "2nd-order nonlinear effects in asymmetric quantum-well structures," *Physical Review B*, vol. 38, no. 6, p. 4056, 1988.

[63] J. Khurgin, "2nd-order susceptibility of asymmetric coupled quantum-well structures," *Applied Physics Letters*, vol. 51, no. 25, p. 2100, 1987.

[64] J. Khurgin, "2nd-order intersubband nonlinear-optical susceptibilities of asymmetric quantum-well structures," *Journal of the Optical Society of America B-Optical Physics*, vol. 6, no. 9, p. 1673, 1989.

[65] L. Tsang, D. Ahn, and S. L. Chuang, "Electric-field control of optical 2nd-harmonic generation in a quantum well," *Applied Physics Letters*, vol. 52, no. 9, p. 697, 1988.

[66] M. J. Shaw, M. Jaros, Z. Xu, P. M. Fauchet, C. W. Rella, B. A. Richman, H. A. Schwettman, and G. W. Wicks, "2nd-harmonic generation in P-type asymmetric GaAs-Al$_x$Ga$_{1-x}$As-AlAs superlattices due to excitations between valence minibands," *Physical Review B*, vol. 50, no. 24, p. 18395, 1994.

[67] M. A. Cusack, M. J. Shaw, and M. Jaros, "Role of localization in determining 2nd-order optical nonlinearities in P-type GaAs-AlAs asymmetric quantum-wells," *Physical Review B*, vol. 49, no. 23, p. 16575, 1994.

[68] M. J. Shaw, K. B. Wong, and M. Jaros, "Microscopic origin of optical nonlinearities associated with excitations between valence minibands in P-type GaAs-AlAs and Si-Si$_{1-x}$Ge$_x$ heterostructures," *Physical Review B*, vol. 48, no. 3, p. 2001, 1993.

[69] X. H. H. Qu and H. Ruda, "2nd-harmonic generation using heavy-hole/light-hole intersubband transitions in asymmetric quantum-wells," *Applied Physics Letters*, vol. 62, no. 16, p. 1946, 1993.

[70] L. Tsang and S. L. Chuang, "2nd-harmonic generation and optical rectification using intersubband transitions in a biased P-type semiconductor quantum-well," *Applied Physics Letters*, vol. 60, no. 20, p. 2543, 1992.

[71] J. Mark and J. Mork, "Subpicosecond gain dynamics in InGaAsP optical amplifiers - experiment and theory," *Applied Physics Letters*, vol. 61, no. 19, p. 2281, 1992.

[72] J. Mork, J. Mark, and C. P. Seltzer, "Carrier heating in InGaAsP laser-amplifiers due to 2-photon absorption," *Applied Physics Letters*, vol. 64, no. 17, p. 2206, 1994.

[73] J. M. Tang and K. A. Shore, "Strong picosecond optical pulse propagation in semiconductor optical amplifiers at transparency," *IEEE Journal of Quantum Electronics*, vol. 34, no. 7, p. 1263, 1998.

[74] P. E. Selbmann, M. A. Dupertuis, S. Haacke, T. Hessler, J. L. Pleumeekers, and B. Deveaud, "Dynamical density matrix theory of multiphoton transitions in semiconductors," *Physica Status Solidi B-Basic Research*, vol. 206, no. 1, p. 219, 1998.

[75] C. N. Ironside, "2-photon gain semiconductor amplifier," *IEEE Journal of Quantum Electronics*, vol. 28, no. 4, p. 842, 1992.

[76] Z. C. Wang and H. Haken, "Theory of 2-photon lasers .2. fokker-planck equation treatment," *Zeitschrift Für Physik B-Condensed Matter*, vol. 56, no. 1, p. 77, 1984.

[77] M. M. T. Loy, "2-photon adiabatic inversion," *Physical Review Letters*, vol. 41, no. 7, p. 473, 1978.

[78] B. Nikolaus, D. Z. Zhang, and P. E. Toschek, "2-photon laser," *Physical Review Letters*, vol. 47, no. 3, p. 171, 1981.

[79] M. Brune, J. M. Raimond, P. Goy, L. Davidovich, and S. Haroche, "Realization of a 2-photon maser oscillator," *Physical Review Letters*, vol. 59, no. 17, p. 1899, 1987.

[80] L. M. Narducci, W. W. Eidson, P. Furcinitti, and D. C. Eteson, "Theory of a 2-photon laser-amplifier," *Physical Review A*, vol. 16, no. 4, p. 1665, 1977.

[81] Z. C. Wang and H. Haken, "Theory of 2-photon lasers .3. 2-photon laser with injected signal," *Zeitschrift Für Physik B-Condensed Matter*, vol. 56, no. 1, p. 83, 1984.

[82] S. Ovadia, M. Sargent, and S. T. Hendow, "Effects of dynamic Stark shifts on 2-photon side-mode instabilities," *Optics Letters*, vol. 10, no. 10, p. 505, 1985.

[83] C. Z. Ning and H. Haken, "Instability in degenerate 2-photon running wave laser," *Zeitschrift Für Physik B-Condensed Matter*, vol. 77, no. 1, p. 157, 1989.

[84] C. Z. Ning and H. Haken, "Generalized Ginzburg-Landau equation for self-pulsing instability in a 2-photon laser," *Zeitschrift Für Physik B-Condensed Matter*, vol. 77, no. 1, p. 163, 1989.

[85] S. Y. Zhu and M. O. Scully, "Theoretical-study of a 2-photon double-beam laser," *Physical Review A*, vol. 38, no. 10, p. 5433, 1988.

[86] A. W. Boone and S. Swain, "Theory of the degenerate 2-photon laser," *Physical Review A*, vol. 41, no. 1, p. 343, 1990.

[87] H. M. Concannon and D. J. Gauthier, "Simple rate-equation model for 2-photon lasers," *Optics Letters*, vol. 19, no. 7, p. 472, 1994.

[88] S. Bay, M. Elk, and P. Lambropoulos, "Aspects of the degenerate two-photon laser," *Journal of Physics B-Atomic Molecular and Optical Physics*, vol. 28, no. 24, p. 5359, 1995.

[89] J. F. Urchueguia, V. Espinosa, and G. J. De Valcarcel, "Nonlinear dynamics of a class-a two-photon laser with injected signal in cascade systems," *Journal of Modern Optics*, vol. 46, no. 10, p. 1483, 1999.

[90] M. Abdel-Aty and A. S. F. Obada, "Semiclassical stability analysis of a two-photon laser including spatial variation of the cavity field," *European Physical Journal D*, vol. 15, no. 3, p. 385, 2001.

[91] J. J. Fernandez-Soler, J. L. Font, R. Vilaseca, D. J. Gauthier, A. Kul'minskii, and O. Pfister, "Two-photon amplification and lasing in laser-driven potassium atoms: Theoretical analysis," *Physical Review A*, vol. 65, no. 3, p. 031803, 2002.

[92] V. C. Coffey, "Two-photon laser - is potassium the key to quantum teleportation?," *Laser Focus World*, vol. 37, no. 7, p. 42, 2001.

[93] O. Pfister, W. J. Brown, M. D. Stenner, and D. J. Gauthier, "Polarization instabilities in a two-photon laser," *Physical Review Letters*, vol. 86, no. 20, p. 4512, 2001.

[94] C. C. Yang, A. Villeneuve, G. I. Stegeman, C. H. Lin, and H. H. Lin, "Anisotropic 2-photon transitions in GaAs/AlGaAs multiple-quantum-well wave-guides," *IEEE Journal of Quantum Electronics*, vol. 29, no. 12, p. 2934, 1993.

[95] G. P. Agrawal and N. K. Dutta, *Long-wavelength semiconductor lasers.* New-York: Van Nostrand Rheinhold, 1986.

[96] U. Oesterle, R. P. Stanley, R. Houdré, M. Gailhanou, and M. Ilegems, “Molecular-beam epitaxy growth of an ultrahigh finesse microcavity,” *Journal of Crystal Growth*, vol. 150, no. 1-4, p. 1313, 1995.

[97] P. Král and J. E. Sipe, “Quantum kinetic theory of two-beam current injection in bulk semiconductors,” *Physical Review B*, vol. 61, no. 8, p. 5381, 2000.

[98] A. F. Starace, “Length and velocity formulas in approximate oscillator-strength calculations,” *Physical Review A*, vol. 3, no. 4, p. 1242, 1971.

[99] R. Girlanda, A. Quattropani, and P. Schwendimann, “2-photon transitions to exciton-states in semiconductors - application to CuCl,” *Physical Review B*, vol. 24, no. 4, p. 2009, 1981.

[100] S. Ismail-Beigi, E. K. Chang, and S. G. Louie, “Coupling of nonlocal potentials to electromagnetic fields,” *Physical Review Letters*, vol. 8708, no. 8, p. 087402, 2001.

[101] E. Desalvo, R. Girlanda, and A. Quattropani, “2-photon interband-transitions in semiconductors in a static magnetic-field - nonlocal effects,” *Nuovo Cimento Della Societa Italiana Di Fisica D-Condensed Matter Atomic Molecular and Chemical Physics Fluids Plasmas Biophysics*, vol. 5, no. 1, p. 63, 1985.

[102] E. Desalvo and R. Girlanda, “2-photon interband-transitions in crossed electric and magnetic-fields in semiconductors - nonlocal effects,” *Nuovo Cimento Della Societa Italiana Di Fisica D-Condensed Matter Atomic Molecular and Chemical Physics Fluids Plasmas Biophysics*, vol. 15, no. 10, p. 1321, 1993.

[103] J. M. Arnold and D. C. Hutchings, “Three-level description of optical nonlinearities in semiconductors,” *Electromagnetics*, vol. 19, no. 6, p. 479, 1999.

[104] C. Aversa and J. E. Sipe, “Nonlinear-optical susceptibilities of semiconductors - results with a length-gauge analysis,” *Physical Review B*, vol. 52, no. 20, p. 14636, 1995.

[105] E. I. Blount, “Formalisms of band theory,” *Solid State Physics-Advances in Research and Applications*, vol. 13, p. 305, 1962.

[106] K. H. Yang, “Gauge transformations and quantum-mechanics .1. gauge invariant interpretation of quantum-mechanics,” *Annals of Physics*, vol. 101, no. 1, p. 62, 1976.

[107] D. H. Kobe, “Gauge-invariant resolution of the controversy over length versus velocity forms of the interaction with electric-dipole radiation,” *Physical Review A*, vol. 19, no. 1, p. 205, 1979.

[108] M. Lindberg and S. W. Koch, "Effective bloch equations for semiconductors," *Physical Review B*, vol. 38, no. 5, p. 3342, 1988.

[109] H. Haug and S. W. Koch, *Quantum Theory of the Optical and Electronic Properties of Semiconductors.* Singapore: World Scientific, 1990.

[110] U. Bockelmann and G. Bastard, "Interband absorption in quantum wires .1. zero-magnetic-field case," *Physical Review B*, vol. 45, no. 4, p. 1688, 1992.

[111] H. Haken, *Quantenfeldtheorie des Festkörpers.* Stuttgart: B. G. Teubner, 1973.

[112] R. Zimmermann, "Theoretical description of collective excitations: Bloch equations and relaxation mechanisms," in *Spectroscopy and Dynamics of Collective Excitations in Solids* (B. Di Bartolo and S. Kyrkos, eds.), p. 123, New York: Plenum Press, 1997.

[113] T. Inui, Y. Tanabe, and Y. Onodera, *Group theory and its applications in physics.* Berlin Heidelberg: Springer-Verlag, 1990.

[114] A. Barenco and M. A. Dupertuis, "Quantum many-body states of excitons in a small quantum dot," *Physical Review B*, vol. 52, no. 4, p. 2766, 1995.

[115] M. A. Dupertuis, "The symmetry of excitons in quantum wires," *Physica Status Solidi a-Applied Research*, vol. 178, no. 1, p. 221, 2000.

[116] A. L. Fetter and J. D. Walecka, *Quantum theory of many-particle systems.* McGraw-Hill, 1971.

[117] G. D. Mahan, *Many particle physics.* New York: Plenum Press, 1986.

[118] H. Haug and A.-P. Jauho, *Quantum kinetics in transport and optics of semiconductors.* Berlin Heidelberg: Springer-Verlag, 1996.

[119] M. G. Burt, "Direct derivation of effective-mass equations for microstructures with atomically abrupt boundaries," *Physical Review B*, vol. 50, no. 11, p. 7518, 1994.

[120] B. A. Foreman, "Strong linear-k valence-band mixing at semiconductor heterojunctions," *Physical Review Letters*, vol. 86, no. 12, p. 2641, 2001.

[121] B. A. Foreman, "Connection rules versus differential equations for envelope functions in abrupt heterostructures," *Physical Review Letters*, vol. 80, no. 17, p. 3823, 1998.

[122] G. L. Bir and G. E. Pikus, *Symmetry and strain-induced effects in semiconductors.* New York: John Wiley & sons, 1974.

[123] E. B. Becker, G. F. Carey, and J. T. Oden, *The Texas Finite Element Series.* London: Prentice-Hall International, Inc., 1981.

[124] S. L. Altmann and P. Herzig, *Point-group theory tables.* Oxford University Press, 1994.

[125] G. F. Koster, *Space groups and their representations.* New York: Academic Press, 1957.

[126] E. Rosencher and B. Vinter, *Optoélectronique.* Paris: Masson, 1998.

[127] L. W. Molenkamp, R. Eppenga, G. W. Thooft, P. Dawson, C. T. Foxon, and K. J. Moore, "Determination of valence-band effective-mass anisotropy in GaAs quantum wells by optical spectroscopy," *Physical Review B*, vol. 38, no. 6, p. 4314, 1988.

[128] R. Atanasov, A. Haché, J. L. P. Hughes, H. M. van Driel, and J. E. Sipe, "Coherent control of photocurrent generation in bulk semiconductors," *Physical Review Letters*, vol. 76, no. 10, p. 1703, 1996.

[129] E. Dupont, P. B. Corkum, H. C. Liu, M. Buchanan, and Z. R. Wasilewski, "Phase-controlled currents in semiconductors," *Physical Review Letters*, vol. 74, no. 18, p. 3596, 1995.

[130] J. B. Khurgin, "Generation of the teraherz radiation using $\chi^{(3)}$ in semiconductor," *Journal of Nonlinear Optical Physics & Materials*, vol. 4, no. 1, p. 163, 1995.

[131] D. Côté, J. M. Fraser, M. DeCamp, P. H. Bucksbaum, and H. M. van Driel, "THz emission from coherently controlled photocurrents in GaAs," *Applied Physics Letters*, vol. 75, no. 25, p. 3959, 1999.

[132] J. Stippler, C. Schlichenmaier, A. Knorr, T. Meier, M. Lindberg, P. Thomas, and S. W. Koch, "Current echoes induced by coherent control," *Physica Status Solidi B-Basic Research*, vol. 221, no. 1, p. 379, 2000.

[133] R. D. R. Bhat and J. E. Sipe, "Optically injected spin currents in semiconductors," *Physical Review Letters*, vol. 85, no. 25, p. 5432, 2000.

[134] M. J. Stevens, A. L. Smirl, R. D. R. Bhat, J. E. Sipe, and H. M. van Driel, "Coherent control of an optically injected ballistic spin-polarized current in bulk GaAs," *Journal of Applied Physics*, vol. 91, no. 7, p. 4382, 2002.

[135] J. Hübner, W. W. Rühle, M. Klude, D. Hommel, R. D. R. Bhat, J. E. Sipe, and H. M. van Driel, "Direct observation of optically injected spin-polarized currents in semiconductors," *Physical Review Letters*, vol. 90, no. 21, p. 216601, 2003.

[136] M. J. Stevens, A. L. Smirl, R. D. R. Bhat, A. Najmaie, J. E. Sipe, and H. M. van Driel, "Quantum interference control of ballistic pure spin currents in semiconductors," *Physical Review Letters*, vol. 90, no. 13, p. 136603, 2003.

[137] H. M. van Driel, R. D. R. Bhat, D. Côté, N. Laman, J. E. Sipe, M. J. Stevens, and A. L. Smirl, "Coherent generation and control of electrical and spin currents in semiconductors," in *26th International Conference on the Physics of Semiconductors* (A. R. L. Davies and J. H., eds.), (Edinburgh, UK), 2002.

[138] A. Leitenstorfer, C. Furst, A. Laubereau, W. Kaiser, G. Trankle, and G. Weimann, "Femtosecond carrier dynamics in GaAs far from equilibrium," *Physical Review Letters*, vol. 76, no. 9, p. 1545, 1996.

[139] A. Haché, J. E. Sipe, and H. M. van Driel, "Quantum interference control of electrical currents in GaAs," *IEEE Journal of Quantum Electronics*, vol. 34, no. 7, p. 1144, 1998.

[140] M. A. Dupertuis, E. Martinet, D. Y. Oberli, and E. Kapon, "The impact of low symmetry on the electronic and optical properties of quantum wires," *Europhysics Letters*, vol. 52, no. 4, p. 420, 2000.

[141] F. Vouilloz, D. Y. Oberli, M. A. Dupertuis, A. Gustafsson, F. Reinhardt, and E. Kapon, "Effect of lateral confinement on valence-band mixing and polarization anisotropy in quantum wires," *Physical Review B*, vol. 57, no. 19, p. 12378, 1998.

[142] M. A. Dupertuis, D. Y. Oberli, and E. Kapon, "Computing excitons in v-shaped quantum wires including band-structure and dielectric effects : binding energies and polarization anisotropy of the bright A_1, B_1, A_2 excitons," in *International Conference on Computational Nanoscience ICCN 2002*, (Puerto Rico, U.S.A.), Computational Publications, 2002.

[143] G. F. Koster, J. O. Dimmock, R. G. Wheeler, and H. Statz, *Properties of the thirty-two point groups.* Cambridge, Massachusetts: M.I.T. Press, 1966.

[144] M. A. Dupertuis, "Consequences of low symmetry in quantum wires: Exciton degeneracies and quasi-equilibrium high-density regime," *Physica Status Solidi B-Basic Research*, vol. 221, no. 1, p. 323, 2000.

[145] E. O. Gobel, K. Leo, T. C. Damen, J. Shah, S. Schmitt-Rink, W. Schafer, J. F. Muller, and K. Kohler, "Quantum beats of excitons in quantum-wells," *Physical Review Letters*, vol. 64, no. 15, p. 1801, 1990.

[146] K. Leo, T. C. Damen, J. Shah, E. O. Gobel, and K. Kohler, "Quantum beats of light hole and heavy hole excitons in quantum- wells," *Applied Physics Letters*, vol. 57, no. 1, p. 19, 1990.

[147] S. Schmitt-Rink, D. Bennhardt, V. Heuckeroth, P. Thomas, P. Haring, G. Maidorn, H. Bakker, K. Leo, D. S. Kim, J. D. Shah, and K. Kohler, "Polarization dependence of heavy-hole and light-hole quantum beats," *Physical Review B*, vol. 46, no. 16, p. 10460, 1992.

List of publications

D. H. Marti, M. A. Dupertuis, B. Deveaud, “Dynamics of optical injection of charge and spin currents in quantum wells,” submitted for publication.

D. H. Marti, M. A. Dupertuis, B. Deveaud, “Feasibility study for degenerate two-photon gain in a semiconductor microcavity,” *IEEE Journal of Quantum Electronics*, vol. 39, no. 9, p. 1066, 2003.

M. S. Nomura, F. Salleras, M. A. Dupertuis, L. Kappei, D. Marti, B. Deveaud, J. Y. Emery, A. Crottini, B. Dagens, T. Shimura, and K. Kuroda, “Density clamping and longitudinal spatial hole burning in a gain-clamped semiconductor optical amplifier,” *Applied Physics Letters*, vol. 81, no. 15, p. 2692, 2002.

J. N. Fehr, M. A. Dupertuis, T. P. Hessler, L. Kappei, D. Marti, F. Salleras, M. S. Nomura, B. Deveaud, J. Y. Emery, and B. Dagens, “Hot phonons and Auger related carrier heating in semiconductor optical amplifiers,” *IEEE Journal of Quantum Electronics*, vol. 38, no. 6, p. 674, 2002.

M. A. Dupertuis, D. Marti, and F. Michelini, “The band structure of Z-like quantum wires,” *Physica Status Solidi B-Basic Research*, vol. 234, no. 1, p. 329, 2002.

J. N. Fehr, M. A. Dupertuis, T. P. Hessler, L. Kappei, D. Marti, P. E. Selbmann, B. Deveaud, J. L. Pleumeekers, J. Y. Emery, and B. Dagens, “Direct observation of longitudinal spatial hole burning in semiconductor optical amplifiers with injection,” *Applied Physics Letters*, vol. 78, no. 26, p. 4079, 2001.

Curriculum Vitæ

DANIEL MARTI

Date of birth	:	July 2, 1976
Nationality	:	Swiss

1999–2003	Ph.D. student at the Institute of Quantum Electronics and Photonics, École Polytechnique Fédérale de Lausanne (EPFL)
1998–1999	Diploma thesis at the Institute of Quantum Electronics and Photonics, EPFL
Aug.–Sep. 1997	Stay at the ABB Research Center, Baden, Switzerland; setup of a measurement chain for the breakdown voltage of insulators at low temperature
1994–1999	Undergraduate studies of physics at EPFL
June 1994	Maturité fédérale, Type C, Gymnase cantonal de La Chaux-de-Fonds, Switzerland

---